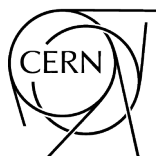


**Proceedings of the
CERN-BINP Workshop for Young Scientists in e^+e^- Colliders**

Geneva, Switzerland
22 – 25 August 2016

Editors: V. Brancolini
L. Linssen



CERN Proceedings

Published by CERN, CH-1211 Geneva 23, Switzerland

ISBN 978-92-9083-451-9 (paperback)

ISBN 978-92-9083-452-6 (PDF)


ISSN 2078-8835 (Print)

ISSN 2518-315X (Online)

DOI <https://doi.org/10.23727/CERN-Proceedings-2017-001>

Available online at <http://publishing.cern.ch/> and <http://cds.cern.ch/>

Copyright © the Authors, 2017

 Creative Commons Attribution 4.0

Knowledge transfer is an integral part of CERN's mission.

CERN publishes this volume Open Access under the Creative Commons Attribution 4.0 license (<http://creativecommons.org/licenses/by/4.0/>) in order to permit its wide dissemination and use. The submission of a contribution to CERN Proceedings shall be deemed to constitute the contributor's agreement to this copyright and license statement. Contributors are requested to obtain any clearances that may be necessary for this purpose.

This volume is indexed in: CERN Document Server (CDS), INSPIRE.

This volume should be cited as:

Proceedings of the CERN-BINP Workshop for Young Scientists in e^+e^- Colliders, Geneva, Switzerland, 22 – 25 August 2016, edited by V. Brancolini and L. Linssen, CERN Proceedings, Vol. 1/2017, CERN-Proceedings-2017-001 (CERN, Geneva, 2017), <https://doi.org/10.23727/CERN-Proceedings-2017-001>

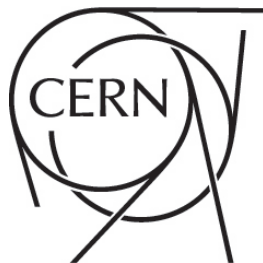
A contribution in this volume should be cited as:



[Author name(s)], in Proceedings of the CERN-BINP Workshop for Young Scientists in e^+e^- Colliders, Geneva, Switzerland, 22 – 25 August 2016, edited by V. Brancolini and L. Linssen, CERN Proceedings, Vol. 1/2017, CERN-Proceedings-2017-001 (CERN, Geneva, 2017), pp. [first page]–[last page], <https://doi.org/10.23727/CERN-Proceedings-2017-001>. [first page]

The group picture on page xv of these proceedings was taken by Steven Schramm.

Acknowledgements

This project has received funding from the European Union's Horizon 2020 Research and Innovation programme under Grant Agreement no. 654166.



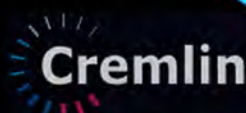
 

CERN-BINP Workshop
for young scientists
in e^+e^- colliders

eCOL 2016

August 22 - 24, 2016

CERN, Geneva, Switzerland
<https://indico.desy.de/conferenceDisplay.py?confid=14124>

 **Cremlin**
<http://www.cremlin.eu/>

Supported
by **Cremlin**
(*Connecting Russian and European
Measures for Large-scale research INfrastructures*)

Abstract

The "CERN-BINP Workshop for Young Scientists in e^+e^- Colliders" was organised in the framework of the [CREMLIN project](#) funded by the European Union. The [workshop](#) took place from August 22nd to August 25th 2016 at CERN. At this occasion some 30 scientists from Budker Institute [BINP](#) and 20 scientists from [CERN](#), as well as 10 further participants from Austria, China, France, Germany and Turkey gathered to present and discuss their research on electron-positron colliders. Within CREMLIN, BINP and CERN coordinate a work package focusing on a future Super-Charm-Tau factory at BINP. Whilst BINP is preparing for the [BINP Super Charm-Tau factory](#), which aims at producing e^+e^- collisions at unprecedented intensity up to 5 GeV centre-of-mass energy, CERN is hosting design studies for two different e^+e^- colliders, [FCC-ee](#) and [CLIC](#), with very high centre-of-mass energies ranging from 90 GeV to 3 TeV. In matters of physics, design and technologies the BINP and CERN studies address technological and scientific questions of common interest. Similar issues are dealt with in the framework of other flavour factories and energy frontier e^+e^- colliders worldwide.

Organizing Committee

Maksim Kuzin (BINP)
Eugene Levichev (BINP)
Lucie Linssen (CERN)
Marko Petric (CERN)
Kate Ross (CERN)
Yuriy Tikhonov (BINP)
Frank Zimmermann (CERN)

Reviewers

Konrad Elsener (CERN)
John Jowett (CERN)
Eugene Levichev (BINP)
Lucie Linssen (CERN)
Andreas Alexander Maier (CERN)
Marko Petric (CERN)
Sergey Serednyakov (BINP)
Eva Sicking (CERN)
Rickard Ström (CERN)
Rogelio Tomás (CERN)

Executive Summary

"Overview on technological requirements and R&D progress, linking European and worldwide know-how to the new generation of highly efficient lepton colliders"

The Super Charm-Tau factory (SCT) at BINP, Novosibirsk is designed as a low energy electron-positron collider with unprecedented high luminosity of $0.5 - 1 \cdot 10^{35} \text{ cm}^{-2}\text{s}^{-1}$ at a centre-of-mass energy between 2 GeV and 5 GeV with possibility to exploit longitudinally polarized electrons at the interaction point (IP). The main aim of the SCT project is the study of charmonium and tau-lepton physics. SCT will provide excellent possibilities for search of new physics and for high-precision measurements of known phenomena. It is essential to create an overview and identify synergies and complementarities between the various lepton colliders worldwide, in particular those under development at CERN, in order to maintain a global basis for the SCT collaboration.

Other lepton colliders operating or planned are CLIC and FCC-ee at CERN, BEPC II and CEPC in China, SuperKEKB and ILC in Japan and DAFNE in Italy LNF/INFN. Despite the fact that all these facilities have different energy ranges (from 0.5 GeV per beam at DAFNE, up to 1 TeV at ILC and 3 TeV final energy at CLIC), different sizes (from 100 m for DAFNE up to 100 km for FCC-ee), different configurations (linear versus circular) and luminosities differing by orders of magnitude, there are still many similarities in the collider designs. The reason is that all these colliders operate at the cutting edge of accelerator physics and technology to achieve their superior performance and therefore they should all use the most advanced solutions.

The Novosibirsk SCT factory will apply a Crab Waist collision scheme (originally proposed in 2006 by Pantaleo Raimondi for the Italian SuperB factory) with a large crossing angle, a large Piwinski parameter and low emittance beams. A novel collision technology was extensively studied and implemented at DAFNE, and the experience of the Frascati ϕ -factory is of great importance for the SCT project realisation. Generally, the same approach is used for DAFNE (where it is called a nano-beam scheme) and FCC-ee. The major features of the lepton colliders stipulating a basis for synergetic collaboration with SCT are listed below:

- An extremely low vertical beta function at the IP (1 mm for FCC-ee and SCT and 0.3 mm for SuperKEKB) and, consequently, a very high vertical beta in the first final-focus quadrupole (up to several kilometres) result in the same problems for all three factories with local chromaticity correction and dynamic aperture and momentum acceptance limitations. The very high beta function in the final-focus quadrupoles requires low nonlinear contents of the quadrupole field, high production accuracy and tough tolerances for assembly and alignment.
- Crab Waist beam-beam effects for high-density colliding-beam studies require fast and effective simulation codes. One of the most popular and widely used codes to explore the beam-beam effects in colliders and to optimize the luminosity is called LIFETRAC. It was developed at BINP and presently it is intensively used at DAFNE, SuperKEKB and FCC-ee. Another popular program was developed at KEK in Japan and is frequently used for crosschecks. The powerful CERN computer cluster is required for this sophisticated and time-consuming computation.
- One of the critical parts of Crab Waist colliders is their final-focus arrangement. Due to the extremely low vertical beta at the IP, the first quadrupole is located closely to the IP inside the detector area. A design of the extremely compact high-gradient (up to 100 T/m) quadrupole magnet is a challenging task. Presently the BINP design of the double-aperture final-focus quadrupole with iron yoke, originally proposed for SCT, is also considered as a possible candidate for the FCC-ee final-focus magnet. Another option based on double-helix superconducting coils was suggested for the Italian SuperB factory and is also studied at FCC-ee and SCT.

- Concerning the machine-detector interface (MDI): the final-focus quadrupole magnets inside the detector volume, the detector solenoid, the anti-solenoids to compensate the solenoid field, as well as the detection equipment (such as the luminometer) render the interaction-region design very complex for both FCC-ee and SCT. Nevertheless, despite the fact that ILC and CLIC are linear colliders, their MDI region with strong quadrupole magnets, solenoid system and local compensation of the IP chromaticity is very similar to the MDI region of circular super-factories, providing a good example of synergetic design and complementarity.
- Another topic common to SCT, FCC-ee and SuperKEKB relates to the high beam current. For SCT and FCC-ee (at the Z-pole energy) the total beam current in each ring is about 1.5 A while for SuperKEKB it exceeds 2 A. High current effects, including beams interacting with their environment, cause lots of dangerous collective instabilities, ion clouds (in the electron ring) and electron clouds (in the positron ring), as well as the heating of vacuum components by the RF bunch field. These effects were carefully studied at PEP (SLAC, USA), KEKB and DAFNE. Unfortunately at BINP the maximum current circulating in the electron-positron colliders is smaller (around 0.5 A). Therefore, relevant assistance to the SCT project in the domains of theoretical calculations and simulations, low-impedance vacuum duct design, HOM free RF cavity design and fast-feedback system development would be extremely useful.
- Due to their high luminosity all the future lepton colliders require intensive and efficient electron and positron sources. The laser driven RF electron source is one of the key elements for such future electron-positron colliders. Similar electron guns with high productivity and beam quality (emittance, stability, energy spread) are necessary for modern synchrotron light sources and free electron lasers. Therefore the relevant laboratories could contribute to the SCT project in the area of electron gun development.
- There is another good example of the synergy between future circular e^+e^- colliders and the light sources. The Crab Waist concept requires beams with very low emittance (the FCC-ee vertical emittance at 45 GeV is 1 pm). This is also an intrinsic feature of light source storage rings. Possible collaboration between the European synchrotron light facilities (ESRF, SOLEIL, PETRA III, MAX IV, etc.) and the Novosibirsk SCT factory (as well as with the CERN FCC-ee project) could be very promising and fruitful. Accurate energy calibration is essential for the FCC-ee experiments at Z and WW centre-of-mass energies. It is planned to measure the Z-boson mass at FCC-ee with an expected statistical accuracy of $\sim 2 \cdot 10^{-6}$ for precise tests of the Standard Model. For this purpose the resonant depolarisation technique, which provides the most precise beam-energy measurement, will be used at FCC-ee. BINP is one of the world leading laboratories exploiting the resonant depolarisation method for beam energy calibration. Presently BINP has a record relative accuracy of the beam energy determination of $\sim 10^{-6}$ at the VEPP-4M collider. The BINP team collaborates with the FCC-ee project for the beam energy measurement by resonant depolarisation or by other methods, such as Compton backscattering or magnetic spectrometers.

Finally we mention briefly some examples of other accelerator technology aspects, which might form a solid basis for collaboration between the SCT factory and other modern electron storage rings (colliders and light sources):

- precise magnets with high-quality magnetic field;
- vacuum chambers with coatings and/or surface treatments to suppress electron clouds;
- superconducting RF systems and solid-state RF generators;
- beam-position monitors with approx 1 μm accuracy;
- control system software based on the EPICS or TANGO platforms.

Concerning synergies in the design and technology development for the physics experiments at the various e^+e^- colliders mentioned above, the situation can be summarised in a similar way. Comparing experiments at SCT in Novosibirsk, CLIC and FCC-ee at CERN, BEPC II in China, DAFNE and ILC in Japan and DAFNE in Italy, there are large overlaps in technology considerations despite the different energy ranges. The BES III

detector at BEPC II and the KLOE detector at DAFNE have collected data since several years. The BELLE II detector at SuperKEKB is currently under construction, while future detectors at SCT, ILC, FCC-ee, CEPC and CLIC are in a design and technology development phase. As the most advanced technologies are of prime interest for the following discussion, we concentrate on the experiments currently in a construction phase or in a design and technology development phase. The corresponding facilities aim for high luminosities in the range of $10^{34} \text{ cm}^{-2}\text{s}^{-1}$ to $10^{36} \text{ cm}^{-2}\text{s}^{-1}$, depending on the collider energy. As e^+e^- colliders are inherently very accurate physics probes, ultimate accuracy is also required for the design and technology choices of the experiments.

As a result, the detector requirements can be summarised as follow:

- excellent momentum resolution for charged particles;
- good energy resolution for photons and electrons (flavour factories) as well as for jets (high-energy colliders);
- ultimate particle-identification capabilities (flavour factories) or good particle-identification capabilities (high-energy colliders);
- excellent flavour-tagging capabilities;
- digitisation and data acquisition systems capable of recording and transmitting data at high rates;
- a high-performance trigger system, required at high-luminosity flavour factories or CEPC/FCC-ee operating at the Z pole.

In practice, going outwards from the interaction point, the experiments are composed of:

- a thin vacuum chamber, typically beryllium of 0.6 mm to 1 mm thickness in the central detector region. In the case of flavour factories and circular high-energy colliders the vacuum chamber includes a thin inner metal layer (e.g. gold, copper) for the absorption of synchrotron radiation or for conductivity reasons related to RF bunch effects;
- a highly accurate vertex detector, located as close as possible to the beam (at radii from 14 mm to 50 mm). The required single point resolution is as small as $3 \mu\text{m}$ at CLIC and ILC. In the case of CLIC hit time-stamping capability of a few ns is required in order to reduce the impact from beamstrahlung particles. The technology choices for the vertex detector are either thin silicon pixel detectors (Belle II, ILC, CLIC, SCT) or a low-mass TPC (Time Projection Chamber) gas detector (SCT);
- a low-mass main tracker. The most prominent choices for the main tracker are a large drift chamber (SCT, Belle II, FCC-ee), a TPC (ILC, CEPC) or a silicon tracking system (ILC, CLIC, FCC-ee). While the gas detectors offer sizeable low-mass volumes and many measurement points for excellent pattern recognition, the silicon-based tracking option offers the most accurate single point resolution;
- a particle-identification detector system based on aerogel ring-imaging technology (SCT, Belle II) or Cherenkov time-of-propagation technology (Belle II). The need for such highly selective particle-identification systems is specific to flavour factories;
- an electromagnetic calorimeter, based on pure CsI crystals (Belle II, SCT) or CsI(Tl) crystals (Belle II) or based on highly granular particle-flow calorimetry with silicon sensors (ILC, CLIC, CEPC, FCC-ee) or dual readout calorimetry with scintillating fibres (FCC-ee, CEPC);
- a hadron calorimeter based on highly granular particle-flow calorimetry using scintillator tiles as sensors (ILC, CLIC, FCC-ee, CEPC) or dual readout calorimetry (FCC-ee, CEPC);
- a superconducting solenoid with a magnetic fields strength ranging from 1 T to 5 T;
- an iron yoke with an embedded muon system. The muon system comprises detectors of large area. Typical technology choices are RPCs or plastic scintillators.

Several of the technologies listed above are forefront detector R&D subjects, exploiting recently developed ideas or are based on technologies, which have become available only recently. One example is the TPC using modern micro-pattern gas detector technology. Micro-pattern gas detector structures, GEM or Micromegas, provide several advantages over traditional wire planes. They offer high-gain signal amplification with superior rate capability as well as new schemes for reducing ion backflow, allowing the TPC to be read out in continuous mode. Moreover they offer superior spatial resolution and allow for more flexible geometries compared to traditional wire planes. So far, the operational experience with TPCs based on GEMs or Micromegas in collider experiments is still limited. Large R&D efforts are ongoing in preparation for such TPC detectors for the upgrade of the ALICE experiment, for the PANDA experiment at FAIR and for the ILD experiment at ILC. BINP has built and operated GEM detectors for the tagging system of the KEDR experiment and for the VEPP-3 deuteron facility. Moreover BINP is developing GEM-based TPCs for the upgrade of the CMD-3 experiment and for SCT. These developments efforts involve ongoing broad international cooperation.

Another example is the novel ring-imaging aerogel technology, such as the multilayer focusing aerogel RICH (FARICH) for SCT. It is able to provide high μ/π separation below 1 GeV/c and excellent $\pi/K/p$ separation for high momentum particles. At SCT the Cherenkov photons will be detected by silicon-photomultipliers (SiPM). About a million SiPM will be needed for FARICH. The high-energy e^+e^- colliders ILC, CLIC and FCC-ee foresee a similar number of SiPM for their fine-grained hadron calorimeters with small scintillator tiles as the active medium. SiPM development and mass production are therefore a prominent example of synergy, where Russian producers are already playing an important role.

Numerous examples of the e^+e^- accelerator and detector concepts and technologies listed in this summary are described in more detail in these proceedings.

Eugene Levichev and Lucie Linssen
(On behalf of the Organizing Committee)

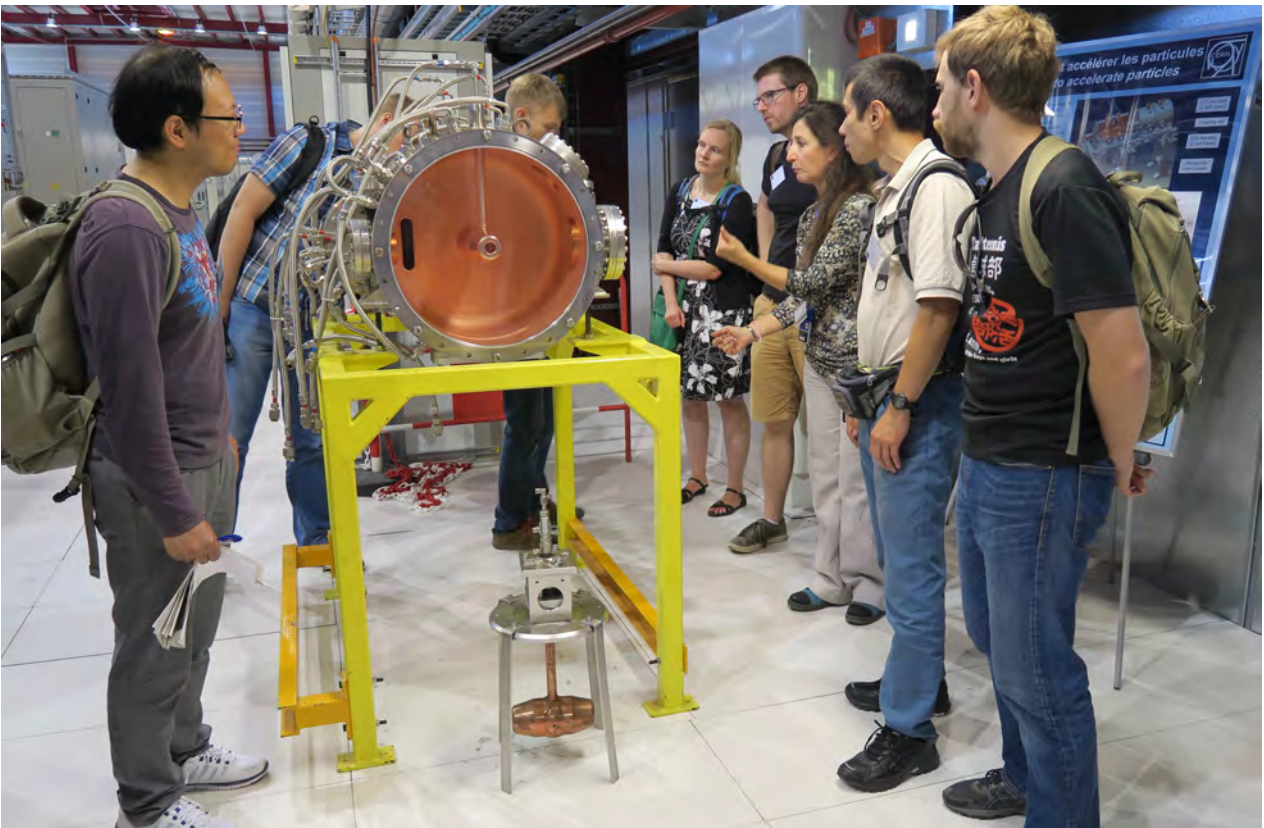
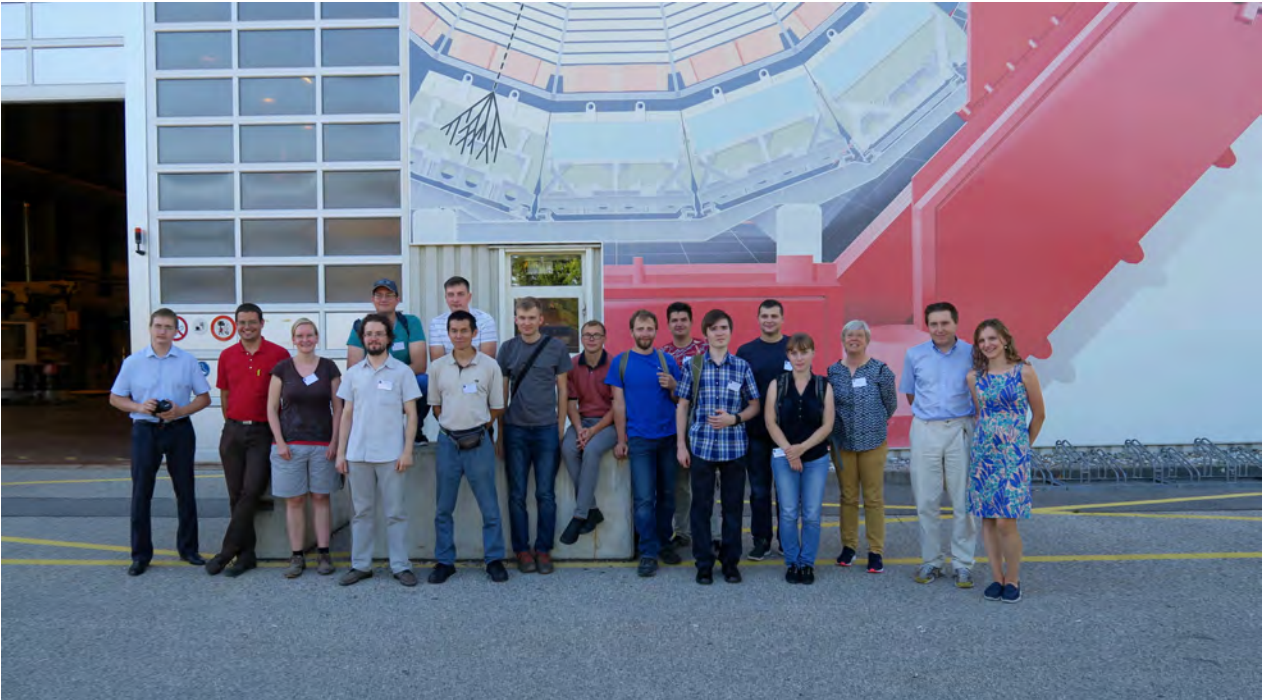
Participants

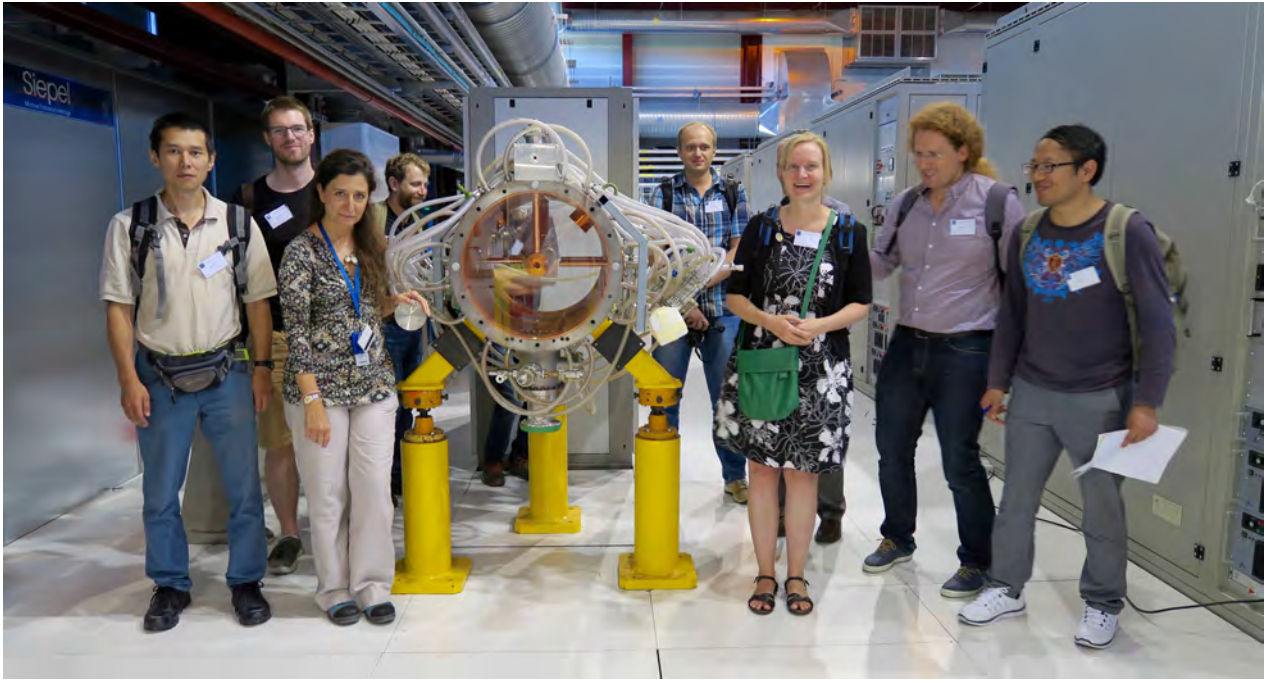
Sarah Aull (CERN, Switzerland)
Grigory Baranov (BINP, Russia)
Alexander Barniakov (BINP, Russia)
Tianjian Bian (IHEP, China)
Kerstin Borrás (DESY, Germany)
Andrey Denisov (BINP, Russia)
Viktor Dorokhov (BINP, Russia)
Jan Ebbing (CERN, Switzerland and Karlsruhe Institute of Technology, Germany)
Dima El Khechen (Laboratoire de l'Accélérateur Linéaire, France)
Ozgun Etisken (Ankara University, Turkey)
Vaagn Gambaryan (BINP, Russia)
Sergey Glukhov (BINP, Russia)
Vyacheslav Ivanov (BINP, Russia)
John Jowett (CERN, Switzerland)
James Kahn (LMU, Germany)
Viacheslav Kaminskiy (BINP, Russia)
Kseniia Kariukina (BINP, Russia)
Aleksey Kasaev (BINP, Russia)
Tatyana Kharlamova (BINP, Russia)
Alexey Kozyrev (BINP, Russia)
Evgeny Kozyrev (BINP, Russia)
Peter Krachkov (BINP, Russia)
Maksim Kuzin (BINP, Russia)
Anastasiya Kuzmenko (BINP, Russia)
Eugene Levichev (BINP, Russia)
Lucie Linssen (CERN, Switzerland)
Andreas Alexander Maier (CERN, Switzerland)
Timofei Maltsev (BINP, Russia)
Livio Mapelli (CERN, Switzerland)
Dmitry Matvienko (BINP, Russia)
Ivan Morozov (BINP, Russia)
Magdalena Munker (CERN, Switzerland and University of Bonn, Germany)
Danila Nikiforov (BINP, Russia)
Ivan Nikolaev (BINP, Russia)
Salim Ogur (CERN, Switzerland)
Ivan Ovtin (BINP, Russia)
Marcin Patecki (CERN, Switzerland)
Marko Petric (CERN, Switzerland)
Florian Pitters (CERN, Switzerland and Vienna University of Technology, Austria)
Fabien Plassard (CERN, Switzerland and University Paris Sud, Orsay, France)
Iaroslava Profatilova (CERN, Switzerland and IAP NAS of Ukraine)
Georgii Razuvaev (BINP, Russia)
Philipp Roloff (CERN, Switzerland)
Kate Ross (CERN, Switzerland)

Artem Ryzhenkov (BINP, Russia)
Alexander Senchenko (BINP, Russia)
Sergey Serednyakov (BINP, Russia)
Dmitry Shemyakin (BINP, Russia)
Eva Sicking (CERN, Switzerland)
Rosa Simoniello (CERN, Switzerland)
Rickard Ström (CERN, Switzerland)
Feng Su (IHEP, China)
Ilya Surin (BINP, Russia)
Yuriy Tikhonov (BINP, Russia)
Rogelio Tomás (CERN, Switzerland)
Marco Alan Valdivia García (CERN, Switzerland and University of Guanajuato, Mexico)
Valentin Volkl (University Innsbruck, Austria)
Daniil Voroshilov (BINP, Russia)
Kechen Wang (DESY, Germany)
Renjun Yang (Laboratoire de l'Accélérateur Linéaire, France)
Frank Zimmermann (CERN, Switzerland)



Photographs







Contents

Acknowledgements	iii
Organizing Committee	vii
Reviewers	vii
Executive Summary	ix
Participants	xiii
Photograph of participants	xv
Photographs	xvi
Accelerator Design and Technologies (Convener: Rogelio Tomás)	
Towards an Optimized Monochromatization for Direct Higgs Production in Future Circular e+e- Colliders <i>M.A. Valdivia García and F. Zimmermann</i>	1
FCC-ee Pre-Booster Accelerators <i>S. Ogur, K. Oide and F. Zimmermann</i>	13
Preliminary Design Study of a Pre-booster Damping Ring for the FCC e ⁺ e ⁻ Injector <i>O. Etisken, Y. Papaphilippou and A.K. Ciftci</i>	19
Comparative Study of the Tuning Performances of the Nominal and Long L* CLIC Final Focus System at $\sqrt{s} = 380\text{GeV}$ <i>F. Plassard, A. Latina, E. Marin and R. Tomás</i>	29
Experiments and Facilities (Convener: Rickard Ström)	
The CLIC Detector Concept <i>F. Pitters on behalf of the CLICdp collaboration</i>	37
The Belle II Experiment <i>J. Kahn on behalf of the Belle II Collaboration</i>	45
Calorimetry (Convener: Andreas Alexander Maier)	
Radiation Hardness Study of CsI(Tl) Crystals for the Belle II Calorimeter <i>D.V. Matvienko, E.V. Sedov, B.A. Shwartz and A.S. Kuzmin</i>	55
X-ray Tomography using Thin Scintillator Films <i>E.A. Kozyrev, K.E. Kuper, A.G. Lemzyakov, A.V. Petrozhitskiy and A.S. Popov</i>	65
Calorimetry at the CMD-3 Detector <i>G.P. Razuvaev et al.</i>	71

Charged Particle Identification using the Liquid Xenon Calorimeter of the CMD-3 Detector <i>R.R. Akhmetshin et al.</i>	77
The CMD-3 Data Acquisition System <i>A.N. Kozyrev et al.</i>	85
Physics (Converner: Yuriy Tikhonov)	
Study of the Conversion Decays of Omega Meson to π^0 Meson and e^+e^- Pair Using the CMD-3 Detector <i>R.R. Akhmetshin et al.</i>	91
Current Status of Luminosity Measurement with the CMD-3 Detector at the VEPP-2000 e^+e^- collider <i>A.E. Ryzhenkov et al.</i>	97
Software and Computing (Convener: Marko Petric)	
iLCDirac and Continuous Integration: Automated Testing for Distributed Computing <i>J. Ebbing</i>	103
Accelerator Design and Technologies (Convener: John Jowett)	
Beam Energy Measurement by Resonant Depolarization Method at VEPP-4M <i>V.E. Blinov et al.</i>	109
Fast and Precise Beam Energy Measurement using Compton Backscattering at e^+e^- Colliders <i>V.V. Kaminskiy et al.</i>	119
High Field Studies for CLIC Accelerating Structures Development <i>I. Profatilova</i>	127
Accelerator Design and Technologies (Convener: Eugene Levichev)	
Low Energy Electron Cooler for NICA Booster <i>A.P. Denisov and V.V. Parkhomchuk</i>	135
Design study of CEPC Alternating Magnetic Field Booster <i>T. Bian et al.</i>	145
Application of a Low-Energy Electron Beam as a Tool for Ultrashort Bunch Length Measurement in Circular Machines <i>D.A. Nikiforov et al.</i>	153
Tracking and Particle ID Detectors (Convener: Eva Sicking)	
Kaon Identification using the Tracking System of the CMD-3 Detector <i>R.R. Akhmetshin et al.</i>	159
Vertex and Tracker Research and Development for CLIC <i>M. Munker on behalf of the CLICdp collaboration</i>	165
GEM Detectors in Experiments at e^+e^- Colliders in BINP <i>T.V. Maltsev</i>	175
Aerogel Cherenkov Counters of the KEDR Detector <i>I.V. Ovtin et al.</i>	187

Accelerator Design and Technologies (Convener: Sergey Serednyakov)

Dynamical Aperture Control in Accelerator Lattices with Multipole Potentials
I. Morozov and E. Levichev 195

Fast Kicker for High Current Beam Manipulation in Large Aperture
V. Gambaryan and A. Starostenko 207

Realistic Approach to Beam Dynamics Simulation with Synchrotron Radiation in High Energy Circular
Lepton Colliders
S.A. Glukhov and E.B. Levichev 217

The VEPP-2000 Collider Control System: Operational Experience
A.I. Senchenko, D.E. Berkaev, A.P. Lysenko, Yu.A. Rogovsky, P.Yu. Shatunov 223

Towards an Optimized Monochromatization for Direct Higgs Production in Future Circular e^+e^- Colliders

M.A. Valdivia García^{*1,2} and *F. Zimmermann*^{1,2}
CERN, Geneva, Switzerland
University of Guanajuato, Mexico

Abstract

Direct s -channel Higgs production in e^+e^- collisions is of interest if the centre-of-mass energy spread can be reduced to be comparable to the width of the standard model Higgs boson. A monochromatization principle, previously proposed for several earlier lower-energy colliders, could be employed to achieve the desired reduction, by introducing a non-zero horizontal dispersion of opposite sign for the two colliding beams at the interaction point. In high-energy, high-luminosity circular colliders, beamstrahlung may increase the energy spread and bunch length. Horizontal emittance increase due to beamstrahlung, a new effect that was not present in past monochromatization proposals, may degrade the performance, especially the luminosity. We study, for the FCC-ee collider at 62.5 GeV beam energy, how to optimize the interaction point optics parameters (β_x^* , D_x^*), along with the number of particles per bunch, so as to obtain maximum luminosity at a desired target value of the collision energy spread.

Keywords

Monochromatization; beamstrahlung; collider; high energy; high luminosity; storage ring.

1 Introduction

Monochromatization is a technique that was proposed several decades ago to reduce the centre-of-mass energy spread at e^+e^- colliders [1], but has never been used in any operational collider. A decrease in collision energy spread σ_ω can be accomplished without reducing the inherent energy spread σ_ϵ of either of the two colliding beams. To achieve this goal, opposite correlations between spatial position and energy are introduced at the interaction point (IP). In beam-optical terms, this can be accomplished through a non-zero dispersion function for both beams of opposite sign at the IP. The dispersion is determined by the respective lattice [2].

The concept of monochromatic collision allows for an interesting option presently under study for the FCC-ee collider [3,4], namely the possibility of direct Higgs production in the s channel, $e^+e^- \rightarrow H$, at a beam energy of 62.5 GeV. This could result in an acceptable Higgs event rate on the Higgs resonance and also provide the energy precision required to measure the width of the Higgs particle [5].

Implementation of a monochromatization scheme has been explored for several colliders in the past [1,2,6–11], but, to our knowledge, no such a scheme has ever been applied, or tested, in any operating collider.

The FCC-ee collider design considers two horizontally separated rings for electrons and positrons. For such a double ring collider, where the two beams circulate in separate beam pipes with independently powered magnets, it will be rather simple to modify the dispersion function for the two beams independently. In particular, a horizontal dispersion at the IP could be generated with opposite sign for the two

*valdivia@fisica.ugto.mx and alan.valdivia@cern.ch

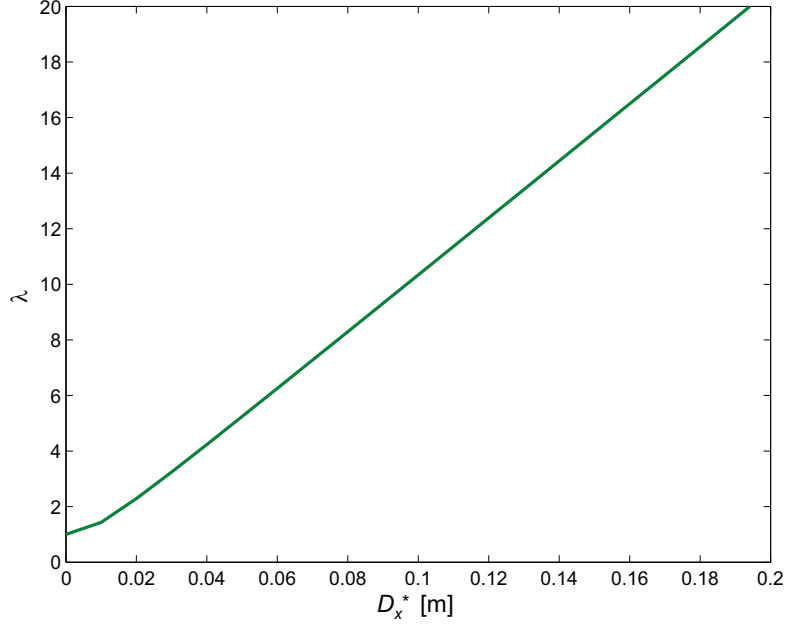


Fig. 1: Monochromatization factor versus D_x^* at fixed $\beta_x^* = 0.25$ m, for constant emittance and energy spread, equal to $\sigma_\delta = 0.06$ and $\epsilon_x = 0.17$ nm.

beams. The impact of this monochromatization on the luminosity and energy spread must be analysed, taking into account the effect of beamstrahlung.

2 Monochromatization principle

For a standard collision, the centre-of-mass energy $W = E_{b+} + E_{b-} = 2E_b$, with relative spread $\Sigma_w = \sigma_w/W$, is a factor of $\sqrt{2}$ less than than the r.m.s. relative beam energy spread $\sigma_w = \sqrt{\sigma_{\delta+}^2 + \sigma_{\delta-}^2} = \sqrt{2}\sigma_\delta$, namely:

$$(\Sigma_w)_{\text{standard}} = \frac{\sigma_\delta}{\sqrt{2}}. \quad (1)$$

In a monochromatic collision, we introduce IP dispersion of opposite sign for the two beams, so that particles with energy $E + \Delta E$ collide on average with particles of energy $E - \Delta E$ and the spread in the centre-of-mass energy is reduced by the monochromatization factor λ ,

$$\text{stable } (\Sigma_w)_\lambda = \frac{\sigma_\delta}{\sqrt{2}} \frac{1}{\lambda}, \quad (2)$$

where this factor is defined, for a horizontal IP dispersion $D_{x+}^* = -D_{x-}^* \neq 0$ and a vertical IP dispersion $D_{y+}^* = D_{y-}^* = 0$, by

$$\lambda = \sqrt{\frac{D_x^{*2} \sigma_\delta^2}{\epsilon_x \beta_x^*} + 1}. \quad (3)$$

Figure 1 illustrates the dependence of the monochromatization factor λ on the IP dispersion D_X^* , for fixed relative energy spread σ_δ and horizontal emittance ϵ_x .

In practice, beamstrahlung affects the values of σ_δ and ϵ_x , and its effects will be included in the subsequent analysis.

3 Beamstrahlung

When charged particles pass through the magnets of a storage ring, synchrotron radiation is emitted as a discrete random process, producing statistically independent discrete changes in the energy of the charged particle. For the beam particles, the cumulative effect of the energy loss introduces a noise excitation of the longitudinal and transverse oscillations, causing their amplitudes to increase until they are balanced, on average, by the radiation damping. This damping depends only on the average rate of emission of energy and not on any of its other statistical properties, whereas the excitation is due to the fluctuation of the radiation about its average rate.

A different type of synchrotron radiation, known as beamstrahlung [12–16], is encountered during the interaction with the opposite beam. For short bunch lengths and small transverse beam sizes, the effective bending radius due to the field of the opposing bunch is exceptionally small compared with the typical arc bending radius. At high collision energies, especially for extremely small bunches where the classical critical photon energy during the collision becomes comparable to the beam energy [16], a quantum mechanical description of the radiation process is necessary.

3.1 Describing the radiation

Synchrotron radiation from charged particles is emitted over a typical time interval of order $\rho/(\gamma c)$, where ρ denotes the radius of curvature of a particle trajectory, c the speed of light, and γ the relativistic Lorentz factor. This time can normally be considered instantaneous compared with the betatron and synchrotron oscillation periods.

The strength of the beamstrahlung is characterized by the parameter Υ , defined as [15, 16] $\Upsilon \equiv B/B_c = (2/3)\hbar\omega_c/E_e$, with $B_c = m_e^2 c^2/(e\hbar) \approx 4.4$ GT, the Schwinger critical field, ω_c the critical energy as defined by Sands [17], and E_e the electron energy before radiation. If the energy of an emitted photon is a few per cent of its initial energy, the emitting particle may fall outside of the momentum acceptance and be lost.

For the collision of Gaussian bunches with r.m.s. sizes σ_x , σ_y , and σ_z , the peak and average values of Υ are given by [16]

$$\Upsilon_{\max} = 2 \frac{r_e^2 \gamma N_b}{\alpha \sigma_z (\sigma_x^* + \sigma_y^*)}, \quad \text{and} \quad \Upsilon_{\text{ave}} \approx \frac{5}{6} \frac{r_e^2 \gamma N_b}{\alpha \sigma_z (\sigma_x^* + \sigma_y^*)}, \quad (4)$$

where α denotes the fine structure constant, $\alpha \approx 1/137$, and r_e the classical electron radius; $r_e \approx 2.8 \times 10^{-15}$ m.

The general emission rate spectrum (photons emitted per second per energy interval) of this radiation is described by [16]

$$\frac{dW_\gamma}{d\omega\hbar} = \frac{\alpha}{\sqrt{3}\hbar\pi\gamma^2} \left(\int_\xi^\infty K_{5/3}(\xi') d\xi' + \frac{y^2}{1-y} K_{2/3}(\xi) \right), \quad (5)$$

where $y \equiv \omega/E_e$ and $\xi \equiv (2/3)(\omega/\Upsilon(E - \hbar\omega))$ have been introduced. In the classical regime ($\Upsilon \rightarrow 0$), this reduces to the well-known expression [17]

$$\left(\frac{dW_\gamma}{d\omega\hbar} \right)_{\text{classical}} = \frac{\alpha}{\sqrt{3}\pi\gamma^2} \int_\xi^\infty K_{5/3}(\xi') d\xi'. \quad (6)$$

The number of photons radiated per unit time is obtained by integrating over ω :

$$\frac{dN_\gamma}{dt} = \int_0^{E_e/\hbar} \frac{dW_\gamma}{d\omega} d\omega. \quad (7)$$

The number of photons emitted during a single collision can be obtained by integrating Eq. (7) over time and averaging over the bunch distribution, taking into account the variation of Υ . The result for head-on collision of Gaussian bunches has been derived previously [16].

All proposed high-energy circular colliders operate in a parameter region where $\Upsilon \ll 1$ and $\sigma_x \gg \sigma_y$, implying that in this case we can approximate the average number of photons per collision as [16]

$$n_\gamma \approx \frac{12}{\pi^{3/2}} \frac{\alpha r_e N_b}{\sigma_x + \sigma_y} \approx \frac{12}{\pi^{3/2}} \frac{\alpha r_e N_b}{\sigma_x}, \quad (8)$$

and the average relative energy loss as

$$\delta_B \approx \frac{24}{3\sqrt{3}\pi^{3/2}} \frac{r_e^3 \gamma N_b^2}{\sigma_z (\sigma_x + \sigma_y)^2} \approx \frac{24}{3\sqrt{3}\pi^{3/2}} \frac{r_e^3 \gamma N_b^2}{\sigma_z \sigma_x^2}. \quad (9)$$

The average photon energy normalized to the beam energy $\langle u \rangle$, i.e., the ratio of δ_B and n_γ , is given by

$$\langle u \rangle = \frac{\delta_B}{n_\gamma} \approx \frac{2\sqrt{3}}{9} \frac{r_e^2 N_b \gamma}{\alpha \sigma_z \sigma_x}. \quad (10)$$

In the classical regime, the average squared photon and the average photon energies are related via [17]

$$\langle u^2 \rangle \approx \frac{25 \times 11}{64} \langle u \rangle^2. \quad (11)$$

Noting that, in the general case,

$$\langle u \rangle \propto \int_0^{E_e} \omega (dW_\gamma/d\omega) d\omega, \quad \langle u^2 \rangle \propto \int_0^{E_e} \omega^2 (dW_\gamma/d\omega) d\omega, \quad (12)$$

we can use the general photon distributions of Eq. (5) to examine the applicability of this relation as a function of Υ . The validity of Eq. (11) up to $\Upsilon \sim 10^{-3}$ is illustrated in Fig. 2.

The excitation term $\{n_\gamma \langle u^2 \rangle\}$ for a single collision will be required in the following. According to Eqs. (8) and (11), for small Υ this can be written as

$$n_\gamma \langle u^2 \rangle \approx 1.4 \frac{r_e^5 N_b^3 \gamma^2}{\alpha \sigma_z^2 (\sigma_x + \sigma_y)^3} \approx 192 \frac{r_e^5 N_b^3 \gamma^2}{\sigma_z^2 \sigma_x^3}. \quad (13)$$

3.2 Energy loss and damping time

The longitudinal damping time in the presence of beamstrahlung is

$$\tau_{E,\text{tot}} = \frac{T_{\text{rev}} E_{\text{beam}}}{U_{0,\text{SR}} + n_{\text{IP}} U_{0,\text{BS}}} \approx \tau_{E,\text{SR}} \left(1 - n_{\text{IP}} \frac{U_{0,\text{BS}}}{U_{0,\text{SR}}} \right), \quad (14)$$

where T_{rev} denotes the revolution period, E_{beam} the beam energy, $U_{0,\text{SR}}$ the average energy loss per turn due to synchrotron radiation in the arc, and $U_{0,\text{BS}}$ the average energy loss due to beamstrahlung in a single collision. Using Eq. (9), the average energy loss per collision due to beamstrahlung is given by

$$U_{0,\text{BS}} = \delta_B E_e \approx 0.84 \frac{r_e^3 E_e \gamma N_b^2}{\sigma_z (\sigma_x + \sigma_y)^2}. \quad (15)$$

For all proposed future circular colliders, we have $U_{0,\text{BS}} \ll U_{0,\text{SR}}$, $\tau_{E,\text{tot}} \approx \tau_{E,\text{SR}}$, and $\sigma_x \gg \sigma_y$. In the following, we will assume these conditions to be fulfilled.

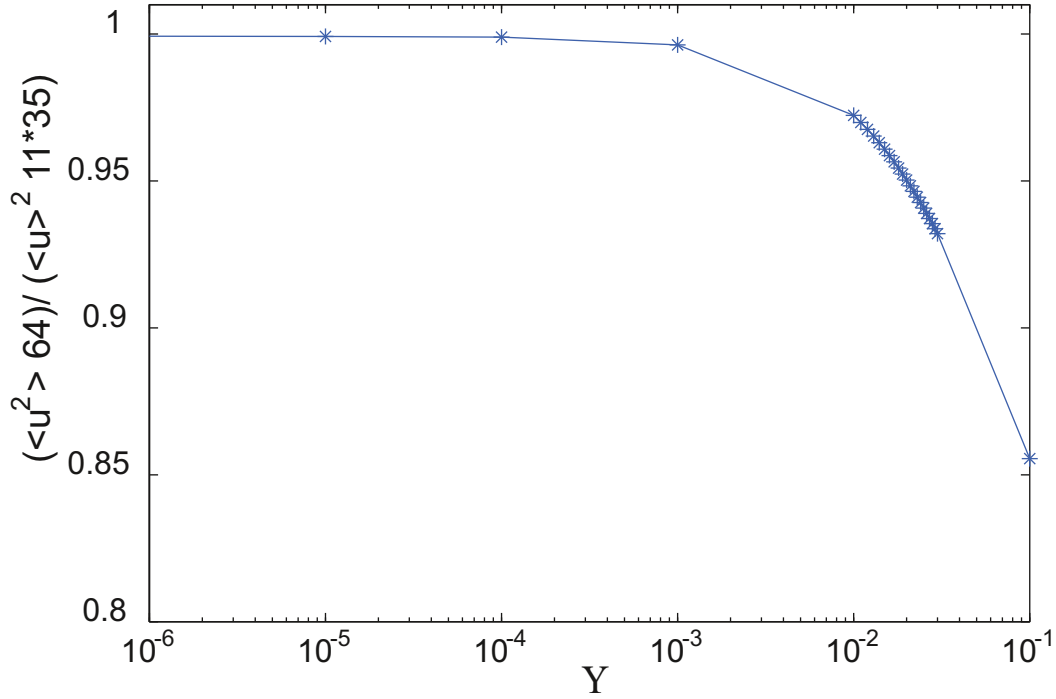


Fig. 2: Mean square photon energy normalized by the square of the mean energy according to Eq. (11) versus Υ

3.3 Self-consistent energy spread without IP dispersion

Consider first the case of zero IP dispersion. The energy spread due to the additional excitation from beamstrahlung at the collision point increases as

$$\sigma_{\text{tot}}^2 = \sigma_{\delta,\text{SR}}^2 + \sigma_{\delta,\text{BS}}^2, \quad (16)$$

with

$$\sigma_{\delta,\text{BS}}^2 = \frac{n_{\text{IP}} \tau_{E,\text{SR}}}{4T_{\text{rev}}} n_{\gamma} \langle u^2 \rangle \approx \frac{A}{\sigma_z^2}, \quad (17)$$

where the parameter A is defined as

$$A \equiv \frac{n_{\text{IP}} \tau_{E,\text{SR}}}{4T_{\text{rev}}} n_{\gamma} \langle u^2 \rangle = \frac{275}{36\pi^{\frac{3}{2}}} \frac{n_{\text{IP}} \tau_{E,\text{SR}}}{4T_{\text{rev}}} \frac{r_e^5 N_b^3 \gamma^2}{\alpha \sigma_x^3}. \quad (18)$$

Using the relation $\sigma_{z,\text{tot}} = \sigma_{\delta,\text{tot}} \sigma_{z,\text{SR}} / \sigma_{\delta,\text{SR}}$, self-consistency requires [18]

$$\sigma_{\delta,\text{tot}}^2 - \sigma_{\delta,\text{SR}}^2 = A \left(\frac{\sigma_{\delta,\text{SR}}}{\sigma_{\delta,\text{tot}}} \frac{1}{\sigma_{z,\text{SR}}} \right)^2, \quad (19)$$

where $\sigma_{z,\text{SR}}$ refers to the bunch length. The energy spread $\sigma_{\delta,\text{SR}}$ is computed with arc synchrotron radiation only, and the explicit solution for the total energy spread is [18]

$$\sigma_{\delta,\text{tot}} = \left[\frac{1}{2} \sigma_{\delta,\text{SR}}^2 + \left(\frac{1}{4} \sigma_{\delta,\text{SR}}^4 + A \frac{\sigma_{\delta,\text{SR}}^2}{\sigma_{z,\text{SR}}^2} \right)^{1/2} \right]^{1/2}, \quad (20)$$

which is solved for the FCC-ee example parameters listed in Table 1, yielding the indicated values of $\sigma_{z,\text{tot}}$ and $\sigma_{\delta,\text{tot}}$, for the cases without monochromatization.

Table 1: Baseline beam parameters for FCC-ee crab-waist collisions at Z pole and WW threshold [4], compared with newly proposed parameters for operation on the Higgs resonance (beam energy $E_e = 62.5$ GeV), in simple head-on collision scheme, and with ‘baseline’ or ‘optimized’ monochromatization, for $n_{\text{IP}} = 2$ identical interaction points.

E_e [GeV]	45.6	62.5	62.5	62.5	80
Scheme	Crab-waist	Head-on	Monochromatization baseline	Monochromatization optimized	Crab-waist
I_b [mA]	1450.3	408.3	408.3	408.3	151.5
N_b [10^{10}]	3.3	1.05	3.3	11.1	6.0
n_b [1]	91500	80960	25760	7728	5260
n_{IP} [1]	2	2	2	2	2
β_x^* [m]	1	1.0	1.0	1.96	1
β_y^* [mm]	2	2	2	1	2
D_x^* [m]	0	0	0.22	0.308	0
$\epsilon_{x,\text{SR}}$ [nm]	0.09	0.17	0.17	0.17	0.26
$\epsilon_{x,\text{tot}}$ [nm]	0.09	0.17	0.21	0.70	0.26
$\epsilon_{y,\text{SR}}$ [pm]	1	1	1	1	1
$\sigma_{x,\text{SR}}$ [μm]	9.5	9.2	132	185.7	16
$\sigma_{x,\text{tot}}$ [μm]	9.5	9.2	144	188.5	16
σ_y [nm]	45	45	45	32	45
$\sigma_{z,\text{SR}}$ [mm]	1.6	1.8	1.8	1.8	2.0
$\sigma_{z,\text{tot}}$ [mm]	3.8	1.8	1.8	1.8	3.1
$\sigma_{\delta,\text{SR}}$ [%]	0.04	0.06	0.06	0.06	0.07
$\sigma_{\delta,\text{tot}}$ [%]	0.09	0.06	0.06	0.06	0.10
θ_c [mrad]	30	0	0	0	30
circ. C [km]	100	100	100	100	100
α_C [10^{-6}]	7	7	7	7	7
f_{rf} [MHz]	400	400	400	400	400
V_{rf} [GV]	0.2	0.4	0.4	0.4	0.8
$U_{0,\text{SR}}$ [GeV]	0.03	0.12	0.12	0.12	0.33
$U_{0,\text{BS}}$ [MeV]	0.5	0.05	0.01	0.01	0.21
τ_E/T_{rev}	1320	509	509	509	243
Q_s	0.025	0.030	0.030	0.030	0.037
Υ_{max} [10^{-4}]	1.7	0.8	0.3	0.85	4.0
Υ_{ave} [10^{-4}]	0.7	0.3	0.1	0.35	1.7
θ_c [mrad]	30	0	0	0	30
ξ_x [10^{-2}]	5	12	1	2.22	7
ξ_y [10^{-2}]	13	15	4	6.76	16
λ [1]	1	1	9.2	5.08	1
L [$10^{35} \text{cm}^{-2} \text{s}^{-1}$]	9.0	2.2	1.0	3.74	1.9
σ_w [MeV]	58	53	5.8	10.44	113

3.4 Self-consistent emittance

In the presence of non-zero dispersion at the IP, not only the energy spread, but also the transverse emittance increases due to the beamstrahlung. The non-zero dispersion may arise either from optics errors or by design, e.g., for a monochromatization scheme [19]. Under these conditions, the dynamics is similar to the well-known effect of horizontal dispersion and conventional synchrotron radiation in the storage ring arcs. The total emittance becomes

$$\epsilon_{x,\text{tot}} = \epsilon_{x,\text{SR}} + \frac{\tau_x n_{\text{IP}}}{4T_{\text{rev}}} \{n_\gamma \langle u^2 \rangle\} \mathcal{H}_x^* , \quad (21)$$

where τ_x denotes the horizontal (amplitude) damping time due to synchrotron radiation. The non-zero dispersion invariant \mathcal{H}_x^* [17] is given by

$$\mathcal{H}_x^* \equiv \frac{(\beta_x^* D_x'^* + \alpha_x^* D_x^*)^2 + D_x^{*2}}{\beta_x^*} , \quad (22)$$

and β_x^* , α_x^* , D_x^* , and $D_x'^*$ denote the optical beta and alpha functions (Twiss parameters), the dispersion, and the slope of the dispersion at the collision point, respectively.

The relative momentum spread is described by

$$\sigma_{\delta,\text{tot}}^2 = \sigma_{\delta,\text{SR}}^2 + \frac{n_{\text{IP}} \tau_{E,\text{SR}}}{4T_{\text{rev}}} \{n_\gamma \langle u^2 \rangle\} , \quad (23)$$

where the bunch length, appearing in Eq. (13), is related to the energy spread via [17]

$$\sigma_{z,\text{tot}} = \frac{\alpha_C C}{2\pi Q_s} \sigma_{\delta,\text{tot}} , \quad (24)$$

with α_C the momentum compaction factor, C the circumference, and Q_s the synchrotron tune.

Equations (21) and (23) are coupled through the excitation term $n_\gamma \langle u^2 \rangle$ (Eq. (13)), leading to the formulation of a set of equations for the longitudinal and transverse plane, which must be solved self-consistently for the two unknowns σ_x and σ_z .

Simplified solutions can be obtained depending on whether $D_x^* \sigma_{\delta,\text{tot}} \ll \sqrt{\beta_x^* \epsilon_x}$ (as usual for zero dispersion), or $D_x^* \sigma_{\delta,\text{tot}} \gg \sqrt{\beta_x^* \epsilon_x}$ (monochromatization).

In the monochromatization approximation, $\tau_x = 2\tau_E$; using Eq. (13), Eqs. (21) and (23) can be rewritten as

$$\epsilon_{x,\text{tot}} \approx \epsilon_{x,\text{SR}} + \frac{2B\mathcal{H}_x^*}{D_x^{*3} \sigma_{\delta,\text{tot}}^5} , \quad (25)$$

$$\sigma_{\delta,\text{tot}}^2 = \sigma_{\delta,\text{SR}}^2 + \frac{B}{D_x^{*3} \sigma_{\delta,\text{tot}}^5} , \quad (26)$$

with

$$B \equiv 48 \frac{n_{\text{IP}} \tau_{E,\text{SR}}}{T_{\text{rev}}} \frac{r_e^5 N_b^3 \gamma^2}{(\alpha_C C / (2\pi Q_s))^2} . \quad (27)$$

After solving Eq. (26) for the relative energy spread $\sigma_{\delta,\text{tot}}$, the emittance follows from Eq. (25). Using Eqs. (26) and (25), we obtain the total bunch length and emittance for the two cases of $D_x^* \neq 0$ (the second and third column) at 62.5 GeV in Table 1. In the standard limit, i.e., the opposite case, we find

$$\epsilon_{x,\text{tot}} \approx \epsilon_{x,\text{SR}} + \frac{2B\mathcal{H}_x^*}{\sigma_{\delta,\text{tot}}^2 \beta_x^{*3/2} \epsilon_{x,\text{tot}}^{3/2}} , \quad (28)$$

$$\sigma_{\delta,\text{tot}}^2 = \sigma_{\delta,\text{SR}}^2 + \frac{B}{\sigma_{\delta,\text{tot}}^2 \beta_x^{*3/2} \epsilon_{x,\text{tot}}^{3/2}} . \quad (29)$$

Equations (28) and (29) are coupled, and must be solved together. Equations (28) and (29) then yield the total bunch length and emittance shown in Table 1 for the three columns with $D_x^* = 0$.

The bunch length always follows from Eq. (24).

4 Baseline monochromatization

In a classical monochromatization scheme, with fixed emittance, energy spread, IP beta function, and only adding opposite IP dispersion for the two beams, the resulting luminosity L scales as λ^{-1} . However, for the FCC-ee, owing to the beamstrahlung in the presence of non-zero dispersion, changes in the horizontal equilibrium emittance are not negligible. A self-consistent calculation of the beam parameters then determines the actual luminosity, which tends to be less than the corresponding standard value. Moreover, the monochromatization factor deviates naively from the value expected, without taking into account the effect of the changing horizontal emittance. The self-consistent parameters must be used to compute the true values of λ and L .

Table 1 presents the nominal FCC-ee parameters for (non-monochromatic) collisions at 45.6 GeV and 80 GeV [4], with an interpolated head-on collision scheme at 62.5 GeV, a ‘baseline monochromatization scheme’ at the same energy (obtained by adding IP dispersion to the former), and an optimized monochromatization, for which the bunch charge and IP beta functions have been re-optimized (plus the value of the IP dispersion in proportion to $\sqrt{\beta_x^*}$).

Given the resonance width of the standard model Higgs of 4.2 MeV and the much larger natural r.m.s. energy spread of the electron and positron beams at 62.5 GeV of about 40 MeV, the monochromatization factor should be large, at least $\lambda \sim 5$ [20].

Requesting $\lambda \sim 10$, to have some margin, while considering the emittance and energy spread due to arc synchrotron radiation alone, from Table 1, the necessary value of the IP dispersion is given by $D_x^{*2} \beta_x^{*-1} \approx 10^{-2}$ m. Using this value, the baseline monochromatization scheme in the second 62.5 GeV column of Table 1 was obtained from the first column. The value includes the effect of beamstrahlung [21].

5 Optimized monochromatization

The smaller the horizontal beta function can be made, the smaller the horizontal beam size becomes, and the smaller the luminosity loss compared with a zero-dispersion collision. As long as the resulting horizontal beam size with monochromatization, dominated by the dispersion, is much larger than the corresponding beam size for a standard collision scheme, the effects of beamstrahlung are small, at least in the longitudinal plane [21].

In an attempt to profit from the larger horizontal beam size, we may tentatively modify the bunch charge N_b (along with the number of bunches n_b) and the IP beta functions, until we reach the maximum luminosity for the selected value of λ .

For operation on the Z pole and at the WW threshold, FCC-ee applies a crab-waist scheme with $\theta_c = 30$ mrad full horizontal crossing angle. The crossing angle also reduces the beam–beam tune shift, especially in the horizontal plane.

For our dispersion-based monochromatization scheme, we may need to avoid the crossing angle and (effectively) operate with head-on collisions. For head-on collisions, the beam–beam parameters (almost equal to the beam–beam tune shifts) are:

$$\xi_{x,y} = \frac{\beta_{x,y}^* r_e N_b}{2\pi\gamma\sigma_{x,y}(\sigma_x + \sigma_y)} . \quad (30)$$

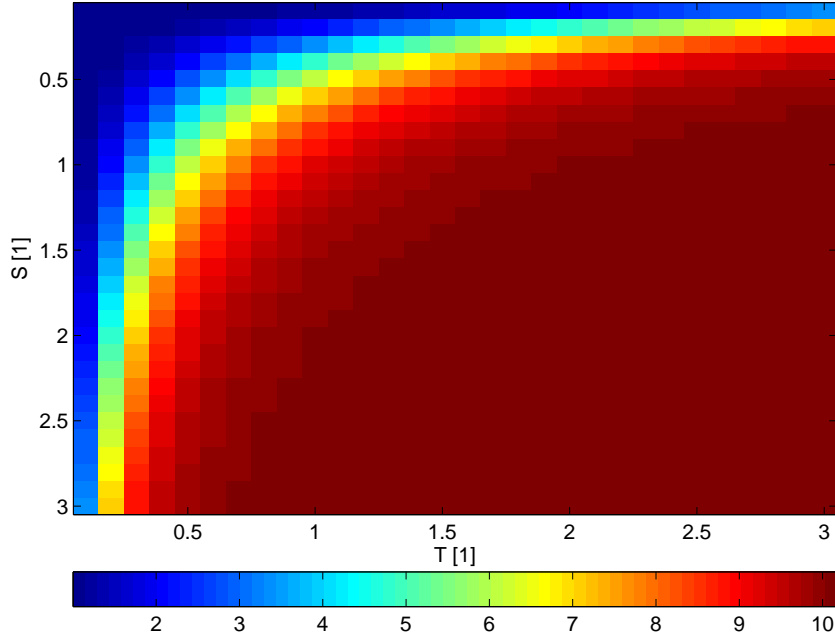


Fig. 3: λ including beamstrahlung effects

Assuming monochromatization, this can be rewritten as

$$\xi_x \approx \frac{\beta_x^* r_e N_b}{2\pi\gamma\sigma_\delta^2 D_x^{*2}}, \quad \xi_y \approx \frac{\beta_y^* r_e N_b}{2\pi\gamma\sigma_\delta D_x^* \sigma_y^*}. \quad (31)$$

Through the constant value of the total current (limited by the synchrotron radiation power), the bunch population also defines the number of bunches per beam, n_b , and the overall luminosity

$$L \approx \frac{f_{\text{rev}} n_b N_b^2}{4\pi\sigma_y^* D_x^* \sigma_\delta} \approx \frac{I_b \gamma \xi_y}{2e r_e \beta_y^*}, \quad (32)$$

where f_{rev} denotes the revolution frequency (3 kHz).

Horizontal emittance and energy spread are normally determined by the optical lattice and the synchrotron radiation in the collider arcs. However, in the FCC-ee, the transverse effect of beamstrahlung may not always be neglected. This can be seen in Table 1, which shows horizontal emittance and beam sizes first without and then with the effect of beamstrahlung [21].

Searching for an optimal point in solution space, we reduce β_y^* from the nominal value of 2 mm to 1 mm, which is permitted by the present collider optics [22]. We then apply the following parametric transformation with parameter S (keeping λ without beamstrahlung fixed): $D_x = S * D_{ox}$, starting from $D_{ox} = 0.22$ m, and $\beta_x = S^2 * \beta_{ox}$, starting from $\beta_{ox} = 1.0$ m. We introduce a second parametric transformation with parameter T (ideally making $L \propto T^{-1}$, for the case of no beamstrahlung and no limit on the beam–beam tune shift): $n_b = n_{ob} * T$ and $N_b = N_{ob}/T$, so that the total beam current is constant. All initial values for D_{ox} , β_{ox} , n_{ob} , and N_{ob} correspond to the parameters of the baseline scheme, where $\lambda_{\text{SR}} \approx 10$ (we here use λ_{SR} to denote the value of λ computed without the effect of beamstrahlung). The actual monochromatization factor is reduced and no longer constant in (S, T) parameter space when the effects of beamstrahlung are included, as illustrated in Fig. 3.

Under the aforementioned conditions and assumptions, including the beamstrahlung effects, the dependencies $L(\epsilon_{x,\text{tot}}(T, S))$ and $\lambda(\epsilon_{x,\text{tot}}(T, S))$ are analysed simultaneously. This allows determination of the maximum luminosity that can be achieved for a given λ . The result is displayed in Fig. 4.

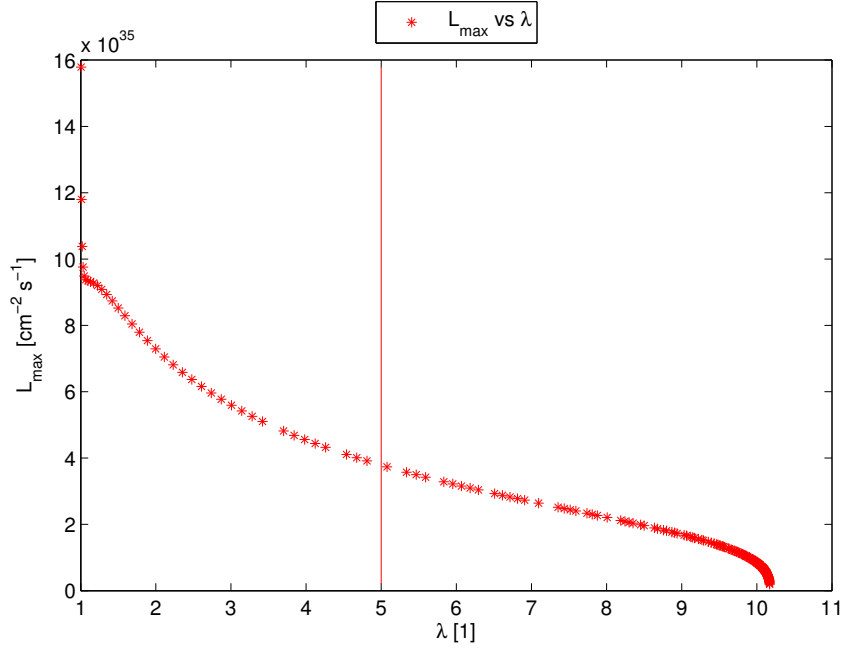


Fig. 4: Optimal luminosity as a function of λ

From this, we obtain a luminosity of $L = 3.74 \times 10^{35} \text{ cm}^{-2} \text{ s}^{-1}$ at $\lambda \approx 5$ (5.08), with the IP optics parameters $\beta = 4.41 \text{ m}$ and $D_x = 0.462 \text{ m}$.

6 Conclusions and outlook

We have derived FCC-ee IP beam parameters that would result in monochromatization by a factor of 5 to 10 at high luminosity. Accounting for the horizontal increase due to beamstrahlung and non-zero IP dispersion, for a baseline monochromatization scheme a luminosity of about $10^{35} \text{ cm}^{-2} \text{ s}^{-1}$ can be achieved at the Higgs resonance with an effective collision energy spread below 6 MeV. Beamstrahlung effects lead to large horizontal increase and a concomitant degradation of the monochromatization. Nevertheless, by increasing the number of bunches, reducing the bunch charge, and increasing the optical function in the horizontal plane, beamstrahlung can be kept under control. Doing so, and keeping the beam current the same as for the baseline monochromatization, for the minimum required monochromatization of $\lambda \approx 5$ (about 10 MeV r.m.s. collision energy spread) our analytical expressions suggest that the luminosity can be increased to about $4 \times 10^{35} \text{ cm}^{-2} \text{ s}^{-1}$.

Optics and layout modification of the FCC-ee final-focus system [22] will represent the next challenge. We must develop a modified final-focus optics to generate the desired antisymmetric IP dispersion, and, at the same time, transit from a crossing angle to a head-on collision scheme. Either the additional bending magnets or electrostatic separators needed to realize the head-on collision that could be used to generate the necessary IP dispersion, or we can maintain a crossing geometry and deploy crab cavities together with horizontal IP dispersion.

7 Acknowledgements

We thank A. Faus-Golfe, J.M. Jowett, K. Oide, D. Shatilov, V. Telnov, and K. Yokoya for helpful discussions.

This work was supported in part by the European Commission under the FP7 Capacities project EuCARD-2, grant agreement 312453, and by the Mexican CONACyT ‘BEAM’ Programme.

References

- [1] A. Renieri, Possibility of achieving very high energy resolution in e^+e^- storage rings, Frascati, Preprint INF/75/6(R) (1975).
- [2] J.M. Jowett, Lattice and interaction region design for tau-charm factories, Proc. Joint US/CERN School on Particle Accelerators, Benalmadena, Spain, 1992, and CERN SL/93-23 (AP) (CERN, Geneva, 1993).
- [3] <http://cern.ch/fcc>, accessed August 22nd 2016.
- [4] J. Wenninger *et al.*, Future circular collider study hadron collider parameters, FCC-ACC-SPC-0003, Rev. 3.0, EDMS no. 1346081 (2016).
- [5] D. d’Enterria *et al.*, Electron Yukawa from s-channel Higgs production at FCC-ee, FCC-ee Physics Workshop, Geneva, CERN, 2016.
- [6] A.A. Avdienko *et al.*, The project of modernization of the VEPP-4 storage ring for monochromatic experiments in the energy range of Ψ and Υ mesons, Proc. 12th Intern. Conf. High Energy Accelerators, Fermilab, 1983, p. 186.
- [7] K. Wille and A.W. Chao, Investigation of a monochromator scheme for SPEAR, SLAC/AP-32 (1984).
- [8] Y.I. Alexahin *et al.*, Proposal on a tau-charm factory with monochromatization, Proc. 2nd European Particle Accelerator Conf., Nice, France, 1990, p. 398.
- [9] M. Bassetti and J.M. Jowett, Improving the energy resolution of LEP experiments, Proc. 1987 IEEE PAC, Washington, DC, 1987, p. 115.
- [10] A. Zholents, Polarized J/Ψ mesons at a tau-charm factory with a monochromator scheme, CERN SL/97-27, (CERN, Geneva, 1992).
- [11] A. Faus-Golfe and J. Le Duff, *Nucl. Instrum. Methods A* **372** (1996) 6. [https://doi.org/10.1016/0168-9002\(95\)01275-3](https://doi.org/10.1016/0168-9002(95)01275-3)
- [12] A. Hofmann and E. Keil, LEP Note 70/86 (1978).
- [13] V.E. Balakin *et al.*, Proc. 6th All Union Conf. on Charged Particle Accelerators, Dubna, 1978, p. 140.
- [14] M. Bassetti *et al.*, Properties and possible uses of beam–beam synchrotron radiation, Proc. PAC, 1983, <http://dx.doi.org/10.1109/tns.1983.4332754>
- [15] K. Yokoya, *Nucl. Instrum. Meth. A* **251** (1986) 1. [https://doi.org/10.1016/0168-9002\(86\)91144-7](https://doi.org/10.1016/0168-9002(86)91144-7)
- [16] K. Yokoya and P. Chen, *Lect. Notes Phys.* **400** (1992) 415. https://doi.org/10.1007/3-540-55250-2_37
- [17] M. Sands, The physics of electron storage rings: an introduction, SLAC Report 121 (1970); also published in Conf. Proc. C6906161 (1969) p. 257.
- [18] K. Ohmi and F. Zimmermann, FCC-ee/CepC beam–beam simulations with beamstrahlung, Proc. IPAC14, Dresden, 2014.
- [19] M.A. Valdivia Garcia *et al.*, Towards a monochromatization scheme for direct Higgs production at FCC-ee, Proc. IPAC’16, Busan, Korea, 2016, p. 2434.
- [20] A. Blondel, statement at FCC-ee physics vidyo meeting, 27 June 2016.
- [21] M.A. Valdivia Garcia *et al.*, Effect of beamstrahlung on bunch length and emittance in future circular e^+e^- colliders, Proc. IPAC’16, Busan, Korea, 2016, p. 2438.
- [22] K. Oide *et al.*, A design of beam optics for FCC-ee collider ring, Proc. IPAC’16, Busan, Korea, 2016, p. 3821.

FCC-ee Pre-Booster Accelerators

S. Ogur¹, K. Oide², and F. Zimmermann¹

¹CERN, Geneva, Switzerland; ²KEK, Ibaraki, Japan

Abstract

CERN's ambitious new project, Future Circular Collider-ee, will have four operations as Z , W , H , and tt factories covering energies from 45.6 to 175 GeV. The main challenge of Z -operation is to achieve currents as high as 1450 mA; this will depend heavily on the injector. For this reason, we conclude that we need a high bunch charge of 3.3×10^{10} , for both e^- and e^+ , and fill 91 500 of each of those bunches into the collider. To achieve the goal, we have designed an S-band (2.856 GHz) normal conducting electron linac up to 6 GeV, which we will use to create and accelerate both electrons and positrons. Positrons will be created inside the linac at 4.46 GeV, will be accelerated up to 1.54 GeV at the linac, and will then be transferred to the designed damping ring. In this paper, we present the designed linac, damping ring, and the operational requirements of the 100 km booster.

Keywords

Future circular collider; damping ring; linac; filling scheme; injection time schedule; positron injector.

1 Introduction

The Future Circular Collider (FCC) is a prospective future project of CERN, and is meant to be the successor of the Large Hadron Collider. The FCC has three different sub-projects for lepton–lepton, hadron–hadron, and hadron–lepton collisions. In this paper, we would like to discuss the FCC-ee which is going to collide positrons and electrons (e^+e^-) via four main operations. The FCC-ee is going to serve as a precision machine with high luminosity by colliding leptons with different energy ranges while varying the bunch population and the number of bunches, as demonstrated in Table 1.

The FCC-ee pre-injectors consist of three main parts: a linac, a damping ring, and a pre-booster. These pre-injectors will be followed by a 100 km booster, which would fill the 100 km collider as a top-up injector. Pre-injectors are designed in such a way as to cover all the operations. The linac is crucial to supply the total charge needed. The total charge is the number of bunches per beam multiplied by the bunch population, which is a maximum for the Z -operation, whereas the Z -operation requires the smallest geometric emittance. Therefore, if the pre-injectors can provide the total charge and smallest geometric emittance required for Z -operation, then it can be safely said that the pre-injectors can cover all operations, excluding the final energy, which will be a matter for the pre-booster or booster, which is beyond the scope of this paper.

Table 1: FCC-ee baseline parameters

Operation type	Z	W	H	tt
Final energy (GeV)	45.6	80	120	175
Number of bunches per beam	91 500	5260	780	81
Bunch population	3.3×10^{10}	6×10^{10}	8×10^{10}	1.7×10^{11}
Horizontal emittance (nm)	0.09	0.26	0.61	1.3
Vertical emittance (pm)	1	1	1.2	2.5

Table 2: Emittance evolution for electron flow [1]

Location	Energy (GeV)	$\epsilon_{\text{geo},x}$ (nm)	$\epsilon_{\text{geo},y}$ (nm)
Collider aims	45.6	0.09	0.001
Collider accepts	45.6	27.3	2.0
Booster exit	45.6	0.09	0.13
Booster entrance	6	0.7	1.0
Linac exit	6	0.7	1.0
Linac entrance	0.012	350	500

Pre-injectors are to operate alternatively to create and accelerate electrons and positrons. An electron linac of 6 GeV has been designed, and positrons will be created at 4.46 GeV of the linac. These positrons will be accelerated in the rest of the linac, 1.54 GeV, and then delivered to the damping ring. The acceleration of the damped positrons is continued at the linac by re-injection at an energy of 1.54 GeV and the positrons are accelerated up to 6 GeV. As a result, the electrons and positrons are at the same energy and emittance when they are transferred directly to the 100 km booster without an intermediate booster in the case of Z -operation.

All the designs and simulations are made using SAD (Strategical Accelerator Design) [2], which has proven successful in the design and commissioning of many linear and circular accelerators. However, before the designs can be prepared, a discussion of the evolution of the emittance throughout the accelerators is of great importance in determining the initial parameters. The values in Table 2 have been calculated by assuming that the normalized emittances are to be conserved at approximately 8/12 μm (hor/vert) throughout the electron acceleration at the pre-boosters.

1.1 The first fill of accelerators

A well-planned time schedule is necessary for the pre-injection complex, owing to the multi-use of accelerators. The booster fill time is suggested as 4 s, plus 6 s for the acceleration of the available bunches. The electrons are injected within a frequency $f = 100$ Hz from the linac as two bunches per RF pulse; the repetition is chosen to be easily feasible in current technology. Therefore, the booster will accumulate and accelerate 800 bunches to the designated energy in each 10 s period. Firstly, the electron bunches are accumulated in the collider, which is filled with 92 000 bunches in about 19 min. Secondly, the positrons would arrive late because they follow a different path, owing to their creation and re-transfer to the linac; in addition, they have to go through the damping ring. The time schedule also determines the available time to reach the designated emittance for the positrons, therefore we have decided to follow the schedule outlined in Table 3.

This scheme continues with a periodicity of $T = 20$ ms, finally reaching 400 bunches in 4050 ms. What is important is that each pair of bunches of positrons spends 50 ms inside the damping ring.

2 Linac

An S-band normal conducting linac operating at 2855.98 MHz will work with a repetition of 100 Hz. The RF frequency was chosen based on previous experience using that famous frequency. Some parameters of the linac are shown in Table 4.

The cavities and their wakes are taken from KEK-ATF [3], with a length of 2.97 m ($27\frac{1}{3}$ wavelengths), having an aperture size of 11 mm at the entrance and 9 mm at the exit to keep the field uniformity inside the cavity. The linac will accelerate 4×10^{10} particles per bunch, which is intentionally more particles than the full charge for Z -operation presented in Table 1, leaving margin for probable transmission loss throughout the linac. The initial emittance of the electrons is taken from Table 2, and we assume a

Table 3: Time schedule of the positrons in FCC-ee pre-injectors

RF time (ms)	Linac	Damping ring	Booster
0–20	2 bunches of e^-	2 bunches of e^+	Empty
20–40	2 bunches of e^-	4 bunches of e^+	Empty
40–50	2 bunches of e^-	6 bunches of e^+	Empty
50–60	2 bunches of e^+	4 bunches of e^+	2 bunches of e^+
60–70	2 bunches of e^-	6 bunches of e^+	2 bunches of e^+
70–80	2 bunches of e^+	4 bunches of e^+	4 bunches of e^+
80–90	2 bunches of e^-	6 bunches of e^+	4 bunches of e^+
90–100	2 bunches of e^+	4 bunches of e^+	6 bunches of e^+
100–110	2 bunches of e^-	6 bunches of e^+	6 bunches of e^+

Table 4: Linac design parameters

Parameter	Value
Initial energy (MeV)	12
Final energy (GeV)	6
Length (m)	257.3
Initial geometric emittance (h/v) (μm)	0.35/0.5
Final geometric emittance (h/v) (nm)	0.7/1.0
Number of cavities	80
Gradient (MV/m)	25
Gradient through accelerator (MV/m)	23

Gaussian beam for the simulation of the beam envelope; the resulting optics are presented in Fig. 1.

The beam profile of the designed linac has a two-horn distribution in the energy dispersion graph, as shown in Fig. 2, because of the wakefields and because the RF phase is chosen as -94° . In addition, the acceleration gradient has been kept low, such that the SLED [4] scheme can be applied and the energy difference between the two bunches in the same RF pulse is also low. The linac elements are tightly allocated for the time being. Some errors are to be introduced in cavity, quadrupole and injection alignments to study robustness of the linac. Therefore, as some beam diagnostic elements are introduced and the orbit correction study continues to keep the transmission high, the designed linac will extend and evolve.

3 Damping ring

The positrons will be created by colliding 4.46 GeV electrons with crystalline and amorphous targets. The positrons' emittance and energy spread would be high as a result of this statistical process; therefore, a damping ring is needed to match the conditions of the electrons for the collisions. After an adiabatic matching section and an energy compressor, we assume that we will produce an emittance compatible with KEKB [5] at the entrance of the damping ring. To produce an initial kick, we adopt the parameters for the SuperKEKB, provided by Iida and Miyahara (KEK), to our bunch charge and energy; the damping necessity of the FCC-ee pre-injection system will then evolve as in Table 5.

The damping ring must have a very low natural emittance, down to 1 nm; meanwhile, the damping time should be small, such that damping from the micrometre to the nanometre level can occur in less than 50 ms. However, a very large dynamic aperture is a fundamental necessity, since there are orders of magnitude difference in the emittance values of the incoming and outgoing beams. Another issue is the bunch spacing, which is again chosen to be easily feasible; the bunch separation is determined to be

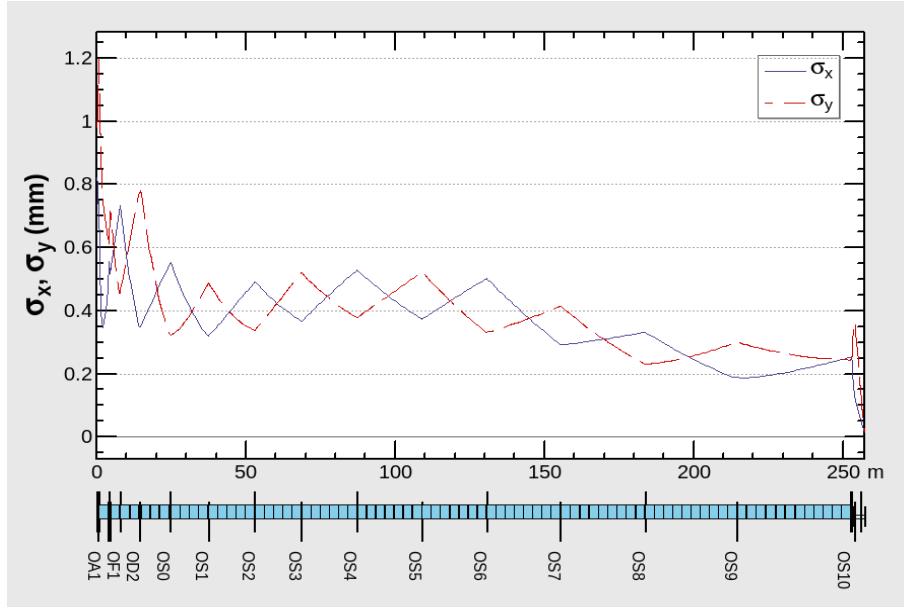


Fig. 1: Linac optics

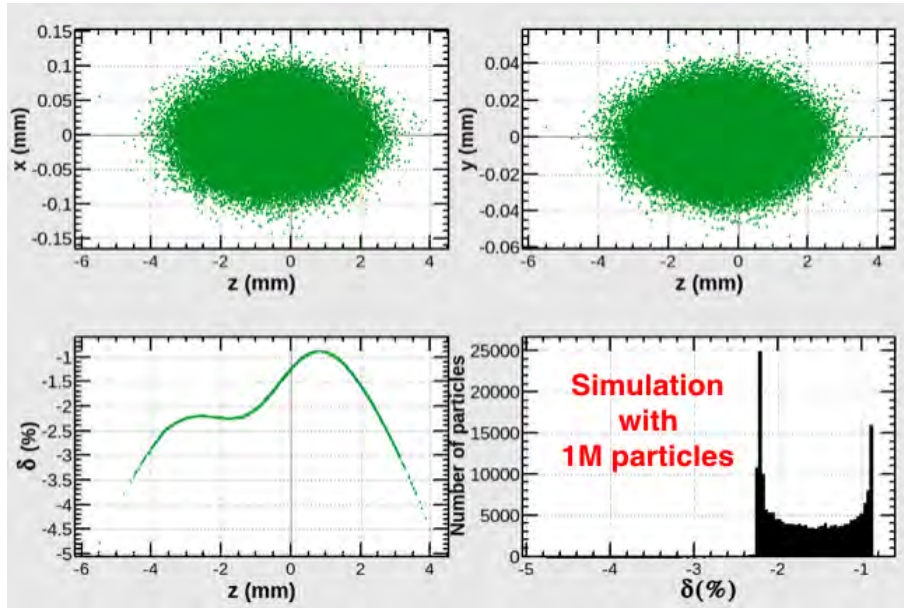


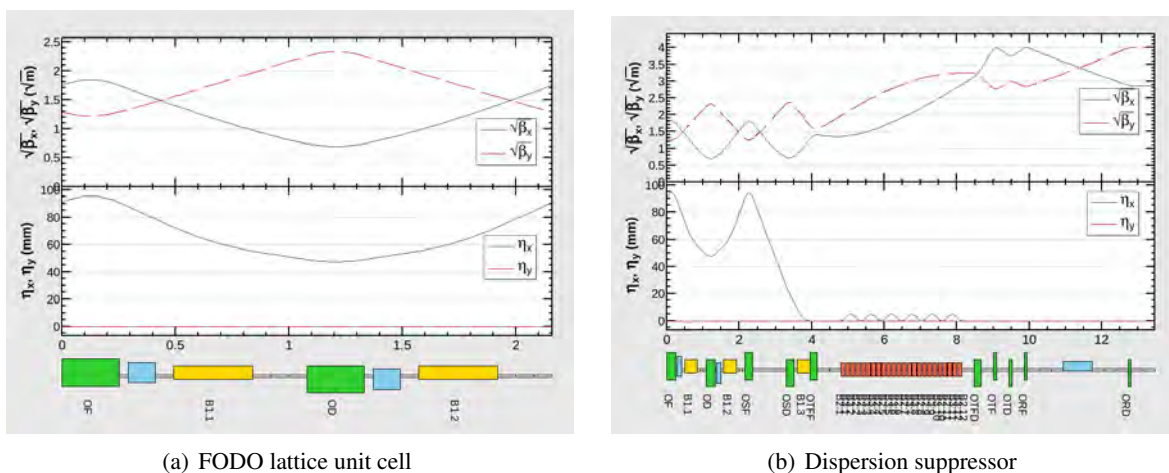
Fig. 2: Linac beam profile

Table 5: Emittance evolution for positron flow

e^+ accelerators	Energy (GeV)	$\epsilon_{\text{geo},x}$	$\epsilon_{\text{geo},y}$
Damping ring entrance	1.54	$0.76 \mu\text{m}$	$0.71 \mu\text{m}$
Damping ring exit	1.54	2.66 nm	3.9 nm
Booster exit	45.6	0.09 nm	0.13 nm
Collider aims	45.6	0.09 nm	1 pm

Table 6: Damping ring design parameters

Parameter	Value
Energy (GeV)	1.54
Number of trains	3
Bunches per train	2
Circumference (m)	178.6
Number of cells	60
Dipole field (T)	0.74
Bending radius (m)	6.96
Kicker time (ns)	<300
Bunch spacing (ns)	99
τ_x (ms)	10.6
τ_y (ms)	11.2
Horizontal natural emittance (nm)	1.7
Vertical natural emittance	–



(a) FODO lattice unit cell

(b) Dispersion suppressor

Fig. 3: Damping ring sections (horizontal axis in m)

around 100 ns for any two consecutive bunches in the damping ring. Some parameters of the damping ring are shown in Table 6.

The damping ring consists of two arcs and two straight sections linking these arcs; each arc consists of 30 FODO cells. The tune values per unit cell are 0.311 rad horizontally and 0.125 rad vertically. The spacing between the elements in the unit cell is optimized individually, as shown in Fig. 3(a). The straight sections are dispersion suppressors and have 3.36 m long normal conducting 1.74 T wigglers. The dispersion suppressor is shown in Fig. 3(b). Finally, the damping ring, shown in Fig. 4, has around 1 nm of natural emittance horizontally and about 11 ms of damping time in both planes. According to Eq. 1, the damping necessities stated in Table 5 can be reached well below 50 ms:

$$\epsilon(t) = \epsilon_{inj}e^{-2t/\tau} + \epsilon_{nat}(1 - e^{-2t/\tau}). \quad (1)$$

Conclusions

The linac is normal conducting with a length of 257.3 m, deploying 80 cavities and 22 quadrupoles, with modest and achievable requirements. Furthermore, some dipoles and beam diagnostic elements will be included in the next phase of the study.

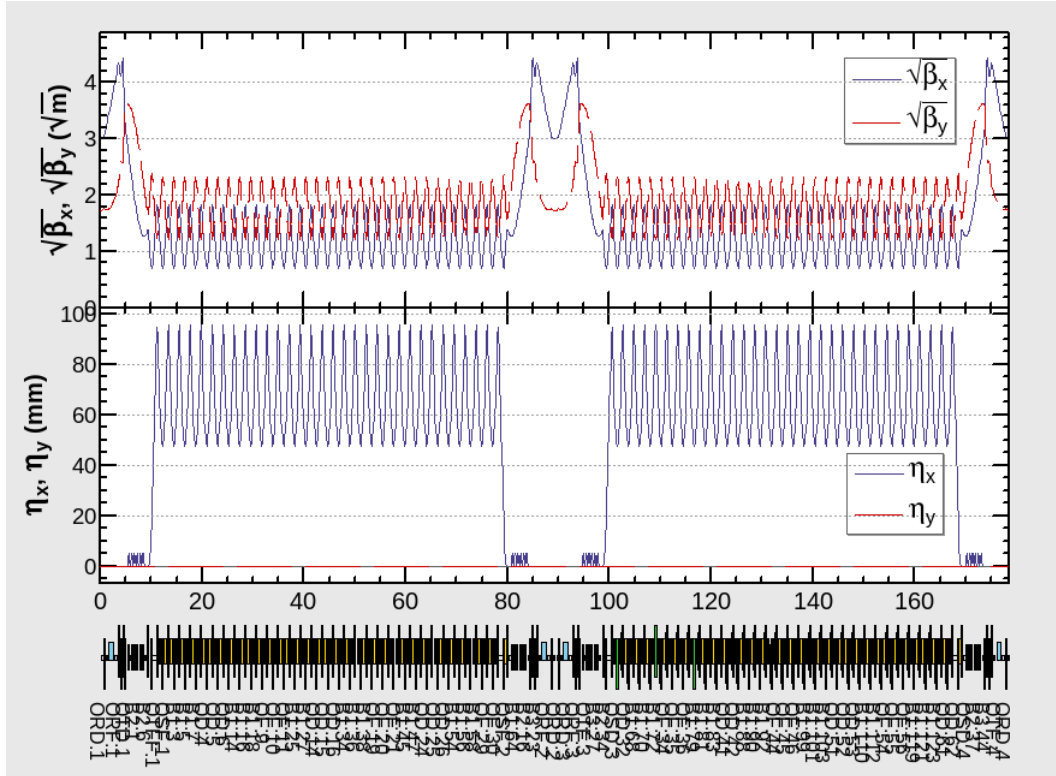


Fig. 4: Damping ring optics

The dynamic aperture of the damping ring is continuously being enhanced, even though we have already surpassed 60 sigmas in the transverse axis, which is sufficient to accept 99% of the positrons, based on experience with KEK positron data [5]. However, additional work is still required to enlarge the dynamic aperture to outstretch the expected shrink in dynamic aperture, owing to probable misalignment errors.

Accelerating more than two bunches per RF pulse is also under consideration, since it is intended to reduce the fill time from the beginning. Conclusively, the scheme presented would enable the collider to be filled with 91 500 bunches of electrons in 19 min, and 91 500 bunches of positrons in 27 min.

References

- [1] K. Oide *et al.*, Design of beam optics for the FCC-ee collider ring, Proc. IPAC16, Busan, South Korea, 2016, no. THPOR022.
- [2] <http://acc-physics.kek.jp/SAD/index.html>, , last accessed May 20th 2017.
- [3] S. Takeda *et al.*, 1.54 GeV ATF injector linac, Proc. 10th Symposium on Accelerator Science and Technology, Ibaraki, Japan, 1995, no. JAERI-Conf 95-021.
- [4] M. Yoshida *et al.*, Study on high-current multi-bunch beam acceleration for KEKB injector linac, Proc. LINAC 2006, Knoxville, TN, no. MOP025.
- [5] N. Iida *et al.*, Beam dynamics in positron injector systems for the next generation B-factories, Proc. IPAC2011, San Sebastián, Spain, 2011, no. THYA01.

Preliminary Design Study of a Pre-booster Damping Ring for the FCC e^+e^- Injector

O. Etisken,¹ Y. Papaphilippou,² and A.K. Ciftci^{1,3}

¹Ankara University, Ankara, Turkey

²CERN, Geneva, Switzerland

³Izmir University of Economics, Izmir, Turkey

Abstract

The aim of the FCC e^+e^- lepton collider is to collide particles in the energy range 40–175 GeV. The FCC e^+e^- injector complex needs to produce and transport high-intensity e^+e^- beams at a fast repetition rate of about 0.1 Hz to top up the collider at its collision energy. A basic parameter set exists for all collider energies, assuming a 10 GeV linac operating with a large number of bunches accumulating in the existing SPS, which serves as pre-accelerator and damping ring before the bunches are transferred to the high-energy booster. The purpose of this study is to provide the conceptual design of an alternative damping and accelerator ring, replacing the SPS in the current scheme. This ring will have an injection energy of around 6 GeV and an extraction energy of around 20 GeV. Apart from establishing the basic ring parameters, the final study will include the optics design and layout, and single particle linear and non-linear dynamics optimization, including magnetic and alignment error tolerances. The study will also involve some basic estimation of collective effects, including intrabeam scattering, single and multibunch instabilities and impedances, two-stream effects (e-cloud and ion instabilities) and address the issue of synchrotron radiation handling. In this document, as part of these studies, basic ring parameters, first results of optical design after some analytical calculations, and layout studies are presented.

Keywords

FCC; damping ring; pre-booster ring.

1 Introduction

The current design plan considers the SPS (super proton synchrotron) as a pre-booster damping ring but there may be issues with it: machine availability, synchrotron radiation, new RF system, etc. For these reasons, a ‘green-field’ alternative design was found interesting; the study is concentrated on a new design for pre-accelerating the bunches before they are transferred to the main booster ring. First, it was planned to design a pre-booster ring design with an injection energy of 6 GeV and an extraction energy of 30 GeV. For this goal, the ring design was studied with parameter scaling and basic calculations to determine general parameters. After investigating parameter scaling of the pre-booster with 30 GeV extraction energy, our results forced us to concentrate on an extraction energy of 20 GeV for the pre-booster, since it gives a more logical perimeter for the machine [1]. Following this determination of the extraction energy as 20 GeV, a parameter scaling study and basic calculations were made and the conceptual design and straight sections were studied; in presenting these studies, phase advance, chromaticity, and emittance changes were also investigated.

2 Parameter scaling

Some important parameters, investigated to determine general parameter scaling of the machine, are:

- energy loss per turn;
- damping times;
- energy spread;
- emittance.

All these parameters are correlated with the circumference and filling factor (FF), so this gives an opportunity to compare all the parameters with each other easily:

$$FF = \frac{Nl}{C}, \quad (1)$$

where N is dipole quantity, l is dipole length, and C is circumference.

Figure 1 shows a plot of energy loss per turn for the extraction energy of 30 GeV.

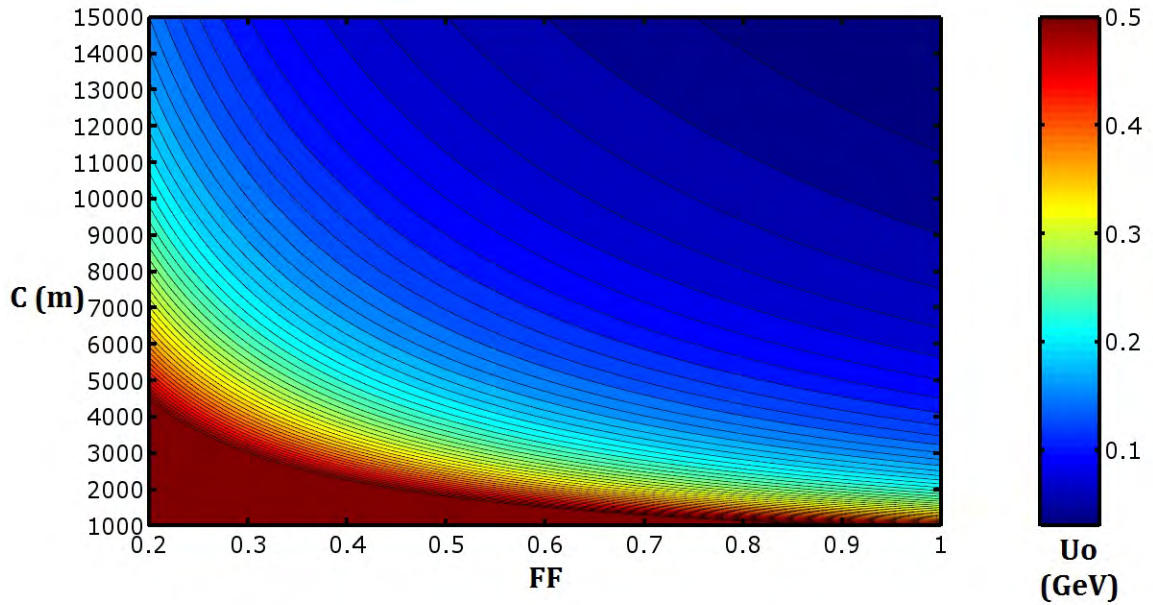


Fig. 1: Scaling of energy loss per turn with filling factor FF and circumference C for 30 GeV

Not having much more than 50 MeV energy loss per turn was one of the assumptions that we made during the study. It is shown in the graph that a circumference shorter than 10 km is not possible for the ≈ 50 MeV energy loss per turn, and having a freshly designed pre-booster 10 km long could not be logical, considering that the existing plan for the SPS is nearly 7 km long [2].

These results motivated us to study 20 GeV extraction energy. Thus, scaling of energy loss per turn was investigated for 20 GeV extraction energy, as shown in Fig. 2.

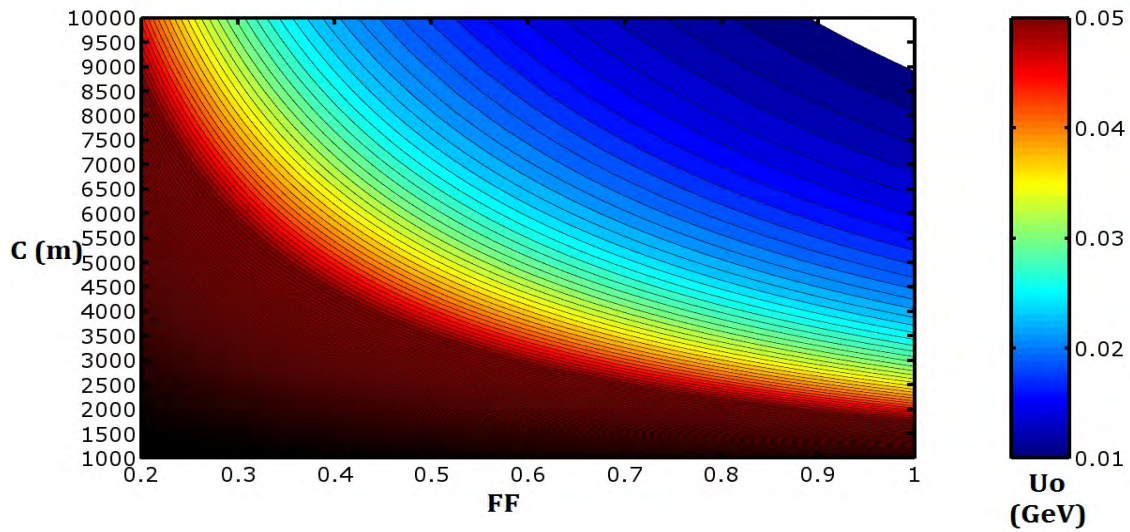


Fig. 2: Scaling of energy loss per turn with filling factor FF and circumference C for 20 GeV

From Fig. 2, it can be seen that 20 GeV enables us to have a circumference of about 2.5 km. With this good result for the machine, it became reasonable to review all other parameters, as shown in Figs. 3–5, for this energy.

As seen from Fig. 2, considering that the FF could be between 0.5 and 0.8, the circumference would have to be between 2 km and 5 km. These parameters give us the necessary frame for considering the other plots.

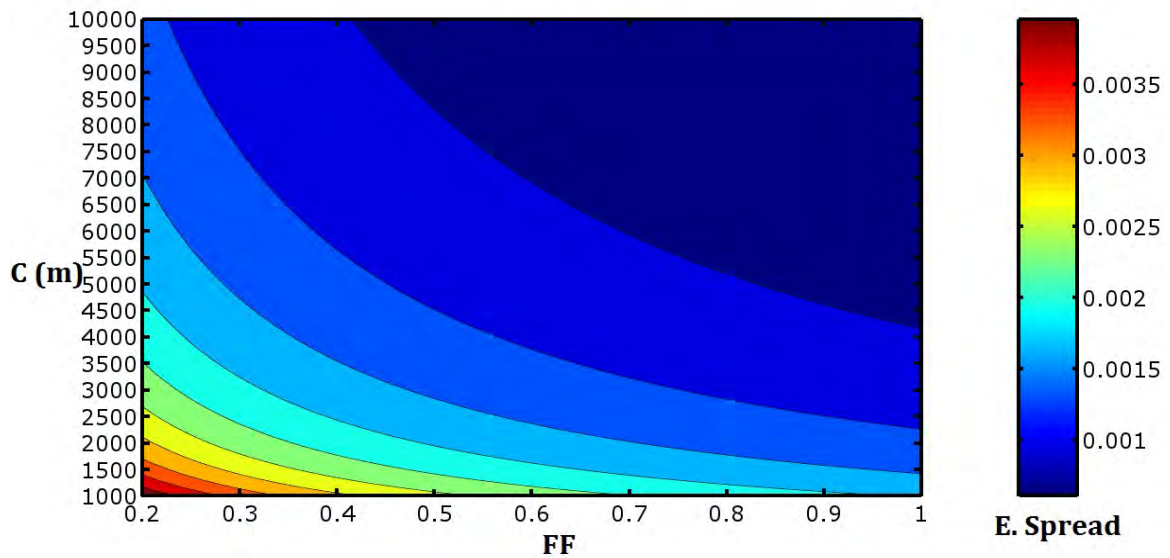


Fig. 3: Scaling of energy spread with filling factor FF and circumference C for 20 GeV

Figure 3 shows that the energy spread is acceptable and does not vary too much in the frame that was determined for our scaling. The same comments can be made for damping time, as can be seen in Fig. 4.

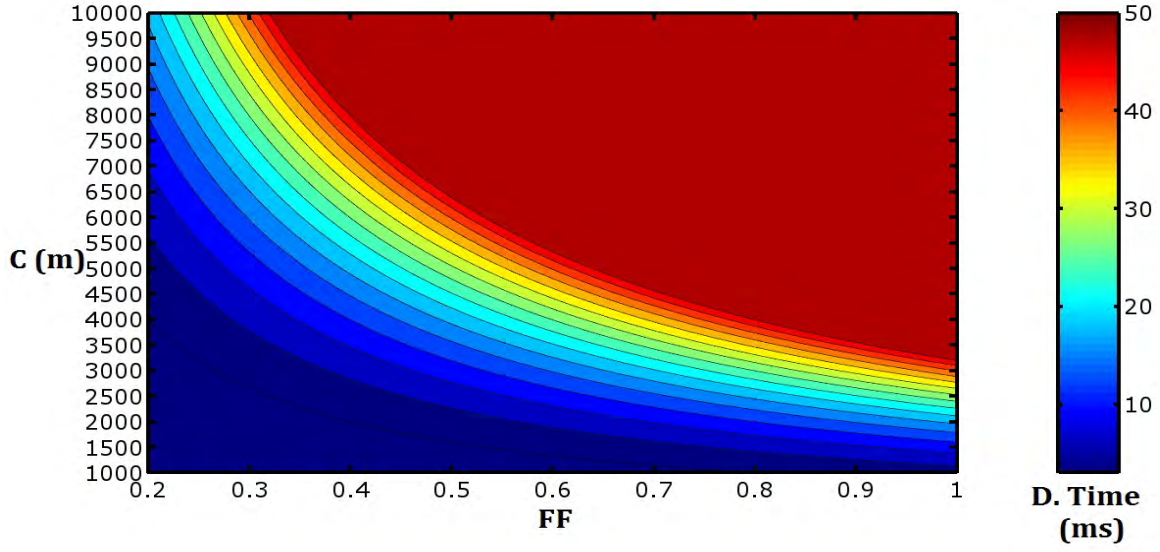


Fig. 4: Scaling of damping time with filling factor FF and circumference C for 20 GeV

After reviewing Figs. 1–4, emittance scaling could also be a good parameter to investigate for the machine:

$$\varepsilon_s = \frac{F_{\text{lattice}} \cdot C_q \cdot \gamma^2 \cdot (2\pi)^3 \cdot l^3}{FF^3 \cdot C^3}. \quad (2)$$

The result shown in Fig. 5 gives us emittance values between 10 and 30 nm.rad for the frame.

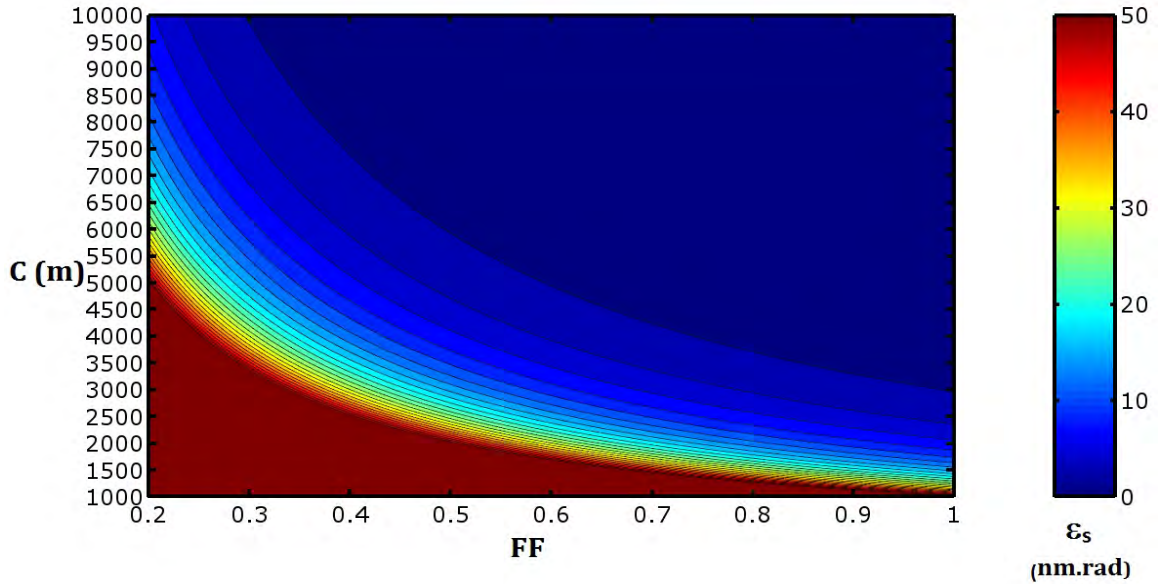


Fig. 5: Scaling of emittance with filling factor FF and circumference C for 20 GeV

3 Preliminary design

3.1 Assumptions and basic calculations

At the starting point of an accelerator design, there are important assumptions to be made and limitations to be determined, such as magnetic fields of magnets, energy loss per turn, and emittance. For this pre-booster design, the energy loss per turn is the main limitation. In the study, it is assumed that the energy loss per turn should be, at most, ≈ 50 MeV per turn, and the emittance can be taken to be 10 nm.rad. Some basic calculations show that this gives a dipole magnetic field of around 0.2–0.3 T with a total number N of about 260, and a bending angle of about 1.3° . Considering 140° for phase advance could be a good starting point. This gives us about 0.6–0.7 m^2 for the quadrupole strength. After all these assumptions and basic calculations, we find that our machine can be around 2.5 km long. Of course, these values will change after detailed calculations are made, as can be seen in the following part of this document. However, these calculations showed us that our studies were progressing in the right direction.

3.2 Chromaticity, phase advance and emittance

Chromaticity, phase advance and emittance: these three parameters are correlated with each other, as can be seen from Eqs. (3)–(7). Thus, in order to choose the optimized point for all three parameters, it is necessary to check how they change according to each other for a period of phase advance. For this, Figs. 6 and 7 are calculated from the relations [3–7].

$$\varepsilon_{\text{fodo}} = F_{\text{fodo}} C_q \gamma^3 \theta^3, \quad (3)$$

$$F_{\text{fodo}} = \frac{1 - \frac{3}{4} \sin^2(\phi/2)}{\sin^3(\phi/2) \cos(\phi/2)} J_x^{-1}, \quad (4)$$

$$\xi_{x0} = -\frac{1}{4\pi} \oint \beta_z k d_z, \quad (5)$$

$$\xi_{y0} = \frac{1}{4\pi} \oint \beta_y k d_z, \quad (6)$$

$$\phi = \arccos\left(\frac{1}{2} \text{trace}(M)\right). \quad (7)$$

The emittance (ε) depends on the lattice design factor (F) and the Lorentz factor (γ); C_q is 3.83×10^{-3} , θ is the total dipole bending angle in Eq. (3). F changes with phase advance (ϕ) as can be seen in Eq. (4), $J_x \approx 1$ is the damping partition number. Eqs. (5)–(6) shows the chromaticities in x and y directions. The chromaticity comes from the quadrupoles (k is the quadrupole strength) and it is proportional to the betatron function ($\beta_{z,y}$). Eq. (7) shows the dependency of the phase advance on the transfer matrix (M),

To see the relations between these parameters, Figs. 6–8 show ‘chromaticity–phase’, ‘chromaticity–emittance’, and ‘phase–emittance’ plots. All three of these plots are important but a study of the details of Fig. 8 could give us more information than the others in defining the optimum point.

Chromaticity increases with increasing phase advance for the period considered, as shown in Fig. 6.

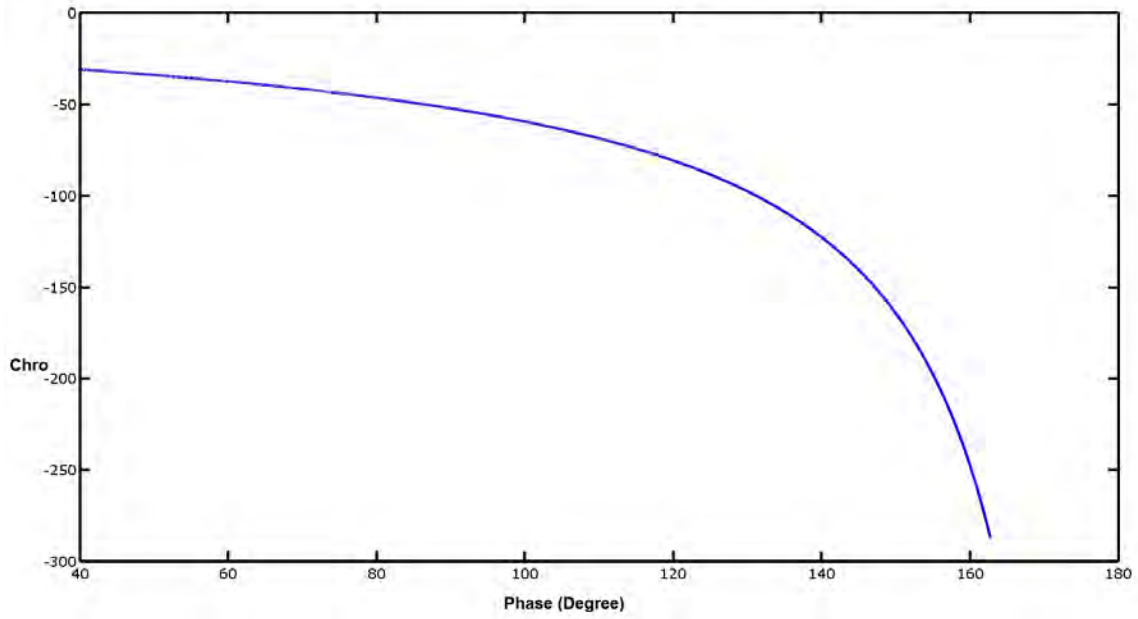


Fig. 6: Relation between chromaticity and phase

Figure 7 shows how emittance changes according to variations in phase advance.

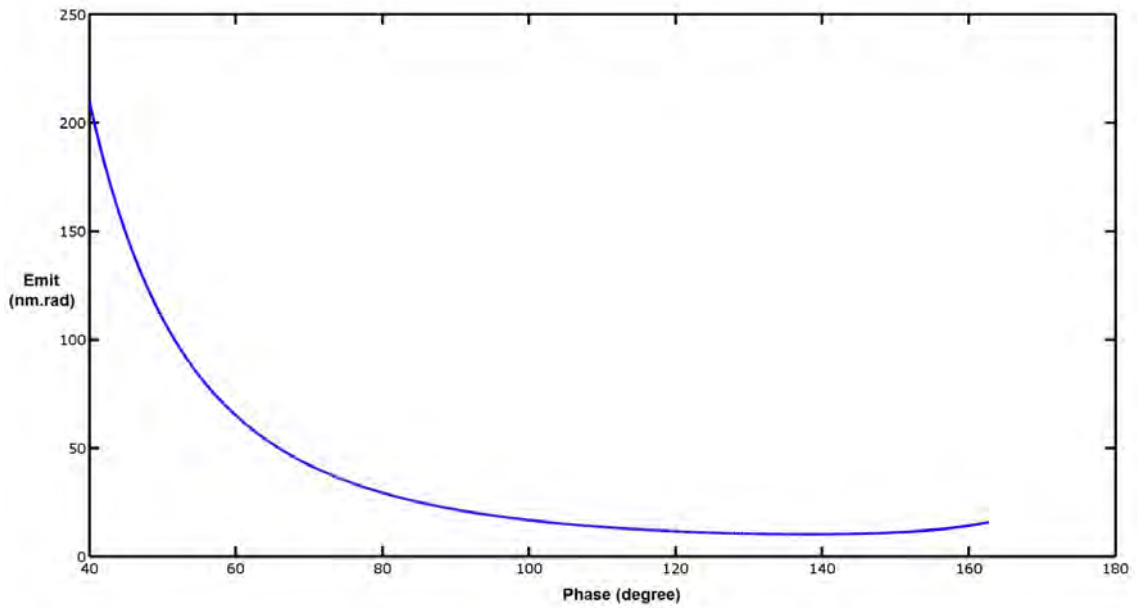


Fig. 7: Relation between emittance and phase advance

Figure 8 shows how emittance and chromaticity change with changes in phase advance. This graph also indicates that after some point the emittance does not vary so much, while the chromaticity changes very sharply. Therefore, this graph gives us useful information about choosing an optimized point for the machine.

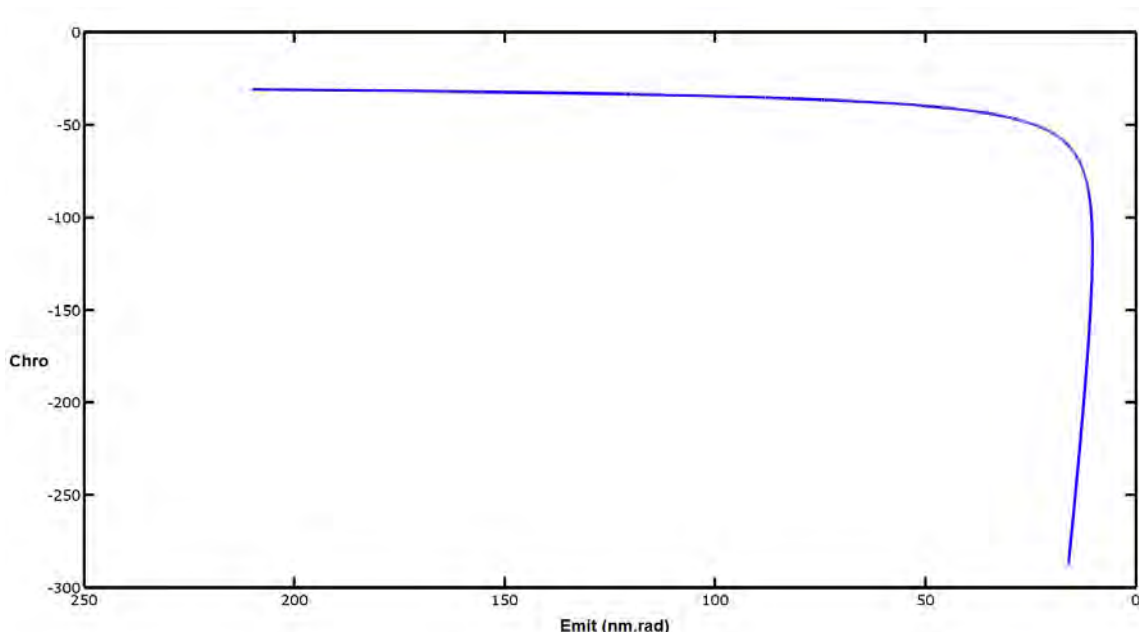


Fig. 8: Relation between chromaticity and emittance

3.3 Conceptual design

All results of abovementioned calculations and plots are evaluated, providing the most optimum design. A FODO type cell is chosen as the main cell for this ring. The ring comprises two arcs and two straight sections. In this design, the ring is 2321.95 m long and the corresponding FODO type cell is illustrated in Fig. 9.

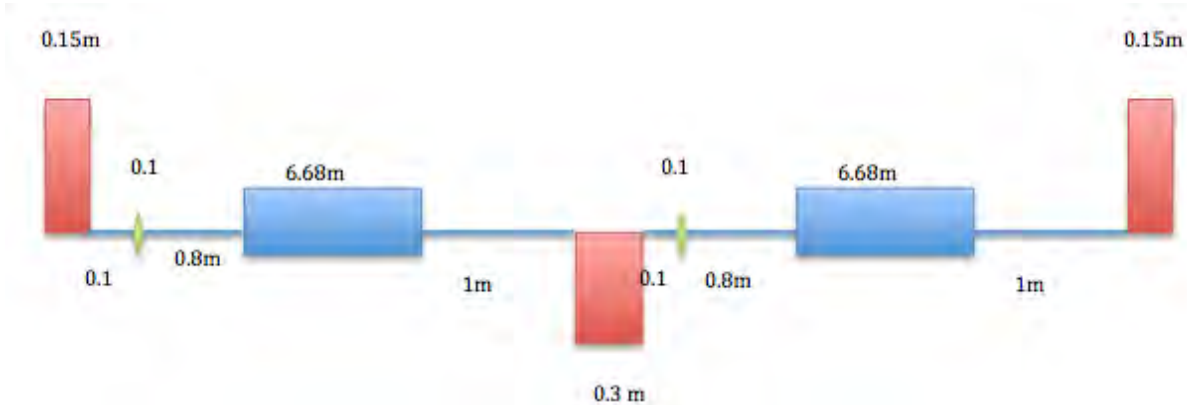


Fig. 9: Main cell of FODO, red shapes symbolize the focusing and defocusing quadrupole magnets, while blue represents bending magnets and green shows possible sextupole magnets.

Since natural chromaticities $\xi_x / \xi_y = -44.195/-42.358$ are high, it is also assumed to use sextupole magnets. In total, 260 dipole magnets (0.06 T/0.248 T) and 266 quadrupole and sextupole magnets are used in the ring. However, using sextupole magnets causes dynamic aperture problems. To limit the dynamic aperture effect, sextupole magnets with low strength are used in each cell instead of using only few sextupole magnets with high strength.

The beta function of the whole ring is shown in Fig. 10. For a booster ring, a straight section with zero dispersion must be allocated, because it is necessary for injection, extraction elements and for RF accelerating structures. From this figure, it can be seen that two straight sections are created in the design and the dispersion is decreased to zero with a matching cell in these sections.

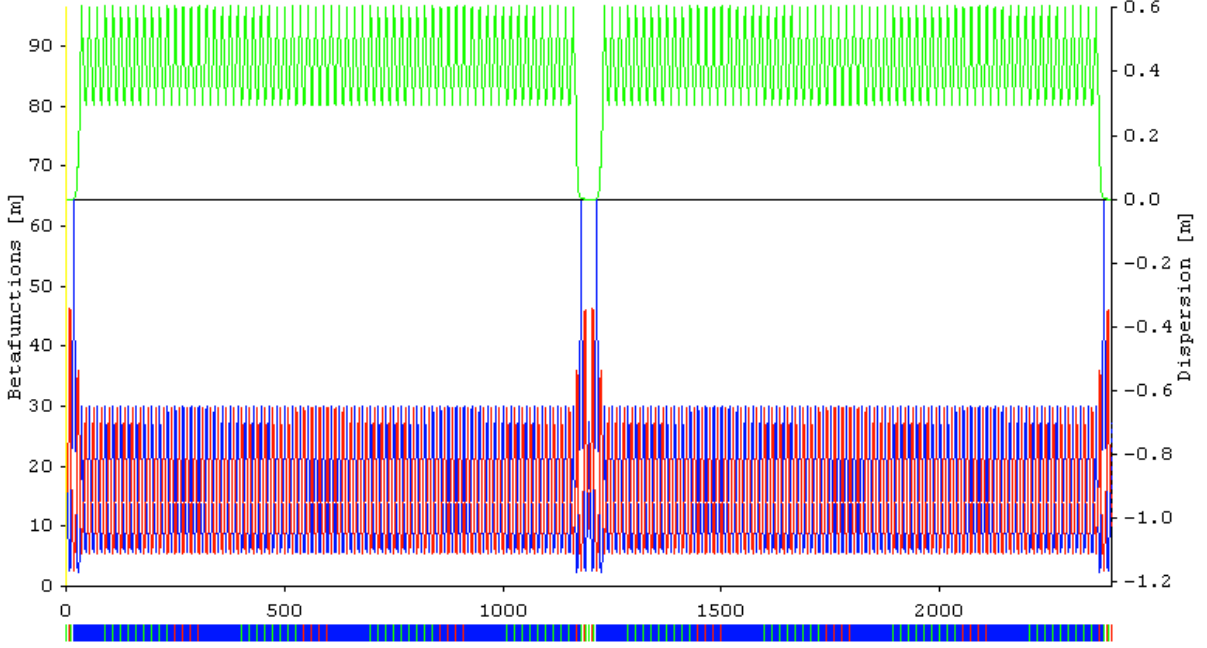


Fig. 10: Betatron functions of the whole ring; the maximum betatron functions (red and blue) around the ring is about 65 m and the dispersion (green) is zero in the straight sections.

The main parameters were calculated and are shown in Table 1.

Table 1: Main parameters

	Injection energy	Extraction energy
Energy	5.0 GeV	20 GeV
Perimeter	2393.54 m	2393.54 m
Emittance $\varepsilon_x/\varepsilon_y$	1.809 nm.rad	28.987 nm.rad
Energy spread (10^{-3})	0.258	1.034
Energy loss per turn	201.5 keV	51586.2 keV
Natural chromaticity ξ_x/ξ_y	-44.195/-42.358	-44.195/-42.358
Cell type	FODO	FODO

4 Conclusion

In this study, we have applied parameter scaling with respect to several radiation-related parameters and have proceeded with a preliminary design based on a FODO cell including sextupole magnets. The study presented in this document is a good starting point to see the general framework of the pre-booster by approaching it through analytical parameter scaling and studying the main parameters such as chromaticity, emittance and phase advance. In future studies, the calculations and preliminary design study will be compared with a study, which will use numeric approaches. It is expected that further studies like dynamic aperture, errors of momentum, alignment and multipolar will give additional limitations influencing the design of the pre-booster. Finally, by evaluating both analytic and numeric approaches, the design will converge further.

References

- [1] O. Etisken *et al.*, Preliminary design study of a pre-booster damping ring for the FCC e^-e^+ injector, FCC Week, Italy, 2016.
- [2] <https://home.cern/about/accelerators/super-proton-synchrotron>, last accessed 6 September 2016.
- [3] H. Wiedemann, *Particle Accelerator Physics* (Springer, Cham, 2007).
- [4] J. Rossbach *et al.*, Basic course on accelerator optics, CAS, 1993.S.Y. Lee, *Accelerator Physics*, 2nd ed. (World Scientific, Singapore, 2004). <https://doi.org/10.1142/5761>.

Comparative Study of the Tuning Performances of the Nominal and Long L^* CLIC Final Focus System at $\sqrt{s} = 380$ GeV

F. Plassard^{*1,2}, A. Latina¹, E. Marin¹ and R. Tomás¹

¹ CERN, Geneva, Switzerland

² University Paris Sud, Orsay, France

Abstract

Mitigation of static imperfections for emittance preservation is one of the most important and challenging tasks faced by the Compact Linear Collider (CLIC) beam delivery system. A simulation campaign has been performed to recover the nominal luminosity by means of different alignment procedures. The state of the art of the tuning studies is drawn up. Comparative studies of the tuning performances and a tuning-based final focus system design optimization for two L^* options are presented. The effectiveness of the tuning techniques applied to these different lattices will be decisive for the final layout of the CLIC final focus system at $\sqrt{s} = 380$ GeV.

Keywords

Linear collider; CLIC; final focus system; alignment; tuning; long L^* .

1 Introduction

The Compact Linear Collider (CLIC) rebaselining foresees a staged machine with an initial centre-of-mass energy of 380 GeV [1], for which the design optimization and tuning of the final focus system (FFS) is presented in this paper. The FFS aims to demagnify the beams down to the nanometre level. The small values of the β -functions at the collision point (Table 1) are provided by two strong quadrupoles (QF1 and QD0), with QD0 located at a distance L^* from the interaction point (IP). Beam size growth, arising from chromatic and higher-order aberrations, is controlled by optics arranged according to the local chromaticity correction scheme [2]. The distance L^* is planned to be 4.3 m [3] for the nominal lattice, forcing QD0 to be integrated inside the experiment and protected by an anti-solenoid, to avoid interplay between the quadrupole and the solenoid fields. Machine detector interface issues are removed with an alternative longer L^* of 6 m [4] but one has to expect a reduction in the maximum luminosity achievable, owing to the increase in chromaticity propagated to the IP (Table 1).

*Corresponding author.

Table 1: CLIC 380 GeV design parameters for both L^* options

L^* [m]	4.3	6
Final focus system length [m]	553	770
$\gamma\epsilon_x/\gamma\epsilon_y$ [nm]	950/20	950/20
β_x^*/β_y^* [mm]	8.2/0.1	8.2/0.1
$\sigma_{x,\text{design}}^*$ [nm]	145	145
$\sigma_{y,\text{design}}^*$ [nm]	2.3	2.3
$L_{\text{tot, design}} [10^{34} \text{ cm}^{-2} \text{ s}^{-1}]$	1.5	1.5
$L_{1\%, \text{ design}} [10^{34} \text{ cm}^{-2} \text{ s}^{-1}]$	0.9	0.9
Chromaticity $\xi_y (\approx L^*/\beta_y^*)$	43000	60000

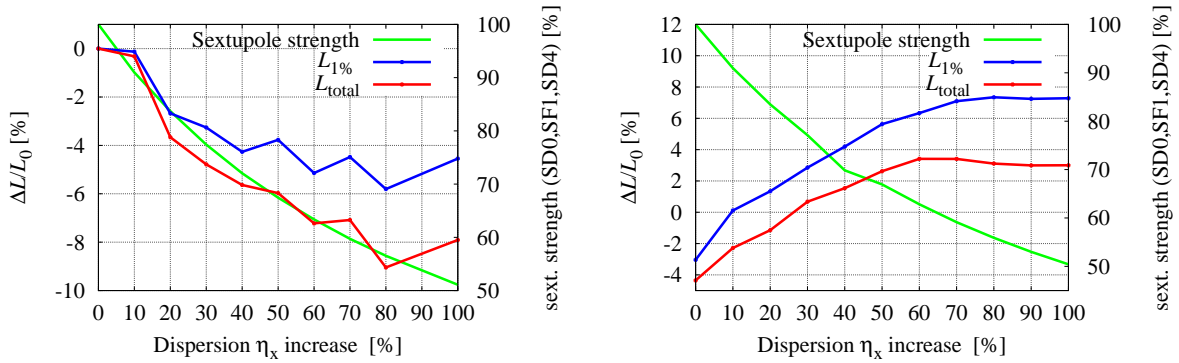


Fig. 1: Relative luminosity and average strength of the last three sextupoles versus dispersion increase through the final focus system. Left: $L^* = 4.3$ m; right: $L^* = 6$ m.

The small tolerances of the FFS on magnet position stability renders the luminosity tuning strategy very challenging. In the presence of realistic transverse magnet misalignments of a few micrometres, the luminosity can decrease by several orders of magnitude. It is thus necessary to prove that the proposed FFS lattice design fulfils the tuning requirements. The FFS designs have been optimized by targeting the optimal luminosity and momentum bandwidth of a perfectly aligned system. A first tuning simulation campaign, comparing both L^* options, has demonstrated the need for changes in the FFS layout to increase the effectiveness of the luminosity tuning. In this paper, it is proposed to promote the tuning efficiency as a figure of merit for the design of our system.

2 Final focus system design optimization with $L^* = 4.3$ m and $L^* = 6$ m

Two optimized lattices with nominal and long L^* have been proposed in previous studies [5] for the first stage of CLIC at $\sqrt{s} = 380$ GeV. The nominal beam delivery system layout was based on the $\sqrt{s} = 500$ GeV beam delivery system design planned in the old staging strategy [6]. A scan of the bending magnet angles of the FFS has been performed in both cases in order to find the optimal dispersion level by considering the total and peak luminosities of an error-free system. Sextupoles need to be coupled with dispersion to correct chromatic aberrations; their strengths can then be reduced by increasing the dispersion level in the FFS, as shown in Fig. 1. According to the scan results in Fig. 1, the optimum performances are found with no changes in the bending magnet angles for the $L^* = 4.3$ m option and with 70% of dispersion increase for $L^* = 6$ m. Details of the performances and the optimization process of the beam size at the IP including the effect of high order aberrations [7, 8] can be found in Ref. [5]. The resulting Twiss functions along the FFS are shown in Fig. 2.

3 Tuning algorithm applied

The tuning procedure aims to mitigate the effect of static displacements in the horizontal and vertical planes [9] of the quadrupoles, sextupoles, and beam position monitors of the FFS. This procedure utilizes beam-based alignment techniques [10, 11], to correct the beam orbit throughout the system, and sextupole tuning knobs, to combat the linear aberrations at the IP. In the tuning simulation discussed here, these optics are randomly misaligned with $\sigma_{RMS} = 10$ μm , according to the pre-alignment specification for the CLIC beam delivery system [12]. Magnet strength, tilt, and roll errors have not yet been implemented. Random misalignments are applied to 100 machines. The beam-based alignment begins with a one-to-one correction technique [13] that aims to steer the beam through the centre of each beam position monitor using transverse kickers. The effectiveness of the orbit correction is compromised by the misaligned beam position monitors, leading to a dispersive orbit. To remove the remaining dispersion deviations from the nominal dispersion profile along the FFS, the so-called dispersion-free steering

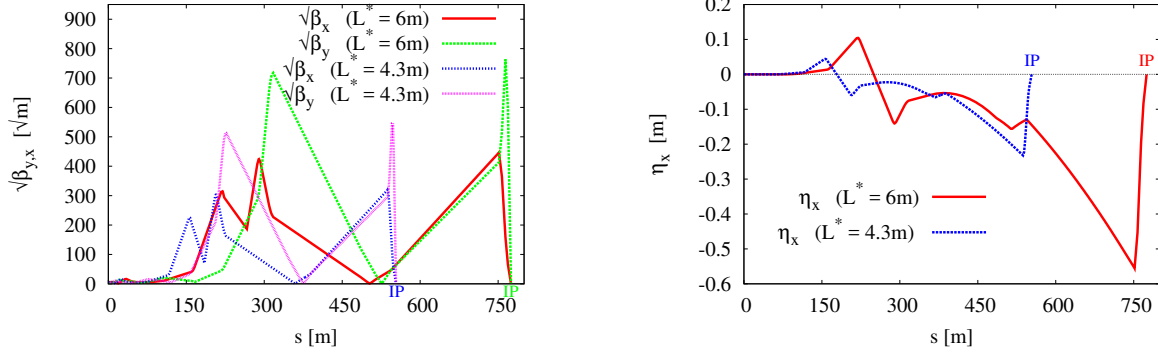


Fig. 2: Comparison of $L^* = 4.3\text{ m}$ and $L^* = 6\text{ m}$ after optimization. Left: Twiss functions $\beta_{x,y}$; right: dispersion η_x . IP, interaction point.

technique [14] is applied. The dispersion is evaluated by collecting two orbit readings, $x_{\Delta E_+}$ and $x_{\Delta E_-}$, of two beams, with energy deviations of $\pm\Delta E$. The dispersion is obtained as:

$$\vec{\eta} = \frac{x_{\Delta E_+} - x_{\Delta E_-}}{2\Delta E}. \quad (1)$$

The value of the corrector kicks k_m for the correction of the orbit and dispersion is obtained by minimizing:

$$\chi^2 = \sum_{\text{BPMs}} x_i^2 + \omega^2 \sum_{\text{BPMs}} (x_{\Delta E,i} - x_i)^2 + \beta^2 \sum_{\text{Correctors}} k_m^2, \quad (2)$$

where i and m are the indices of the beam position monitors and kickers, respectively. The weighting factors ω and β are used to limit the value of the applied corrector kicks.

Linear aberrations at the IP created by the misaligned optics are corrected using pre-computed combinations of sextupole displacements in the transverse plane. Each set of sextupole knobs is constructed to be orthogonal, so that the chosen aberrations are corrected independently. Horizontal and vertical sextupole offsets Δx and Δy introduce feed-down normal and skew quadrupole fields (Eqs. (3) and (4)), which create distortions in the $\beta_{x,y}$ and $\eta_{x,y}$ functions and introduce betatron coupling at the IP:

$$\Delta B_x = B\rho[(k_2\Delta x)y + (k_2\Delta y)x + k_2\Delta x\Delta y], \quad (3)$$

$$\Delta B_y = B\rho\left[(k_2\Delta x)x - (k_2\Delta y)y + \frac{1}{2}k_2(\Delta x^2 - \Delta y^2)\right], \quad (4)$$

with

$$\Delta k_{1n} = k_2\Delta x, \quad \Delta k_{1s} = k_2\Delta y, \quad (5)$$

where $B\rho$ is the magnetic rigidity, k_2 is the normalized sextupole strength, k_{1n} and k_{1s} are the normalized normal and skew quadrupole strengths, respectively. Knobs for shifting the waist position $\Delta\omega_{x,y}$ and horizontal dispersion $\Delta\eta_x^*$ aberrations are constructed by moving the sextupoles in the horizontal plane. Vertical dispersion $\Delta\eta_y^*$ and coupling aberrations are corrected using the vertical displacement of the sextupoles [15, 16]. As the knobs are not fully orthogonal, one must scan the knobs iteratively to increase the luminosity further. In the tuning procedure applied here, the set of knobs is scanned twice with a large knob amplitude and twice with a smaller amplitude for better determination of the optimal luminosity. Finally, we define the four tuning steps as the first iteration of the linear knobs:

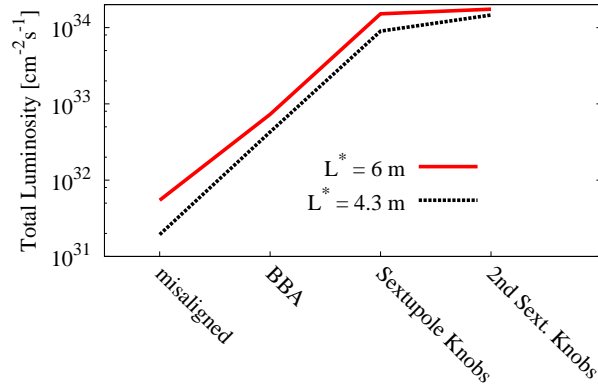


Fig. 3: Average luminosity over 100 machines after each tuning step for the two L^* options of the final focus system optimized in Ref. [5]. BBA, beam-based alignment.

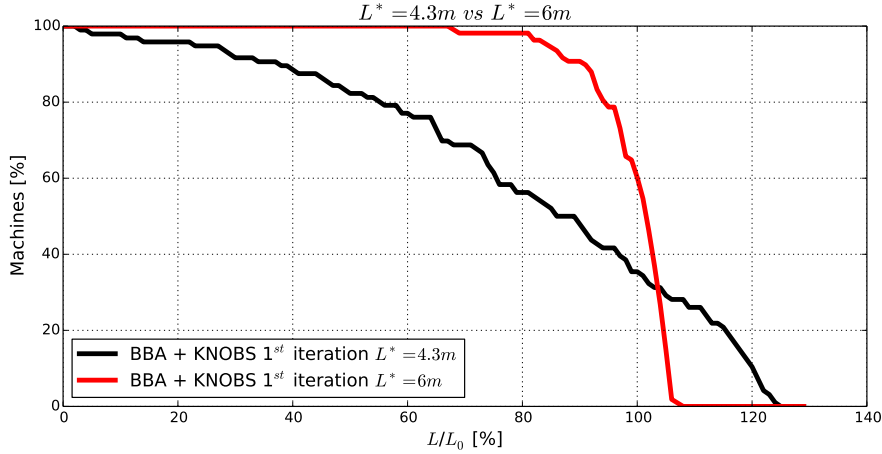


Fig. 4: Tuning simulation results of 100 machines achieving L/L_0 for the two L^* options of the final focus system optimized in Ref. [5]. BBA, beam-based alignment.

1. one-to-one correction;
2. dispersion-free steering;
3. sextupole knob tuning;
4. second iteration of linear knob tuning.

4 Tuning simulation results

4.1 Final focus system tuning comparison: nominal versus long L^*

The following tuning simulations were applied on the optimized designs of the nominal and long L^* options presented in Section 2. The average results at each tuning iteration, for the four tuning steps described in Section 3, are compared for both lattices in Figs. 3 and 4. One can see that the luminosity, after beam-based alignment and linear knob tuning, is better recovered for the $L^* = 6$ m case, thanks to higher luminosity after transverse optics misalignments, as shown in Fig. 3.

To quantify the tuning effectiveness, one must consider the number of machines that recover the design luminosity ($L_0 = 1.5 \times 10^{34} \text{ cm}^{-2}\text{s}^{-1}$). As shown in Fig. 4, for $L^* = 4.3$ m, only 35% of the

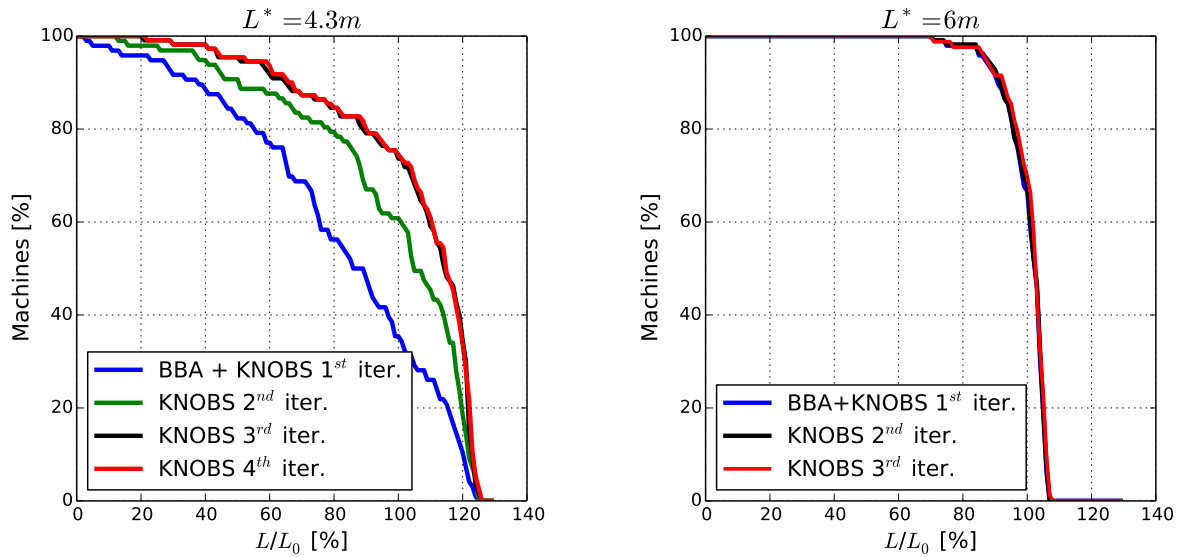


Fig. 5: Tuning simulation results of 100 machines achieving L/L_0 for the final focus system optimized in Ref. [5] after several iterations of the linear knobs. Left: $L^* = 4.3$ m; right: $L^* = 6$ m.

machines achieve L_0 , compared with 60% for $L^* = 6$ m after the first iteration of the knobs. Despite a smaller achievable maximum luminosity, the long L^* option shows better tuning efficiency than the nominal one. This can be improved by applying iterations of linear knobs until no further increase of the luminosity is observed. However, the tuning time is also a concern, owing to the impact of ground motion. Here, one iteration of linear knobs corresponds to ≈ 720 luminosity measurements. Figure 5 compares the luminosity increase after several knob iterations applied to both designs. The impact of the linear knobs reaches its limit after the third iteration for $L^* = 4.3$ m, with 75% of the machines achieving L_0 . For $L^* = 6$ m, the limit is reached at the second iteration, with 70% of the machines recovering the design luminosity.

4.2 Tuning-based design optimization

From the comparative study described in Section 4.1, one may suspect that the tuning efficiency could be improved by optimizing the dispersion level in the FFS. The design optimization strategy applied in this study involves tuning a set of FFS lattices with different bending magnet angles. The tuning results of the dispersion scan will help to decide the optimal layout that maximizes the luminosity and tuning effectiveness.

All lattices have been randomly misaligned by $\sigma_{\text{RMS}} = 10$ μm in the transverse plane. When the sextupoles are displaced horizontally, feed-down normal quadrupole kicks are generated and the corresponding changes in the IP spot size are evaluated by:

$$\Delta\sigma_x^* = k_s \Delta_x \beta_{x,s} \sigma_{x0}^*, \quad (6)$$

$$\Delta\sigma_y^* = k_s \Delta_x \beta_{y,s} \sigma_{y0}^*, \quad (7)$$

where $\beta_{x,s}$ and $\beta_{y,s}$ are the β -functions at the sextupole location. Vertical sextupole displacements generate skew quadrupole kicks that increase the spot size by

$$\Delta\sigma_y^* = k_s \Delta_y \sigma_{x,s} |R_{34}^{s \rightarrow *}|, \quad (8)$$

where $\sigma_{x,s}$ is the horizontal beam size at the sextupole location and $R_{34}^{s \rightarrow *}$ is the matrix element from the sextupole to the IP. As a consequence of the chromatic correction, the strength of sextupoles k_2

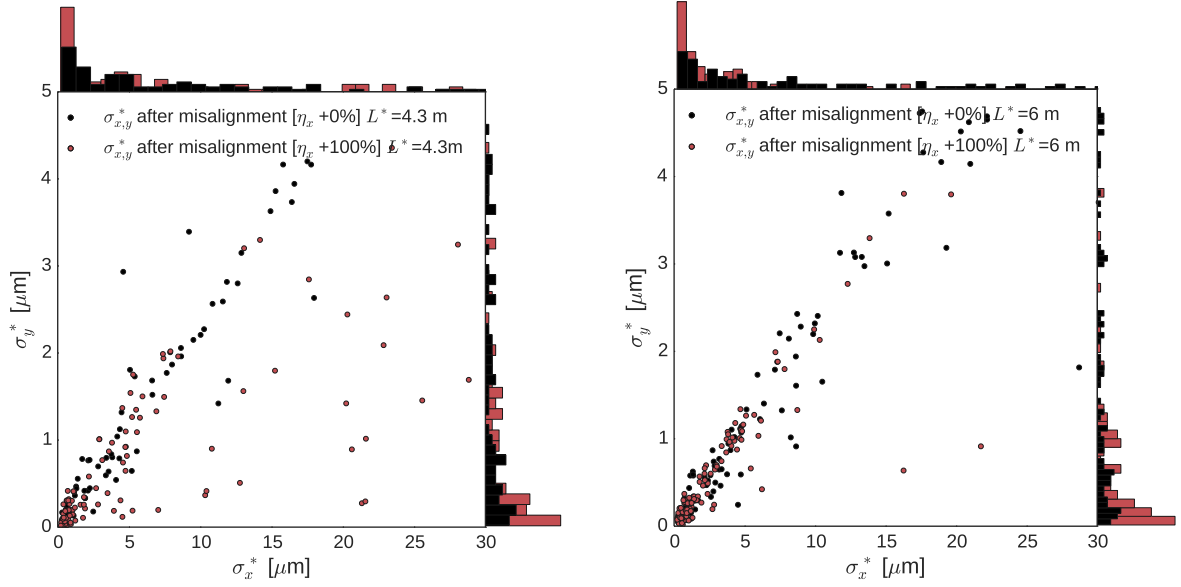


Fig. 6: Comparison of beam size distribution at the interaction point after misalignment of the magnets for two scenarios, 0% and 100% dispersion increase. Left: $L^* = 4.3$ m; right: $L^* = 6$ m. Histograms of $\sigma_{x,y}^*$ are plotted on mirror axes.

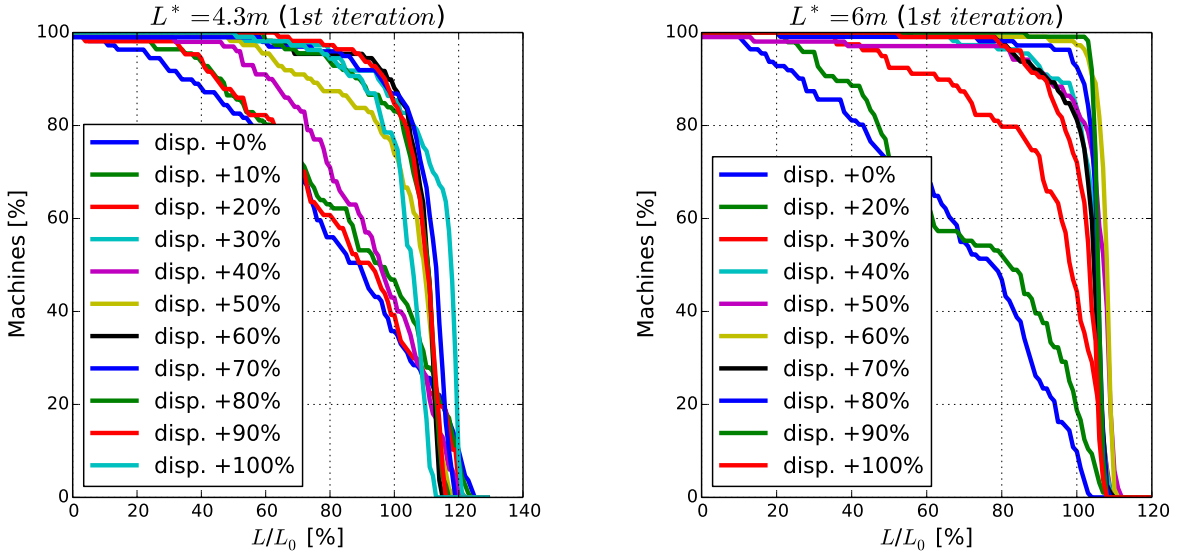


Fig. 7: Tuning effectiveness comparison between different dispersion levels from 0% to 100% increase. Left: $L^* = 4.3$ m; right: $L^* = 6$ m.

decreases when dispersion is increased, as shown in Fig. 1. From Eqs. (6)–(8), one can see that the impact of the sextupole misalignments on the beam size at the IP is reduced when k_2 decreases. In Fig. 6, the comparison of the beam sizes of the 100 machines after misalignment shows how the lattice becomes more tolerant to misalignment with an increase of dispersion in the FFS by a factor of two. A tuning simulation campaign has been performed on lattices with dispersion level intervals of 10% for the nominal and long L^* options; the results are presented in Fig. 7.

Increasing the dispersion level by 60% results in an increase in the number of machines that achieve L_0 , from 35% to 88% with only a 7% loss of maximum luminosity achievable for $L^* = 4.3$ m.

Increasing the dispersion by 20% (from +70% to +90%) results in 99% of the machines recovering L_0 with almost no loss in luminosity, considering an error-free lattice.

5 Conclusions

Optimizing the FFS by targeting the luminosity of an error-free lattice is not sufficient to prove its feasibility. Introducing tuning effectiveness as a new figure of merit for the design optimization is a more realistic approach in evaluating the performances of FFSs. It has been shown that reduction of the sextupole strengths is very helpful for tuning the machine, especially in the nominal L^* case, where the tuning performance has been significantly improved. More tuning iterations of the new optimized lattices are needed in order to determine the final layout of the FFS for both L^* options. One must balance between maximum luminosity achievable and tuning time, according to the need of the machine during operation.

References

- [1] P. Burrows (CLIC Accelerator Collaboration), CLIC accelerator: status, plans and outlook, CLIC Workshop, CERN, Geneva, 2016.
- [2] P. Raimondi and A. Seryi, *Phys. Rev. Lett.* **86** (2001) 3779.
<http://dx.doi.org/10.1103/PhysRevLett.86.3779>
- [3] A Multi-TeV Linear Collider Based on CLIC Technology: CLIC Conceptual Design Report, CERN-2012-007 (CERN, Geneva, 2012). <https://doi.org/CERN-2012-007>
- [4] A. Seryi, Near IR FF design including FD and longer L^* issues, CLIC08 (2008).
- [5] F. Plassard *et al.*, CLIC beam delivery system rebaselining and long L^* lattice optimization, TH-PMR045 Proc. IPAC2016, Busan, Korea, 2016.
- [6] R. Tomas *et al.*, The CLIC BDS towards the conceptual design report, SLAC-PUB-15156 (2010).
- [7] R. Tomas. *Phys. Rev. ST Accel. Beams* **9** (2006) 081001.
<http://dx.doi.org/10.1103/PhysRevSTAB.9.081001>
- [8] R. Tomas *et al.*, CLIC final focus studies, Proc. EPAC 2006, Edinburgh, Scotland, 2006.
- [9] B. Dalena *et al.*, *Phys. Rev. ST Accel. Beams* **15** (2012) 051006.
<http://dx.doi.org/10.1103/PhysRevSTAB.15.051006>
- [10] P. Tenenbaum and T. O. Raubenheimer, *Nucl. Instrum. Methods Phys. Res. A* **302** (1991) 191.
[http://dx.doi.org/10.1016/0168-9002\(91\)90403-D](http://dx.doi.org/10.1016/0168-9002(91)90403-D)
- [11] A. Latina *et al.*, Alignment of the CLIC BDS, CERN-AB-2008-011; CLIC-Note 753, (CERN, Geneva, 2008).
- [12] H. Mainaud Durand *et al.*, Alignment challenges for a future linear collider, IPAC13, Shanghai, 2013, WEPME046.
- [13] Y. Chung *et al.*, Closed orbit correction using singular value decomposition of the response matrix, Particle Accelerator Conf., Dallas, Texas, 1993.
- [14] C. Fischer and G. Parisi, Trajectory correction algorithms on the latest model of the CLIC main LINAC, CERN-SL-96-065-BI, CLIC Note 315, (CERN, Geneva, 1996).
- [15] Y. Nosochkov *et al.*, Tuning knobs for the NLC Final Focus, Proc. EPAC 2002, Paris, 2002.
- [16] T. Okugi *et al.*, *Phys. Rev. ST Accel. Beams* **17** (2014) 023501.
<http://dx.doi.org/10.1103/PhysRevSTAB.17.023501>

The CLIC Detector Concept

F. Pitters (on behalf of the CLICdp collaboration)

CERN, Geneva, Switzerland

Vienna University of Technology, Austria

Abstract

The Compact Linear Collider (CLIC) is a concept for a future linear collider that would provide e^+e^- collisions at up to 3 TeV. The physics aims require a detector system with excellent jet energy and track momentum resolution, highly efficient flavour tagging and lepton identification capabilities, full geometrical coverage extending to low polar angles, and timing information of the order of nanoseconds to reject beam-induced background. To deal with these requirements, an extensive R&D programme is in place to overcome current technological limits. The CLIC detector concept includes a low-mass all-silicon vertex and tracking detector system and fine-grained calorimeters designed for particle flow analysis techniques, surrounded by a 4 T solenoid magnet. An overview of the requirements and design optimisations for the CLIC detector concept is presented.

Keywords

CLIC; CLICdp; CLIC detector; new detector concepts.

1 Introduction

The LHC has pushed the energy frontier to new heights. For the precision frontier to maintain the pace, a high-energy lepton collider is needed. The Compact Linear Collider, CLIC, is a proposed concept for such a lepton collider. The study, hosted by CERN, aims to provide e^+e^- collisions at up to $\sqrt{s} = 3$ TeV in the post-LHC era.

CLIC offers a unique sensitivity to particles produced in electroweak interactions. The rich physics programme includes precision measurement of Higgs and top quark properties as well as direct and indirect searches of physics beyond the Standard Model. An overview of the physics potential of CLIC is given in Ref. [1] and a more detailed view on Higgs physics can be found in Ref. [2].

2 The CLIC accelerator

For a linear collider to be able to accelerate particles to multi-TeV energies at reasonable lengths, the accelerating structures must operate at very high electrical field gradients. This excludes the use of superconducting RF structures because their maximum gradient is intrinsically limited by the critical field of the used material. Normal conducting cavities, however, have been shown to hold accelerating gradients of 120 MV/m with reasonable breakdown rates when operated at a frequency of several GHz [3]. For CLIC, the goal is to obtain gradients of 100 MV/m at a frequency of 12 GHz.

To power the accelerating cavities efficiently at this frequency, CLIC is based on a novel two-beam acceleration scheme, shown in Fig. 1. The idea is to use a high-intensity but rather low-energy electron beam, the so-called drive beam, and restructure it into 12 GHz bunches via a series of delay loops and combiner rings. This beam is then decelerated in dedicated cavities and the extracted 12 GHz power is transferred via wave guides to the accelerating cavities of the main electron and positron beams. The resulting beam structure shows a bunch spacing of 0.5 ns with 312 bunches making up one train. The repetition rate is 50 Hz.

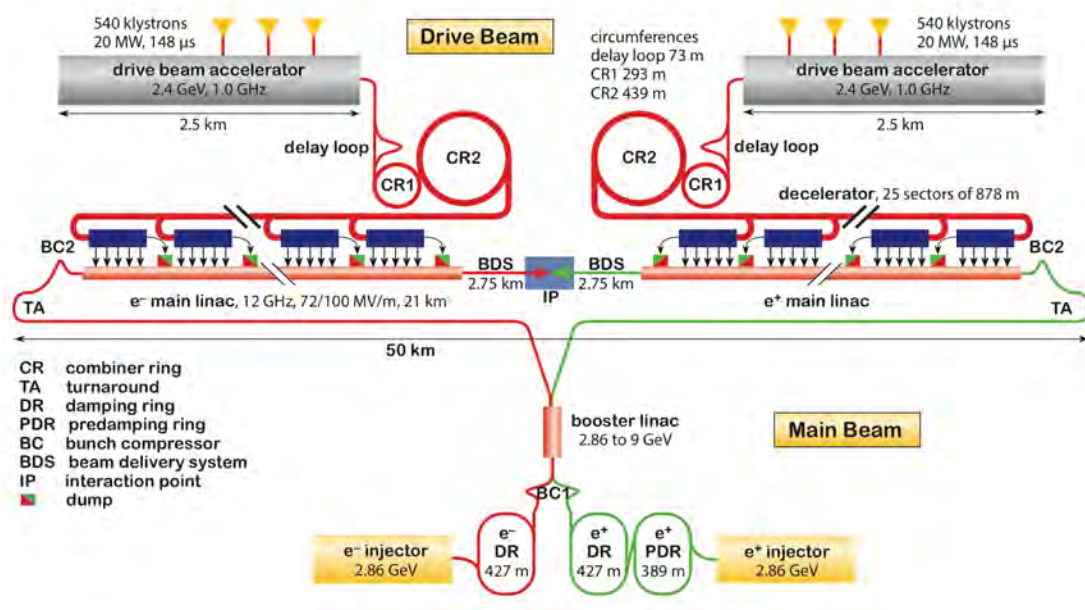


Fig. 1: Two-beam acceleration scheme for CLIC, used to accelerate electrons and positrons to 3 TeV. A low-energy but high-intensity drive beam is bunched and decelerated to power the cavities for the main beam at the desired frequency of 12 GHz. This allows for accelerating gradients of 100 MV/m. Figure is taken from Ref. [3].

To achieve the desired luminosity of $5.9 \times 10^{34} \text{ cm}^{-2} \text{ s}^{-1}$, the beam sizes at the interaction point are focused to $\sigma_x \approx 40 \text{ nm}$ and $\sigma_y \approx 1 \text{ nm}$ at 3 TeV. The strong focusing, together with the beam structure of the two-beam acceleration scheme, creates very high charge densities. As a result, beamstrahlung reduces the energy of individual electrons and positrons. Collisions therefore take place over a wide range of energies. At 3 TeV, 35% of all collisions are within 1% of the nominal \sqrt{s} value [1]. This distribution, called the luminosity spectrum, must be measured and deconvoluted in every physics study.

Due to the wide range of the physics programme, it is convenient to build CLIC in several energy stages, each one optimised for a certain part of the programme. The current baseline foresees three stages, of 380 GeV, 1500 GeV, and 3000 GeV. These energy stages have recently been revisited and updated [4].

3 Detector requirements

The design requirements for the detector are driven by the desired precision of the physics measurements. The track momentum resolution determines the feasibility and precision of many physics studies, e.g., via the reconstruction of the di-muon invariant mass. The aim is set to $\sigma_{p_T}/p_T^2 \approx 2 \times 10^{-5} \text{ GeV}^{-1}$. Another crucial parameter is the jet energy resolution. A value of $\sigma_E/E \approx 3.5\%$ for jet energies above 100 GeV allows for about 2.5σ separation of W and Z candidates in hadronic decays [1]. Moreover, efficient identification of secondary vertices for flavour tagging of heavy quark states is needed. The derived requirement is a transverse impact parameter resolution of $\sigma_{r\phi} \approx (5 \oplus 15/p[\text{GeV}]) \sin^{\frac{3}{2}} \theta \text{ } \mu\text{m}$.

In addition to the physics-driven detector requirements, the strongly focused beams and short bunch spacing set requirements on pile-up mitigation and background suppression. Incoherent e^+e^- pairs and low p_T hadronic jets from the beamstrahlung interactions are the dominant background processes. Owing to the boosted nature of this production, tagging of very forward particles plays an important role in improving the efficiency of background identification. Therefore, a large geometrical coverage in the forward region is desired. Time stamping capabilities of 1–10 ns and a high granularity throughout the detector are also required.

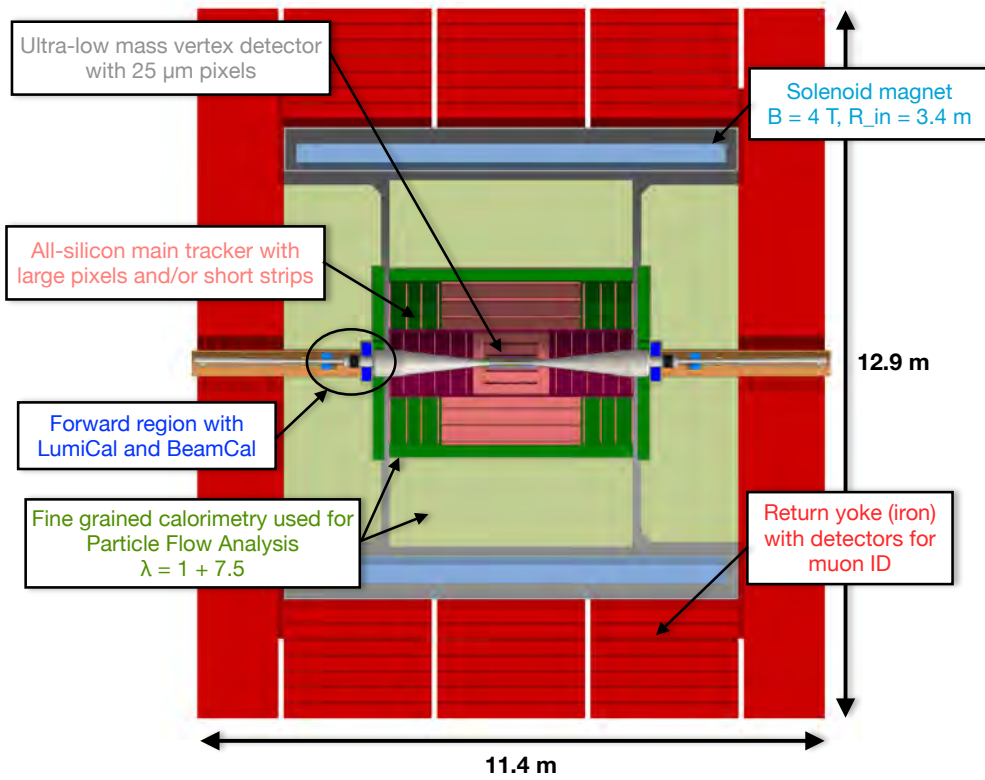


Fig. 2: Top view of CLIC detector model

4 The CLIC detector

Starting from the ILD and SiD concepts [5, 6], adaptations were made towards CLIC's specific requirements. The resulting two concepts were consequently merged into one optimised detector model (Fig. 2). The innermost layer of the CLIC detector is a low-mass vertex detector followed by an all-silicon tracker. The detector is optimised for particle flow algorithms; therefore, the calorimeters must be placed inside the magnet and as close to the tracker as possible. The electromagnetic calorimeter has a depth of $23X_0$ and the hadronic calorimeter is $7.5\lambda_I$ deep. A superconducting solenoid that produces a 4 T magnetic field and an iron return yoke with interleaved muon chambers are located on the outside. The forward region is equipped with two additional calorimeters for extended geometrical coverage and luminosity measurements. The overall dimensions of the detector are 11.4 m in length and 12.9 m in height.

4.1 Vertex detector

The requirements for the vertex detector are determined mainly by the desired momentum resolution and flavour tagging capabilities as well as the need for efficient background suppression. To achieve the aims outlined in the previous section, the goal is to reach a single-point resolution of $\sigma_{x,y} \approx 3 \mu\text{m}$ and time stamping capabilities of better than 10 ns. In addition, for occupancy reasons, the pixel pitch should not exceed $25 \times 25 \mu\text{m}^2$. Another challenge comes from the low material budget. The goal of $0.2\%X_0$ per layer translates to an equivalent of roughly 200 μm of silicon for sensor, readout, cooling, support, and cabling. The geometry of the vertex detector is shown in Fig. 3. It is designed in three double layers and has an overall length of 560 mm. The innermost barrel layer is located 31 mm from the interaction point.

A concept based on hybrid silicon pixel detectors is under development to fulfil the requirements. Due to the low material budget, the sensors and readout ASICs are both foreseen to be thinned to 50 μm thickness. As sensors, either capacitively coupled HV-CMOS sensors or bump-bonded active-edge planar

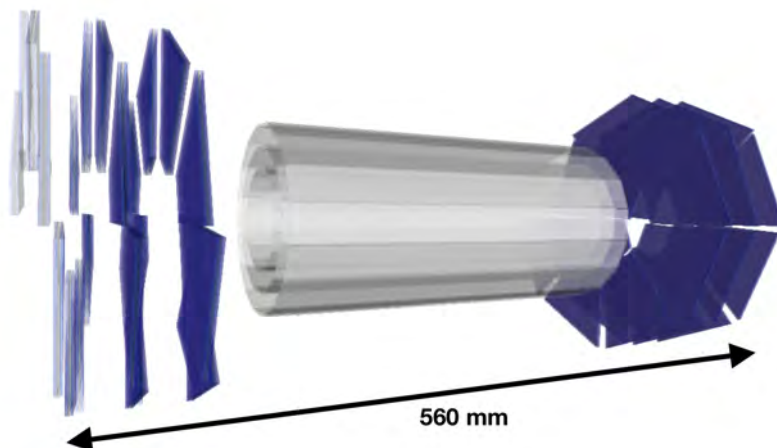


Fig. 3: Geometry of CLIC vertex detector. A barrel design with spiral endcaps, together with power pulsing of the electronics, allows for forced gas flow cooling. This is necessary to fulfil the strict material budget.

sensors are considered. The capacitive coupling of the HV-CMOS sensors to the readout ASIC is realised via a layer of glue. CLICpix, a demonstrator chip in 65 nm technology with $25 \times 25 \mu\text{m}^2$ pixel pitch, has been developed for the readout. The chip enables simultaneous time and energy measurements via time-over-threshold and time-of-arrival counters. An improved version, CLICpix2, is currently in the final verification stage.

To avoid the need for liquid cooling, the layout of the vertex detector is optimised for low power dissipation. This is achieved via power pulsing of the electronics: taking advantage of the pulsed beam structure, most of the electronics is powered down after every particle train and only switched back on a few μs before the next. Together with an optimised spiral geometry in the endcaps, this allows for forced air flow cooling.

4.2 Tracking detector

For the tracker, a single-point resolution of $\sigma_{r\phi} \approx 7 \mu\text{m}$ in the $r\phi$ plane and time stamping capabilities of better than 10 ns are needed to achieve the desired momentum resolution and background suppression. Moreover, track reconstruction requires that occupancies should be kept below 3%. An all-silicon tracker is under development to meet these requirements. The maximum cell pitches needed are between 1 mm and 10 mm in the z direction, depending on the position inside the detector. In the $r\phi$ plane, a $50 \mu\text{m}$ pitch is needed to reach the required single-point resolution. Several monolithic silicon pixel technologies are being evaluated as possible sensor candidates.

The mechanical design is divided into inner and outer regions with separate supports. The inner tracker consists of three barrel layers and seven forward discs; the outer tracker of three barrel layers and four forward discs. A radius of 1.5 m together with a 4 T magnetic field were chosen to achieve the required momentum and jet energy resolution at a reasonable field strength and bore radius. The variations of the magnetic field across the tracker volume are below 9%. The overall length of the tracker is 4.4 m.

A lightweight support is needed to meet a total material budget of $\approx 1.5\% X_0$ per layer. To achieve this goal, a carbon fibre support frame is envisaged. A prototype to validate this concept has been built and is under evaluation.

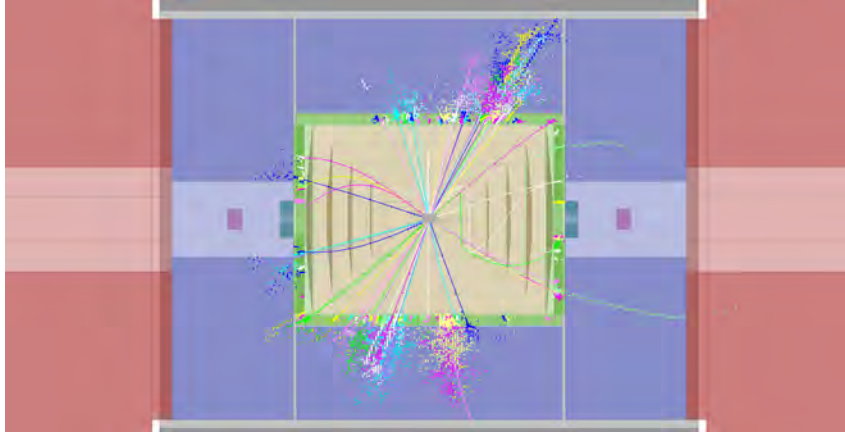


Fig. 4: Event display of a $t\bar{t}H$ decay event at $\sqrt{s} = 1.4$ TeV in the CLIC_SiD detector. The high granularity of the calorimeter enables tracking of the shower development and can be used as input to a particle flow algorithm. Figure taken from Ref. [2].

4.3 Calorimetry

To achieve a jet energy resolution of approximately 3.5%, the CLIC calorimeter is optimised for particle flow calorimetry. The basic principle here is to improve the jet energy resolution by resolving energy depositions of the individual particles in a jet and using the most precise energy measurement available for those particle types. For example, the energy measurement for charged hadrons is typically far more precise in the tracker than in the hadronic calorimeter. The jet energy resolution is then strongly dependent on error contributions coming from wrongly associated depositions [7]. These contributions are represented by a newly introduced confusion term that contributes to the uncertainty of the jet energy resolution. Any detector dedicated to particle flow calorimetry must be carefully optimised to minimise this term. Effectively, this approach changes the problem of summing up energy depositions in the calorimeters into a problem of pattern recognition. Dedicated software to reconstruct the particle flow is necessary for the analysis. For CLIC, Pandora PFA is used [8,9].

4.3.1 Electromagnetic and hadronic calorimeter

To resolve the individual shower components and minimise the confusion term, a high cell granularity and precise time information are required (see Fig. 4). The granularity choices for the CLIC detector are 5×5 mm² in the electromagnetic calorimeter and 30×30 mm² in the hadronic calorimeter. The timing requirements are set to $\sigma_t \approx 1$ ns at the cell level. Current technological choices are silicon pad sensors and tungsten absorbers for the electromagnetic calorimeter and scintillating tiles with silicon photomultiplier readout and steel absorbers for the hadronic calorimeter. Developments in R&D and prototyping in this area are pursued within the CALICE collaboration [10] and have strong synergies with other projects, such as the planned upgrade of the CMS forward calorimeters [11].

4.3.2 Forward calorimeters

The very forward region consists of two additional calorimeters that extend to very low angles. Fig. 5 displays this region. The BeamCal is used for forward tagging of high-energy electrons and can deliver fast luminosity estimation. For precise luminosity measurement, the LumiCal is used. It measures the absolute luminosity via the number of Bhabha scattering events at low angles. To determine the shape of the luminosity spectrum, information on large-angle scattering from the tracker and calorimeter are also used [12]. The LumiCal and BeamCal cover polar angles of 38–110 mrad and 10–40 mrad, respectively. The final focusing magnet QD0 is situated outside the detector. Design efforts for both forward

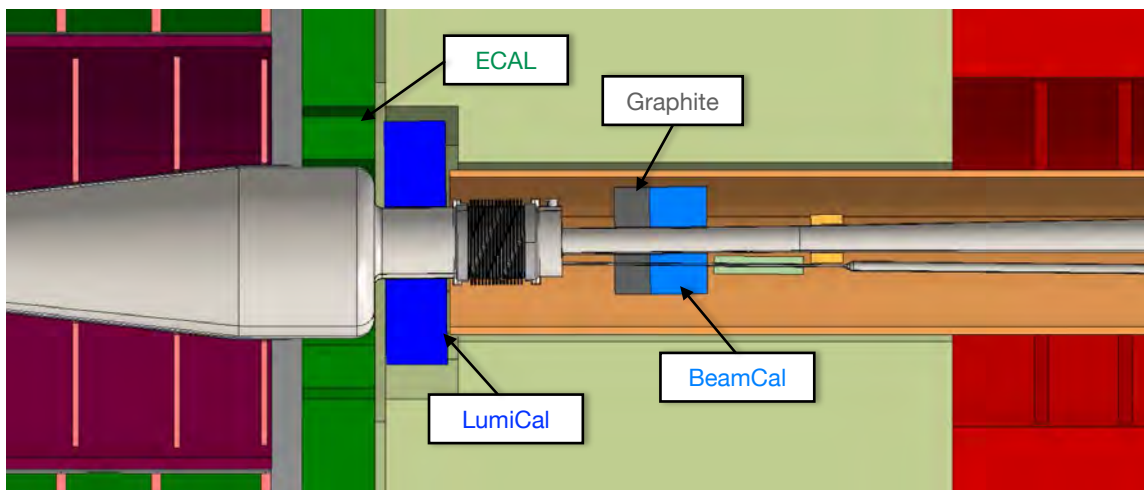


Fig. 5: Forward region of the CLIC detector. The BeamCal is used to tag forward-boosted high-energy electrons; the LumiCal delivers a precise luminosity measurement. A block of graphite is used to reduce the flux of back-scattered particles into the interaction region.

calorimeters are performed within the FCAL collaboration [13].

One issue is the flux of backscattered particles from the forward region into the interaction region. To minimise this flux, a graphite block is situated upstream of the BeamCal. For the BeamCal, radiation-hard sensors are also important, as this device will see radiation doses of several MGy in the innermost regions. Both GaAs and CVD diamond sensors are under consideration [14].

4.4 Muon identification system

The most important task of the muon system is to identify muons with high efficiency and purity. The system is arranged in six layers interleaved in the return yoke. It does not improve the momentum resolution any further but the first layer acts as a tail catcher to improve the jet energy resolution. The time resolution needed is $\sigma_t \approx 1$ ns and cell sizes of 30×30 mm² are used to keep the muon tagging efficiency close to 1 and occupancies at manageable levels. Resistive plate chambers or scintillating tiles with silicon photomultiplier readout are considered to fulfil these requirements.

5 Conclusions

The physics goals and accelerator design set challenging requirements on a future CLIC detector. This includes an excellent jet energy and track momentum resolution, efficient flavour tagging capabilities, large geometrical coverage, and efficient suppression of the beam-induced background. A detector concept to meet these requirements has been presented. It is optimised for particle flow calorimetry and builds on fast timing capabilities and high cell granularities throughout the detector. An extensive R&D programme to show the technical feasibility of the detector design is in progress.

References

- [1] L. Linssen *et al.*, CLIC Conceptual Design Report: Physics and Detectors at CLIC, CERN-2012-003, (CERN, Geneva, 2012). <https://doi.org/10.5170/CERN-2012-003>
- [2] H. Abramowicz *et al.*, Higgs physics at the CLIC electron–positron linear collider, CLICdp-Pub-2016-001, 2016. arXiv:<https://arxiv.org/abs/1608.07538>

- [3] M. Aicheler *et al.*, A multi-TeV linear collider based on CLIC technology: CLIC conceptual design report, CERN-2012-007, (CERN, Geneva, 2012). <https://doi.org/10.5170/CERN-2012-007>
- [4] H. Abramowicz *et al.*, Updated baseline for a staged Compact Linear Collider, CERN-2016-004, (CERN, Geneva, 2016). <https://doi.org/10.5170/CERN-2016-004>
- [5] T. Abe *et al.*, The International Large Detector: letter of intent, DESY-2009-87, (2010). [arXiv:http://arxiv.org/abs/1006.3396](http://arxiv.org/abs/1006.3396)
- [6] H. Aihara *et al.*, SiD letter of intent, SLAC-R-989 (2009). [arXiv:http://arxiv.org/abs/0911.0006](http://arxiv.org/abs/0911.0006)
- [7] J.S. Marshall and M.A. Thomson, Pandora particle flow algorithm, (2013). [arXiv:http://arxiv.org/abs/1308.4537](http://arxiv.org/abs/1308.4537)
- [8] M.A. Thomson, *Nucl. Instrum. Methods Phys. Res. A* **611** (2009) 25. <https://doi.org/10.1016/j.nima.2009.09.009>
- [9] J.S. Marshall *et al.*, *Nucl. Instrum. Methods Phys. Res. A* **700** (2013) 153. <https://doi.org/10.1016/j.nima.2012.10.038>
- [10] F. Sefkow *et al.*, *Rev. Mod. Phys.* **88** (2016) 015003. <https://doi.org/10.1103/RevModPhys.88.015003>
- [11] D. Contardo *et al.*, Technical proposal for the Phase-II upgrade of the compact muon solenoid, CERN-LHCC-2015-010, (CERN, Geneva, 2015). <https://cds.cern.ch/record/2020886>
- [12] S. Poss and A. Sailer, *Eur. Phys. J. C* **74** (2014) 2833. <https://doi.org/10.1140/epjc/s10052-014-2833-3>
- [13] FCAL collaboration webpage, last accessed October 27th 2016 <http://fcal.desy.de>
- [14] H. Abramowicz *et al.*, *J. Instrum.* **10** (2015) P05009. <https://doi.org/10.1088/1748-0221/10/05/P05009>

The Belle II Experiment

J. Kahn (on behalf of the Belle II Collaboration)

Ludwig Maximilians University, Munich, Germany

Abstract

Set to begin data taking at the end of 2018, the Belle II experiment is the next-generation B-factory experiment hosted at KEK in Tsukuba, Japan. The experiment represents the cumulative effort from the collaboration of experimental and detector physics, computing, and software development. Taking everything learned from the previous Belle experiment, which ran from 1998 to 2010, Belle II aims to probe deeper than ever before into the field of heavy quark physics. By achieving an integrated luminosity of 50 ab^{-1} and accumulating 50 times more data than the previous experiment across its lifetime, along with a rewritten analysis framework, the Belle II experiment will push the high precision frontier of high energy physics. This paper will give an overview of the key components and development activities that make the Belle II experiment possible.

Keywords

Belle II; SuperKEKB; B physics.

1 Introduction

The Belle II experiment is a detector based high energy physics experiment designed to make precision measurements of heavy quark and lepton physics processes. The experiment has two key components: the SuperKEKB e^+e^- collider which will produce a large volume of B meson pairs, and the Belle II detector which will record the products of the decays of the B mesons. The Belle II collaboration was formed in 2009 with the aim of taking everything learned from the predecessor Belle experiment and using it to build a high statistics B physics factory detector that would be sensitive enough to probe for New Physics (NP). The goal was for the detector to achieve a performance similar to or better than that of the Belle detector in the harsher beam background environment produced by the upgraded SuperKEKB collider. There was already a decade-long history of success at e^+e^- colliders from not only Belle, but also its companion experiment BaBar. Most notably for Belle was the confirmation of the Kobayashi–Maskawa–mechanism with the charge–parity (CP) asymmetries in the decays of b–quarks which led to the Nobel prize being awarded to Kobayashi and Maskawa in 2008 [1]. Other great achievements in flavour physics including measurements of unitarity triangle angles, time–dependent CP violation (CPV), new resonances [2], etc., are summarised nicely in Ref. [3]. The Belle collaboration is currently sustaining ~ 20 publications a year with further analyses ongoing. The latest hint of new physics to come out of these ongoing analyses is from the measurement of the ratio $R(D^{(*)}) = \frac{B^0 \rightarrow D^{*+} \tau^- \bar{\nu}_\tau}{B^0 \rightarrow D^{*+} \ell^- \bar{\nu}_\ell}$ ($\ell = e, \mu$) using semi–leptonic tagging [4]. When averaged with BaBar and LHCb they show a 4.0σ disagreement with Standard Model (SM) predictions, as seen in Fig. 1 [5].

With the 50 ab^{-1} of data expected to be collected at Belle II the hope is to give insight into some of the big questions that plague the SM. One of these being to look for new sources of CPV, as the SM does not provide enough to explain the matter–antimatter asymmetry we see in the universe today. In addition, NP searches in semi–leptonic and leptonic decays can be performed, along with investigations of other NP areas such as lepton flavour violation, dark sector, etc. More details on NP opportunities at Belle II can be seen in Ref. [6], and the theoretical prospects for B physics are discussed in Ref. [7].

There are several unique experimental advantages to using a B–factory as opposed to measuring B decays from a hadron collider as is done at LHCb. Most prominently the environment is exceptionally

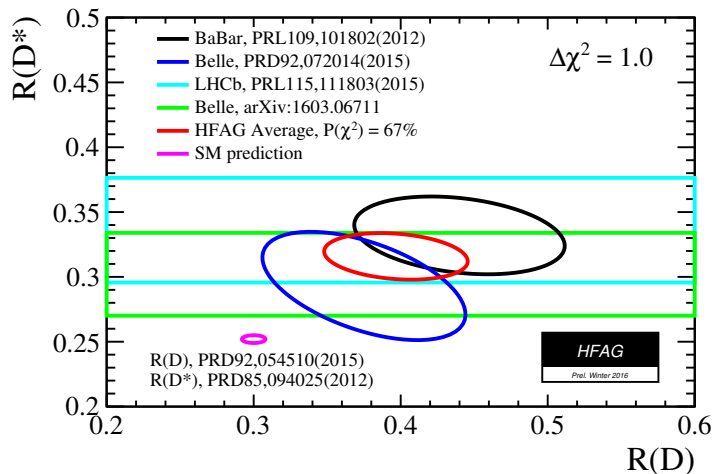


Fig. 1: Measured values and SM prediction of $R(D)$ and $R(D^*)$ [5]

clean: only two B mesons are produced and their initial energy is very well known. This allows us to fully reconstruct everything that happened inside the detector which is exceptionally useful in the case of making time-dependent CPV measurements. The ability to look at higher order decays makes us sensitive to particles with masses above those that can be produced directly at the colliders energy. This opens the door to a whole range of NP particle searches. Additionally, the clean environment allows us to look for invisible final states.

In addition to an upgrade of the hardware, the analysis software framework is also undergoing a major upgrade. The new framework, called the Belle Analysis Framework 2 (basf2), has been rewritten mostly from scratch with an emphasis on efficient use of resources and collaboration wide consistency. Making use of a central repository of common analysis modules, basf2 manages the processing of data and interaction with a central data store. The fact that each physics event is independent also allows for trivial parallelisation, either across a single machine's cores or multiple machines in a batch system.

2 SuperKEKB

The Belle II detector experiment is based at the Japanese High-Energy Accelerator Research Organisation (KEK) in Tsukuba, Japan. It will use SuperKEKB (Fig. 2), the upgraded KEKB electron-positron collider. SuperKEKB is an asymmetric e^+e^- collider with a 7 GeV electron high energy ring (HER) and a 4 GeV positron low energy ring (LER) inside a ~ 3 km circumference tunnel which has been reused from KEKB. The energies are selected such that they are at the $\Upsilon(4S)$ resonance, which is at almost exactly double the B meson rest mass. This results in a very high production rate of B meson pairs which are essentially at rest in the centre-of-mass (CoM) frame. The key changes made from KEKB are the so called Nano-Beam scheme which will squeeze the electron bunches and increase the instantaneous luminosity, and a change in the beam energies from 8 and 3.5 GeV to reduce emittance. The Nano-Beam scheme squeezes the electron bunches by minimizing the longitudinal size of the interaction point (IP) overlap region to effectively limit the minimum value of the beta function via the hourglass effect. The resulting Lorentz boost factor of the CoM system will be $\gamma = 0.28$, two thirds of that in Belle.

SuperKEKB is expected to achieve a peak instantaneous luminosity of $8 \times 10^{35} \text{ cm}^{-2}\text{s}^{-1}$ (Belle achieved: $2.11 \times 10^{34} \text{ cm}^{-2}\text{s}^{-1}$). Over the six year lifetime of the experiment this will result in a total integrated luminosity of 50 ab^{-1} (Belle: 1 ab^{-1}). The projected luminosity profile is shown in Fig. 3, from which we expect roughly $55 \times 10^9 B\bar{B}$ events, $186 \times 10^9 q\bar{q}$ hadronisation events (the main source of background), and $46 \times 10^9 \tau^+\tau^-$ events.

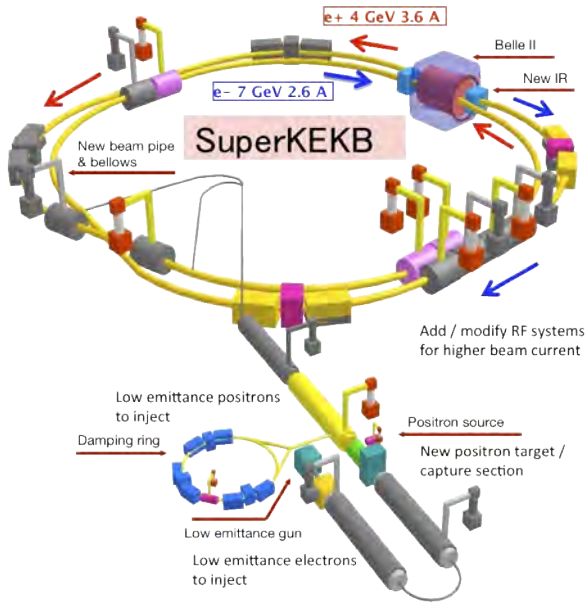


Fig. 2: The SuperKEKB accelerator.

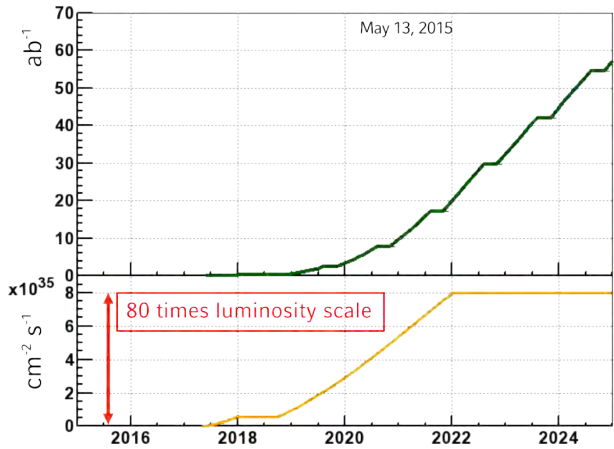


Fig. 3: Instantaneous and integrated luminosity projections for SuperKEKB.

3 The Belle II Detector

The Belle II detector is the centrepiece of the experiment. It is a 7×7.5 m full-solid-angle detector with many sub-detector layers surrounding the interaction point. The detector is based on the design of the predecessor Belle detector with the goal of maintaining the performance of the Belle detector in the presence of considerably higher background levels. A sketch of the Belle II detector is shown in Fig. 4. The detector is comprised of the following sub-detectors which will be described in detail in the next sections: Vertex detector (VXD), Central drift chamber (CDC), Particle identification (PID) detector, Electromagnetic calorimeter (ECL), K-Long and Muon detector (KLM). The key changes from the Belle detector are [3]:

- The beam pipe radius at the interaction point has been reduced from 15 to 10 mm allowing the vertex detector to be closer to the interaction point. This allows for more precise vertex reconstruction but also increases the backgrounds faced by the innermost layers which increases roughly with the inverse square of the radius.
- The inner two layers of the silicon strip detector, immediately outside the beam pipe, will be replaced with a two-layer pixel detector to provide high precision track position measurements. This will provide excellent spatial resolution complementary to the fast timing resolution of the silicon strip detectors, while also being radiation hard enough to handle the high occupancy close to the beam pipe.
- The remaining silicon strip detector will be extended to larger radius. This will allow for a higher quality of track reconstruction and occupies the full volume inside the CDC.
- The CDC will have a larger volume and smaller cell sizes than in Belle, resulting in a much better momentum and dE/dx resolution.
- Particle identification will be performed by entirely new devices using Čerenkov imaging with faster read-outs than in Belle. The upgrade is necessary to cope with a higher background environment and also improves the K/π separation.
- The end-cap scintillator crystals, CsI(Tl), in the ECL will be replaced with faster, more radiation tolerant pure CsI crystals, and new electronics will be used. This allows the ECL to be resistant to the radiation induced degradation and pile-up noise caused by the increased luminosity.

- The end–cap and inner layers of the KLM are to be replaced with scintillators to allow for a shorter dead time and shielding from neutrons and other ambient backgrounds.

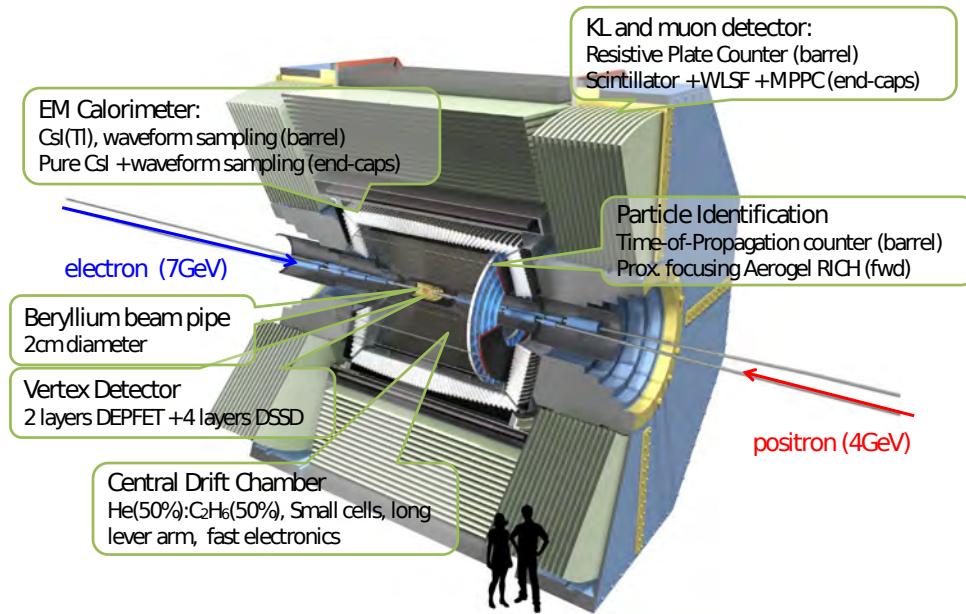


Fig. 4: Cross–section of planned Belle II detector [8]

3.1 Vertex Detector

The vertex detection module is comprised of two sub-detectors: a pixel detector (PXD) and a silicon vertex detector (SVD). The PXD contains two layers of the DEPLETED p–channel Field Effect Transistor (DEPFET). The SVD is made of four layers of Double Sided Strip Detectors (DSSD). The primary purpose of the vertex detection system is to measure the vertices of the two B meson decays for mixing–induced CPV measurements and the vertices of D meson and τ lepton decays. Given the lower CoM boost in SuperKEKB, the two B meson decay vertices will have a smaller separation than in Belle. Despite this, the smaller beam pipe width at the interaction region and the larger radius of the SVD will allow Belle II to have as good as or better vertexing performance than Belle.

3.1.1 Pixel Detector

At the high luminosity expected the detector components closest to the beam pipe will experience incredibly high hit rates coming from beam–related backgrounds (e.g. Touschek effect) and low–momentum–transfer QED processes (e.g. photon–photon interactions). The beam pipe radius at the IP is only 10 mm, and since the background increases roughly with the inverse square of the radius strip detectors can no longer be used for the innermost layer due to the large fraction of channels hit in each triggered event (i.e. larger occupancy). Thus pixel detectors, which have a larger number of channels, will be used for the two innermost layers of the vertex detector. The two layers of the PXD will be at radii 14 mm and 22 mm from the beam line. Pixel detectors have been successfully used in detectors at the LHC [9] [10], however the lower energy of SuperKEKB means that thinner sensors need to be used. The DEPFET technology will allow for sensors as thin as 50 microns which only require air cooling and that are sufficiently radiation hard. A schematic of the DEPFET sensor layout in the PXD can be seen in Fig. 5, note the ladder structure to ensure full coverage of the acceptance region. The pixels, shown in Fig. 6, performs both detection and amplification in one [3] [11]. The inner layer of the pixel detector will contain

8 modules (ladders) with a total of 3.072 M pixels. The outer layer will have 12 modules with a total 4.608 M pixels. Two of the PXD modules have been produced and undergone beam tests along with the SVD. The remaining modules are still in production with ongoing lithography and quality tests.



Fig. 5: Ladder structure of pixel detector modules.

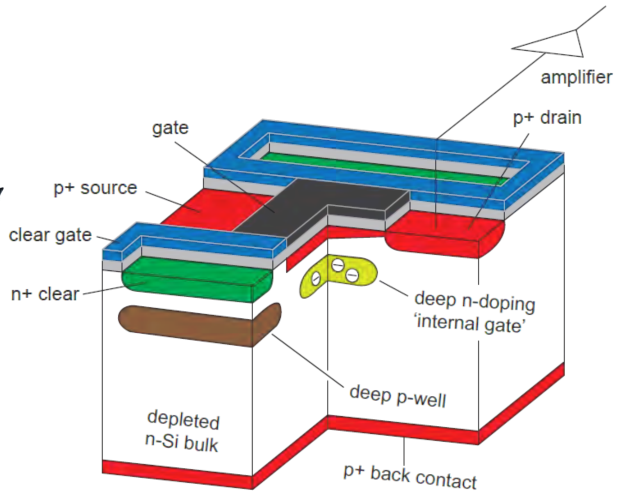


Fig. 6: Single DEPFET pixel components.

3.1.2 Silicon Vertex Detector

The SVD comprises the outer four layers of the vertex detection sub-detector at radii 38, 80, 115, 140 mm [12]. Comparing this with Belle, which had its outermost SVD layer at a radius of only 88 mm, the reconstruction efficiency of low-momentum particles and long-lived particles is expected to improve significantly. The SVD in Belle II will cover the full detector acceptance range of $17^\circ < \theta < 150^\circ$. The hit occupancy will be required to be less than 10% to ensure that hits in the SVD are correctly associated with tracks in the CDC. The higher beam current and luminosity will increase the required trigger rate to 30 kHz, compared to the $\sim 1\text{kHz}$ trigger rate required in Belle.

Three sizes of double-sided silicon microstrip detectors (DSSDs) are used for the outer, inner, and forward sections. Each DSSD will be 123 mm long, and 300 or 320 μm thick. The DSSDs on the innermost SVD layer (layer 3 of the VXD) will have a width of 38 mm while the remaining layers will have DSSDs which are 58 mm wide. The DSSDs provide excellent timing resolution ($\sim 2\text{-}3\text{ ns}$) which will complement the excellent spatial resolution of the PXD. The SVD ladders are still in construction; however, recently a test setup of the SVD and PXD (VXD mock-up) underwent beam tests at The Deutsches Elektronen-Synchrotron (DESY) in Hamburg, Germany, to measure the spatial resolution and hit efficiency.

3.2 Central Drift Chamber

The CDC is the main tracker for charged particles in Belle II. It contains 14,336 sense wires and 42,240 field wires, while a superconducting solenoid coil surrounding the ECL supplies a 1.5 T magnetic field. The CDC has three key roles in Belle II: to reconstruct charged tracks with high momentum precision, to provide particle identification information using measurements of energy loss (e.g. for identifying low momentum tracks which do not reach the PID detector), and to provide efficient and reliable trigger signals for charged particles. Given the success of the CDC design in Belle the same design structure will be used in Belle II. A comparison of the major parameters in Belle and Belle II can be seen in Table 1.

The key changes to the CDC design are:

- New readout electronics will be used to handle the higher trigger rates with less deadtime.
- The CDC inner radius and outer radii will be changed to avoid high backgrounds near the IP and to make room for the new, larger VXD.
- The CDC will generate 3D trigger information using a trigger in the z-direction.

The CDC has recently undergone cosmic ray testing in partnership with the barrel PID sub-detector and is now being calibrated and moved into its final position.

Table 1: Comparison of main CDC parameters in Belle and Belle II.

	Belle	Belle II
Radius of inner cylinder (mm)	77	160
Radius of outer cylinder (mm)	880	1130
Radius of innermost sense wire (mm)	88	168
Radius of outermost sense wire (mm)	863	1111.4
Number of layers	50	56
Number of sense wires	8,400	14,336
Gas	$He - C_2H_6$	$He - C_2H_6$
Diameter of sense wire (μm)	30	30

3.3 Particle Identification

The PID sub-detector is completely new in Belle II and contains two components: a Time Of Propagation (TOP) detector and an Aerogel Ring Imaging Čerenkov (ARICH) detector. The TOP detector is used for particle identification in the barrel region of Belle II, while the ARICH detector performs particle identification in the forward end-cap region.

3.3.1 Time of Propagation Detector

The goal of the TOP detector is to improve K/π separation while coping with the increased backgrounds expected from SuperKEKB. Overall the TOP contains sixteen modules, each module comprised of: two 2.7 m long quartz bars, a spherical mirror on one end of the bars, and an expansion prism with an array of photo-detectors attached on the other. The setup of a single TOP module can be seen in Fig. 7. It will use micro-channel-plate photomultiplier tubes (MCP-PMTs) and waveform sampling electronics for high precision position and timing measurements. The Čerenkov ring is reconstructed in three-dimensions from the measured time and the $x - y$ position of the Čerenkov photon hits on the MCP-PMTs. TOP modules have been tested at SPring-8 at LEP in 2013 during beam tests and met the required timing resolution of $\sim O(100 \text{ ps})$. The modules have been installed in Belle II and are undergoing background tests and timing calibration.

3.3.2 Aerogel Ring Imaging Čerenkov Detector

The ARICH detector will be used for particle identification in the forward end-cap. Each detector module contains two adjacent layers of aerogel ($20 + 20$ mm thick) separated by an expansion volume (200 mm) from an array of 420 Hybrid Avalanche Photo Detectors (HAPD). The two layers of aerogel have differing refractive indices to provide overlapping of the Čerenkov rings for a better photon yield. The focusing of the ARICH has been optimized to separate kaon Čerenkov photons from pion Čerenkov photons across most of their momentum range, while also discriminating between pions, muons, and

electrons in the momentum range below 1 GeV/c. An example of how kaons and pions can be discriminated between is shown in Fig. 8. The aerogel crystal installation will be completed in September 2016, with full system testing scheduled for January 2017.

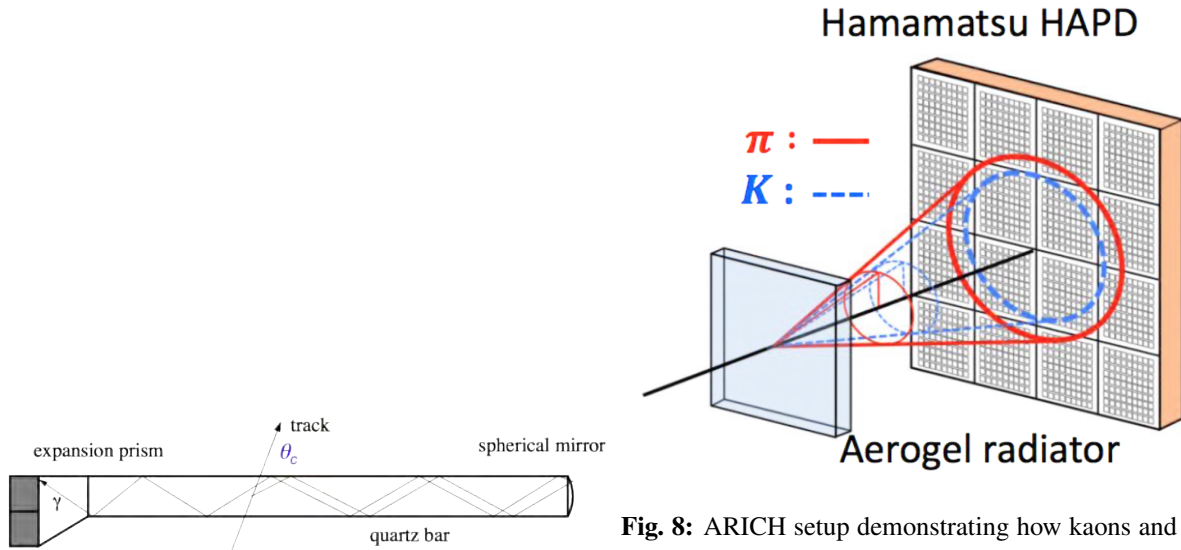


Fig. 7: Single TOP detector module components [13].

Fig. 8: ARICH setup demonstrating how kaons and pions with the same momentum can be discriminated between [13].

3.4 Electromagnetic Calorimeter

Following the success of the ECL in Belle, the Belle II ECL will follow the same design with upgrades to handle the higher backgrounds expected. The CsI(Tl) barrel crystals from Belle will be reused while in the end-cap they will be replaced with pure CsI crystals [14]. New electronics will also be used with bias filtering and waveform sampling for faster readouts. The coverage of the ECL will be $12.4^\circ < \theta < 155.1^\circ$, excluding two $\sim 1^\circ$ gaps where the barrel and end-caps join. The key roles of the ECL will be to: detect photons with precision measurements, identify electrons, take on-line and off-line luminosity measurements, and help detect K_L^0 together with the KLM. Performance studies are currently being carried out on the new crystals, whilst the electronics have been installed and tested.

3.5 K_L and μ Detector

The KLM in Belle II will be made of alternating layers of 470 mm thick iron plates and detector components. The resistive plate chambers (RPCs) that were used throughout the entire Belle KLM to detect charged particles will not be efficient enough to handle the ambient hit rate expected in the Belle II end-caps and barrel inner-layers. Instead scintillators will be used in the entire end-cap and first two layers of the barrel section, with RPCs used for the remaining barrel layers. In the barrel there are 15 detector components and 14 iron plates. In the forward (backward) end-cap there are 14 (12) detector layers and 14 (12) iron plates. The iron plates also serve as a magnetic return flux for the solenoid and provide interaction material in which K_L^0 mesons can shower hadronically. The total coverage of the KLM (barrel + end-caps) will be $20^\circ < \theta < 155^\circ$. The barrel KLM was the first sub-detector to be installed in Belle II in 2013. The end-caps were installed in 2014. The end-cap hardware is finished and undergoing software geometry and alignment calibration, while the final barrel components are being installed and tested. Cosmic ray testing for the entire KLM is ongoing.

4 Milestones

Currently the Belle II collaboration has ~ 650 members from 99 institutes in 22 countries, and is on track to begin data taking by the end of 2018. The first electrons circulated SuperKEKB at the beginning of 2016 as part of the first of three major phases in the Belle II experiment schedule. Phase 1, which ran from February until June this year, involved the beam commissioning with the dedicated detector BEAST II used to take beam background measurements. Phase 2 is currently scheduled to begin in December 2017 when SuperKEKB will begin to tune the collisions. At this point the Belle II detector, without the VXD, will be in place taking measurements. The start of the full physics run, the so-called phase 3, is set to begin in November 2018, at which point the completed Belle II detector will be installed and fully operational.

5 Summary

Having proved themselves as invaluable tools in the precision flavour frontier, B-factories offer a unique angle from which to probe the Standard Model and beyond. The Belle II experiment will play an important role in new physics searches as a complement to searches at other experiments. The upgraded luminosity of SuperKEKB will provide the high statistics needed for precision measurements, while improvements in all sub-detectors from its predecessor Belle will allow the Belle II detector to record clean data in the presence of the expected high backgrounds. The construction and testing of hardware and software components are progressing well, with the Belle II experiment set to begin taking data in 2018, with the aim of collecting a total of 50 ab^{-1} by the end of 2024.

References

- [1] M. Kobayashi and T. Maskawa, CP Violation in the Renormalizable Theory of Weak Interaction, *Prog. Theor. Phys.* **49** (1973) 652. <https://doi.org/10.1143/PTP.49.652>
- [2] S. K. Choi *et al.* [Belle Collaboration], Observation of a resonance-like structure in the π^+ - ψ' prime mass distribution in exclusive $B \rightarrow K \pi^+$ - ψ' prime decays, *Phys. Rev. Lett.* **100** (2008) 142001. <https://doi.org/10.1103/PhysRevLett.100.142001>
- [3] T. Abe *et al.* [Belle-II Collaboration], Belle II Technical Design Report. [arXiv:1011.0352 [physics.ins-det]].
- [4] A. Abdesselam *et al.* [Belle Collaboration], Measurement of the branching ratio of $\bar{B}^0 \rightarrow D^{*+} \tau^- \bar{\nu}_\tau$ relative to $\bar{B}^0 \rightarrow D^{*+} \ell^- \bar{\nu}_\ell$ decays with a semileptonic tagging method. [arXiv:1603.06711 [hep-ex]].
- [5] Heavy Flavor Averaging Group (HFAG) Winter 2016, http://www.slac.stanford.edu/xorg/hfag/semi/winter16/winter16_dtaunu.html.
- [6] P. Urquijo, Physics prospects at the Belle II experiment, *Nucl. Part. Phys. Proc.* **263-264** (2015) 15. <https://doi.org/10.1016/j.nuclphysbps.2015.04.004>
- [7] R. Fleischer, Theoretical prospects for B physics, PoS FPCP **2015** (2015) 002. [arXiv:1509.00601 [hep-ph]].
- [8] Belle II website, <https://www.belle2.org>.
- [9] J. Karancsi [CMS Collaboration], Operational Experience with the CMS Pixel Detector, *JINST* **10** (2015) C05016. <https://doi.org/10.1088/1748-0221/10/05/C05016>. [arXiv:1411.4185 [physics.ins-det]].
- [10] Y. Takubo [ATLAS Collaboration], The Pixel Detector of the ATLAS experiment for the Run2 at the Large Hadron Collider, *JINST* **10** (2015) C02001. <https://doi.org/10.1088/1748-0221/10/02/C02001>, [10.1088/1748-0221/10/12/C12001](https://doi.org/10.1088/1748-0221/10/12/C12001). [arXiv:1411.5338 [physics.ins-det]].
- [11] J. Schieck [DEPFET Collaboration], DEPFET pixels as a vertex detector for the Belle II experiment, *Nucl. Instrum. Meth. A* **732** (2013) 160. <https://doi.org/10.1016/j.nima.2013.05.054>

- [12] G. B. Mohanty, Belle II Silicon Vertex Detector, *Nucl. Instrum. Meth. A* **831** (2016) 80. <http://doi.org/10.1016/j.nima.2016.04.013>. [arXiv:1511.06197 [physics.ins-det]].
- [13] B. Wang [Belle-II Collaboration], The Belle II Experiment and SuperKEKB Upgrade, [arXiv:1511.09434 [physics.ins-det]].
- [14] B. Shwarz [BELLE II calorimeter group Collaboration], Electromagnetic Calorimeter of the Belle II detector, PoS PhotoDet **2015** (2016) 051.

Radiation Hardness Study of CsI(Tl) Crystals for the Belle II Calorimeter

D.V. Matvienko, E.V. Sedov, B.A. Shwartz and A.S. Kuzmin

Budker Institute of Nuclear Physics, SB RAS
and Novosibirsk State University, Novosibirsk, Russia

Abstract

The Belle II calorimeter consists of CsI(Tl) scintillation crystals which have been used at the Belle experiment. A radiation hardness study of typical Belle crystals is performed and it is found that light output reductions are acceptable for the Belle II experiment where the absorption dose can reach 10 krad during the detector operation. CsI(Tl) crystals have high stability and low maintenance cost and are considered a possible option for the calorimeter of the future Super-Charm-Tau Factory (SCT) in Novosibirsk. The study also demonstrates sufficiently high radiation hardness of CsI(Tl) crystals for SCT conditions.

Keywords

Belle II calorimeter; CsI(Tl) crystals; radiation hardness; light output.

1 Introduction

The Belle detector [1] operated at the KEKB factory [2] from 1999 until 2010 was a universal magnetic detector including several sub-detectors and had excellent performance. The electromagnetic calorimeter (ECL) of the Belle detector contained 8736 CsI(Tl) scintillation crystals. Each crystal has a truncated pyramid shape of an average size about $6 \times 6 \text{ cm}^2$ in cross section and 30 cm ($16.1X_0$) in length. The Belle calorimeter based on these crystals demonstrated high quality and performance. Additionally, it had multiple functions.

- The ECL allowed to detect photons in a wide range of energies (from a few MeV to a few GeV) with excellent resolution. The energy resolution achieved at 1 GeV was 1.8% and about 4% at 100 MeV.
- The ECL provided the determination of photon space coordinates. The space resolution was about $5 \text{ mm}/\sqrt{E(\text{GeV})}$.
- The Belle calorimeter also served for the separation of electrons and hadrons.
- Information from the ECL was used for the formation of a neutral trigger signal.
- The ECL provided the luminosity measurement independent from the data acquisition system.

The absorbed dose collected by the crystals during the operation of the Belle experiment is shown in Fig. 1 (see Ref. [3]). The measured integrated dose for the luminosity of 1000 fb^{-1} is about 100 rad for the barrel crystals and 400 rad for the highest-dose endcap crystals. The light output degradation corresponding to the integrated absorbed dose and shown in Fig. 2 is about 7% in the barrel and up to 13% in the endcap parts of the ECL. The results shown in Figs. 1, 2 are in good agreement with previous measurements of the radiation hardness for a large set (55 samples) of the Belle typical crystals [4]. This study has been performed for a distributed absorbed dose up to 3700 rad. However the expected dose for the Belle II endcap crystals is up to 10 krad after 10 years of the Belle II experiment operation. It has been decided to keep all the CsI(Tl) crystals in the Belle II calorimeter, at least at the first stage of the experiment [3]. Thus, the Belle II conditions require an additional measurement of the radiation hardness for the CsI(Tl) crystals. This problem is discussed in Ref. [5]. For our study four crystals produced for the Belle calorimeter but rejected due to their geometry specifications or small mechanical defects have been

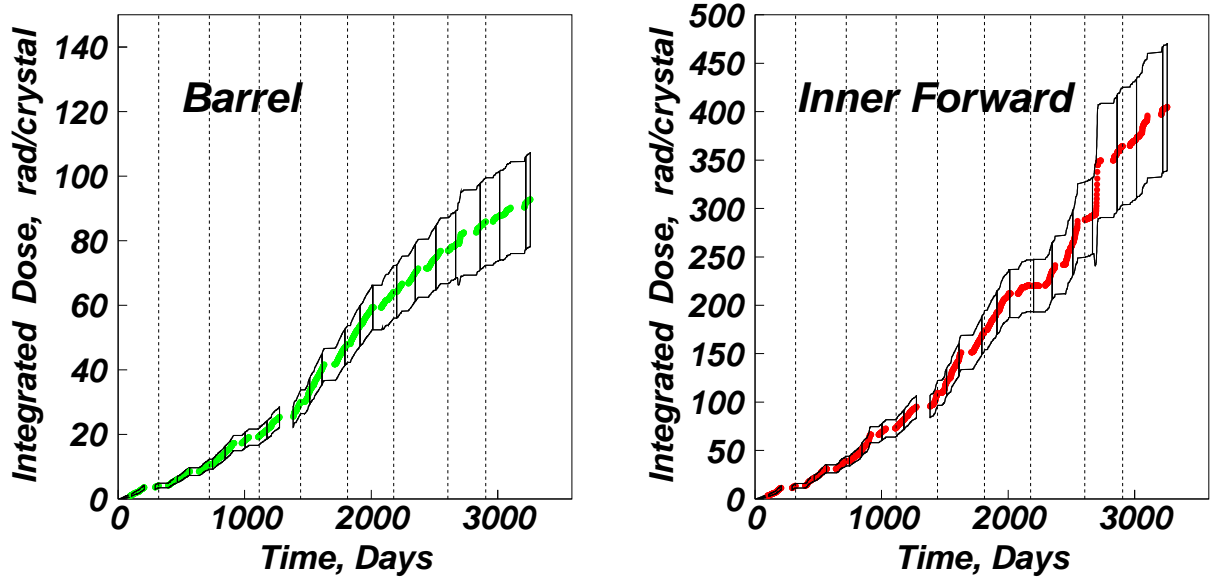


Fig. 1: Integrated absorbed dose collected by the Belle calorimeter based on CsI(Tl) crystals

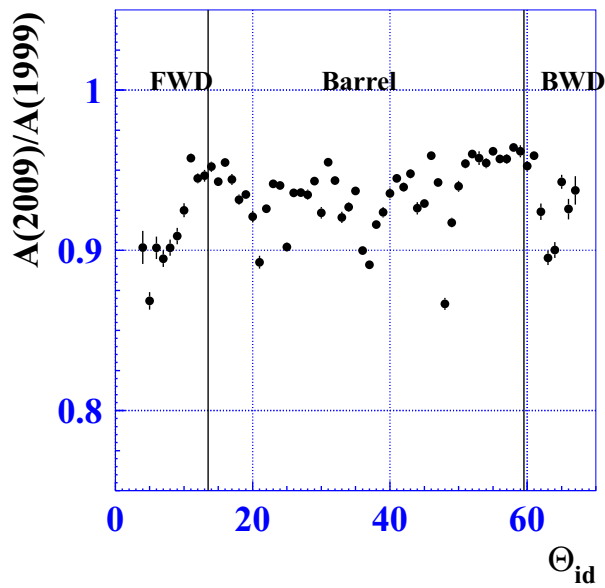


Fig. 2: Light output loss after 10 years of the Belle experiment

selected. Their scintillation properties met Belle requirements. These crystals have shapes of truncated pyramids with slightly different sizes and have been used in a previous study [4] which was held in 2003. Thus, their characteristics are known from this previous radiation hardness study. The measured light output degradation for the studied crystals is shown in Fig. 3. Prior to previous measurements all these crystals were polished, wrapped in 200 μm porous teflon and covered with a 20 μm thick aluminized mylar film. These wrappers are kept in the study.

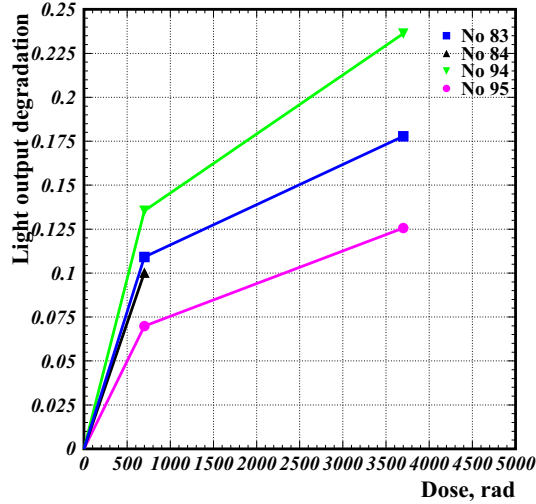


Fig. 3: Light output degradation for the selected crystals 83, 84, 94 and 95 measured in Ref. [4]

2 Crystal irradiation

The studied samples are irradiated with the industrial electron accelerator ELV-6 [6] at Budker Institute of Nuclear Physics in Novosibirsk. The ELV-6 accelerator provides a continuous electron beam with the energy of 1.4 MeV and a beam current up to 100 mA. The specific features of the ELV-type accelerators are the simplicity of design, convenience and ease in control and also reliability in operation. The scheme of the irradiation setup is shown in Fig. 4. The electron beam hits the converter in which bremsstrahlung

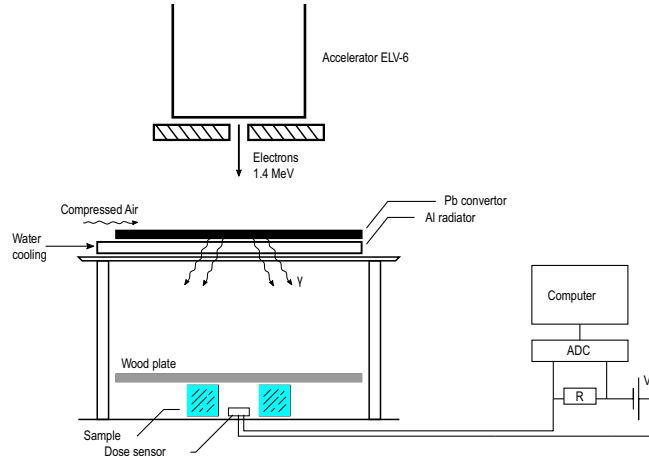


Fig. 4: The setup for irradiation of the crystals with the ELV-6 accelerator

photons are created due to the electron scattering in the converter material. Two different types of converters are used: lead and tantalum. The lead converter containing a 3 mm lead plate and cooled by a water radiator and air flux is used with absorbed doses less than 7 krad. For higher doses the power absorbed in the converter can melt the lead plate. In this case the tantalum converter is used consisting of 0.5 mm of Ta, 2 mm of water and 2 mm of stainless steel. The photons from these converters have a wide energy spectrum with an average value around 0.6 MeV and uniformly irradiate the crystals over an area which is the horizontal surface at about 1m distance below the converter. The wood plate over the crystals is used to suppress the electrons scattered in air.

The average bremsstrahlung photon interaction length in CsI material is about 3 cm. Since the transverse size of the irradiated crystals is about 6 cm, the absorbed dose in the upper side of the crystal is a few times higher than at the bottom one. To compensate this nonuniformity, each sample is irradiated with equal doses from opposite sides.

To control the dose absorbed in the crystals during the irradiation two special designed dose sensors are placed together with the crystals. The dose sensor shown in Fig. 5 consists of a CsI(Tl) crystal with the dimensions $1 \times 2 \times 2 \text{ cm}^3$ coupled with an optical contact with silicon-based photodiode (PIN diode) Hamamatsu S2744-08 which has an active area of $1 \times 2 \text{ cm}^2$. One more photodiode identical with

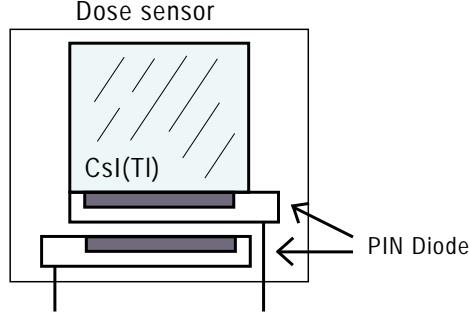


Fig. 5: The dose sensor for the dose rate measurement during the irradiation

the previous one is placed without light connection with the crystal. The second photodiode is needed to control the dark current during irradiation. Currents from two photodiodes are recorded each 100 ms using control resistances and an ADC L-CARD E14-440 connected to a PC. The difference between these currents is taken as the signal current I .

The dose rate $dD/dt = kI$ absorbed in the sensor is proportional to the current I and can be calculated from the average energy deposition per photon \bar{E} , the counting rate ν and the crystal mass M :

$$\frac{dD}{dt} = \frac{\bar{E}\nu}{M}. \quad (1)$$

Thus, to calibrate the dose sensor, the coefficient $k = \bar{E}\nu/M/I$ has to be determined.

3 Dose sensor calibration

To determine k , two radioactive ^{137}Cs sources with intensities $\mathcal{J} \sim 10^5 \text{ Bq}$ and $\mathcal{J} \sim 10^8 \text{ Bq}$ are used. Two sources are necessary because the current I cannot be measured with a lower intensity source and the source with higher intensity leads to a significant pile-up effect. Thus, \bar{E} is determined from the spectrum of the lower intensity source shown in Fig. 6. The measured energy threshold is about 100 keV. To take into account the spectrum region below this threshold, a constant approximation is used. Another problem is measuring the counting rate $\nu_{\text{high}}(0)$ for the higher intensity source with null distance from the dose sensor surface. The counting rate $\nu_{\text{low}}(0)$ for the source with $\mathcal{J} \sim 10^5$ is well measured. To calculate $\nu_{\text{high}}(0)$, the relation

$$\nu_{\text{high}}(0) = \frac{\nu_{\text{high}}(r)}{\nu_{\text{low}}(r)} \nu_{\text{low}}(0) \quad (2)$$

is used, where the counting rates $\nu_{\text{high}}(r)$ and $\nu_{\text{low}}(r)$ are measured for a finite distance r perpendicular to the sensor surface when the pile-up effect is not significant. The ratio $\nu_{\text{high}}(r)/\nu_{\text{low}}(r)$ is permanent with good accuracy for control distances r .

The coefficient k measured by this method has an uncertainty of about 15%. The main effect is due to the current measurement I .

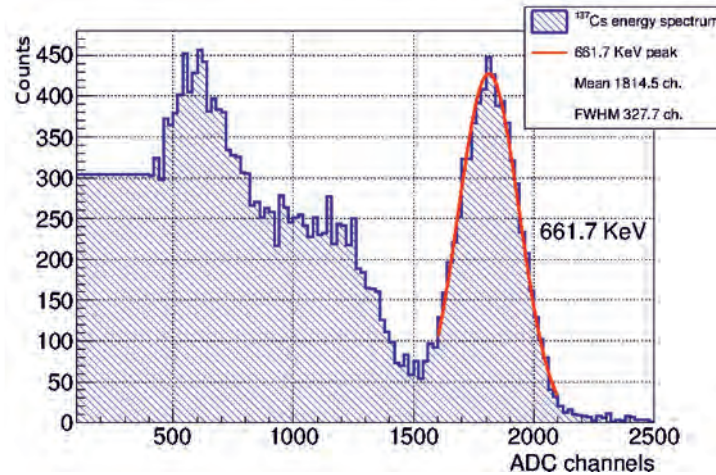


Fig. 6: The spectrum from the ^{137}Cs radioactive source with constant approximation to the region below the threshold.

4 Light output measurements

To measure the scintillation properties of the crystals the testbench shown in Fig. 7 is used. The crystal under study is placed on the input window of the photomultiplier (PMT) Hamamatsu R1847S without optical contact. The PMT R1847S has a bialkali photocathode and a ten dynode system of electron multipliers with a typical gain of the order of 10^7 . The radioactive source of ^{137}Cs placed in the lead

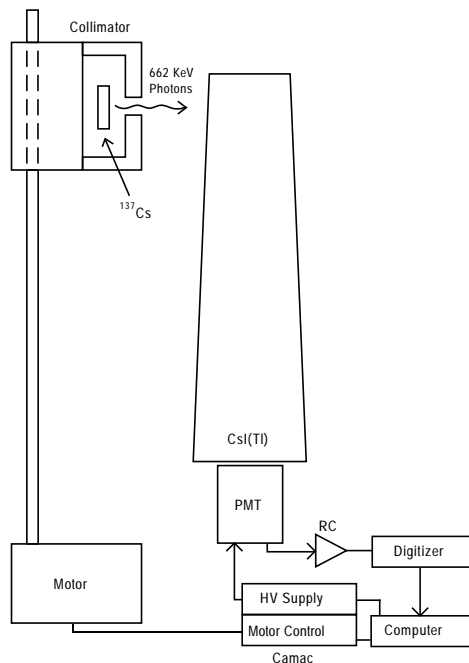


Fig. 7: Testbench for light output measurement

collimator, which can move along the crystal axis and irradiates the crystal with 662 keV photons. The measurements are carried out in nine positions with a step size of 30 mm. The PMT signal after shaping (based on an RC-circuit with the time constant $\tau = 75$ ns) is digitized continuously at a frequency of

250 MHz by a 12 bit multifunctional desktop waveform digitizer CAEN DT5720A [7]. The digitizer houses USB 2.0 which allows data transfers up to 30 MB/s. The digital pulse processing firmware [8] provided with this device allows to record the input signal, integrate the pulse waveform samples within a programmable acquisition gate and save the pulse integral spectrum to a text file. For each spectrum, corresponding to the collimator position, the total absorption position A_i ($i = 1, \dots, 9$) is determined. The light output of the studied sample is defined relative to the light output for the reference crystal as

$$L_i = \frac{A_i}{A_0}, \quad (3)$$

where A_0 is the photoelectric peak position for the reference crystal, which is a standard CsI(Tl) crystal of 15 mm height and 15 mm diameter packed in the aluminium container.

The average light output is defined as:

$$\bar{L} = \frac{L_1 + \dots + L_9}{9} \quad (4)$$

and the light output non-uniformity along the crystal axis is defined as

$$\frac{\Delta L}{\bar{L}} = \frac{L_{\max} - L_{\min}}{\bar{L}}, \quad (5)$$

where L_{\max} and L_{\min} are the maximum and minimum values of the light output.

5 Results

Four expositions for selected crystals are performed with the total dose of 30 krad and their light outputs are measured using the above described testbench. Results for the average light output \bar{L} are shown in Fig. 8 (a) for the crystals 83, 84 and in Fig.8 (b) for the crystals 94, 95.

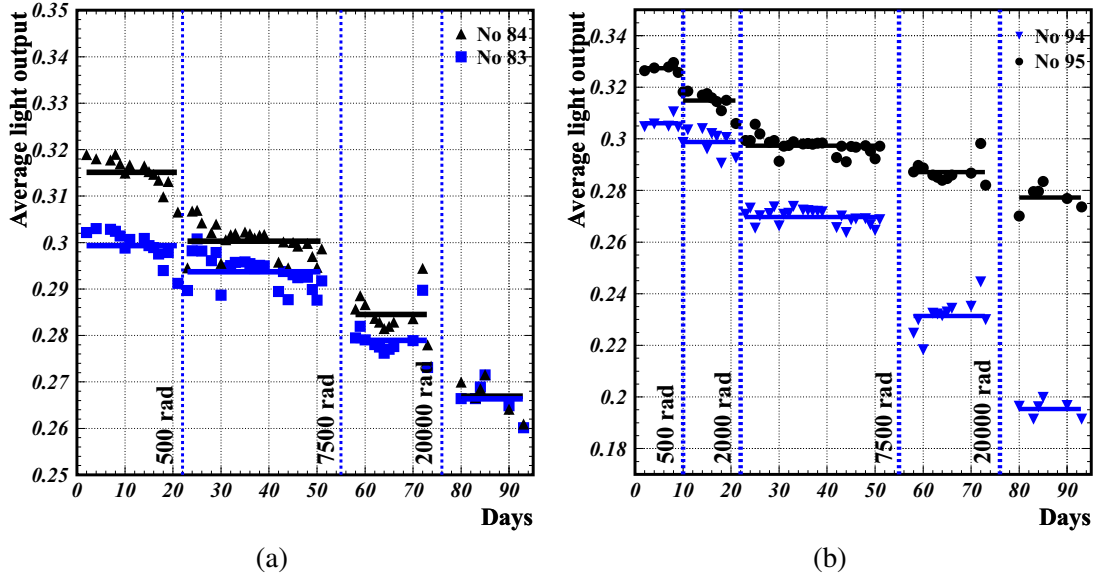


Fig. 8: Time dependencies of average light output for crystals (a) 83, 84 and (b) 94, 95. Vertical lines show the dose absorbed in the crystals during one exposition.

Different degradations of the average light output are observed. The light output loss for the crystal 94 is not essential after a dose of 500 rad but significantly increases with higher doses (drop of 25% after a dose of 10 krad and 37% after 30 krad). Another effect is observed for the crystals 83, 84 and 95: the light output deterioration is 7 to 10% after a dose of 10 krad and 16 to 18% after 30 krad.

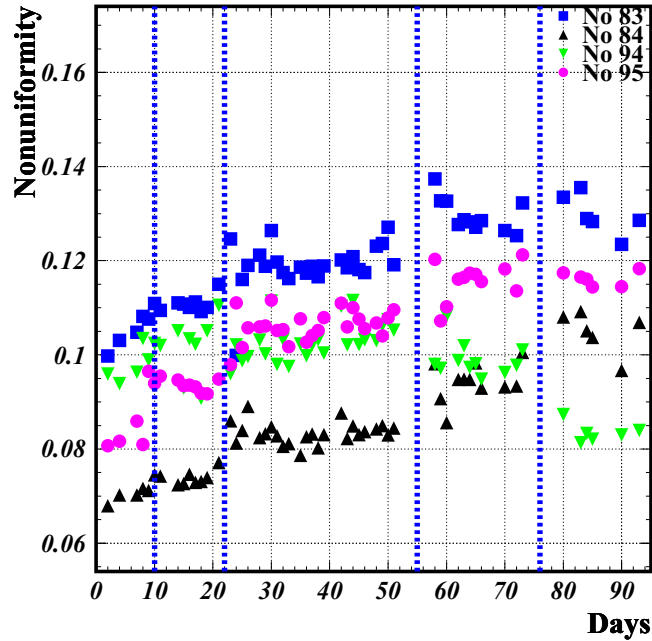


Fig. 9: Time dependence of non-uniformity for the crystals 83, 84, 94 and 95. Vertical lines demonstrate exposition moment.

The measured light-output non-uniformity is shown in Fig. 9. A deterioration of the light output non-uniformity is observed except for the crystal 94, where the opposite tendency takes place after the fourth exposition. The non-uniformity after all expositions is less than 14% for all samples. There are no any stringent requirements on the CsI(Tl) non-uniformity measurements for the Belle II calorimeter because all the crystals used at Belle are kept to be used at Belle II. The non-uniformity for the Belle experiment was required to be less than 9% for all crystals and less than 7% for 90% of total crystals.

It is interesting to combine the results for selected samples with the previous study (see Fig. 3). Since the absolute light output is not measured, the results are normalised to the previous measurements for the crystal 95. This is under the assumption, that the natural recovery of the light output for the crystal 95 is absent and its light output is stable during the period between the studies. The average light output in dependence of the absorbed dose for studied crystals is shown in Fig. 10. The dashed lines in Fig. 10 represent the previous study and the solid lines show the new results. The last values of the previous study are close to the first points of the new study. Thus, the assumption is valid. Fig. 10 also demonstrates that the light output drops slower after increasing the dose for all samples. Another feature is that the behavior of the curves for the average light output loss obtained from the previous measurements is similar for each studied crystal. For example, the crystal 94 has maximum light output loss in both studies.

The degradation of the light output versus the absorbed dose is shown in Fig. 11. As before, the dashed lines correspond to the previous study [4] and solid lines demonstrate the new measurements. The light output loss is described by similar curves for the crystals 83, 84 and 95. The light output degradation after a total dose of about 35 krad is 30% for the crystals 83, 84, 95 and 50% for the crystal 94. The light output drops significantly after all expositions.

According to the latest simulation of a beam-induced background at SuperKEKB, the radiation dose rate for the most radiation loaded parts of the calorimeter can exceed 600 rad/year. Our estimation of the light output degradation at expected doses is demonstrated in Fig. 11. This degradation results in the deterioration of the energy resolution mostly due to the increasing of energy equivalent of the

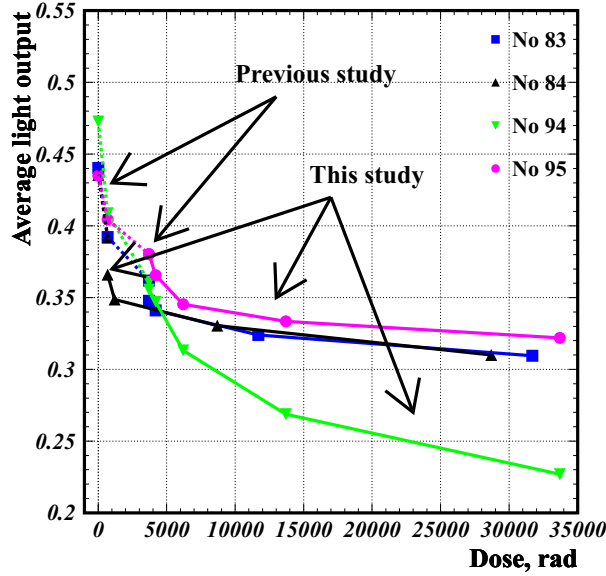


Fig. 10: Average light output in dependence of the total absorbed dose for the crystals 83, 84, 94 and 95 obtained in previous study [4] (dashed lines) and in this study (solid lines).

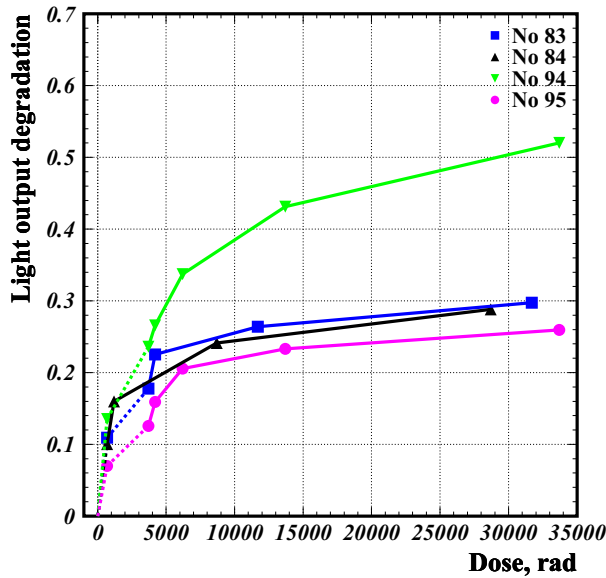


Fig. 11: The distribution of the light output degradation over the total absorbed dose for the crystals 83, 84, 94 and 95 obtained in previous study [4] (dashed lines) and in this study (solid lines).

electronic noise (especially for low energies). The average output signal of the Belle crystals is about 5000 photoelectrons per 1 MeV while the electronic noise level is about 300 keV. The light output loss for the worst tested sample 94 is 40% at the total Belle II expected dose of 10 krad. In such a case, the noise level increases proportionally up to 500 keV. However, the pile up noise with the level of about 2 – 5 MeV caused by the soft background photons substantially exceeds the electronic noise (< 1 MeV) even for the crystals with relatively low radiation hardness like the crystal 94 [9]. Therefore, the radiation damage of the CsI(Tl) crystals is not the serious problem for the Belle II calorimeter.

6 CsI(Tl) crystals for the calorimeter of the Super Charm-Tau Factory

The future detector of the Super Charm-Tau (SCT) Factory in Novosibirsk should include an electromagnetic calorimeter. Since most of the photons produced in the conditions of this experiment have energies of the order of 100 MeV, the calorimeter needs good resolution for these energies. The Belle calorimeter based on the CsI(Tl) scintillation crystals had excellent performance for the photons in the range of energies. Thus, CsI(Tl) crystals could be considered as possible option for a future SCT calorimeter. These crystals have high light output (5×10^4 photons per MeV) and an emission spectrum with a maximum of about 550 nm matching with the high sensitivity region of the silicon photodiodes. Since the designed SCT luminosity is expected to be $1 \times 10^{35} \text{ cm}^{-2}\text{s}^{-1}$, the integrated absorbed dose can reach 1 krad after 5 years of detector operation. This study together with the studies in Refs. [4, 5] demonstrates sufficient radiation hardness of CsI(Tl) crystals for the conditions of e^+e^- colliders including the SCT factory. One more advantage of CsI(Tl) crystals is their low maintenance cost. They are approximately two times cheaper than pure CsI crystals. It is also worth noting that the scientific group from Budker Institute of Nuclear Physics in Novosibirsk has considerable experience of working with alkali-halide crystals such as CsI(Tl).

7 Conclusion

A radiation hardness study of CsI(Tl) crystals produced for the Belle calorimeter has been performed to investigate their scintillation characteristics in conditions of the Belle II experiment. Selected crystals have been exposed in an earlier study with a total dose of about 3.5 krad. In this study four expositions with the integrated dose of 30 krad have been investigated. The results are consistent with the previous measurements. The light output falls faster for doses less than 1 krad and it has more slower degradation for higher doses. The total degradation is about 30% for the three studied samples and 50% for the worst crystal. The relative behavior of the light output loss obtained in the previous measurements for the studied samples remains the same in the study. Measured light output non-uniformity is less than 14% after a dose of about 35 krad.

In summary, the scintillation properties of the Belle CsI(Tl) crystals are acceptable for the Belle II experiment as well as for a SCT factory conditions.

Acknowledgements

This work has been supported by Russian Science Foundation (project N 14-50-00080).

References

- [1] A. Abashian *et al.* (Belle Collaboration), *Nucl. Instrum. Methods Phys. Res. A* **479** (2002) 117.
[https://doi.org/10.1016/S0168-9002\(01\)02013-7](https://doi.org/10.1016/S0168-9002(01)02013-7)
- [2] S. Kurokawa and E. Kikutani, *Nucl. Instrum. Methods Phys. Res. A* **499** (2003) 1.
[https://doi.org/10.1016/S0168-9002\(02\)01771-0](https://doi.org/10.1016/S0168-9002(02)01771-0)
- [3] T. Abe *et al.*, Belle II technical design report, arXiv:1011.0352.
- [4] D.M. Beylin *et al.*, *Nucl. Instrum. Methods Phys. Res. A*, **541** (2005) 501.
<https://doi.org/10.1016/j.nima.2004.11.023>
- [5] S. Longo and J.M. Roney, *J. Instrum.* **11** (2016) P08017.
<https://doi.org/10.1088/1748-0221/11/08/P08017>
- [6] S.N. Fadeev *et al.*, *Radiat. Phys. Chem.* **57** (2000) 653.
- [7] E-publishing service, DT5720 user manual,
www.caen.it/servlet/checkCaenManualFile?Id=10257.
- [8] E-publishing service, Digital Pulse Charge Integrator user manual,
www.caen.it/servlet/checkCaenManualFile?Id=11275.

- [9] V. Aulchenko *et al.*, *J. Phys. Conf. Ser.* **587** (2015) 012045.
<https://doi.org/10.1088/1742-6596/587/1/012045>

X-ray Tomography using Thin Scintillator Films

E.A. Kozyrev, K.E. Kuper, A.G. Lemzyakov, A.V. Petrozhitskiy and A.S. Popov

Budker Institute of Nuclear Physics, SB RAS; Novosibirsk State University, Novosibirsk, 630090, Russia

Abstract

2-14 μm thin CsI:Tl scintillation screens with high spatial resolution were prepared by the thermal deposition method for low energy X-ray imaging applications. The spatial resolution was measured as a function of the film thickness. It was proposed that the spatial resolution of the prepared conversion screens can be significantly improved by an additional deposition of a carbon layer.

Keywords

CsI:Tl; thin scintillation films; high spatial resolution; X-ray imaging; vacuum deposition method; carbon layer.

1 Introduction

CsI:Tl scintillator films are widely applied as the conversion screens for indirect X-ray imaging. CsI:Tl is characterized by one of the highest conversion efficiencies of any known scintillators [1]. Many authors have studied different approaches to the performance of the scintillation films. The methods to fabricate thin scintillators using a vacuum deposition process have been developed since the 1960s by C.W. Bates [2]. In general, there are two approaches to improve the spatial resolution of the X-ray image obtained using scintillators. The first one consists of the growth of the CsI:Tl scintillator with micro-columnar structure [3–5]. The micro-structure of the crystals decreases the lateral spreading of the scintillating light. The second approach considers post-deposition additional coating by carbon to decrease multiple scattering of photons inside the scintillator volume [6]. It is observed that the intrinsic properties of the structured CsI:Tl screens are heavily influenced by post deposition carbon coating. In this work the influence of carbon layer on the spatial resolution and the light output of the films with different thicknesses and energy of incident X-ray photons is studied. Additionally, the paper is dedicated to demonstrate the X-ray imaging applications of thin scintillation films.

2 Experimental Setup

2.1 Preparation of CsI:Tl Scintillation Films

The CsI:Tl scintillation films were manufactured by the thermal deposition method. Glass substrates with 150 μm thickness and 25x25 mm^2 area have been used. The source material CsI:Tl is held in a tantalum boat. The doping concentration of Tl is about 0.08 mol%. During the deposition process the tantalum boat temperature was set to 680°C as nominal value. To achieve homogeneous substrate coverage of the scintillator a relatively low deposition rate ($17 \pm 2 \text{ \AA/s}$) was used. All samples were prepared at a pressure of $5 \cdot 10^{-3}$ Pa and a substrate temperature at 25°C as recommended by the Thornton Zone Model [8]. A rotated disk with substrates was situated at a distance of 65 cm from the tantalum boat. Four thicknesses of CsI:Tl films were prepared: about 2, 4, 8 and 14 μm .

It was observed that the Tl concentration decreases with the increase of deposition time. The Tl density in the 8 μm sample is 80% the one of the 2 μm sample, due to larger evaporation velocity of Tl relative to CsI. The deposited CsI:Tl scintillator is characterized by sufficient Tl concentration for thicknesses less than 10 μm . For larger thicknesses a serial deposition procedure has to be used increasing the CsI:Tl layer step by step. The scintillator morphology of the CsI:Tl film deposited on

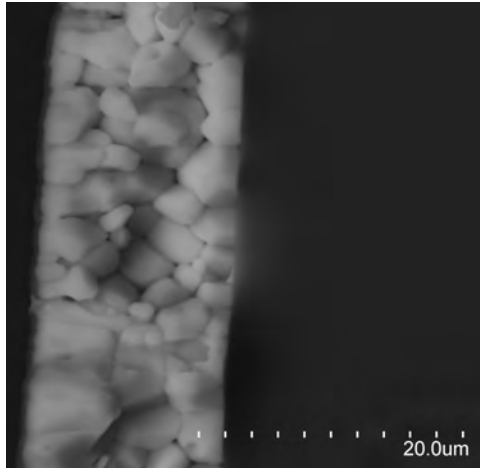


Fig. 1: The cross section of the CsI:Tl film deposited on a glass substrate with thickness $14.4 \pm 0.4 \mu\text{m}$

the glass substrate was investigated by a scanning electron microscope and is shown in Fig. 1. The film consists of a well-defined grain structure with a typical size of the grain about $3 \pm 2 \mu\text{m}$.

In order to improve spatial resolution of the prepared screens an additional carbon layer is deposited on the CsI:Tl surface by the magnetron deposition method using the AUTO 500 Vacuum Coater (BOC EDWARDS). All images that will be shown below were generated using CsI:Tl films with a 70 nm carbon layer, unless otherwise stated.

2.2 Micro-structure measurement and quantification of X-ray imaging performance

The examination of the thin film scintillators was carried out at the "Microscopy and tomography" beam-line of the VEPP-3 synchrotron source (BINP, Novosibirsk). The stability of the electron orbit in the VEPP-3 storage ring was better than $50 \mu\text{m}$ and the electron bunch with a size of $0.5 \times 1.5 \text{ mm}^2$ provided a spatial resolution around $1 \mu\text{m}$. The X-ray working wavelength was selected by a double-crystal Si(111) monochromator used in the parallel Bragg-geometry and installed at a distance of 14.5 m from the synchrotron radiation (SR) emission point. The energy of the photons of the X-ray monochromatic beams, used in the experiments, varied from 5 to 40 keV. Slits installed upstream the sample were applied for suppression of parasitic reflections from the monochromator and formed a $2 \times 2 \text{ mm}^2$ collimated X-ray beam. The scintillator was placed at a distance of 16.5 m from the SR source. The scintillator was pre-aligned in a translated axis with an accuracy of $10 \mu\text{m}$ and in a rotation axis with an accuracy of 0.01 degrees. The visible light from the scintillator was collected by the precise digital camera Hamamatsu ORCA-Flash2.8, placed at a distance of 5 cm from the scintillator screen. The CsI:Tl film was fixed facing to the X-ray source while the glass substrate was directed to the optical detector.

3 Results and Discussion

3.1 Spatial resolution

In order to test the intrinsic spatial resolution of the resulting system images of gold patterns produced at BINP are taken. The patterns are manufactured by e-beam lithography (SEM HITACHI S 3400 type II with Nanomaker system). The PMMA 950k e-beam positive tone resist with a $2 \mu\text{m}$ thickness was used. The X-ray absorber pattern was obtained by gold electroplating. Fig. 2 was obtained using the X-ray imaging technique with a $2 \mu\text{m}$ thick CsI:Tl screen where the numbers indicate the width of the corresponding gold line. The image of the pattern with $6 \mu\text{m}$ width can be reasonably resolved. The image also demonstrates that the response of the X-ray conversion screen is uniform across the area of the film. The total spatial resolution of the system is caused, predominantly, by the following factors:

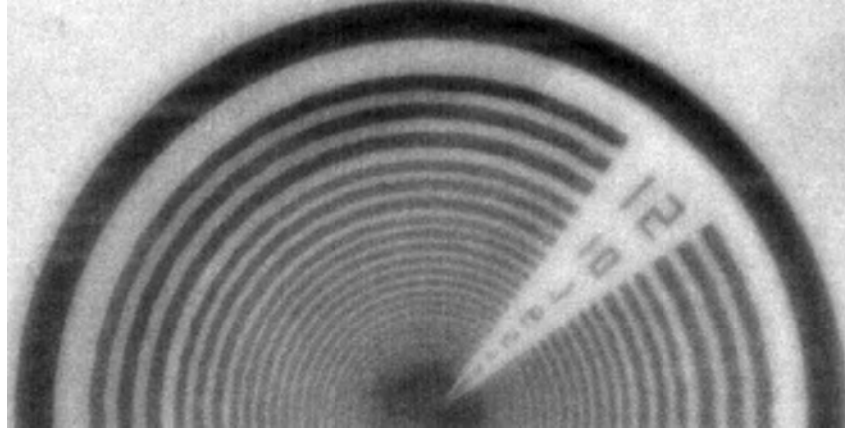


Fig. 2: Image of gold patterns obtained by X-ray imaging technique using CsI:Tl films

non-collinearity of the incident X-ray beam, mechanical oscillation of the holder of the detector relative to beam line and lateral spreading of visible photons inside the scintillator volume. The last two effects contribute about equally. An anti-vibration platform is used to reduce the contribution of the vibrations.

In order to perform a measure of the ability of our imaging detector to reproduce image contrast at various spatial frequencies in the range of 0 to 160 line-pairs/mm (lp/mm) the modulation transfer function $MTF(f)$ is given by the following equation:

$$MTF(f) = \frac{FFT[LSF](f)}{FFT[LSF](f=0)} \quad (1)$$

where f means the spatial frequency (the inverse of the frequency equals the distance in millimeters between two resolved lines), FFT - the Fast Fourier Transform and LSF - the line spread function. A steel plate placed in front of the scintillator with thickness 1 mm is utilized to obtain the edge image, from which the oversampled LSF is calculated [9]. The MTF at each line-pair frequency can be defined as a function of the brightness of the line pairs as (max. brightness - min. brightness)/(max. brightness + min. brightness). So, the higher MTF corresponds to the better sharpness and resolution of an image.

Fig. 3 shows the MTFs for screens of various thicknesses. It is seen that there is a reduction in resolution with increased film thickness due to lateral light spreading and imperfect channeling inside the scintillator volume. This dependence is in agreement with previous results reported in Refs. [6, 7] and illustrates that the scintillation screens are characterized by micro-columnar structure. The most thin $2 \mu\text{m}$ screen provides the highest spatial resolution required by low energy micro-tomography of biological objects as well as the high stopping power of the X-ray beam. For example, the conversion efficiency of the X-ray beam in the $2 \mu\text{m}$ screen is still 20% at 9 keV energy of the incident X-ray.

In order to demonstrate the improvement of resolution, related with the carbon deposition, $MTF(f)$ of patterns with different conditions are calculated. Lines 1, 2, and 3 in the Fig. 3 correspond to a screen with $14 \mu\text{m}$ thickness of CsI:Tl and with 0, 70, and 140 nm of carbon, respectively. The improvement can be explained as following. The additional carbon layer suppresses the reflection of scintillation photons on the interface between the carbon layer and the CsI:Tl, removing the multiple scattering of visible photons inside the scintillator volume. Simultaneously, the additional carbon layer leads to a decrease of light output by a factor 3 ± 1 . The factor is significantly larger than 2, indicating the presence of multiple reflection between scintillator surfaces. Also the MTFs were investigated as a function of the incident X-ray energy. It was observed that there is no significant improvement of the spatial resolution with an increase of the X-ray energy from 5 to 40 keV.

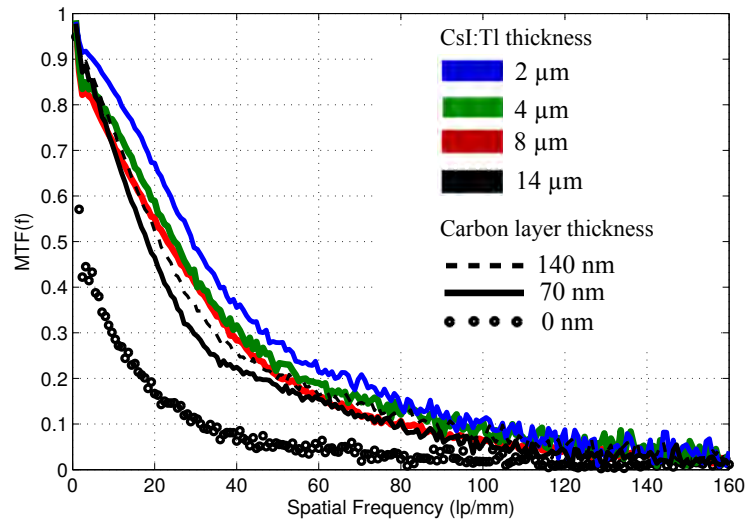


Fig. 3: Measured MTF curves with different thicknesses of CsI:Tl scintillating screens and carbon layers

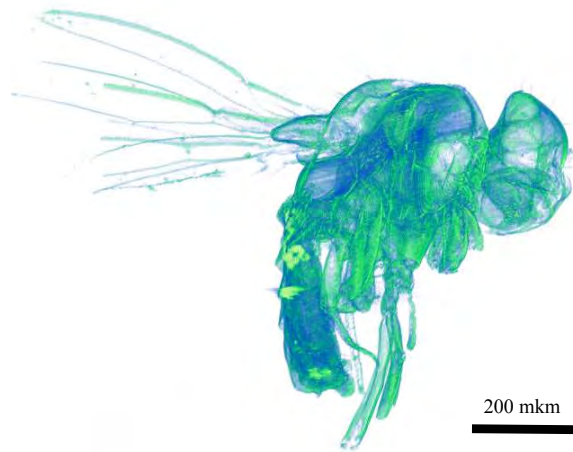


Fig. 4: The example of the tomography of drosophila

3.2 3-D tomography

The high resolution images obtained by the screens were used to reconstruct 3D structures of different samples with the X-ray computer tomography method. Each tomography scan consists of 720 projections with an angular step of 0.25° (from 0° to 180°) obtained at monochromatic beam with photon energy of 15 keV. Small angle SR deviation of about 0.2 mrad makes it possible to use an algorithm for a parallel beam geometry, which simplifies the process of the 3D reconstruction of the object and significantly improves the quality of the image. The example of the tomography of drosophila can be found in Fig. 4.

To nondestructively investigate objects which are bigger than field of view of the detector the local computed tomography mode and a polychromatic beam with an average photon energy of about 25 keV are used. For example, kimberlite is an important source of diamond deposits that contain xenoliths. One of the possible types of xenoliths are garnet peridotite depleted of silicon and aluminum and rich of magnesium and iron. The study of diamondiferous xenoliths by X-ray computer tomography allows to determine the spatial distribution of rock-forming minerals and to characterize genetic relationships and the process of crystallization in the deep areas of our planet. Fig. 5 depicts a 3D image of garnet distribution on the diamondiferous rock.

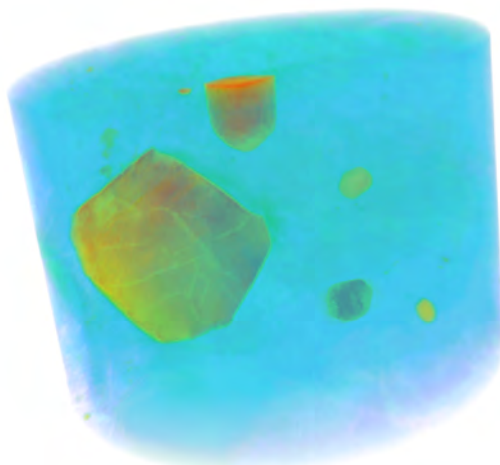


Fig. 5: 3D image of garnet distribution on the diamondiferous rock

3.3 Other prospects

Also thin CsI:Tl films deposited on mylar substrates can be used for non-destructive diagnostics of the spatial profiles of low energy beams of charged particles (such as muon beams at the MEG experiment). The proposed method allows to perform the beam monitoring simultaneously with the experimental data acquisition. Also the developed technique of CsI:Tl deposition allows to perform low cost X-ray converters with arbitrary thickness, that can be used in medicine and other fields.

4 Conclusion

The technique of the production of thin CsI:Tl films with the thermal deposition method has been developed. The spatial resolution of the produced conversion screens can be significantly improved by additional deposition of a carbon layer with a thickness of about 100 nm which is designed to absorb photons propagating in backward direction. All X-ray low energy radio-graphic methods can be employed with films in polychromatic and monochromatic modes to investigate the internal structure of a large variety of objects varying from 10 μm of biological tissue up to 10 cm of dense rock.

References

- [1] Martin Nikl, Scintillation detectors for x-ray, Meas. Sci. Technol. **17** (2006).
- [2] C.W. Bates, Scintillation Processes in Thin Films of CsI(Na) and CsI(Tl) used to Low Energy X-rays, Electrons and Protons, in Photo-Electronic Image Devices, pp. 451-459, Academic Press, (1969).
- [3] V.V. Nagarkar, et al., Structured CsI(Tl) Scintillators for X-ray Imaging Applications. IEEE Trans. Nucl. Sci, **45**, pp. 492-496, (1998).
- [4] V.V. Nagarkar, et al., A Comparative Study of CsI(Tl) Screens for Macromolecular Crystallography, Proc. SPIE, Vol. **4508**, pp.15-19, (2001).
- [5] D. Yao, et al., IEEE Transactions on Nuclear Science, **60**, 3 (2013).
- [6] F. Zhao-Dong, et al., Chinese Phys. C **39** 078202 (2015).
- [7] B.Z. Zhao, et al., Chinese Physics C, **38** 116003 (2009).
- [8] J.A. Thornton, "Influence of apparatus geometry and deposition conditions on the structure and topography of thick sputtered coatings", J. Vac. Sci. Technol. **11** (1974).
- [9] H. Illers, et al., Radiat Prot Dosimetry, **114**, 214-219 (2005).

Calorimetry at the CMD-3 detector

G. P. Razuvaev^{*1,2}, R. R. Akhmetshin^{1,2}, A. V. Anisenkov^{1,2}, V. M. Aulchenko^{1,2}, N. S. Bashtavoy^{1,2}, D. A. Epifanov^{1,1}, L. B. Epshteyn^{1,2,3}, A. L. Erofeev^{1,2}, A. A. Grebenuk^{1,2}, D. N. Grigoriev^{1,2,3}, V. F. Kazanin^{1,2}, O. A. Kovalenko^{1,2}, A. N. Kozyrev^{1,2,3}, A. E. Kuzmenko^{1,2}, A. S. Kuzmin^{1,2}, I. B. Logashenko^{1,2}, K. Yu. Mikhailov^{1,2}, V. S. Okhapkin¹, A. A. Ruban¹, V. E. Shebalin^{1,2}, B. A. Shwartz^{1,2}, V. M. Titov¹, A. A. Talyshv^{1,2}, and Yu. V. Yudin^{1,2}

¹Budker Institute of Nuclear Physics, SB RAS, Novosibirsk, 630090, Russia

²Novosibirsk State University, Novosibirsk, 630090, Russia

³Novosibirsk State Technical University, Novosibirsk, 630092, Russia

Abstract

The general purpose detector CMD-3 has been collecting data since 2010 in an energy range 0.32–2 GeV at the e^+e^- collider VEPP-2000 at the Budker Institute of Nuclear Physics. The detector physics program includes the study of the e^+e^- annihilation into hadrons. To supply high registration efficiency for neutral particles the CMD-3 has an electromagnetic calorimeter consisting of three subsystems: BGO endcap calorimeter and barrel with an inner part based on LXe and an outer one based on CsI crystals. The main parameters of calorimeters, cluster reconstruction and calibration procedures with performance results are described.

Keywords

Calorimetry; liquid xenon; scintillation crystals.

1 Introduction

The VEPP-2000 [1, 2] is an e^+e^- collider at the Budker Institute of Nuclear Physics (Novosibirsk, Russia). It operates in a center-of-mass (c. m.) energy range from 0.32 to 2 GeV. The designed luminosity of the collider at 2 GeV c. m. energy is $10^{32} \text{ cm}^{-2} \text{ s}^{-1}$. In order to reach the design luminosity in a single-bunch mode the novel round beam technique developed at the BINP is used. The beam energy is monitored with a precision of $\Delta E/E = 6 \cdot 10^{-5}$ using the Compton backscattering process [3, 4]. There are two interaction points at the collider and two detectors are mounted there: the Spherical Neutral Detector (SND) [5, 6] and the Cryogenic Magnetic Detector (CMD-3) [7]. Data taking started in 2010. The integrated luminosity collected by each detector during three years of operation is about 60 pb^{-1} . In 2013 the collider operation was stopped for a collider and detectors upgrade, and it has been resumed in 2017.

The physical program [8, 9, 10] includes measurement of the $e^+e^- \rightarrow \text{hadrons}$ cross sections, study of the properties of known and search for new vector mesons, measurement of $n\bar{n}$ and $p\bar{p}$ cross sections near their thresholds and search for exotic hadrons. These tasks require a detector with high efficiency for multiparticle events and good energy and angular resolutions for both charged particles and photons.

The CMD-3 is a general purpose detector. Its layout is presented in Figure 1. The electromagnetic calorimeter is one of the most important systems of the CMD-3 detector. Its main goals are measurements of energy and coordinate of the photons, the separation of electrons from hadrons and a generation of signals for the neutral trigger. The calorimetry of the detector consists of barrel and endcap parts. The

*G.P.Razuvaev@inp.nsk.su

barrel calorimeter combines the inner liquid xenon calorimeter (LXe) [11] and the outer one based on CsI crystals [12]. The endcap calorimeter [13] is based on the bismuth germanium oxide $\text{Bi}_4\text{Ge}_3\text{O}_{12}$ (BGO) crystals. The total solid angle coverage of the CMD-3 calorimeter is equal to $0.94 \times 4\pi$.

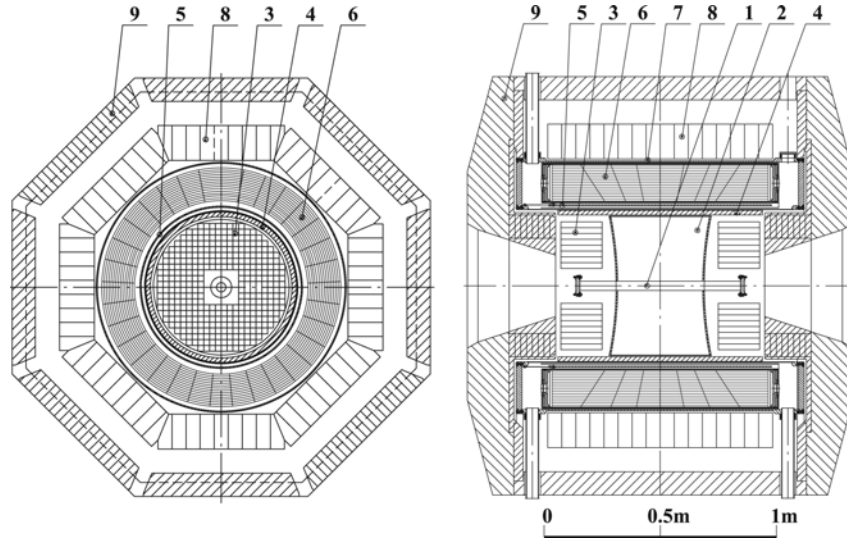


Fig. 1: The CMD-3 detector layout: 1 — beam pipe, 2 — drift chamber, 3 — BGO endcap calorimeter, 4 — Z-chamber, 5 — superconducting solenoid, 6 — liquid xenon calorimeter, 7 — time-of-flight system, 8 — CsI calorimeter, 9 — yoke

2 General description

The inner LXe calorimeter is a set of 14 ionization chambers with 7 cylindrical cathodes and 8 anodes divided by 10.2 mm gaps between them. The calorimeter is placed in the same vacuum vessel with a superconducting solenoid to reduce passive material in front of the calorimeter. The electrodes are made of a 0.5 mm thin G-10 plate foiled with copper. The conductive surfaces of the anode cylinders are divided into 264 rectangular pads (8 along the Z-axis and 33 in the $r - \phi$ plane) forming so-called “towers” oriented to the beam interaction point. Pads within one tower are electrically connected. The average tower size is $8 \times 10 \times 15 \text{ cm}^3$. The signals from the towers are used to measure the deposited energy. The cathode cylinders are divided into 2112 strips to provide a precise coordinate measurement together with the measurement of specific energy losses. Each side of the cathode cylinder contains about 150 strips. The strips on the opposite sides of the cylinder are mutually perpendicular. One signal strip consists of four joined 2 mm width strips. Such semi-transparent electrode structures provide charge induction on both sides of cathode electrode. That allows one to determine both coordinates of the photon conversion point using the information from one gap only. The design of the liquid xenon calorimeter is described in detail in [14, 11].

Since the LXe calorimeter is rather thin ($5.4 X_0$) it is surrounded by the CsI scintillation crystals calorimeter to improve the energy resolution. The CsI calorimeter consists of 1152 $6 \times 6 \times 15 \text{ cm}^3$ Na- or Tl-doped CsI crystals assembled in 8 octants. Each octant consists of 9 rows (modules) of crystals. The modules are oriented along the Z-axis. Both sides of the modules of each octant have a special truncated shape in order to avoid gaps between octants. Each module consists of 16 counters. The length of the crystals corresponds to a thickness of $8.1 X_0$. The total sensitive material thickness of the barrel calorimeter for a normal incident particle is equal to $13.5 X_0$. The thickness of the passive material in front of the barrel calorimeter is $0.35 X_0$ and passive material between LXe and CsI parts of the barrel calorimeter is $0.25 X_0$. The design of the CsI calorimeter is described in detail in [12].

To increase the solid angle coverage the CMD-3 is equipped with the endcap calorimeter. It consists of 680 BGO crystals of $2.5 \times 2.5 \times 15 \text{ cm}^3$ arranged in two identical arrays. The endcap calorimeters cover polar angles from 17° to 50° and from 130° to 163° . The length of the crystals corresponds to the thickness of $13.4 X_0$. The design of this calorimeter is described in detail in [15].

3 Cluster reconstruction

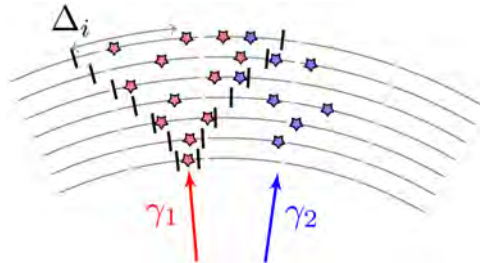


Fig. 2: Cluster reconstruction in the LXe calorimeter from strip information

The standard cluster reconstruction procedure in crystal and LXe calorimeters begins with searching for a calorimeter element with energy deposition, greater than 5 MeV, a seed. Then all neighbour elements having at least 2 MeV of energy deposition are grouped together in one cluster and the procedure is repeated. This algorithm introduces a limitation on the minimal distance between clusters in the LXe calorimeter to be properly reconstructed. The distance equals a tower size corresponding to $\sim 40 \text{ mrad}$. This is not sufficient for multiparticle processes and for high energy π^0 decaying into two photons. Because of that the development of the new reconstruction algorithm [16] has been started to separate close incident photons based on LXe strip information. Firstly, using simulation the most probable radius Δ_i of an electromagnetic shower for each cathode layer was determined. Then for a tower cluster the conversion point — closest to the interaction point cross-section of strip clusters — is treated as a seed to which the connection of strip clusters with respect of Δ_i is performed, see Figure 2. Groups of leftover strips in the tower cluster are considered as another photon. At the next step sorting of strip photons by energy calculated from strip information is done and the top two energetic photons are saved, the others are rejected. In the end one has precise knowledge about the photons' conversion points and their combined energy measured with the anode structure and rough energy estimation of each photon by cathode signals. A test of the new algorithm was done with simulation data of the $e^+e^- \rightarrow \pi^0\gamma$ process for energies from 1 GeV to 2 GeV in the centre of mass frame. The result shows a significant growth in the detection efficiency for high energies.

4 Calibrations and resolutions

Several procedures are used for the calorimeter calibration. Electronic channel calibration with a pulse generator provides the measurement of the pedestals, electronic gain and electronic noise of each calorimeter channel. For crystal calorimeters cosmic ray particles in special calibration runs are used. Since the standard CMD-3 trigger does not suppress all cosmic rays events the experimental data sample contains such events and they are also used for the calibration. This type of calibration is used for both endcap and combined barrel calorimeters. For LXe calorimeter a calibration with e^+e^- elastic scattering events is used. For the endcap calorimeter the energy corrections are performed using the two-photon annihilation process, $e^+e^- \rightarrow \gamma\gamma$, to obtain absolute energy calibration. The calibration procedures for the joined barrel calorimeter are described in [17] and for the endcap calorimeter in [13].

Two-photon annihilation and Bhabha events were used to obtain the energy and spatial resolutions of the calorimeters. The results are shown in Figure 3 and Figure 4. The problems in the

calorimeter electronics in 2010–2013 caused the rise of LXe+CsI σ_E/E for high beam energies in Figure 3. The electronics were fixed during the collider shutdown. The energy resolution for the barrel calorimeter can be parametrized as $\sigma_E/E = 0.034/\sqrt{E/\text{GeV}} \oplus 0.020$ and for the endcap as $\sigma_E/E = 0.024/\sqrt{E/\text{GeV}} \oplus 0.023$.

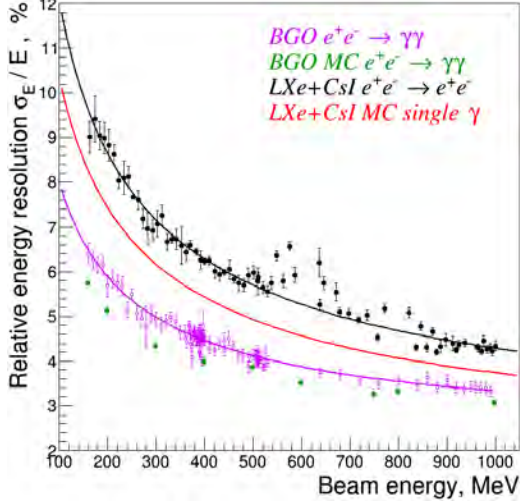


Fig. 3: Energy resolution of calorimeters

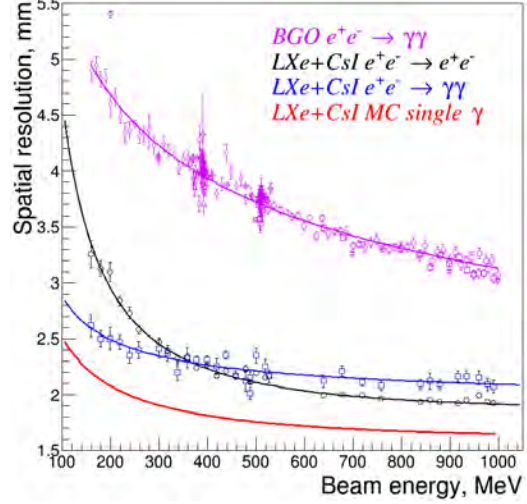


Fig. 4: Spatial resolution of calorimeters

To obtain the spatial resolution of the calorimeters the distribution of the azimuth angle acollinearity $\Delta\phi = \pi - |\phi_1 - \phi_2|$ was used, where ϕ_1 and ϕ_2 are the azimuth angles of the photons. This distribution was approximated by a Gaussian function, the angular resolution of the calorimeter σ_ϕ was defined as the standard deviation of the Gaussian function. The coordinates of most (95%) photons detected in the barrel calorimeter are measured using LXe strips data with an angular precision of about 0.005 rad, which slightly depends on the photon energy. In this case the angular resolution can be fitted as $\sigma_\phi/\text{mrad} = 3.70 + 0.33/(0.25 + E/\text{GeV})$. For about 5% of events the conversion point is not reconstructed by strip data and the photon coordinates are determined as the centre of gravity of the cluster. For such a case the correction function for the photon coordinates was determined from the simulation. The angular resolution in this case can be fitted as $\sigma_\phi/\text{mrad} = 37.0 + 3.6/(0.1 + E/\text{GeV})$.

The spatial resolution of the endcap calorimeter was calculated as $\sigma_x = \sigma_\phi \cdot Z_0 \cdot \tan\theta/\sqrt{2}$ where Z_0 is the distance from the interaction point to the front plane of the endcap and θ is the polar angle of the photon. The resolution can be fitted as $\sigma_x/\text{mm} = 3.03/\sqrt[4]{E/\text{GeV}}$.

Finally, to demonstrate the calorimetry performance Fig. 5 and Fig. 6 contain the distribution of photon invariant masses obtained during analyses of $e^+e^- \rightarrow \pi^+\pi^-\pi^0$ and $e^+e^- \rightarrow \pi^0\gamma, \eta\gamma$ with pseudo-scalars decaying into two photons. For the first process the π^0 mass resolution is about 8.5% and 5.8% for η -meson in the second process.

5 Conclusion

The calorimeters were installed into the CMD-3 detector and have been used in the experimental data taking since 2010. The calibration procedures of the calorimeters have been developed and used during all three physics seasons. The standard photon energy reconstruction procedures have been developed and applied, the new algorithm using strip information to separate close photons is under design. The energy and spatial resolutions at 1 GeV have been determined to be 4.5% and 2 mm for the barrel calorimeter and 3.5% and 3 mm for the endcap calorimeter respectively.

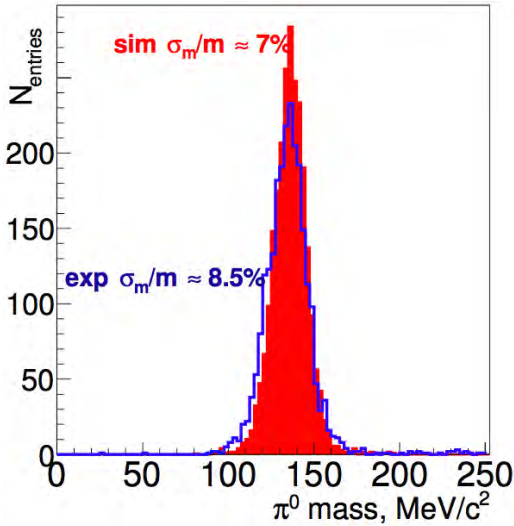


Fig. 5: The distribution of the two photon invariant mass in the $e^+e^- \rightarrow \pi^+\pi^-\pi^0$ process before kinematic reconstruction. The comparison of experimental (open blue) and simulation (closed red) data is presented.

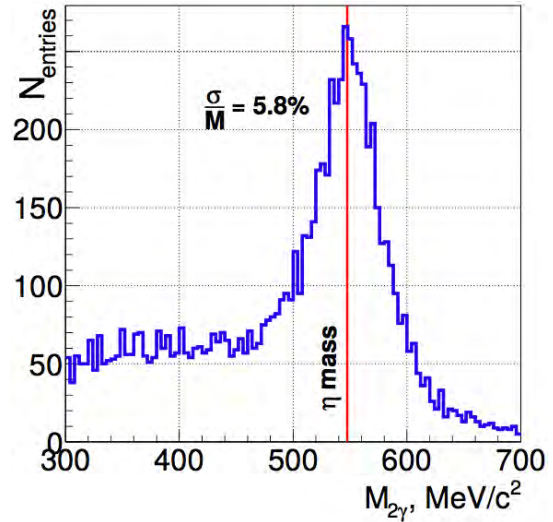


Fig. 6: The distribution of the two photon invariant mass in the $e^+e^- \rightarrow 3\gamma$ process before kinematic reconstruction. The signal peak shown from $e^+e^- \rightarrow \eta\gamma$.

Acknowledgements

This work has been supported by Russian Science Foundation (project N 14-50-00080).

References

- [1] Yu. M. Shatunov et al. “Project of a new electron positron collider VEPP-2000”. In: *Conf. Proc.* C0006262 (2000). [439(2000)], pp. 439–441 (cit. on p. 1).
- [2] D. Berkaev et al. “VEPP-2000 operation with round beams in the energy range from 1-GeV to 2-GeV”. In: *Nucl. Phys. Proc. Suppl.* 225-227 (2012), pp. 303–308. DOI: 10.1016/j.nuclphysbps.2012.02.063 (cit. on p. 1).
- [3] E. V. Abakumova et al. “A system of beam energy measurement based on the Compton backscattered laser photons for the VEPP-2000 electron–positron collider”. In: *Nucl. Instrum. Meth.* A744 (2014), pp. 35–40. DOI: 10.1016/j.nima.2014.01.020. arXiv: 1310.7764 [physics.acc-ph] (cit. on p. 1).
- [4] E. V. Abakumova, M. N. Achasov, A. A. Krasnov, et al. “The system for delivery of IR laser radiation into high vacuum”. In: *JINST* 10.09 (2015), T09001. DOI: 10.1088/1748-0221/10/09/T09001. arXiv: 1504.00130 [physics.acc-ph] (cit. on p. 1).
- [5] M. N. Achasov et al. “First experience with SND calorimeter at VEPP-2000 collider”. In: *Nucl. Instrum. Meth.* A598 (2009), pp. 31–32. DOI: 10.1016/j.nima.2008.08.012 (cit. on p. 1).
- [6] M. N. Achasov et al. “Time resolution of the SND electromagnetic calorimeter”. In: *JINST* 10.06 (2015), T06002. DOI: 10.1088/1748-0221/10/06/T06002 (cit. on p. 1).
- [7] B. Khazin. “Physics and detectors for VEPP-2000”. In: *Nucl. Phys. Proc. Suppl.* 181-182 (2008), pp. 376–380. DOI: 10.1016/j.nuclphysbps.2008.09.068 (cit. on p. 1).
- [8] S. Eidelman. “Physics at VEPP-2000”. In: *Nucl. Phys. Proc. Suppl.* 162 (2006). [323(2006)], pp. 323–326. DOI: 10.1016/j.nuclphysbps.2006.09.122 (cit. on p. 1).

- [9] R. R. Akhmetshin et al. “Search for the process $e^+e^- \rightarrow \eta'(958)$ with the CMD-3 detector”. In: *Phys. Lett.* B740 (2015), pp. 273–277. DOI: 10.1016/j.physletb.2014.11.056. arXiv: 1409.1664 [hep-ex] (cit. on p. 1).
- [10] D. N. Shemyakin et al. “Measurement of the $e^+e^- \rightarrow K^+K^-\pi^+\pi^-$ cross section with the CMD-3 detector at the VEPP-2000 collider”. In: *Phys. Lett.* B756 (2016), pp. 153–160. DOI: 10.1016/j.physletb.2016.02.072. arXiv: 1510.00654 [hep-ex] (cit. on p. 1).
- [11] A. V. Anisenkov et al. “Status of the Liquid Xenon calorimeter of the CMD-3 detector”. In: *JINST* 9 (2014), p. C08024. DOI: 10.1088/1748-0221/9/08/C08024 (cit. on p. 2).
- [12] V. M. Aulchenko et al. “CsI calorimeter of the CMD-3 detector”. In: *JINST* 10.10 (2015), P10006. DOI: 10.1088/1748-0221/10/10/P10006 (cit. on p. 2).
- [13] R. R. Akhmetshin, D. N. Grigoriev, V. F. Kazanin, et al. “Performance of the BGO endcap calorimeter of the CMD-3 detector”. In: *JINST* 9.10 (2014), p. C10002. DOI: 10.1088/1748-0221/9/10/C10002 (cit. on pp. 2, 3).
- [14] A. V. Anisyonkov, L. M. Barkov, N. S. Bashtovoy, et al. “Liquid xenon calorimeter for a CMD-3 detector”. In: *Nucl. Instrum. Meth.* A598 (2009), pp. 266–267. DOI: 10.1016/j.nima.2008.08.091 (cit. on p. 2).
- [15] R. R. Akhmetshin, D. N. Grigoriev, V. F. Kazanin, et al. “Status of the endcap BGO calorimeter of the CMD-3 detector”. In: *Physics of Atomic Nuclei* 72.3 (2009), pp. 477–481. DOI: 10.1134/S1063778809030119 (cit. on p. 3).
- [16] Andrey Rabusov. “The study of the annihilation process $e^+e^- \rightarrow \eta\gamma, \eta \rightarrow \pi^+\pi^-\pi^0$ with the CMD-3 detector at the VEPP-2000 collider”. MA thesis. Novosibirsk, Russia: Novosibirsk State University, June 2016 (cit. on p. 3).
- [17] V. E. Shebalin et al. “Combined Liquid Xenon and crystal CsI calorimeter of the CMD-3 detector”. In: *JINST* 9.10 (2014), p. C10013. DOI: 10.1088/1748-0221/9/10/C10013 (cit. on p. 3).

Charged Particle Identification using the Liquid Xenon Calorimeter of the CMD-3 Detector

R.R.Akhmetshin, A.N.Amirkhanov, A.V.Anisenkov, V.M.Aulchenko, V.Sh.Banzarov, N.S.Bashtovoy, A.E.Bondar, A.V.Bragin, S.I.Eidelman, D.A.Epifanov, L.B.Epshteyn, A.L.Erofeev, G.V.Fedotov, S.E.Gayazov, A.A.Grebenuk, S.S.Gribanov, D.N.Grigoriev, F.V.Ignatov, V.L.Ivanov, S.V.Karpov, V.F.Kazanin, O.A.Kovalenko, A.A.Korobov, A.N.Kozyrev, E.A.Kozyrev, P.P.Krokovny, A.E.Kuzmenko, A.S.Kuzmin, I.B.Logashenko, P.A.Lukin, K.Yu.Mikhailov, V.S.Okhapkin, Yu.N.Pestov, A.S.Popov, G.P.Razuvaev, A.A.Ruban, N.M.Ryskulov, A.E.Ryzhenkov, V.E.Shebalin, D.N.Shemyakin, B.A.Shwartz, A.L.Sibidanov†, E.P.Solodov, V.M.Titov, A.A.Talyshev, A.I.Vorobiov, Yu.V.Yudin*
Budker Institute of Nuclear Physics, SB RAS, Novosibirsk, 630090, Russia

Abstract

This paper describes a currently being developed procedure of the charged particle identification for the CMD-3 detector, installed at the VEPP-2000 collider. The procedure is based on the application of the boosted decision trees classification method and uses as input variables, among others, the specific energy losses of charged particle in the layers of the liquid Xenon calorimeter. The efficiency of the procedure is demonstrated by an example of the extraction of events of the $e^+e^- \rightarrow K^+K^-$ process in the center of mass energy range from 1.8 to 2.0 GeV.

Keywords

Particle identification; specific energy losses; boosted decision trees.

1 Introduction

The electron-positron collider VEPP-2000 [1], installed at the Budker Institute of Nuclear Physics (Novosibirsk, Russia), was operating in 2010-2013 and currently is undergoing the final stage of modernization, which will allow it to reach a luminosity of $10^{32} \text{cm}^{-2} \text{s}^{-1}$ at its maximum center of mass (c.m.) energy of 2 GeV. At the two beam intersection points the SND [2] and CMD-3 [3] particle detectors are installed, the main task of which is the measurement of the exclusive cross sections of the electron-positron annihilation into hadrons. Such measurements are necessary to reduce the uncertainty of the hadronic contribution to the anomalous magnetic moment of muon $a_\mu^{\text{had, LO}}$ [4, 5].

The tracking system of the CMD-3 detector consists of a cylindrical drift chamber (DC) and a double-layer cylindrical multiwire proportional Z-chamber, installed inside a superconducting solenoid with 1.0–1.3 T magnetic field (see CMD-3 layout in Fig. 1). Amplitude information from the DC wires is used to measure the specific ionization losses (dE/dx_{DC}) of charged particles. Bismuth germanate crystals of $13.4 X_0$ thickness are used in the endcap calorimeter. The barrel calorimeter, placed outside the solenoid, consists of two parts: external (based on CsI crystals of $8.1 X_0$ thickness) and internal (based on liquid Xenon (LXe) of $5.4 X_0$ thickness) [6].

The LXe calorimeter consists of 14 cylindrical ionization chambers formed by 7 cylindrical cathodes and 8 anodes with a 10.2 mm gap between them (see Fig. 2). Each anode is divided into 264 rectangular pads (8 along the z -axis and 33 in the $r - \phi$ plane), forming so-called "towers" oriented to the beams interaction point (see Fig. 1). Signals from pads within one tower are summed up and this information is used to measure the particle energy deposition. Cathodes are divided into 2112 strips

*Corresponding author.

†University of British Columbia, Vancouver, Canada.

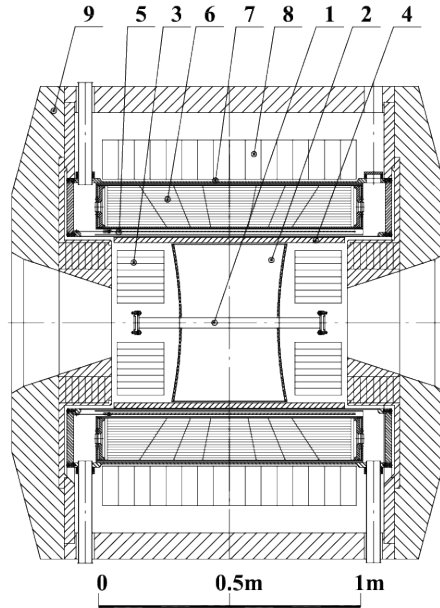


Fig. 1: The CMD-3 detector layout: 1 - beam pipe, 2 - drift chamber, 3 - BGO endcap calorimeter, 4 - Z-chamber, 5 - superconducting solenoid, 6 - LXe calorimeter, 7 - time-of-flight system, 8 - CsI calorimeter, 9 - yoke.

to provide precise coordinate measurement along with the measurement of the specific energy losses (dE/dx_{LXe}) in each of 7 double anode-cathode-anode layers (see Fig. 3). Each side of the cathode cylinder contains about 150 strips. The strips on the opposite sides of the cathode are mutually perpendicular, which allows one to measure z and ϕ coordinates of the "hit" in the strips channels. The total amount of material in front of the LXe calorimeter is $0.13 X_0$, which includes the solenoid, the radiation shield and vacuum vessel walls.

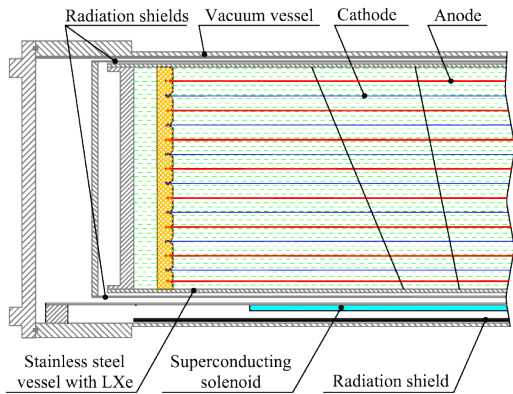


Fig. 2: LXe calorimeter electrodes structure.

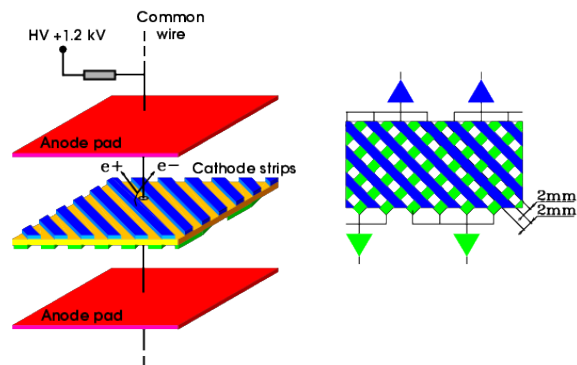


Fig. 3: Anode-cathode-anode layer of the LXe calorimeter. A strip structure of cathode is shown.

For a more accurate measurement of the exclusive cross sections one has to extract a sufficiently background-free sample of the events of the studied process, which requires the development of the effective particle identification (PID) procedure. This paper describes a currently being developed procedure of the charged PID for the CMD-3 detector, which involves the dE/dx_{DC} and dE/dx_{LXe} , as well as the energy depositions of charged particles in the LXe (E_{LXe}) and CsI (E_{CsI}) calorimeters. The efficiency of the procedure is demonstrated by an example of the extraction of the events of the $e^+e^- \rightarrow K^+K^-$ process in the c.m. energy range from 1.8 to 2.0 GeV.

2 Charged particle identification with the use of dE/dx_{LXe}

In this paper we will focus on the issue of identification of charged kaons. The separation of the *single* kaons from pions or muons using only dE/dx_{DC} can be reliably performed only for particle momenta lower than 450 MeV/c. This is seen from Figure 4, which shows the distribution of dE/dx_{DC} versus particle momentum for the events of the final state $K^+K^-\pi^+\pi^-$, selected in the experiment [7]. With the use of the energy-momentum conservation law, in the case of this final state a reliable K/π -separation can be performed even up to momenta 700 MeV/c. But for the final states K^+K^- , $K^+K^-\pi^0$, $K^+K^-\pi^0\pi^0$ at high c.m. energies it is hard or impossible to obtain a sufficiently background-free sample of signal events using only dE/dx_{DC} and the energy-momentum conservation law. Hence the dE/dx_{LXe} should be used for PID purposes.

2.1 Binding of the tracks in the DC and LXe

Since the tracks in the DC (DC-tracks) and LXe calorimeter (LXe-tracks) are reconstructed independently, their mutual connection is required. From the kinematics of spiral motion one can derive the rotation angle ϕ_{rot} of the DC-track in the magnetic field B of the solenoid, the expected LXe-cluster polar angle $\theta_{\text{LXe,exp}}$ (measured relative to the central point of the detector) and the penetration angle α_{pen} of the particle to the LXe (the angle between the particle velocity vector and the tangent plane to the surface of the calorimeter at the entry point of the particle):

$$\phi_{\text{rot}} = \text{sign}(q) \arcsin\left(\frac{1.515 \cdot R_{\text{LXe}}[\text{cm}] \cdot B[\text{T}]}{p_{\perp}[\text{MeV}/c]}\right), \quad (1)$$

$$\theta_{\text{LXe,exp}} = \arctg\left(\frac{R_{\text{LXe}}}{|z_{\text{DC}} + 2R_{\text{curv}} \text{ctg}(\theta_{\text{DC}}) \arcsin\left(\frac{R_{\text{LXe}}}{2R_{\text{curv}}}\right)|}\right) + \pi(1 - \text{sign}(z_{\text{DC}} + 2R_{\text{curv}} \text{ctg}(\theta_{\text{DC}}) \arcsin\left(\frac{R_{\text{LXe}}}{2R_{\text{curv}}}\right))), \quad (2)$$

$$\alpha_{\text{pen}} = \arcsin\left(\sin(\theta_{\text{DC}}) \sqrt{1 - \left(\frac{R_{\text{LXe}}}{2R_{\text{curv}}}\right)^2}\right), \quad (3)$$

where q is the particle charge, $R_{\text{LXe}} = 38$ cm the radius of the first cathode cylinder, p_{\perp} the transverse particle momentum, z_{DC} is the z -coordinate of the point of the particle origin (lying on the axis of the beams), θ_{DC} the polar angle of the DC-track, R_{curv} the curvature radius of the DC-track in the $r - \phi$ plane. To bind the DC and LXe tracks we apply the following conditions:

$$|\delta\phi| \equiv |\phi_{\text{LXe,meas}} - \phi_{\text{DC}} + \phi_{\text{rot}}| < 0.03 \text{ rad}, \quad (4)$$

$$|\delta\theta| \equiv |\theta_{\text{LXe,meas}} - \theta_{\text{DC,exp}}| < 0.03 \text{ rad}, \quad (5)$$

where ϕ_{DC} is the azimuthal angle of the departure of DC-track from the beams interaction region, $\phi_{\text{LXe,meas}}$ and $\theta_{\text{LXe,meas}}$ the measured azimuthal and polar angle of the first strips hit, associated with a reconstructed LXe-track. The $|\delta\phi|$ vs $|\delta\theta|$ distribution in the simulation is shown in Figure 5. It is seen that the mutual connection of the tracks can be performed with a precision of about 0.02 rad for both azimuthal and polar angles.

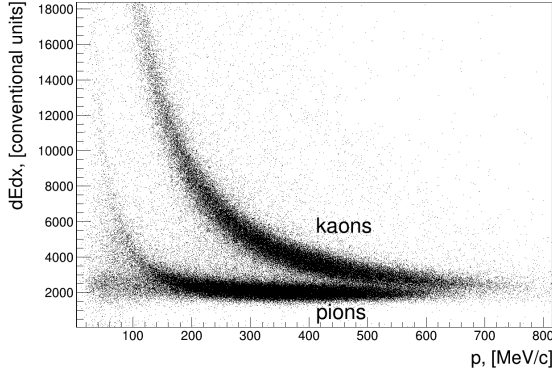


Fig. 4: The dE/dx_{DC} versus particle momentum distribution for the events of the process $K^+K^-\pi^+\pi^-$, selected in the experiment. All energy points from the reaction threshold up to 2 GeV are combined.

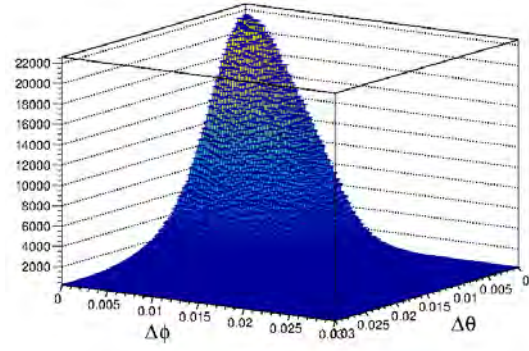


Fig. 5: The $|\delta\phi|$ vs $|\delta\theta|$ parameters distribution for the simulated charged kaons with the momenta, uniformly distributed from 0.04 to 1.0 GeV/c.

2.2 dE/dx_{LXe} vs dE/dx_{DC} : general considerations

Distributions of the dE/dx_{LXe} in seven LXe double layers depending on the particle momentum in the DC for the simulated single electrons, muons, charged pions and kaons are shown in Figs 6–7. The following are the most important DC-LXe differences:

- since the particle is inhibited in the layers of calorimeter, dE/dx_{LXe} on average increases layer by layer (see Fig. 8);
- due to dead material in front of LXe calorimeter, and since the procedure of LXe-track reconstruction requires at least 4 strips "hits", there are different momentum thresholds p_{thr} for (anti)protons, kaons, pions, muons and electrons, below which the track in the LXe does not exist or cannot be reconstructed (e.g. for kaons $p_{thr}^K \sim 300 - 350$ MeV/c (see Fig. 6));
- the values of p_{thr} , as well as the distributions of dE/dx_{LXe} in each layer, depend on the parameter $d = 1/\sin(\alpha_{pen})$, which characterizes the dependence of the distance passed by the particle in the dead matter and liquid Xenon on the penetration angle α_{pen} of the particle to the LXe;
- in the LXe the kaon and pion interactions with nuclei play important roles. Since the simulation of such interactions can be unreliable, the careful study of the Monte Carlo-experiment differences is required.

2.3 General idea of the particle identification procedure

The idea of the particle identification procedure presented here is the following: for each DC-track, for which the corresponding LXe-track was found, one calculates 10 values of the responses $Resp$ of some multivariate classifier (taken from TMVA package [8]), trained for the separation of the corresponding pairs of particles in the particular momentum p and d parameter ranges δp_i and δd_j (see Table 1). For the training of the classifiers we simulate $4 \cdot 10^6$ events with single e^\pm , μ^\pm , π^\pm , K^\pm , p^\pm , having the momentum and d parameter uniformly distributed in the ranges from 0.04 GeV to 1.1 GeV and from 1.0 to 1.4 correspondingly. Currently we use uniform partitions $\delta p_i = 20$ MeV/c and $\delta d_j = 0.1$ of the whole available ranges of these parameters, having 53×4 cells in total.

2.4 The most powerful classifier

Since the K/π separation for 450 MeV/c $< p < 900$ MeV/c is very demanding, the most powerful classifier from about 40 classification methods, proposed by the TMVA package is chosen. $4 \cdot 10^4$ simu-

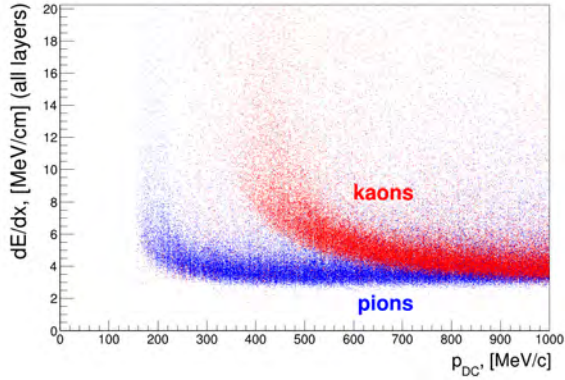


Fig. 6: dE/dx_{LXe} in each of the 7 layers vs particle momentum in the DC for the simulated charged kaons and pions, with the momenta uniformly distributed from 0.04 to 1.0 GeV/c.

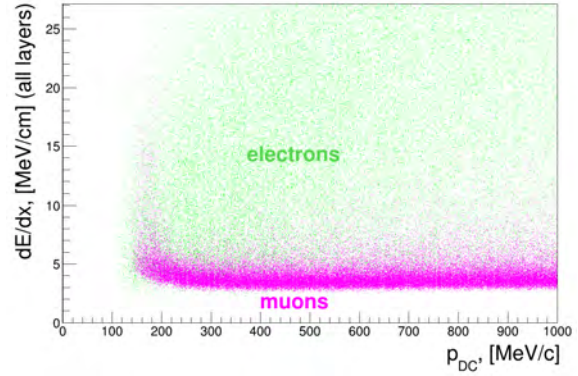


Fig. 7: dE/dx_{LXe} in each of the 7 layers vs particle momentum in the DC for the simulated charged muons and electrons, with the momenta uniformly distributed from 0.04 to 1.0 GeV/c.

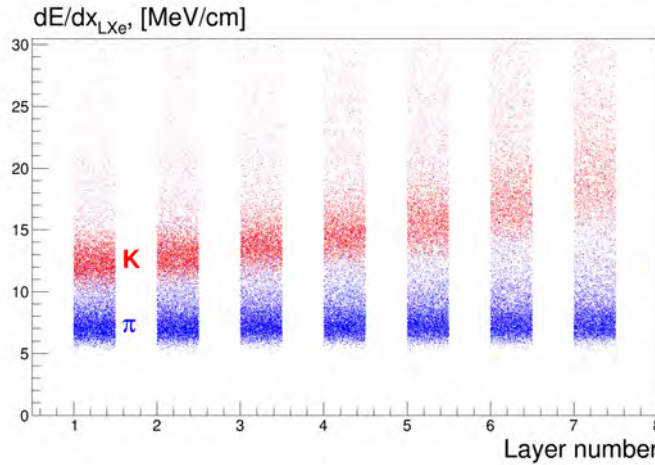


Fig. 8: dE/dx_{LXe} in 7 layers for the simulated charged kaons and pions with the momenta in range from 0.475 to 0.5 GeV/c.

lated kaons and pions are used for training and testing different classifiers, using as the input variables 7 dE/dx_{LXe} values, dE/dx_{DC} , E_{LXe} and E_{CSI} . In Fig. 9 the dependence of the background rejection efficiency on the signal selection efficiency (so-called ROC-curve) is shown for the different classification methods. It is evident, that the globally most powerful method (at default classifiers settings) is BDT (Boosted Decision Trees). In addition, BDT, compared to different implementations of projective likelihood estimation (PDE) and multi-layer perceptron (MLP), is trained faster. In Fig. 10 one can see the ROC-curves for K/π separation using BDT for different particle momentum ranges from 300 MeV/c to 900 MeV/c.

2.5 Example: selection of $e^+e^- \rightarrow K^+K^-$ events for $\sqrt{s} \in \{1.8 \text{ GeV}; 2.0 \text{ GeV}\}$

The operation of the described PID procedure can be illustrated by a simple example: the extraction of the events of the $e^+e^- \rightarrow K^+K^-$ process in the c.m. energy range from 1.8 to 2.0 GeV. This selection is performed in the experiment on the basis of 11 pb^{-1} of integrated luminosity, collected by CMD-3 at 18 c.m. energy points in 2011-2012. The events of signal and the major background processes ($e^+e^- \rightarrow \pi^+\pi^-$, $\mu^+\mu^-$, e^+e^-) at the same c.m. energy points are simulated.

Table 1: The responses of the multivariate classifiers, trained for the separation of the different pairs of particles in the δp_i and δd_j cell.

	e^\pm	μ^\pm	π^\pm	K^\pm
μ^\pm	$Resp_{i,j}(\mu^\pm/e^\pm)$	-	-	-
π^\pm	$Resp_{i,j}(\pi^\pm/e^\pm)$	$Resp_{i,j}(\pi^\pm/\mu^\pm)$	-	-
K^\pm	$Resp_{i,j}(K^\pm/e^\pm)$	$Resp_{i,j}(K^\pm/\mu^\pm)$	$Resp_{i,j}(K^\pm/\pi^\pm)$	-
p^\pm	$Resp_{i,j}(p^\pm/e^\pm)$	$Resp_{i,j}(p^\pm/\mu^\pm)$	$Resp_{i,j}(p^\pm/\pi^\pm)$	$Resp_{i,j}(p^\pm/K^\pm)$

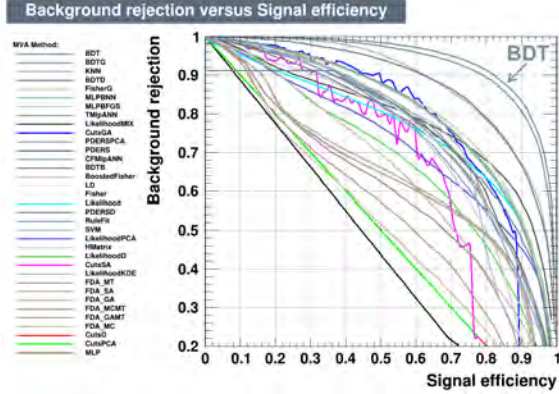


Fig. 9: The ROC-curves for K/π separation at the momenta 870 MeV/c for different classification methods trained and tested.

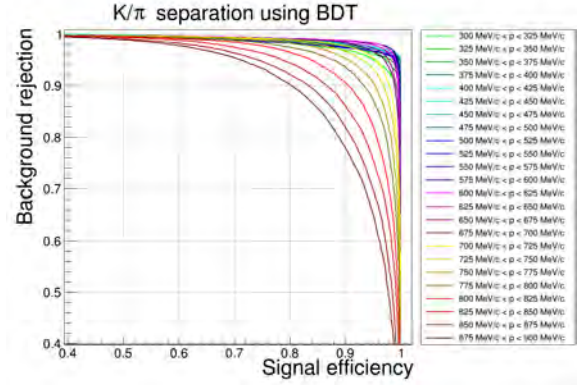


Fig. 10: The BDT ROC-curves for the K/π separation in the different momentum ranges from 300 MeV/c to 900 MeV/c.

First of all, in the experiment and simulation events having two oppositely charged DC-tracks with polar angles $\theta_{DC}^{1,2} \in (1.0; \pi - 1.0)$ and satisfying the conditions of collinearity $|\theta_{DC}^1 + \theta_{DC}^2 - \pi| < 0.25$ and $|\phi_{DC}^1 - \phi_{DC}^2| - \pi| < 0.15$ are selected. Further, Figs. 11a–11c show the sum over all c.m. energy point distributions of the average of the positively and negatively charged particles BDT response for the simulated events of signal and the major background processes.

The distribution of the average energy deposition of the charged particles in the calorimeter vs the parameter $\Delta E \equiv \sqrt{\vec{p}_{K^+}^2 + m_K^2} + \sqrt{\vec{p}_{K^-}^2 + m_K^2} - 2E_{\text{beam}}$ in the experiment and simulation is shown in Fig. 12a. In addition to the clusters of K^+K^- , $\pi^+\pi^-$, $\mu^+\mu^-$, e^+e^- final states the horizontal band of cosmic muons is visible. Small dislocations, indicated by arrows, are caused by the tracks passing through the endcap BGO-calorimeter before arriving at the LXe. The long tails to the left of K^+K^- and $\pi^+\pi^-$ clusters are caused by the initial state radiation. To suppress the contribution of the e^+e^- final state, the selection criteria on the averaged BDT response $(BDT_{K^+/e^+} + BDT_{K^-/e^-})/2 > 0.2$ (see Fig. 11a) are used. As a result the e^+e^- cluster is almost completely disappeared (see Fig. 12b). Further, to suppress the $\mu^+\mu^-$ background, $(BDT_{K^+/\mu^+} + BDT_{K^-/\mu^-})/2 > 0.1$ (see Fig. 11b) is required. As result the contribution of $e^+e^- \rightarrow \mu^+\mu^-$ process, as well as the background from the cosmic muons are significantly suppressed (see Fig. 12c). Finally, to suppress the $\pi^+\pi^-$ background $(BDT_{K^+/\pi^+} + BDT_{K^-/\pi^-})/2 > 0.05$ (see Fig. 11c) is required, and as a result we obtain an almost background-free sample of K^+K^- events (see Fig. 12d).

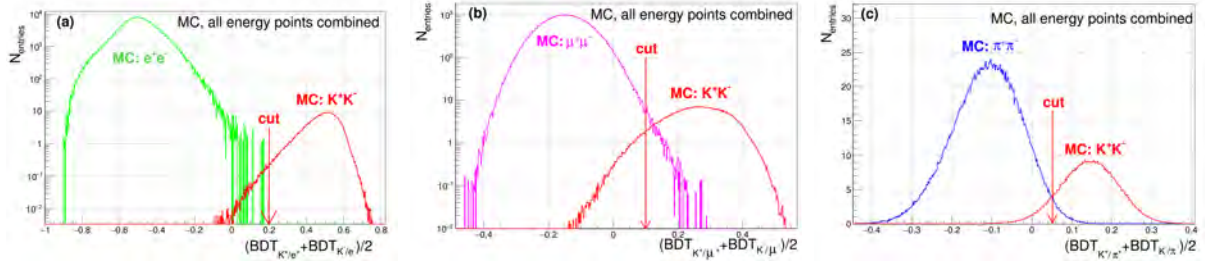


Fig. 11: The distributions of the averaged over the positively and negatively charged particles BDT response for the simulated events of signal and $e^+e^- \rightarrow e^+e^-$ (left), $e^+e^- \rightarrow \mu^+\mu^-$ (middle), $e^+e^- \rightarrow \pi^+\pi^-$ (right) processes. All c.m. energy points are combined. The number of events in each histogram bin is the expected number of events in this bin, in accordance with the luminosity, process cross section and detection efficiency.

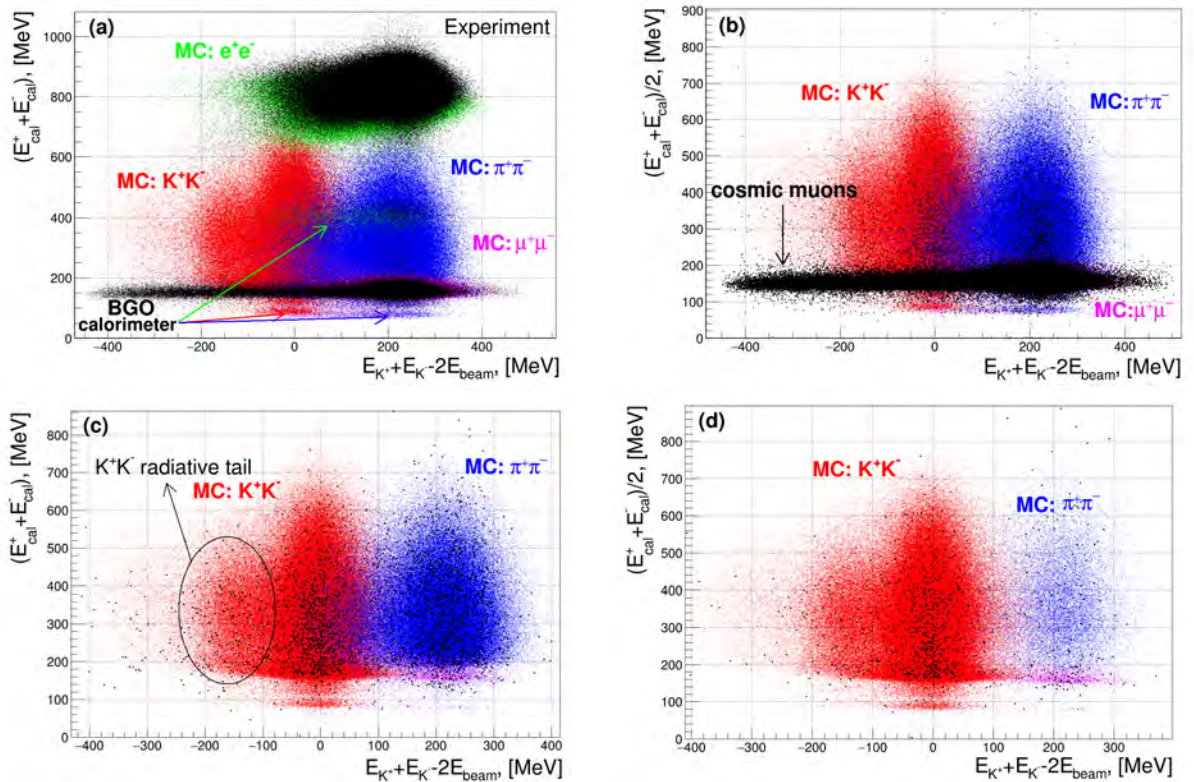


Fig. 12: The distribution of the average energy deposition of the charged particles in the calorimeter vs the ΔE parameter in the experiment and simulation before background suppression (a), after e^+e^- background suppression (b), after e^+e^- , $\mu^+\mu^-$ and cosmic backgrounds suppression (c), after e^+e^- , $\mu^+\mu^-$, cosmic and $\pi^+\pi^-$ backgrounds suppression (d).

3 Plans

Plans for the near future are the following:

1. To allow participation in the PID procedure for the DC-tracks, for which the corresponding LXe-track does not exist or was not reconstructed (which is typical for kaons and (anti)protons at $p < p_{\text{thr}}^{K, p^\mp}$);
2. To study the Monte Carlo-experiment differences, especially in the efficiency of LXe-tracks reconstruction:

- for e^\pm - on the base of the events of BhaBha scattering;
- for μ^\pm - on the base of cosmic muons;
- for π^\pm - on the base of a pure π^\pm sample from the $2\pi^+2\pi^-$ final state;
- for K^\pm - on the base of a pure K^\pm sample from the $K^+K^-\pi^+\pi^-$ final state;
- for p^\pm - on the base of p^+p^- events at low momenta and on the base of protons, ejected from the residual gas at high momenta;

3. To add the response of the muon veto system as a classifier input variable.

4 Conclusion

In this paper the currently being developed charged particle identification procedure for CMD-3 detector was described. The procedure uses, among other input, the information about the specific energy losses of charged particles in the layers of the liquid Xenon calorimeter. Particle identification is based on the responses of 10 multivariate classifiers, trained for the optimal separation of the different types of particles. About 40 different classification methods, provided by TMVA package, were trained and tested, and the most powerful and fast of them was found to be BDT method. The efficiency of the described procedure was demonstrated by an example of the extraction of events of the $e^+e^- \rightarrow K^+K^-$ process in the c.m. energy range from 1.8 to 2.0 GeV.

Acknowledgements

We wish to thank the VEPP-2000 personnel for the excellent machine operation. This work is supported in part by the Russian Education and Science Ministry (grant No. 14.610.21.0002, identification number RFMEFI61014X0002), by the Russian Foundation for Basic Research grants RFBR 13-02-00991-a, RFBR 13-02-00215-a, RFBR 12-02-01032-a, RFBR 13-02-01134-a, RFBR14-02-00580-a, RFBR 14-02-31275-mol- a, RFBR 14-02-00047-a, RFBR 14-02-31478-mol-a, RFBR 14-02-91332, RFBR 15-02-05674-a and the DFG grant HA 1457/9-1.

References

- [1] I. Koop *et al.*, Nucl. Phys. B, Proc. Suppl. **181**, 371 (2008).
- [2] M. N. Achasov *et al.*, Nucl. Instrum. Meth. **A598**, 31 (2009).
- [3] B. I. Khazin *et al.*, Nucl. Phys. B, Proc. Suppl. **181-182**, 376 (2008).
- [4] K. Hagiwara, R. Liao, A.D. Martin, D. Nomura, T. Teubner, J. Phys. G **38**, 085003 (2011).
- [5] M. Davier, A. Hoecker, B. Malaescu, and Z. Zhang, Eur. Phys. J. C **71**, 1515 (2011); Eur. Phys. J. C **72**, 1874 (2012).
- [6] V. E. Shebalin *et al.*, JINST **9** no.10, C10013 (2014).
- [7] D.N. Shemyakin *et al.*, Phys. Lett. B **756**, 153-160 (2016).
- [8] A. Hoecker, P. Speckmayer, J. Stelzer, J. Therhaag, E. von Toerne, and H. Voss, PoS A CAT 040 (2007).

The CMD-3 Data Acquisition System

*A.N.Kozyrev^{a,b,c}, V.M.Aulchenko^{a,b}, L.B.Epshteyn^{a,c}, D.A.Epifanov^a, I.B. Logashenko^{a,b},
K.Yu.Mikhailov^{a,b}, A.S.Popov^{a,b}, A.A.Ruban^a, A.N.Selivanov^a, A.A.Talyshev^{a,b}, V.M.Titov^a, Y.V.Yudin^a*

^a Budker Institute of Nuclear Physics, SB RAS,

Novosibirsk, 630090, Russia

^b Novosibirsk State University,

Novosibirsk, 630090, Russia

^c Novosibirsk State Technical University,

Novosibirsk, 630073, Russia

Abstract

The specialized data acquisition system designed for CMD-3 detector is presented at the electron-positron collider VEPP-2000 to the Budker Institute of Nuclear Physics, Novosibirsk, Russia. The structure of electronic hardware and firmware is described.

Keywords

Data acquisition; signal processing; fast electronics; trigger; digitizer.

1 Introduction

The electron-positron collider VEPP-2000 [1] is installed at the Budker Institute of Nuclear Physics (Novosibirsk, Russia). The design parameters of the VEPP-2000 collider are the following: the center-of-mass (c.m.) energy covers from 0.3 GeV up to 2 GeV. The peak luminosity is $10^{32} \text{ cm}^{-2} \text{ s}^{-1}$ at c.m. energy of 2 GeV. Two detectors SND[2] and CMD-3[3,4] are installed at the interaction regions of the collider. One of the goals of experiments at VEPP-2000 is the study of electron-positron annihilation into hadrons at the available energies. In particular, the precise measurement of cross sections of electron-positron annihilation into hadrons is extremely important for calculating the contribution of hadron polarization of vacuum to the anomalous magnetic moment of the muon [5].

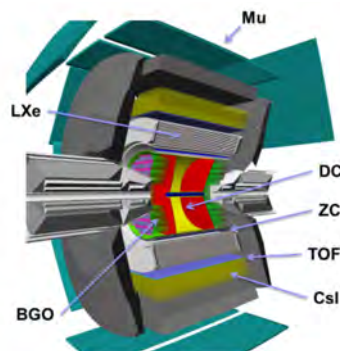


Fig. 1: The CMD-3 detector

The CMD-3 (Cryogenic Magnetic Detector) is a general-purpose detector shown in Fig. 1. The detector includes a magnetic spectrometer and an electromagnetic calorimeter. The magnetic spectrometer consists of the cylindrical drift chamber (DC) and the two layer multiwire proportional chamber (ZC), placed outside the DC. Coordinates, angles and momentum of charged particles are measured by the DC of a hexagonal wire structure. The ZC provides measurement of the Z coordinate of the track with an accuracy of about 0.5 mm. The magnetic spectrometer is immersed in a magnetic

field produced by a thin superconducting solenoid, placed between the DC and barrel the calorimeter [6]. The average field strength is 1.3 T.

The energy deposition of particles is measured by the electromagnetic calorimeter. The electromagnetic calorimeter is divided in the three path liquid Xenon-based internal barrel, outer CsI crystal based barrel and the $\text{Bi}_4\text{Ge}_3\text{O}_{12}$ (BGO) crystal based endcap calorimeter. The detector also includes the time-of-flight (TOF) counters, placed between two barrel calorimeters, and the muon range system (Mu system), placed outside the magnet yoke.

The CMD-3 is equipped with a data acquisition (DAQ) system specially developed for the experiments. The DAQ system of the CMD-3 detector solves several problems simultaneously: data acquisition and transfer to first-level trigger systems, generation of synchronization signals for time meters, triggering of measurements, collection of digitized data, interaction with accelerator facility, calibration of coefficients and efficiency, and monitoring of the status. The CMD-3 DAQ capacity is to process some 12k channels with mean trigger rates up to 1kHz thus producing about 3.8Gbps data rate. Here the structure of the electronic hardware and firmware of the CMD-3 DAQ is described.

2 The CMD-3 DAQ system

The overview picture of the CMD-3 DAQ electronics is shown in Fig. 2. The analog signals from the detector subsystems are amplified and shaped in the front-end electronics. Then it goes into the trigger electronics, which is organized as a pipeline and makes decisions at the collision rate (each 80 ns). If the first level trigger takes a positive decision the digitized data from digitizing electronics are readout by the DAQ.

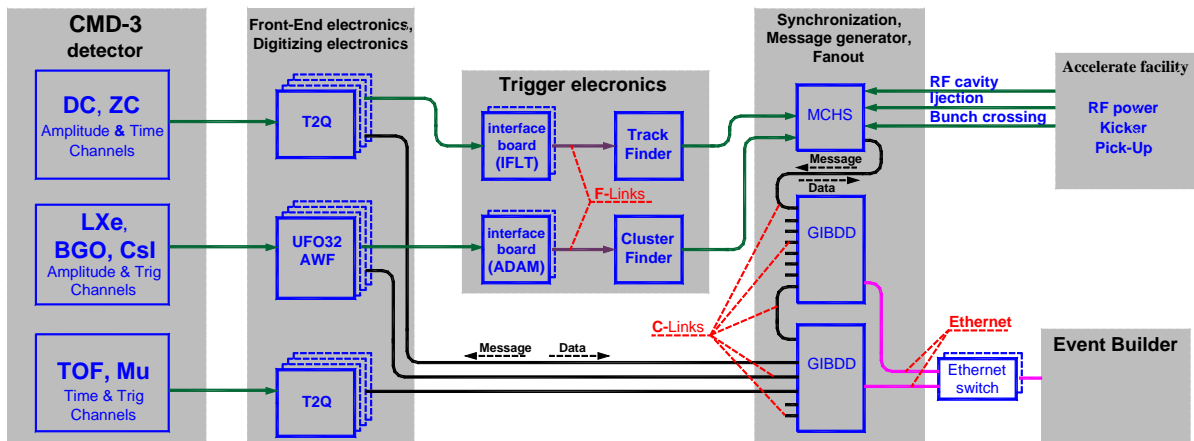


Fig. 2: The CMD-3 data acquisition electronics layout

The MCHS board (“Master Chronopher System board”) receives information from the first level trigger, resynchronizes it with the RF cavity frequency because it is the source with lowest possible jitter and the highest stability to the bunch position. Then the MCHS initiates the transaction with a command to start measurements which fanout to each digitizer of the CMD-3 DAQ via a C-Link, which is described in detail below. It is a special interface for synchronization and the data transport in the CMD-3 DAQ system. The fanout is provided by the General Interface Board for Data Delivery (GIBDD). Each digitizer sends data back to the GIBDD. Here these data are buffered in memory, packed and transmitted with a local Ethernet network to the Event Builder. Each GIBDD board can be connected by C-Links to up to 30 boards. To increase the number of C-Links GIBDD boards can be cascaded.

The first-level trigger system consists of interface boards (interface of first level trigger (IFLT), adder discriminator adder module (ADAM)) that prepare arguments for Finders (track and cluster

finders, see Fig. 2). The arguments are transferred from interface boards to Finders via an F-Link (Fast-Link). It is a serial line of data transfer with a rate of 375 Mbit/s. The operation of the triggering electronics is based on the pipeline algorithm of data processing.

The digitizing electronics is presented by three unified families of boards (referred as T2Q, UFO32 and AWF) designed for different types of measurements. Each family has several modifications unified in terms of the base of elements, basic internal architecture solutions, and overall design. More details about CMD-3 electronics can be found in the article “The CMD-3 TOMA DAQ Infrastructure” [7].

3 The CMD-3 C-Link

A unified approach for the data transport and synchronization was used during the development of the CMD-3 DAQ. A special interface has been developed, referred to as C-Link. The unified requirement on the data transport allows using a single method for different tasks, such as physical data and scaler data readout or digitizer status control. So each link transaction is associated with an event. If an event occurs the transaction starts. And the end of the transaction terminates the current event.

The C-Link provides message transport to the boards and data gathering from the boards. On physical level it is low voltage differential signal (LVDS) based two twisted pairs serial bus, which allows low electromagnetic interference (EMI), low power and low cost. The basic parameters of the C-Link for CMD-3 are listed in Table 1.

Tab 1: Technical parameters of C-Link

Modulation	Two levels: log.0 = high, log.1 = low
Data transfer rate	25 Mbit/s (50 and 100 Mbit/s also possible)
Voltage levels	LVDS, 4 mA, as in the IEEE1394 standard
Transfer environment	Two twisted pairs
Electrical connector	USB, type A

The clock signal is always transferred through one twisted pair from the transmitter (Down-Link) to the receiver (Up-Link). This is a meander whose frequency is 25 MHz. It is used for synchronization of time meters rather than for synchronization of data. The data are transferred through the second twisted pair. No special interface hardware is used – the signals are transmitted and readout directly by the C-Link. The logical part of the C-Link is FPGA-based.

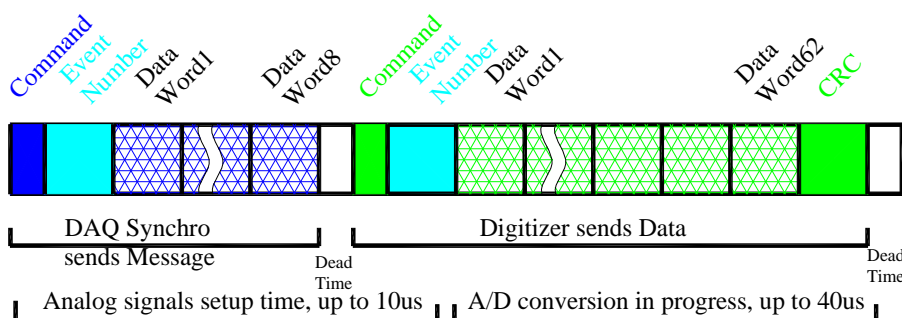


Fig. 3: C-Link transaction format

The C-Link is designed for asymmetric traffic (see Fig. 3). This means that in response to a short C-Link command a large amount of data is returned. The exchange between the transmitter and receiver occurs in two phases. The first phase of transaction sends a command, event number and eight data words from the DAQ to the digitizer. The second phase of transaction returns status and data from the digitizer to the DAQ.

4 The CMD3 “Skeletal” project for the board’s unification

During the DAQ system development, particular attention was paid to the unification of the internal block structure of the electronic boards. For this purpose, a special “Skeletal” project was developed for a field programmable gate array (FPGA). The internal structure of the “Skeletal” project is shown in Fig. 4.

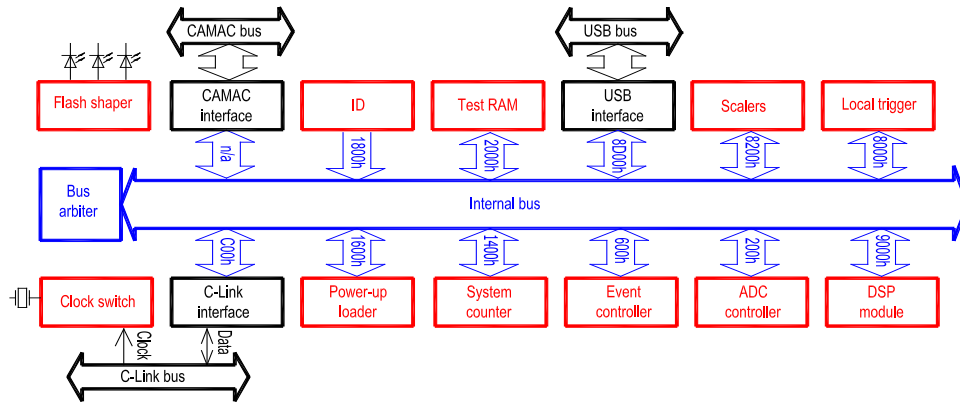


Fig. 4: The “Skeletal” project structure

The main goal of the “Skeletal” project development is to use the same solutions in different devices and their versions. The project is a set modules, possessing unified interfaces and common methods of their implementation.

The hardware part of the project is described in the form of isolated modules aimed at solving particular problems performed by the electronic devices. The basis of the “Skeletal” project is the internal bus and the bus arbiter module. All modules are connected to the internal bus of the project in a standard manner, which simplifies the connection of new modules and their arrangement in the address space. This bus has a 16-bit width both for data and for addresses of the modules connected to it. The rectangles in Fig. 4 show the service modules implemented in most electronic boards of the CMD-3 DAQ system.

Three types of modules are available on the bus: master, slave and arbiter modules (see Fig. 5). The master module can request access to the bus. The slave module supports data transfer only. The arbiter module can initiates the bus cycle, provides the bus for the data transfer and prevents conflicts by building a request queue.

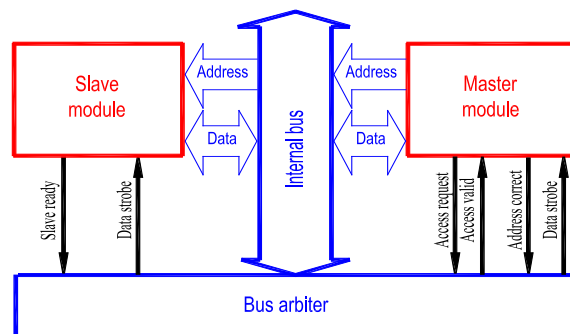


Fig. 5: Bus access control

The access cycle time can vary due to the response of the slave module, so a handshake mechanism is used. It is based on the readiness acknowledgement signal. In Fig. 6 the sequence of the bus states during the data exchange cycle is shown.

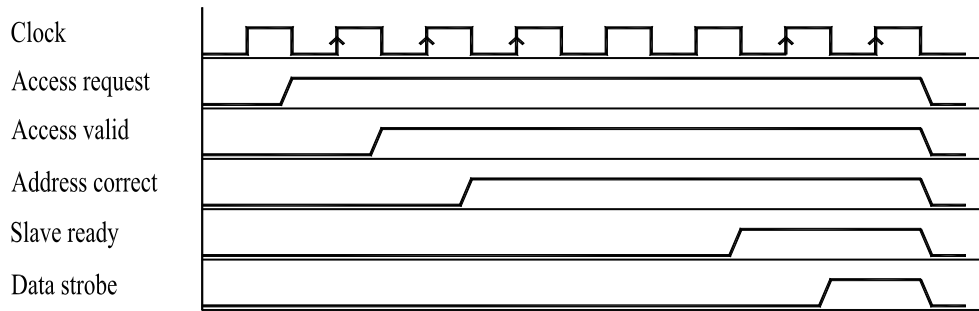


Fig. 6: The access cycle to the internal bus

To perform a data exchange the master module activates the signal "access request". This signal goes to the bus arbiter. If several requests arrive simultaneously, the arbiter uses the priority diagram to choose which master module request will be processed first. The arbiter returns the "access valid" signal to the selected master module. The master module sets the address of the slave module to the internal bus and sends the "address correct" signal. The slave module decodes this address. It sets the acknowledgement signal "slave ready" if the address is identified. This signal is transferred to the arbiter. In response, the arbiter sets the "data strobe" signal for one period of the clock generator. The slave module takes the data by this signal. The "data strobe" signal finishes the cycle of exchange on the internal bus. After that, the next cycle of exchange on the internal bus can be started. If none of the slave modules responds, the cycle is terminated after the timeout period, and the arbiter sets the error signal.

5 Performance example

One of the parts of the CMD-3 detector tracking system is the drift chamber [8]. It has uniform structure of hexagonal cells with size of about 0.9 cm. The charge division technique is used to measure hit coordinates along the wire. The maximal drift time at the nominal high voltage value and magnetic field of 1.3 T is 650 ns. To process DC signals a special digitizing board (T2Q) was designed and produced. Each T2Q board allows to measure two amplitudes and one time from 16 independent cells in the DC. The spatial resolution of the CMD-3 detector drift chamber is shown in Fig. 7.

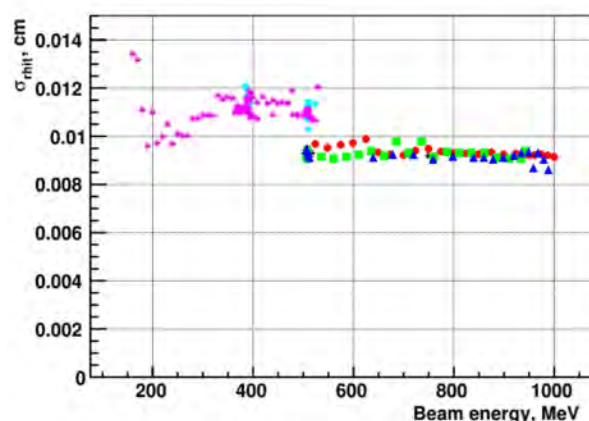


Fig. 7: The spatial resolution of the CMD-3 Drift Chamber

The average time resolution is less than 100 μm which corresponds to the DC project parameters. So the CMD-3 DAQ system does not limit the time resolution of the detector subsystem.

6 Conclusion

The CMD-3 detector has been collecting experimental information for a few years. During experimental runs design parameters of the DAQ system were achieved, the system demonstrated good performance and stability. All electronic blocks were designed and produced by experts at BINP. The electronics for each physical subsystem of CMD-3 have reached the target parameters. All data transfer rate requirements have been met. The CMD-3 DAQ system does not limit the time resolution of the detector subsystem. At the moment about 300 electronic blocks are in operation in the CMD-3 DAQ. The CMD3 DAQ can be scaled to the DAQ for a super c-tau factory.

Acknowledgements

This work is supported in part by the Russian Science Foundation (project No. 14-50-00080), by the Russian Foundation for Basic Research grants RFBR 13-02-00991-a, RFBR 13-02-00215-a, RFBR 12-02-01032-a, RFBR 13-02-01134-a, RFBR14-02-00580-a, RFBR 14-02-31275-mol-a, RFBR 14-02-00047-a, RFBR 14-02-31478-mol-a, RFBR 14-02-91332, RFBR 15-02-05674-a.

References

- [1] D. Berkaev, et al., *Nucl. Phys. Proc. Suppl.* **225-227** (2012) 303.
- [2] M. N. Achasov et al., *Nucl. Instr. and Meth.* **A598** (2009) 31.
- [3] G.V. Fedotovitch, et al., *Nucl. Phys. Proc. Suppl.* **162** (2006) 332.
- [4] B. I. Khazin et al., *Nucl. Phys. B, Proc. Suppl.* **181-182** (2008) 376.
- [5] G. W. Bennett, et al., Muon G-2 Collaboration. Final Report of the Muon E821 Anomalous Magnetic Moment Measurement at BNL, *Phys. Rev. D* **73** (2006).072003.
- [6] K. Yu. Mikhailov, et al., *Nucl. Instr. and Meth.* **A732** (2013) 463.
- [7] A. N. Kozyrev, et al., The CMD-3 TOMA DAQ Infrastructure, *J. Instrum.* **9** (2014) C10016.
- [8] F. Grancagnolo, et al., *Nucl. Instr. and Meth.* **A623** (2010) 114.

Study of the Conversion Decays of Omega Meson to π^0 Meson and e^+e^- Pair Using the CMD-3 Detector

R.R. Akhmetshin, A.N. Amirkhanov, A.V. Anisenkov, V.M. Aulchenko, V.S. Banzarov, N.S. Bashtovoy, A.E. Bondar, A.V. Bragin, S.I. Eidelman, D.A. Epifanov, L.B. Epshteyn, A.L. Erofeev, G.V. Fedotov, S.E. Gayazov, A.A. Grebenuk, S.S. Gribanov, D.N. Grigoriev, F.V. Ignatov, V.L. Ivanov, S.V. Karpov, V.F. Kazanin, O.A. Kovalenko, A.A. Korobov, A.N. Kozyrev, E.A. Kozyrev, P.P. Krovovny, A.E. Kuzmenko, A.S. Kuzmin, I.B. Logashenko, P.A. Lukin, K.Y. Mikhailov, V.S. Okhapkin, Y.N. Pestov, A.S. Popov, G.P. Razuvaev, A.A. Ruban, N.M. Ryskulov, A.E. Ryzhenkov, V.E. Shebalin, D.N. Shemyakin, B.A. Shwartz, A.L. Sibidanov, E.P. Solodov, V.M. Titov, A.A. Talyshev, A.I. Vorobiov, and Y.V. Yudin*
Budker Institute of Nuclear Physics, Novosibirsk, Russia

Abstract

The conversion decay $\omega \rightarrow \pi^0 e^+ e^-$ was studied in the centre-of-mass energy range 760–840 MeV using about 8 pb^{-1} of data collected with the CMD-3 detector at the VEPP-2000 e^+e^- collider in Novosibirsk. The visible cross-section of the process $\omega \rightarrow \pi^0 e^+ e^-$ was measured. The current status of the analysis is presented.

Keywords

Conversion decay; close tracks; vertex.

1 Introduction

The interest in the decay $\omega \rightarrow \pi^0 e^+ e^-$ is related to the transition form factors of the ω meson that can be measured in this decay [1]. The precise value of the decay branching ratio can be useful for interpretation of experiments on quark–gluon plasma [2, 3]. This analysis is based on 8 pb^{-1} of data, which were collected in the centre-of-mass energy range 760–840 MeV by the CMD-3 detector. This data sample is twice as large as the sample previously used at the former CMD-2 detector.

The general purpose detector CMD-3 has been described in detail elsewhere [4]. The tracking system consists of the cylindrical drift chamber and double-layer multiwire proportional Z-chamber, both also used for the trigger. The tracking system is placed inside a thin superconducting solenoid with a field of 1.3 T. Electromagnetic calorimeters are placed outside the solenoid: a LXe barrel calorimeter with a thickness of $5.4X_0$ and CsI crystals with a thickness of $8.1X_0$. An endcap calorimeter is made of BGO scintillation crystals, with a thickness of $13.4X_0$.

2 Data analysis

The decay $\omega \rightarrow \pi^0 e^+ e^-$ has been studied using the π^0 dominant decay mode $\pi^0 \rightarrow \gamma\gamma$. It corresponds to a final state with two opposite charge particles and two photons. One of the significant resonant backgrounds comes from the $\omega \rightarrow \pi^+ \pi^- \pi^0$ decay, which has the same topology as the final state and more than three orders of magnitude larger probability. Another source of resonant background is the $\omega \rightarrow \pi^0 \gamma$ decay, followed by the Dalitz decay of the π^0 or γ -quantum conversion in the material in front of the drift chamber. The non-resonant background includes contributions from the following quantum electrodynamics (QED) processes with the same final state topology: $e^+e^- \rightarrow e^+e^- \gamma\gamma$, $e^+e^- \rightarrow 3\gamma$ followed by γ -quantum conversions, $e^+e^- \rightarrow e^+e^- \gamma$ with one background photon as well as a two-quantum annihilation followed by a γ -quantum conversion and one background photon in the calorimeters.

To select events of the process under study, we used the following criteria.

*Corresponding author.

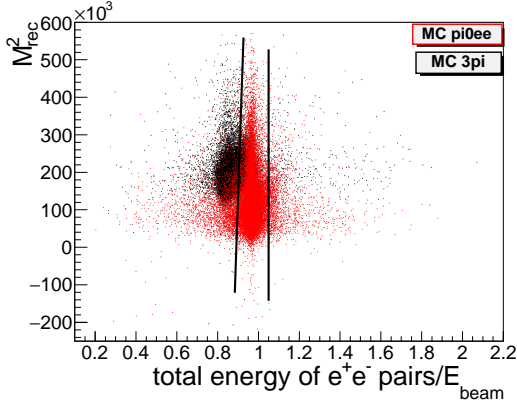


Fig. 1: Recoil mass of photon pairs versus total energy of electron–positron pairs, normalized to beam energy for Monte Carlo simulation of $\pi^0 e^+ e^-$ (red dots) and $\pi^+ \pi^- \pi^0$ (black dots). Black line shows selection cut.

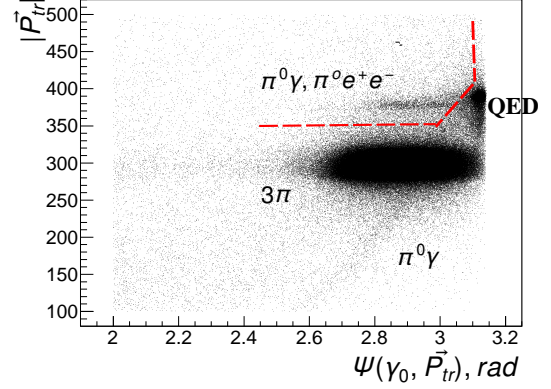


Fig. 2: Total momentum of charged particles P_{tr} versus angle between the most energetic photon and P_{tr} . The red line presents the selection cut.

- $N_\gamma \geq 2$ with energy $40 \text{ MeV} < E_{\gamma \max 0,1} < 2 \cdot E_{\text{beam}}$ to suppress background photons in the calorimeters.
- The impact parameter of the tracks $\rho < 1 \text{ cm}$ and the Z -coordinate of the vertex $|Z_{\text{vert}}| < 5 \text{ cm}$ to reject cosmic rays and beam background events.
- Two ‘good’ tracks in the drift chamber (with transverse moment $P_{1,2}^{\text{tr}} > 40 \text{ MeV}/c$ and with polar angle $0.9 < \Theta_{1,2} < \pi - 0.9$).
- The opening angle between tracks $\Delta\psi < 1 \text{ rad}$ to suppress events of the $\omega \rightarrow \pi^+ \pi^- \pi^0$ decay.
- Noncollinear tracks in the R – ϕ projection $|\pi - |\phi_1 - \phi_2|| > 0.15$.
- The angle between the total momentum of the tracks and each photon is greater than 1.5 rad to suppress QED events.
- The angle between photons is less than 1.6 rad to suppress events from the decay $\omega \rightarrow \pi^0 \gamma$.
- The recoil mass of photon pairs, where it is understood that they originated from the π^0 decay $M_{\text{rec}}^2 = (2 \cdot E_{\text{beam}})^2 - 4E_{\text{beam}}E_{\pi^0} + m_{\pi^0}^2$, where $E_{\pi^0} = E_{\gamma,1} + E_{\gamma,2}$, and $E_{\gamma,i}$ is the energy of photon i in the calorimeter. The recoil mass of photon pairs is shown in Fig. 1. The black line in Fig. 1 presents the selection cut.
- The dependence of the total momentum of charged particles (P_{tr}) from the angle between the most energetic photon and P_{tr} is used to suppress $\omega \rightarrow \pi^+ \pi^- \pi^0$ events as well as $\omega \rightarrow \pi^0 \gamma$ events followed by the Dalitz decay of π^0 . The red line in Fig. 2 is used for selection.
- The invariant mass of the electron–positron pair and the most energetic photon $M_{\text{inv}}(e^+ e^- \gamma_{\max 0})$ is less than $1.9 \cdot E_{\text{beam}}$ to suppress $e^+ e^- \rightarrow \gamma \gamma$ events followed by the conversion of the γ .

3 Separation of $\pi^0 e^+ e^-$ and $\pi^0 \gamma$ (with γ conversion on detector material)

The only difference between the $\pi^0 e^+ e^-$ and $\pi^0 \gamma$ with γ conversion on the detector material is that the vertex of tracks is shifted from the beam by 1.7–2 cm (vacuum tube) in the transverse plane. To analyse these events, we use $\gamma \gamma$ events, in which one γ is converted on the material. For separation, we use a neural network with input parameters:

- the angle between the tracks;
- The total momentum normalized to beam energy;

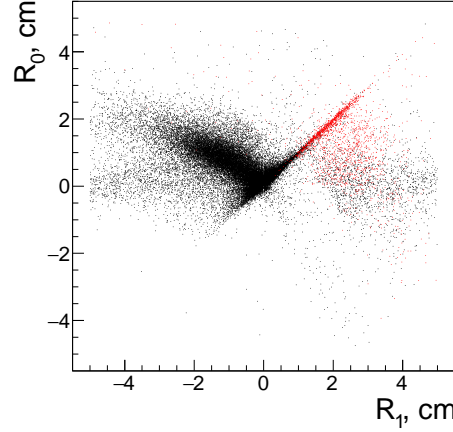


Fig. 3: Distance from beam point to first cross-point versus distance to second cross-point for Monte Carlo simulation of $\pi^0 e^+ e^-$ (black dots) and $\gamma\gamma$ with photon conversion on material (red dots).

- the track momentum normalized to beam energy;
- the distance from the vertex to the centre of the beam. The sign of the distance is ‘+’ when the angle between the beam point direction to a cross-point and the average momentum of the tracks is sharp and ‘-’ otherwise. In the transverse plane, circles from tracks have two cross-points: the first is the vertex and the second is additional. These parameters are shown in Fig. 3.

The output parameter of the neural network determines the event type (signal ($\pi^0 e^+ e^-$) or background (conversion γ on the detector material)). Using this option to separate the events, we achieved the following efficiency of suppression: for $\pi^0 \gamma$ – 84% (for $\gamma\gamma$ – 90%), while we lost 2% of signal events.

4 Reconstruction efficiency of close tracks

Since Monte Carlo simulation does not completely describe the experiment, a correction $\varepsilon_{\Delta\psi}$ for a difference between the reconstruction efficiencies of close tracks in simulation and experiment was included. Its value was obtained using events of $\omega \rightarrow \pi^+ \pi^- \pi^0$ decays followed by the conversion decay $\pi^0 \rightarrow e^+ e^- \gamma$ with a similar $\Delta\psi$ distribution. $\varepsilon_{\Delta\psi}$ is calculated by averaging the integral in Eq. (1) for simulation events ($\omega \rightarrow \pi^0 e^+ e^-$):

$$\varepsilon_{\Delta\psi} = \int \frac{\varepsilon_{\Delta\psi, \text{exp}}^-(P_{\perp}^-)}{\varepsilon_{\Delta\psi, \text{sim}}^-(P_{\perp}^-)} \cdot \frac{\varepsilon_{\Delta\psi, \text{exp}}^+(P_{\perp}^+)}{\varepsilon_{\Delta\psi, \text{sim}}^+(P_{\perp}^+)} f(P_{\perp}^-) f(P_{\perp}^+) dP_{\perp}^- dP_{\perp}^+, \quad (1)$$

where $\varepsilon_{\Delta\psi, \text{exp}}^-(P_{\perp}^-)$ is the efficiency of track reconstruction (P depending on the transverse momentum (for e^- or e^+ , and for simulation or experiment) (see Fig. 4):

$$\varepsilon_{\Delta\psi} = 0.970 \pm 0.008 \pm 0.020. \quad (2)$$

5 Results

The detection efficiency, $\varepsilon_{\text{det}}^{\pi^0 e^+ e^-} = 23\%$, was determined using Monte Carlo simulation based on the GEANT4 [5].

The number of signal and background events has been obtained from a fit of the $\gamma\gamma$ invariant mass distribution at each energy point. The signal was described by a two-Gauss function, the background shape was described by a Gauss function and a constant. The shapes of the signal and background curve

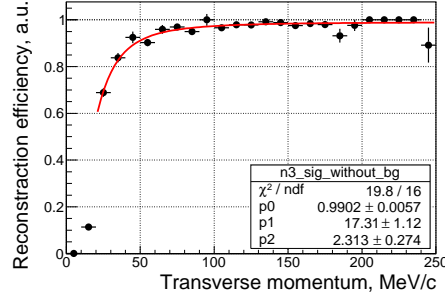


Fig. 4: Efficiency of track reconstruction versus transverse momentum for e^- for experimental data

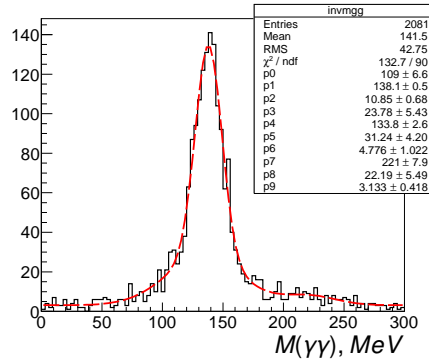


Fig. 5: Invariant mass of $\gamma\gamma$ for experimental data in energy range 760–840 MeV

Table 1: Results from current and other experiments

Experiment	$\text{Br}(\omega \rightarrow \pi^0 e^+ e^-)$	Events	Data, pb^{-1}
ND [6]	$(5.9 \pm 1.9) \cdot 10^{-4}$	43	
CMD-2 [7]	$(8.19 \pm 0.71 \pm 0.62) \cdot 10^{-4}$	230	3.3
SND [8]	$(7.61 \pm 0.53 \pm 0.64) \cdot 10^{-4}$	613	9.8
CMD-3 (preliminarily) ^a	$(8.81 \pm 0.35) \cdot 10^{-4}$ (stat.)	1380	8

^a The trigger efficiency and the contributions of $\omega \rightarrow \pi^+ \pi^- \pi^0$, $\omega \rightarrow \pi^0 \gamma$ were not taken into account.

were fixed from the fit of experimental data in the energy range 760–820 MeV (see Fig. 5), so the varying parameters at each energy point were the number of signal and background events. These values were used to determine the visible cross-section of the signal (see Fig. 6), using Eq. (3) and background events (see Fig. 7), using Eq. (4):

$$\sigma_{\text{vis}} = \frac{N_{\text{sig},i}}{L_i(1 + \delta_i) \cdot \varepsilon_{\text{det}} \cdot \varepsilon_{\Delta\psi} \cdot \text{Br}(\pi^0 \rightarrow \gamma\gamma)}, \quad (3)$$

$$\sigma_{\text{vis bg}} = \frac{N_{\text{bg},i}}{L_i \cdot \varepsilon_{\text{det}}}. \quad (4)$$

The current value of $\text{Br}(\omega \rightarrow \pi^0 e^+ e^-)$ (the trigger efficiency and the contributions of $\omega \rightarrow \pi^+ \pi^- \pi^0$, $\omega \rightarrow \pi^0 \gamma$ were not taken into account) obtained and the most important results from other experiments are presented in Table 1.

The study of the trigger efficiency, a test of the method of determining $\pi^0 \gamma / \pi^0 e^+ e^-$, and separa-

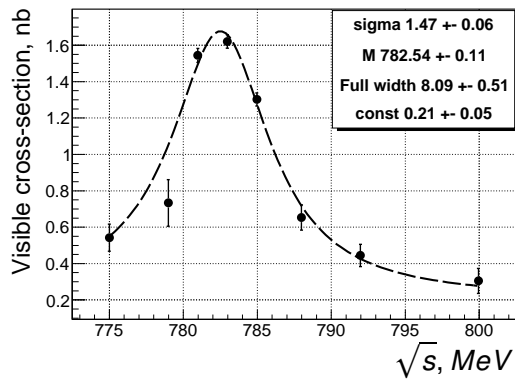


Fig. 6: Visible cross-section of signal process, fitted with Breit-Wigner distribution.

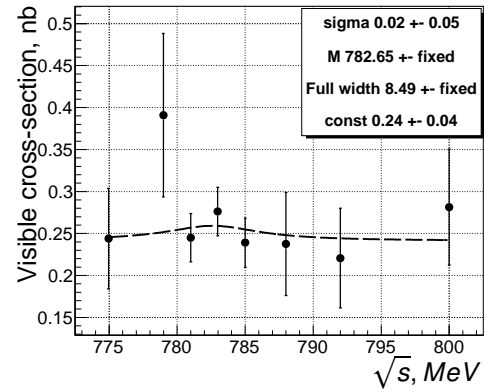


Fig. 7: Visible cross-section of background events, fitted with Breit-Wigner distribution.

tion using QED events and analysis of systematics are included in our plans for the future. We also plan to measure the transition form factor of the ω meson.

References

- [1] L. Landsberg, *Phys. Rep.* **128** (1985) 301. [https://doi.org/10.1016/0370-1573\(85\)90129-2](https://doi.org/10.1016/0370-1573(85)90129-2)
- [2] E.V. Shuryak, *Phys. Lett.* **B 78** (1978) 150. [https://doi.org/10.1016/0370-2693\(78\)90370-2](https://doi.org/10.1016/0370-2693(78)90370-2)
- [3] D. Adamova *et al.*, *Phys. Rev. Lett.* **91** (2003) 042301. <https://doi.org/10.1103/PhysRevLett.91.042301>
- [4] B.I. Khazin *et al.* (CMD-3 Collaboration), *Nucl. Phys. B Proc. Suppl.* **181–182** (2008) 376. <https://doi.org/10.1016/j.nuclphysbps.2008.09.068>
- [5] S. Agostinelli *et al.* (GEANT4 Collaboration), *Nucl. Instrum. Methods Phys. Res. A* **506** (2003) 250. [https://doi.org/10.1016/S0168-9002\(03\)01368-8](https://doi.org/10.1016/S0168-9002(03)01368-8)
- [6] S.I. Dolinsky *et al.*, *Sov. J. Nucl. Phys.* **48** (1988) 277.
- [7] R.R. Akhmetshin *et al.* (CMD-2 Collaboration), *Phys. Lett.* **B613** (2005) 29. <https://doi.org/10.1016/j.physletb.2005.03.019>
- [8] M.N. Achasov *et al.* (SND Collaboration), *J. Exp. Theor. Phys.* **107** (2008) 61.

Current Status of Luminosity Measurement with the CMD-3 Detector at the VEPP-2000 e^+e^- collider

*A.E.Ryzhenenkov**, *R.R.Akhmetshin*, *A.N.Amirkhanov*, *A.V.Anisenkov*, *V.M.Aulchenko*, *V.Sh.Banzarov*, *N.S.Bashtovoy*, *A.E.Bondar*, *A.V.Bragin*, *S.I.Eidelman*, *D.A.Epifanov*, *L.B.Epshteyn*, *A.L.Erofeev*, *G.V.Fedotov*, *S.E.Gayazov*, *A.A.Grebenuk*, *S.S.Gribanov*, *D.N.Grigoriev*, *F.V.Ignatov*, *V.L.Ivanov*, *S.V.Karpov*, *V.F.Kazanin*, *O.A.Kovalenko*, *A.A.Korobov*, *A.N.Kozyrev*, *E.A.Kozyrev*, *P.P.Krokovny*, *A.E.Kuzmenko*, *A.S.Kuzmin*, *I.B.Logashenko*, *P.A.Lukin*, *K.Yu.Mikhailov*, *V.S.Okhapkin*, *Yu.N.Pestov*, *A.S.Popov*, *G.P.Razuvaev*, *A.A.Ruban*, *N.M.Ryskulov*, *V.E.Shebalin*, *D.N.Shemyakin*, *B.A.Schwartz*, *A.L.Sibidanov*, *E.P.Solodov*, *V.M.Titov*, *A.A.Talyshev*, *A.I.Vorobiov*, *Yu.V.Yudin*
Budker Institute of Nuclear Physics, SB RAS, Novosibirsk, 630090, Russia

Abstract

The CMD-3 detector has taken data at the electron-positron collider VEPP-2000 since december 2010. The collected data sample corresponds to an integrated luminosity of 60 pb^{-1} in the c.m. energy range from 0.32 up to 2 GeV. Preliminary results of the luminosity measurement are presented for various energy ranges and its accuracy is estimated to be 1%.

Keywords

Luminosity; VEPP-2000; CMD-3 detector.

1 Introduction

The electron-positron collider VEPP-2000 [1] has been operating at Budker Institute of Nuclear Physics since 2010. The collider is designed to provide a luminosity of up to $10^{32} \text{ cm}^{-2} \text{ s}^{-1}$ at a maximum center-of-mass energy of $\sqrt{s} = 2 \text{ GeV}$. There are two detectors, CMD-3 [2] and SND [3], installed in the two interaction regions of the collider. Both detectors have high detection efficiency and good energy and angular resolutions for charged particles and for photons.

Precise luminosity measurement is a key requirement for many experiments studying hadronic cross sections at e^+e^- colliders. As a rule, the systematic error of the luminosity determination is one of the largest sources of uncertainty, which can cause significant reduction in the hadronic cross section accuracy. Therefore it is very important to have several well-known QED processes such as $e^+e^- \rightarrow e^+e^-$, $\mu^+\mu^-$, $\gamma\gamma$ to determine the luminosity. The combined usage of them will help to better understand and estimate the systematic accuracy of the luminosity measurement. The CLEO collaboration was the first to show in practice how a combined usage of the processes $e^+e^- \rightarrow e^+e^-$, $\mu^+\mu^-$ and $\gamma\gamma$ helped to achieve a 1% accuracy for luminosity [4].

The process $e^+e^- \rightarrow \gamma\gamma$ has essential advantages in luminosity determination [5, 6] over the first two ones. This process is free of effects due to radiation of the final state particles and Coulomb interaction. It is also of importance that the corresponding Feynman graphs do not contain photon propagators affected by vacuum polarization effects. Events of this process have two collinear photons with similar energy depositions in calorimeters, providing a clean signature for their selection among other events. These reasons are the main motivation to explore this process as an independent tool for luminosity determination. Preliminary results of the luminosity determination are presented in a wide energy range.

*Corresponding author. Email: tem_mc@mail.ru

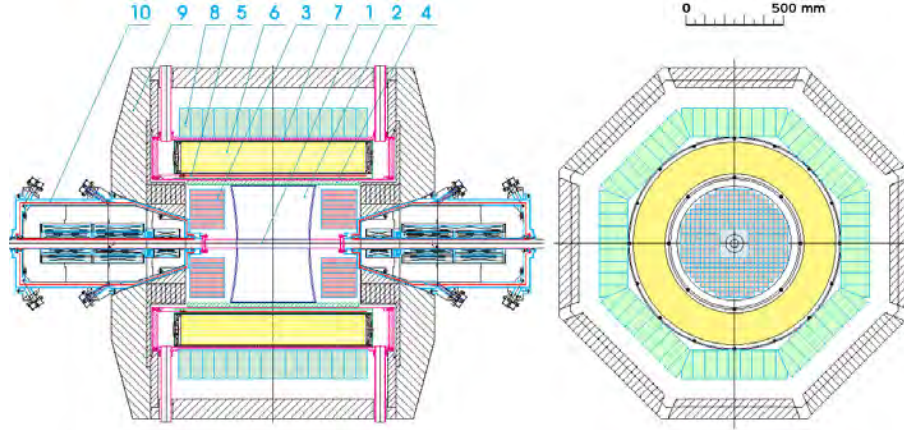


Fig. 1: The CMD-3 detector: 1 – beam pipe, 2 – drift chamber, 3 – BGO, calorimeter, 4 – Z-chamber, 5 – SC solenoid ($0.13X_0$, $1.3T$), 6 – LXe calorimeter, 7 – TOF system, 8 – CsI electromagnetic calorimeter, 9 – yoke, 10 – VEPP-2000 SC solenoids ($13T$). The outer muon range system is not shown.

2 CMD-3 detector and dataset

The Cryogenic Magnetic Detector, CMD-3, is a general purpose detector, shown in Fig. 1. The cylindrical drift chamber (DC) measures the coordinates, angles and momenta of charged particles. The position resolution in the r - ϕ plane is $\sim 120 \mu\text{m}$. The resolution along the beam axis is $\sim 2 \text{ mm}$ as measured from charge division along the wires. The proportional Z-chamber mounted outside the DC provides a more accurate z -coordinate measurement of the tracks. The resulting z -coordinate resolution is $\sim 400 \mu\text{m}$. The signals coming from the anode wires are used for the first level trigger and have a time jitter of $\sim 5 \text{ ns}$.

The calorimeter consists of three subsystems. The endcap BGO calorimeter with a depth of $13.4X_0$ is placed on both sides of the DC flanges. The barrel part, which is placed outside the superconducting solenoid with a 1.3 T magnetic field ($0.13X_0$), consists of two systems: an inner Liquid Xenon calorimeter ($5.4X_0$) and a calorimeter based on CsI crystals with a depth of $8.1X_0$. The latter comprises 1152 crystals, which are spread over 8 octants. The LXe calorimeter has a tower structure (264 channels) and seven cylindrical double layers with strip readout (2112 channels). The strip information allows one to measure coordinates of the photon conversion point with a precision of about 1-2 mm.

The outer muon range system, located outside the iron yoke, consists of 36 scintillation counters in the barrel part and 8 counters in the endcap. This system is used as a cosmic veto and has a time resolution of $\sim 1 \text{ ns}$.

In 2011 the energy range from 1 to 2 GeV was scanned up and down with a step size of 50 MeV. At each energy point an integrated luminosity of $\sim 500 \text{ nb}^{-1}$ was collected. During the scan down the energy points were shifted by 25 MeV with respect to the previous scan. The data were collected at an average luminosity of $\sim 4 \cdot 10^{30} \text{ s}^{-1} \text{ cm}^{-2}$. At the highest energies the peak luminosity reached approximately $2 \cdot 10^{31} \text{ s}^{-1} \text{ cm}^{-2}$ and was limited by the positron storage rate in the booster. The design luminosity of $\sim 10^{32} \text{ s}^{-1} \text{ cm}^{-2}$ will be reached only with the new positron injection facility, starting in 2016. In 2012 the luminosity was measured at 16 energy points from 1.32 GeV to 1.98 GeV and the collected luminosity was about $\sim 14 \text{ pb}^{-1}$.

In 2013 the energy range from 0.32 GeV to 1 GeV was scanned with 10 MeV steps. Integrated luminosities of about 8.3 and 8.4 pb^{-1} were collected around the ω and ϕ mesons, respectively. In 2013 an integrated luminosity of $\sim 25 \text{ pb}^{-1}$ was collected.

The average trigger counting rate was about 200 - 400 Hz and strongly depended on the fine tuning of the beam optics.

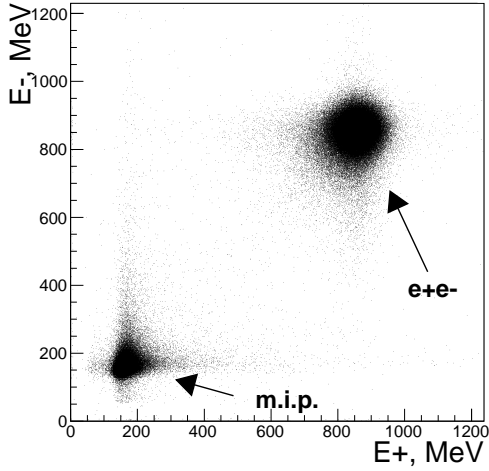


Fig. 2: Correlation between energy depositions in calorimeters for two collinear tracks.

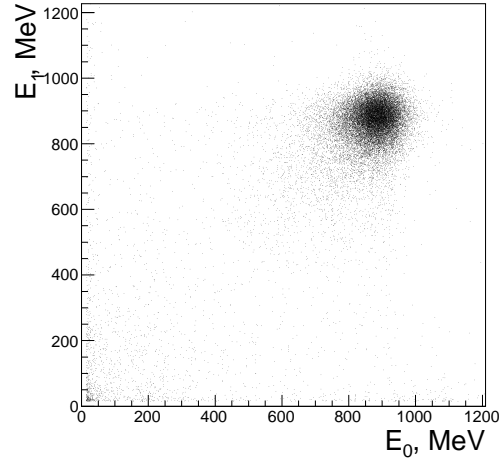


Fig. 3: Correlation between energy depositions in calorimeters for two collinear photons.

3 Event selection

At first, collinear events with back-to-back tracks in the DC were selected according to the following criteria: two tracks with opposite charge were reconstructed in the DC; the distance from both tracks to the beam axis in the r - ϕ plane was less than 0.5 cm; the distance from both tracks along beam axis to the interaction point did not exceed 10 cm; the acollinearity angle between the two tracks in the scattering plane (containing the beam axis) $|\Delta\Theta| = |\Theta_1 - (\pi - \Theta_2)| \leq 0.25$ rad; the acollinearity angle between the two tracks in the azimuthal plane (perpendicular to the beam axis) $|\Delta\Phi| = |\pi - |\Phi_1 - \Phi_2|| \leq 0.15$ rad; the average polar angle of the two tracks $[\Theta_1 + (\pi - \Theta_2)]/2$ should be between 1 and $(\pi - 1)$ rad.

Samples of collinear events e^+e^- , $\mu^+\mu^-$, $\pi^+\pi^-$, K^+K^- and cosmic background were selected for the luminosity determination. Correlation between energy depositions in calorimeters for these events is presented in Fig. 2 for a beam energy of 950 MeV. It is clearly seen that Bhabha events are located predominantly in the upper right corner, whereas other particles are concentrated in the bottom left corner. Collinear events are accepted as Bhabha events if the energy deposition of each particle is within the interval from $0.5E_{beam}$ to $1.5E_{beam}$. Thus, the integrated luminosity can be determined from selected Bhabha events:

$$\int L \cdot dt = \frac{N_{ee}}{\sigma_{ee} \cdot \epsilon_{rad} \cdot \epsilon}, \quad (1)$$

where N_{ee} is the number of selected Bhabha events, σ_{ee} is the Bhabha cross section integrated within the detector acceptance, $\epsilon_{rad} \sim 0.947 \pm 0.002$ is the radiative correction calculated according to [7] and ϵ is the event detection efficiency.

Events of the process $e^+e^- \rightarrow \gamma\gamma$ were also used to determine the integrated luminosity. It is worth noting that this method has completely different systematic uncertainties. It is important that this method has absolutely different systematic errors as compared to the method based on the Bhabha events. The $\gamma\gamma$ neutral collinear events were selected according to the following criteria: back-to-back clusters in the barrel calorimeters; the energy of each cluster is required to be within the interval from $0.5E_{beam}$ to $1.5E_{beam}$; no tracks in the DC coming from the interaction region and no hits in the Z-chamber sectors associated with the clusters. The last condition helps to eliminate Bhabha events which slip through the previous cuts. The polar angle of the cluster is calculated by the center-of-gravity method using the

information from strips in the LXe calorimeter [8]. A two dimensional plot of the energy deposition E_0 vs E_1 is presented in Fig. 3.

The detection efficiency of the $e^+e^- \rightarrow e^+e^-$ events is determined as $\epsilon = \epsilon_{2tr} \cdot \epsilon_{trg} \cdot \epsilon_{cal} \cdot \epsilon_{en}^2$, where ϵ_{2tr} is the track reconstruction efficiency in the DC, ϵ_{trg} is the trigger efficiency, ϵ_{cal} is the cluster reconstruction efficiency, ϵ_{en} is the cluster selection efficiency for the energy depositions in the calorimeters.

The detection efficiency of the $e^+e^- \rightarrow \gamma\gamma$ events is determined as $\epsilon = \epsilon_{cal} \cdot \epsilon_{en}^2 \cdot \epsilon_{ntr}$, where ϵ_{cal} is the cluster reconstruction efficiency, ϵ_{en} is the cluster selection efficiency for the energy deposition in the calorimeters, ϵ_{ntr} is the neutral trigger efficiency. The radiation length of the LXe calorimeter for photons is about $5X_0$ only, resulting in a $\sim 99\%$ interaction probability of one photon in this calorimeter.

Since the Bhabha and $\gamma\gamma$ cross sections are complex functions of the polar angle θ , systematic corrections have to be applied because of the finite angular resolution σ_θ . For example, for $\sigma_\theta \sim 0.03$ rad and polar angle $\theta = 60^\circ$ the correction is about 0.5% for Bhabha events. Bhabha events were used to determine the calorimeter angular resolution. To this end the tracks from the DC were extended to the intersection with the LXe calorimeter. The width of the distribution of the difference in the coordinates determined by the strips and by the track serves as the angular resolution. It is better than ~ 0.05 rad.

4 Systematic uncertainties

The fiducial volume of the CMD-3 detector can be determined independently with the LXe calorimeter and Z-chamber. It allows one to monitor the detector operation stability during data collection. The possibility of cross-checking a z-scale measurement with two subsystems will allow one to keep the systematic uncertainty from this source at a level of $\sim 0.1\%$. Measurement of the beam energy by the Compton back scattering of laser light with a precision σ_E below 50 keV [9] will keep the systematic uncertainty from this source below 0.1%.

Another important source of systematic uncertainty is the theoretical precision of radiative corrections [10]. Additional studies are required in this field and a comparison with experimental data is necessary. We expect that this uncertainty can be reduced to 0.1%.

The axis of the CMD-3 detector has a slight slope with respect to the beam axis and this parameter is unstable in time. Therefore the measured luminosity can change by up to 0.4% and thus a careful monitoring is required. Event selection criteria for collinear tracks also contribute to the systematic error of the integrated luminosity, as well as energy and momentum resolutions, angular resolution, the stability of the z-scale in the DC and similar factors.

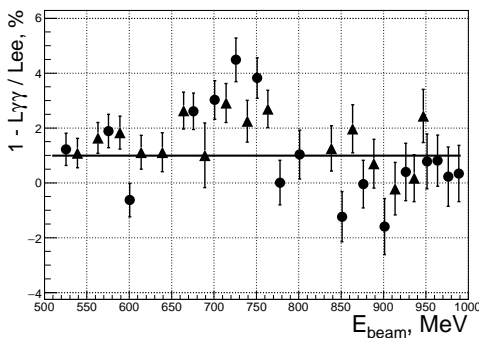


Fig. 4: The ratio of the luminosities for the processes e^+e^- and $\gamma\gamma$ as a function of energy. Scan 2011, circles - scan up ($0.9 \pm 0.4\%$), triangles - scan down ($1.5 \pm 0.3\%$). Only statistical errors are shown.

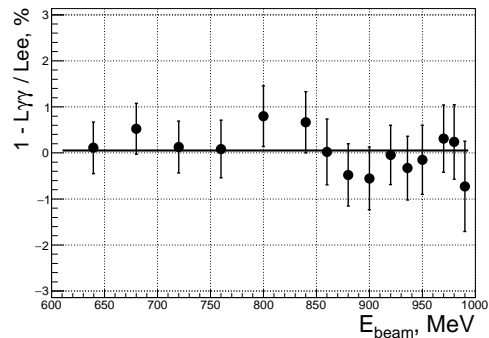


Fig. 5: The ratio of the luminosities for the e^+e^- and $\gamma\gamma$ processes as a function of energy. Scan 2012. The horizontal line represents the average result.

5 Results, Conclusion, Summary

The VEPP-2000 collider successfully operates with a goal to collect $\sim 1 \text{ fb}^{-1}$ in 5-10 years and provide new precise results on hadron physics. Two types of the first level triggers, "CHARGED" and "NEUTRAL", delivered independent information, thereby enabling the determination of trigger efficiencies and estimation of their uncertainties. The collected integrated luminosity is $\sim 60 \text{ pb}^{-1}$ with about 34.5 pb^{-1} above the ϕ resonance energy, 8.3 and 8.4 pb^{-1} at the ω and ϕ resonances respectively, and 9.4 pb^{-1} from a scan below the ϕ . A peak luminosity of $\sim 2 \cdot 10^{31} \text{ s}^{-1} \text{ cm}^{-2}$ was reached. It is currently limited by the deficit of positrons and the maximum beam energy of the booster (825 MeV now). Data analysis is in progress. The already collected data sample has the same or better statistical precision for the hadronic cross sections than achieved in previous experiments. An upgrade of the injection facility will increase the luminosity ten-fold at least. The current integrated luminosity of the collider was measured using two well known QED processes $e^+e^- \rightarrow e^+e^-$ and $\gamma\gamma$. The luminosity ratio determined using the two processes as a function of energy is shown in Fig. 4 and Fig. 5, where only statistical errors are shown. It is worth noting that the systematic uncertainties of the luminosity measurement are totally different for the e^+e^- and $\gamma\gamma$ processes and cannot be compensated in their ratio. The current luminosity accuracy is estimated to be 1%. The study of the different systematics is still in progress. In the forthcoming future we hope to reduce it to a $\sim 0.5\%$ level.

Acknowledgements

We wish to thank the VEPP-2000 personnel for the excellent machine operation. This work is supported in part by the Russian Science Foundation (grant No. 14-50-00080) and by the Russian Foundation for Basic Research grants RFBR 13-02-00991-a, RFBR 13-02-00215-a, RFBR 12-02-01032-a, RFBR 13-02-01134-a, RFBR 14-02-00580-a, RFBR 14-02-31275-mol-a, RFBR 14-02-00047-a, RFBR 14-02-31478-mol-a, RFBR 14-02-91332 and RFBR 15-02-05674-a.

References

- [1] I. Koop *et al.*, Nucl. Phys. B, Proc. Suppl. **181**, 371 (2008).
- [2] B. I. Khazin *et al.*, Nucl. Phys. B, Proc. Suppl. **181-182**, 376 (2008).
- [3] M. N. Achasov *et al.*, Nucl. Instrum. Meth. **A598**, 31 (2009).
- [4] G. Grawford *et al.*, NIM **A345**, 429 (1994).
- [5] E. Bartos *et al.*, JETP Lett. **87**, 73 (2008).
- [6] S. Eidelman *et al.*, EPJ **C71**, 1597 (2011).
- [7] A. Arbuzov *et al.*, EPJ **C46**, 689 (2006).
- [8] R. R. Akhmetshin *et al.*, Phys. Lett. **B669**, 217-222 (2008).
- [9] E. V. Abakumova *et al.*, Phys. Rev. Lett. **110**, 140402 (2013).
- [10] S. Actis *et al.*, Eur. Phys. J. **C66**, 585 (2010).

iLCDirac and Continuous Integration: Automated Testing for Distributed Computing

J. Ebbing

CERN, Geneva, Switzerland

Karlsruhe Institute of Technology, Karlsruhe, Germany

Abstract

Detector optimization studies for future high-energy physics experiments require the simulation and reconstruction of many physics processes and detector geometries. As an efficient way of accessing the necessary computational and storage resources, DIRAC has been developed and extended to form iLCDirac, which is specialized for the applications used in the context of linear collider detector studies. We give a short introduction of grid computing and the concept of high-throughput computing behind DIRAC before explaining the unique features of DIRAC and iLCDirac. With this preparation we explain how we leveraged continuous integration to provide smooth day-to-day operations and ensure that changes to the underlying code base do not cause an interruption of the service.

Keywords

Continuous integration; iLCDirac; grid computing; quality assurance.

1 Introduction

To design experiments for future e^+e^- linear colliders that would take the place of the Large Hadron Collider (LHC), extensive studies on different variations are performed. These Monte Carlo simulations require vast computational resources that are provided by grid computing, specifically by the Worldwide LHC Computing Grid [1], as well as the Open Science Grid [2, 3]. To use these resources as efficiently as possible, the LHCb experiment developed the grid middleware DIRAC [4], which handles software installation, job scheduling, workload management, data bookkeeping, and replica management. The resources of the International Linear Collider (ILC) and Compact Linear Collider (CLIC) communities are bundled and shared via the ILC virtual organization. The iLCDirac extension [5], which was developed on top of DIRAC, offers workflow modules for the linear collider software. The members of the virtual organization share the software for event generation, detector simulation, event reconstruction, and data analysis, as well as their computational resources.

Thus, iLCDirac has been developed to offer a simple interface for users and has been adopted generally by the linear collider community. Originally developed for the CLIC Conceptual Design Report [6], iLCDirac has been used successfully for data production and analysis for the Silicon Detector concept in the ILC Detailed Baseline Design document [5, 7] and is now also in use for the International Large Detector concept. The available resources are mostly opportunistic, i.e., not guaranteed to be available at all times; for example, there can be another user with higher priority but when the resource has been idle for some time the resource is allocated to the grid. At most, around 20,000 concurrent jobs are handled by the system [8].

2 Grid computing and high-throughput computing

2.1 Introduction to grid computing

Grid computing refers to a special kind of distributed computing, with the machines usually being heterogeneous (using hardware with differing architectures, different operating systems, or preinstalled

libraries), geographically dispersed (worldwide) and connected to reach a common goal. It is used to provide the LHC experiments with the enormous amounts of computational resources and storage capacities necessary for functioning. The ideas of the grid were pioneered in the 1990s, mainly by Foster *et al.* [9]. In 2002, Foster released a three-point checklist [10] to determine whether a system can be called a grid. It states:

I suggest that the essence of the definitions [...] can be captured in a simple checklist, according to which a grid is a system that:

1. co-ordinates resources that are not subject to centralized control [...];
2. using standard, open, general-purpose protocols and interfaces [...];
3. to deliver nontrivial qualities of service.

Unlike conventional supercomputers, machines of a single grid can be spread across the world. This means that, for example, the round-trip time will be rather high and the data transmission rate not as high as it would be if the machines were in the same building. This is offset by several advantages of distributed systems, e.g., not containing a single point of failure. In the case of simulations for high-energy physics it is also noteworthy that the problems are of such a kind that two machines do not have to communicate in order to finish their computation, so-called *embarrassing parallelism*. This is also referred to as a *loose coupling* of parallel tasks, which can be seen as a characteristic of grid computing (again as a result of the long-range connection). There are also designated (including undersea) cables deployed for CERN and the LHC experiments, further alleviating the issues.

2.2 The high-throughput computing paradigm

Most physical supercomputers follow the high-performance computing paradigm, aiming to maximize, e.g., the number of floating point operations per second (FLOPS) that the machine can perform. However, scientific computation tasks, such as those that arise in high-energy physics, can take much longer, making the number of floating point operations per month or year (FLOPM or FLOPY) a much more realistic and thus important metric. Owing to general downtime, idleness, and inefficiencies of the system, and many other reasons, the number of FLOPS cannot simply be scaled up to FLOPM or FLOPY. For this reason, high-throughput computing was developed, focusing on the reliability and robustness of a system that executes a large number of jobs in parallel.

To maximize the computational efficiency with the allotted resources, DIRAC follows the high-throughput computing paradigm and introduced novel concepts such as *pilot jobs*, which are described in Section 3.1, to grid computing.

3 DIRAC and iLCDirac

This section discusses the grid software developed by the LHCb experiment, DIRAC, as well as the extension for the ILC community, iLCDirac. DIRAC was originally developed to fulfil the grid needs of LHCb. However, to encourage reuse of the general-purpose DIRAC code for other applications, the LHCb-specific code was moved to its own extension, LHCbDirac. Today, DIRAC is also used by many researchers outside of collider-based high-energy physics, for example in using the Cherenkov Telescope Array [11] and the Fermi Large Area Telescope [12].

3.1 DIRAC grid middleware

DIRAC was developed to provide common services exclusive to LHCb. A special focus was put on the system requiring as little manpower for site management as possible and on the need to scale to forty or more sites easily. A *pull* model has been implemented for scheduling so that instead of a centralized job

queue looking for resources for its jobs, each free resource site will ask a central service for a free job to execute. This has benefits for scalability and efficiency in the high-performance computing paradigm. An innovation introduced to grid computing by DIRAC is the introduction of so-called *pilot jobs*, which are first sent to a free resource. As opposed to actual jobs, these pilot jobs do not require large input files, making them a lot cheaper to send; their purpose is to check whether a following normal job can be executed in this environment. If this check fails, a real job is not sent and much time is saved, compared with the case in which the normal job is sent immediately. This extra step before an actual job submission is an improvement, since grid resources can be unreliable. Without pilot jobs, a defective site would continuously request jobs, putting unnecessary strain on the system and not doing anything productive. Since the resources of the grid are, by nature, heterogeneous, the purpose of DIRAC is to provide homogeneous access to these heterogeneous resources; this is achieved through the job interface—a user is usually not concerned with selecting sites on which the jobs are run.

3.2 Extending DIRAC for the linear collider community

To use DIRAC in the linear collider community, the iLCDirac extension has been developed. Analogous to LHCbDirac for LHCb specifics, this system encapsulates the software specifics for the needs of the linear collider community. It builds on DIRAC by using the core, configuration, and general framework of DIRAC, as well as the file catalogue, workload management for job handling, workflow management for job submission, and existing transformation system. Owing to the linear-collider-specific software necessary for grid jobs, the software installation in iLCDirac changed to downloading tarballs from the grid, which was later extended to optional use of the shared area for software installations. Interfaces for the aforementioned specific applications were added, to simplify job submission for the users, as well as some internal modules for typical ILC use cases.

4 Software testing

Since all sufficiently complex software contains bugs the need for quality assurance in software development arises. This is especially true for the large-scale programs being developed today, as the hardware and maintenance costs of the necessary data centres are high. Testing has been researched extensively in the past, with, e.g., Dijkstra stating “Testing shows the presence, not the absence of bugs.” [13]. Owing to the complexity of distributed computing and the importance of providing a working system to the physicists working with DIRAC/iLCDirac, extensive testing is paramount.

There are many ways to categorize software testing. One of the most important is automated testing, by contrast with manual testing; automated testing refers to small test programs that test a larger piece of software.

Another important distinction is the knowledge of the underlying system: in whitebox testing, the test knows how the system under test works internally and can use this information, whereas a blackbox test only knows the public application program interface (API) of the software and thus provides an input and checks the final output of the program. Since all types of testing generally have advantages and disadvantages, it is usually advised to mix different categories in real software projects with the concrete distribution, depending on the specific software under test.

4.1 Test hierarchy

Simultaneously with the proposal of agile programming methods, such as extreme programming, test automation became an important topic in software development and is a core part of many agile methods. In short, agile software development is based on many small iterations, which means that a small part of the system is planned in close collaboration with the customer and implemented as well as deployed in a short timeframe. This flexibility contrasts with the long planning phases used previously, which often did not adequately reflect customers’ needs. Owing to this workflow, core parts of the software are changed

multiple times, requiring the entire software package to be tested again after each small change. This presents an excellent use case for automated tests, as they can be run quickly and at no cost.

Writing smaller programs that test a large piece of software automation presents several advantages.

- It is much faster than executing the same test manually (although, in some cases manual tests might in fact be *faster* than automated ones).
- When a test suite is developed, its execution for each new version guarantees that the old functionality (for which the tests check) is not broken with the update, preventing so-called *regressions*.
- It allows for new software development models, such as test-driven development, in which the tests are specified first and then the actual code is developed.
- It facilitates the development of new features, since the developer can concentrate on his or her part of the program only.
- For the same reason, it saves a lot of work when refactoring older parts of the code since the basic functionality is ensured. Without these tests, a developer tasked with refactoring faces the vicious circle that the code is too complex to be tested before refactoring, but the refactoring might change the behaviour of the code.

To structure the problem better, automated tests are usually divided into several types. *Unit tests* are the most low-level tests and should usually be the most numerous. They are specific to a ‘unit’ of software—in object-oriented languages, usually an object or a method—and test whether it fulfils its design contract by setting a state, providing an input, and checking for the correct output and the correct new state of the system. Dependencies on other parts of the code should not be tested and are usually avoided through special mock objects that replace the original dependencies. This process is colloquially known as *mocking*. A unit test should make as few assumptions about its environment as possible and run as quickly as possible (a usual aim is of the order of several milliseconds). This means that all calls to databases, file systems, network connections, etc., in the original code should be mocked.

To check for the correct interaction of code units, *integration tests* are written. Depending on the application, these tests can take much longer than unit tests. For example, an integration test might involve setting up a database with some basic values, performing actions in a graphical user interface (GUI), and checking whether the correct results are displayed. Owing to these more complex interactions between modules and, e.g., interactions of a user with a GUI, these tests can be more difficult to automate.

Finally, *system tests* test the basic functionality of the system as it would be used later, e.g., not setting up any system state beforehand. These tests are usually very complex; thus, only a few of them will be written. They can take a very long time to run and may require special infrastructure to be executed. System tests can be even harder to automate than integration tests and may also be performed manually.

The correct use of these types of test is very specific to the software project in question. For example, a custom sophisticated data structure implementation will require many unit tests with a large underlying dataset and predefined expected behaviour, whereas a simple application for a non-tech-savvy user with a GUI will require a larger proportion of system tests.

4.2 Testing metrics

Especially in commercial software development, project metrics are an important factor to measure with respect to, e.g., the progress and success of a project. However, these metrics are always just a heuristic and the specific project will determine many of the testing requirements. For example, a compiler would need as many tests as possible and every line should be touched at least several times, whereas simple end-user application code does not have such high requirements, since the code complexity is far lower. For test coverage, different metrics have been proposed, each with its own shortcomings.

The most simple metric is *statement coverage*. This involves leaving all lines of code untouched by default, then executing the test suite and marking every line that is being executed as touched. At the end of the test, the coverage is the number of touched lines or statements divided by the number of total lines. This is a very weak metric and should not be used, for many reasons. It is easily possible for code still to contain lots of bugs even though the statement coverage is 100%.

A slight improvement is *branch coverage*, which is concerned with the amount of branches that the code contains. An if-condition has two branches, the if-part and the else-part. Similarly, loops can be executed at least once or never. Then the coverage is calculated as the number of executed branches divided by the number of total branches. This metric should be seen as the bare minimum; more complex metrics can lead to an improvement in software quality. To give an intuition of how defects can still happen with this metric, consider a method that consists of two if-conditions. The bug occurs when the first if evaluates to `true` and the second if to `false` but the two test cases that have both ifs evaluate to `true` and `false`, respectively, achieve 100% branch coverage.

A theoretical metric is *path coverage*, which considers all possible paths through a program. This could lead to provable correctness but the number of tests required for this metric leads to a combinatorial explosion even in very simple programs. Writing a test suite with 100% coverage could be replaced by simply writing a table that maps all possible input values to the correct output values, defeating the purpose of the software in the first place.

4.3 Continuous integration

Continuous integration is a concept that is critical for most agile methods. It revolves around writing a large base of unit tests that can be executed very quickly and then setting up an automatic system that executes these tests whenever a developer commits a change to the code base. This prevents regressions by adding a unit test for every bug that has been found and fixed. If a new change breaks old behaviour, the corresponding test will fail and the code base can be fixed very quickly, since the developers get almost immediate feedback. Aside from the benefits this has for larger collaborations due to a healthy code base and preventing repeating the same work again, this technique also allows for fast release cycles.

5 Continuous integration in iLCDirac

The iLCDirac team uses continuous integration to ensure that bugs do not reach production. Since the project uses GitLab, this is implemented using GitLab-CI. Several dedicated test machines run the suites on each commit in parallel, resulting in short feedback times (around 10–15 min for all suites, including system tests). While executing the tests, we also measure and report branch coverage and use tools to analyse overall code quality. The tests are run on both CERN CentOS 7 and Scientific Linux CERN 6 (as both operating systems are in use) using docker images. This has the additional advantage of being able to use test specific environments.

Several test suites have been written.

1. Code style checks and checks for basic errors with Pylint. Since Python is a dynamic and interpreted language, this is necessary to display some basic errors that a compiler would catch. A common code convention is necessary for any software project.
2. A large suite of unit tests, which is currently being extended. These are written on a per-class basis and test individual methods, using blackbox testing for public API methods and whitebox testing for private methods.
3. System tests, mainly sample job submissions for the simulation software used by the linear collider community. A collection of configuration and input files for tests is used and success of the job is expected.
4. System tests for the storage elements used on the grid. These upload a file with random bits to

storage elements, replicate it to and delete it on several storage elements, and retrieve the copies and the original file. Consistency between the original and the downloaded file is expected and all operations are checked for success.

Where necessary, a script performs a full installation of DIRAC and iLCDirac in a docker image before executing these suites. To perform manual testing as well, newest versions are not automatically pushed to production. These updates are handled manually once a certain maturity of a version has been proved. During my technical studentship, branch coverage has improved from 32.2% to 52.1%.

6 Summary

To conclude, we established an automated testing system for iLCDirac that leverages several types of automated tests to provide high software quality and prevent regressions. Since it is automatically executed on each commit to the main code base, we ensure a healthy code base and are able to pinpoint new bugs to concrete commits very quickly. As anecdotal evidence, we recently updated to a new DIRAC version without any major problems. The usage of continuous integration revealed bugs in the original DIRAC that could be fixed before causing problems in production. Continuous integration also proved useful for refactoring code, which is a large part of everyday work. The current development focus in the continuous integration area is the further extension of the unit test suite.

References

- [1] C. Eck *et al.*, LHC computing grid: technical design report, CERN-LHCC-2005-024, (CERN, Geneva, 2005).
- [2] R. Pordes *et al.*, *J. Phys. Conf. Ser.* **78** (2007) 012057.
<http://dx.doi.org/10.1088/1742-6596/78/1/012057>
- [3] I. Sfiligoi *et al.*, The pilot way to grid resources using glideinWMS. 2009 WRI World Congress on Computer Science and Information Engineering, 2009, vol. 2, p. 428.
<http://dx.doi.org/10.1109/CSIE.2009.950>
- [4] N. Brook *et al.*, DIRAC-distributed infrastructure with remote agent control, Computing in High Energy and Nuclear Physics (CHEP03), La Jolla, CA, 2003, cs.DC/0306060.
- [5] C. Grefe *et al.*, *J. Phys. Conf. Series* **513** (2014) 3.
- [6] L. Linssen *et al.* (eds.), Physics and detectors at CLIC: CLIC conceptual design report (2012).
- [7] T. Behnke *et al.*, The International Linear Collider technical design report—volume 1: executive summary (2013).
- [8] A. Sailer. Talk: iLCDirac and the grid, ECFA-Linear Collider Workshop, 2016.
- [9] I. Foster and C. Kesselman (eds.), *The Grid: Blueprint for a New Computing Infrastructure* (Morgan Kaufmann Publishers Inc., San Francisco, CA, 1998).
- [10] <http://www.mcs.anl.gov/~itf/Articles/WhatIsTheGrid.pdf>, last accessed September 26th 2016.
- [11] L. Arrabito *et al.*, *J. Phys. Conf. Series* **664** (2015) 032001.
- [12] L. Arrabito *et al.*, *J. Phys. Conf. Series* **513** (2014) 032003.
- [13] J.N. Buxton and B. Randell (eds.), Software Engineering Techniques, Report on a Conference Sponsored by the NATO Science Committee, Rome, Italy, 27th to 31st October 1969 (NATO, Scientific Affairs Division, Brussels, 1970).

Beam Energy Measurement by Resonant Depolarization Method at VEPP-4M

V.E. Blinov^{1,2,3}, V.O. Ivakin^{1,3}, V.V. Kaminskiy^{1,2}, V.N. Kudryavtsev¹, S.A. Nikitin¹, I.B. Nikolaev^{1,2} * and L.I. Shekhtman^{1,2}

¹ Budker Institute of Nuclear Physics, Novosibirsk, Russian Federation

² Novosibirsk State University, Novosibirsk, Russian Federation

³ Novosibirsk State Technical University, Novosibirsk, Russian Federation

Abstract

Experiments on high precision mass measurement of particles require precise beam energy calibration. The most accurate method of beam energy measurement is the resonant depolarization technique. This article describes the beam energy measurement at the VEPP-4M storage ring using this method together with a Touschek polarimeter. The accuracy achieved is about 10^{-6} . More than thousand energy calibrations were used in the KEDR detector for the precise experiments on the measurement of J/ψ , $\psi(2S)$, $\psi(3770)$, D^+ , D^0 meson and τ lepton masses.

Keywords

Beam energy measurement; resonant depolarization; Touschek, intra-beam scattering; Compton backscattering; polarized beam; VEPP-4M; KEDR.

1 Introduction

High precision measurements in high energy physics requires accurate knowledge of the initial state of the colliding particles. In particular, precise measurement of the mass of elementary particles requires precision measurement of the beam energy. The most accurate method of beam energy calibration is the resonant depolarization (RD) technique. It is based on the measurement of the spin precession frequency, which is associated with the Lorentz factor of the beam and the well known normal and anomalous part of the magnetic moment of the electron due to the Thomas precession. The spin precession frequency is determined from the frequency of resonant destruction of beam polarization. The polarization degree can be measured via intra-beam scattering (Touschek), Compton backscattering or the synchrotron radiation process.

The VEPP-4M [1] accelerator complex (Fig. 1) with the KEDR [2] detector is designed for experiments in charm-tau physics in the $E=1-5.5$ GeV energy range. High precision mass measurement experiments on J/ψ $\psi(2S)$ [3], $\psi(3770)$ [4], D^0 , D^+ [5] mesons and τ lepton [6] were done using the resonant depolarization method. The main advantage of the resonant depolarization method is the best accuracy (10^{-6} for VEPP-4M) among other methods. However, it requires a polarized beam and a special run to prepare a polarized beam and perform an energy measurement. During a luminosity run the beam energy is interpolated with an accuracy of 10 – 30 keV using NMR and temperature sensors in the storage ring.

2 Resonant depolarization method

The method of resonant depolarization has forty years of successful history. It was first proposed in [7] and applied in experiments on Φ meson mass measurement [8] at Budker Institute of Nuclear Physics (Novosibirsk, Russia) in 1975. Later on it was used in the high precision mass measurement of K^+ [9]

*E-mail: I.B.Nikolaev@inp.nsk.su

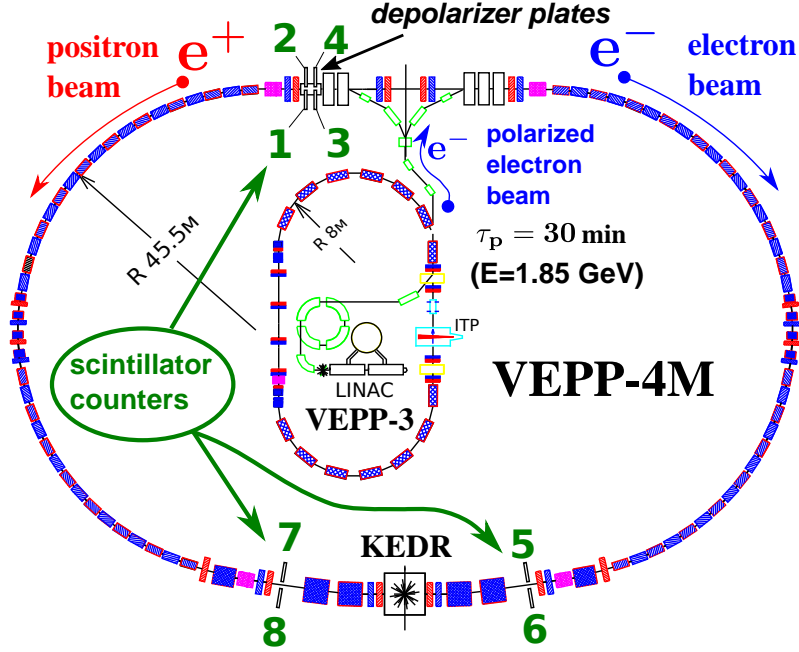


Fig. 1: The VEPP-4M storage ring with the KEDR detector. The location of eight scintillator counters of the Touschek polarimeter at VEPP-4M are labeled by numbers.

mesons at VEPP-2M with the OLYA detector, K^0 [10] and ω [11] mesons at VEPP-2M with the CMD detector, J/ψ and $\psi(2S)$ [12, 13] at VEPP-4 with the OLYA detector, $\Upsilon(1S)$, $\Upsilon(2S)$ and $\Upsilon(3S)$ mesons at VEPP-4 with the MD-1 detector, at CESR with the CUSB detector [14] and at DORIS-II with the ARGUS and Crystal Ball detectors [15], Z boson [16] at LEP with the OPAL, DELPHI, L3 and ALEPH detectors. It was also used in the recent storage ring lattice calibration at SPEAR3 and AS [17] as well.

The spin evolution is described by the following equation:

$$\frac{d\vec{s}}{dt} = 2\mu \frac{\vec{s} \times \vec{B}'}{\gamma} + (\gamma - 1) \frac{\vec{s} \times [\vec{v} \times \dot{\vec{v}}]}{v^2}, \quad (1)$$

where \vec{s} is the spin direction; \vec{v} is the electron velocity; γ is the Lorentz factor; μ is the magnetic moment of the electron. The first part of the equation corresponds to dynamic spin rotation in a magnetic field B' in the electron rest frame. The second term corresponds to the pure relativistic kinematic effect, which was discovered by Thomas [18] and is called the Thomas precession. Bargmann, Michel, and Telegdi have derived the full relativistic equation [19]. In a storage ring it gives the spin precession with a frequency Ω :

$$\Omega = \omega_0 \left(1 + \frac{E}{m_e} \frac{\mu'}{\mu_0} \right), \quad (2)$$

where ω_0 is the revolution frequency. It depends on $a = \mu'/\mu_0$, the anomalous and normal parts of the electron magnetic moment ratio (magnetic moment anomaly), the beam energy E and the electron mass m_e ¹. The electron mass and magnetic moment anomaly are known with great accuracy: $\delta a \approx 2.3 \times 10^{-10}$ and $\delta m_e \approx 2.2 \times 10^{-8}$ [20], which allows one to calibrate the beam energy through measuring the spin precession frequency. Earlier experiments of ψ and Υ meson mass measurement were revised [21] after improvement of the electron mass measurement accuracy. Now the beam energy accuracy is limited only by the width of the spin line which is formed by the beam orbit disturbance in the presence of field

¹Here and further the system of units with $\hbar = 1$ and $c = 1$ is used

quadratic non-linearity and by magnetic field fluctuations. For example, the spin line width is about 5×10^{-7} at VEPP-4M.

The spin precession frequency is determined by the moment of resonant destruction of the beam polarization in an external electromagnetic field with ω_d . The resonant condition is $\Omega = n\omega_0 \pm \omega_d$, where $n \in \mathbb{Z}$. Thus one can calculate the beam energy as follows:

$$E = (440.6484431 \pm 0.0000097) [\text{MeV}] \times \left(n - 1 \pm \frac{\omega_d}{\omega_0} \right), \quad n \in \mathbb{Z}. \quad (3)$$

3 Radiative polarization

A polarized beam is obtained by the well known effect of radiative polarization, which was described by Sokolov and Ternov in 1963 [22]. The synchrotron radiation (SR) intensity of electrons in the storage ring has a small part of spin flip contribution: $W^{\uparrow\downarrow} \approx W_0 \frac{4}{3} (\omega_c/E)^2$, where W_0 is the total SR intensity and ω_c is the SR critical photon energy. It results in beam polarization with the characteristic time

$$\tau_p = \frac{8\sqrt{3}}{15} \frac{\lambda_C}{c} \frac{1}{\alpha\gamma^2} \left(\frac{H_0}{H} \right)^3, \quad (4)$$

and maximum polarization degree $P_0 = 8\sqrt{3}/15 \approx 92.4\%$. Here λ_C is the Compton wavelength of the electron; $H_0 = m_e^2 c^2 / e\hbar \approx 4.41 \times 10^{13}$ Gs is the Schwinger magnetic induction; H is the magnetic field of the storage ring; $\alpha \approx 1/137$ is the fine structure constant. Radiative polarization was first seen at VEPP-2 [7] in 1970 and at the ACO storage ring [23] in 1971. Then it became the main method of obtaining polarized beams for storage rings. A storage ring has a number of depolarizing spin resonances which satisfy the condition for the spin tune $\nu = \Omega/\omega_0 - 1 = k + l\nu_x + m\nu_y + n\nu_s$, where $k, l, m, n \in \mathbb{Z}$; ν_x, ν_y and ν_s are the horizontal betatron, vertical betatron and synchrotron tunes, respectively. Depolarizing resonances reduce the maximum polarization degree and polarization time by the factor $G = \tau_d/(\tau_p + \tau_d)$. The polarization process is described by the following dependence:

$$P(t) = P \left(1 - e^{-t/\tau} \right), \quad (5)$$

where $P = P_0 G$ is the reduced maximum polarization degree and $\tau = \tau_p G$ is the relaxation time of polarization. Calculation of the G-factor shows the possibility of obtaining polarization at ψ and Υ energies except of the $\Upsilon(4S)$ resonance. It is impossible to polarize a beam in VEPP-4M at low energies $E=1.5-2$ GeV because of the large polarization time (~ 100 hours). The beam is polarized in the VEPP-3 storage ring and injected into VEPP-4M. The non-planar injection channel results in a degradation of the vertical beam polarization. A 2.5 T·m pulsed solenoid is used to increase the polarization degree of the positrons [24]. The threshold energy $E = 1777$ MeV of τ lepton production is in a close vicinity to the $\nu = 4$ integer spin resonance, so there are special efforts were made [6, 25] for obtaining polarization.

4 Depolarizer device

The beam is depolarized by the TEM wave which is created by two matched striplines (Fig. 2). They are connected to a high frequency generator with tunable frequency, which is computer controlled. The depolarization time is:

$$\frac{1}{\tau_d} = 2 \frac{(2\mu' H l_d 2\pi\omega_0)^2}{c^2 \Delta\omega_d} |F^\nu|^2, \quad (6)$$

where H is the magnetic field of the TEM wave; l_d is the depolarizer length; $\Delta\omega_d \approx \sqrt{\dot{\omega}_d/2\pi}$ is the width of the depolarizer frequency, which depends on the frequency scan speed $\dot{\omega}_d$. F^ν is the spin response function, which depends on the depolarizer azimuth in the storage ring and the beam energy. The amplitude of the TEM wave H_0 is adjusted to get $\tau_d \sim 1$ s. The frequency generator and the VEPP-4M revolution frequency are stabilized by a rubidium atomic clock with stability of 10^{-10} .

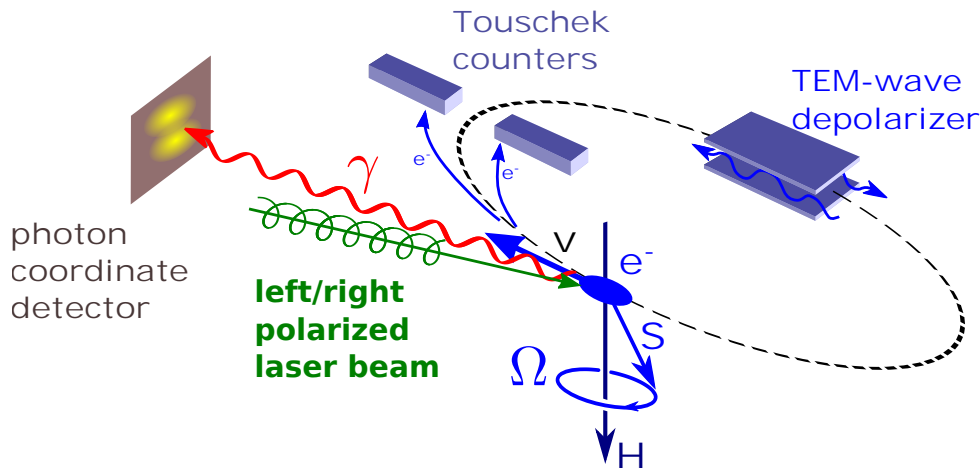


Fig. 2: Scheme of the resonant depolarization method with Touschek and Compton polarimeters

5 Polarization measurement

There are several methods of polarization measurement in storage rings. One of the most effective methods at lower energies ($\lesssim 2$ GeV) is the Touschek polarimeter, which is based on the polarization dependence of the intra-beam scattering intensity. Another method for higher energies is the Compton backscattering polarimeter, which relies on up-down asymmetry of the Compton backscattering of circularly polarized photons on vertically polarized electrons. The principal scheme of the resonant depolarization method with the Touschek and the Compton polarimeters is shown on Figure 2. The third method is based on the polarization dependence of the synchrotron radiation intensity.

5.1 Intra-beam scattering

The well known process of intra-beam scattering, which is called the Touschek (AdA) effect [26], is the main factor which limits the beam life time. In 1968 Baier and Khoze noticed [27] that the beam life time depends on beam polarization. This effect can be used for polarization measurement. In 1970 G. Tumaikin suggested [7] to use scintillator counters for the measurement of the intensity of intra-beam scattering. The problem associated with intra-beam scattering is the fast intensity and polarization contribution, decreasing at higher energies.

Pioneer work [27] assumed non-relativistic approximation with a flat beam. The calculation in [28] uses a two-dimensional beam; [29] takes into account relativistic effects, which become sufficient at energies of $\gtrsim 5$ GeV, and in [30] the Coulomb effects are concerned. Thus the intra-beam scattered intensity for a 2D relativistic (in the bunch rest frame) beam with the only assumption of small momentum transition $\varepsilon = \Delta p/p \ll 1$ has the following form:

$$\frac{dN}{dt} = -\frac{2\pi r_e^2 c N^2}{\gamma^2 V_b \varepsilon^2 \delta_x \delta_y} (I_1 + I_2 P^2) \quad v \rightarrow 1 \quad -\frac{4\pi r_0^2 c N^2}{\gamma^2 V_b \varepsilon^2} \left(1 - \frac{\varepsilon P^2}{2\delta_x \delta_y}\right), \quad (7)$$

where $I_{1,2}$ are some integrals [30]; r_e is the classical electron radius; N is the number of particles in a beam; γ is the Lorentz factor; V_b is the effective beam volume; δ_x and δ_y are the horizontal and vertical momentum spreads in the $m_e c$ units, respectively; $\varepsilon = \Delta p/p$ is the relative momentum transition after scattering; v is the velocity of the electrons in the center of mass frame of the interacting particles. To calculate the count rate for a specific storage ring one has to take into account the betatron oscillation, location and distance to the beam orbit from the counters. Such calculations for VEPP-4M were done in [31]. The polarization effect $\Delta = \dot{N}_{pol}/\dot{N}_{unpol} - 1$ is about 3.5 % for $E = 1.85$ GeV and 2.5 % for $E = 1.5$ GeV, where \dot{N}_{pol} and \dot{N}_{unpol} are the count rate from the polarized and unpolarized beams, respectively. The intra-beam scattering intensity and polarization effect Δ decrease quickly at higher

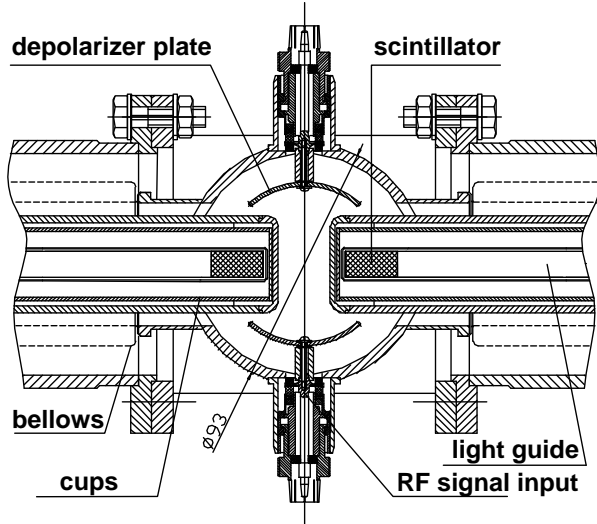


Fig. 3: Profile of the Touschek polarimeter with scintillator counters and depolarizer plates.

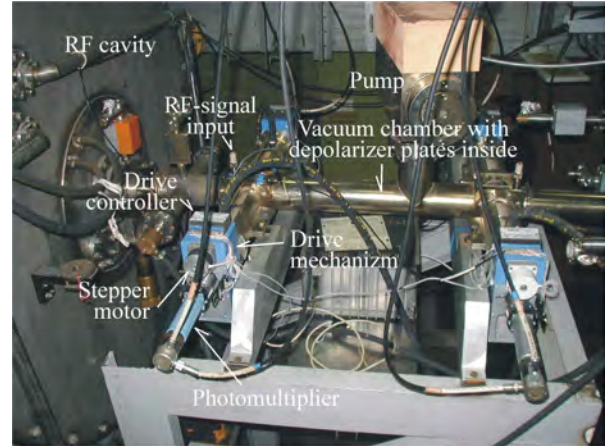


Fig. 4: View of the Touschek polarimeter.

energies. In the ultra relativistic limit $v \rightarrow 1$ the count rate behaves as $\dot{N} \propto E^{-5}$ and has the polarization contribution $\Delta \propto E^{-4}$. The measurement of the energy dependence of the count rate is described in [32]. At the Υ mesons energy region the Touschek count rate and the depolarization effect are expected to be 10 kHz and 0.1 %, respectively, for 10 mA beam current. This is a reason to use another method for the polarization measurement.

5.2 Compton backscattering

For higher energies $E \gtrsim 4$ GeV, the Compton backscattering polarimeter is useful. This method was first proposed in 1968 by Baier and Khoze [33]. The first realization of the laser polarimeter was done in 1979 at SPEAR [34]. Later on this method was applied at VEPP-4 [35], CESR [14], DORIS [15] and LEP [16].

The Compton cross section of the scattering of circularly polarized photons on polarized electrons in the rest frame is described by the following equation:

$$d\sigma = d\sigma_0 - \frac{r_e^2}{2} \left(\frac{\omega'}{\omega} \right)^2 \frac{1 + \cos\theta}{m} \left(\vec{k}' - \vec{k} \cos\theta \right) \vec{P} V d\Omega, \quad (8)$$

where \vec{P} is the polarization of the electron; V is the Stokes parameter of the circular polarization of the initial photon; $d\sigma_0$ is the Compton cross section of the unpolarized particle; ω and ω' are the initial and final photon energy in the electron rest-frame; \vec{k} and \vec{k}' are the initial and final photon momentum; θ is the azimuthal angle between the scattered and backward photon directions. The total up-down asymmetry is

$$A = \frac{N_{up} - N_{down}}{N_{up} + N_{down}} \approx -\frac{3}{4} \frac{\omega_0 E}{m_e^2} V P_{\perp}, \quad (9)$$

where P_{\perp} is the vertical electron polarization. A laser [14–16, 34, 35] or a synchrotron [36–40] can be used as a source of photons. The asymmetry is proportional to the initial photon energy ω_0 . This effect depends on the source of polarized photons and its value varies from $\sim 1\%$ to $\sim 10\%$.

6 Touschek polarimeter at VEPP-4M

The Touschek polarimeter at VEPP-4M has eight scintillator counters located at different locations around the VEPP-4M storage ring (Fig. 1). The counters are grouped into pairs inside and outside

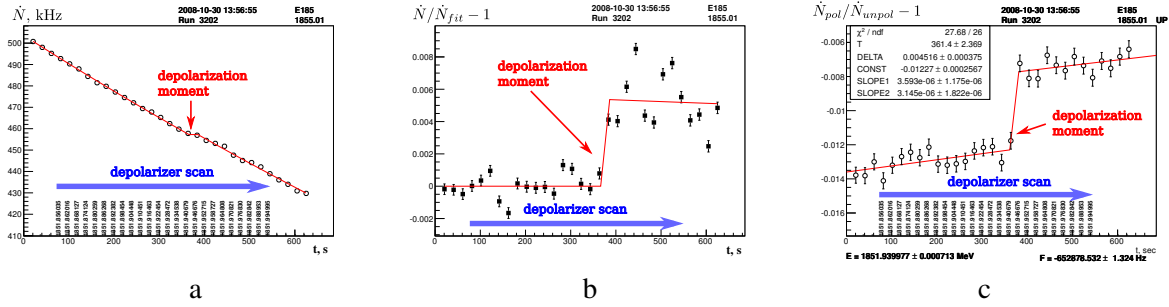


Fig. 5: (a) Count rate behavior during depolarizer frequency scan. It is hard to recognize the depolarization jump due to the wide range of count rate changes. (b) Count rate behavior with slope dependence removed. There is clear evidence of the beam depolarization, but count rate instabilities still exist. (c) Count rate from the polarized beam normalized on the unpolarized one. Instabilities of count rates are suppressed.

the beam orbit and can be moved inside the vacuum chamber in order to adjust their distance to the beam orbit and optimize the count rate (Fig. 3, 4). They have a water cooling shield to protect from synchrotron radiation heating. The typical count rate is about 50 kHz/mA² per counter. The total count rate of all counters is about 1–2 MHz. The counters share the same amount of Touschek electrons, and thus if a counter is moving, then the others change their count rate. Two counters are used in routine energy calibrations in order to simplify the counter position tuning and reduce the overall energy calibration time.

The data acquisition system (DAQ) is based on the CAMAC electronic standard and allows to measure the count rate from four electron or positron bunches with coincidence of counters in each pair. Using the coincidence allows to suppress the background from inelastic scattering on the residual gas because the Touschek events have two scattered electrons, which go inside and outside the beam orbit. Because of the features of particle tracking inside VEPP-4M, there turned out to be many events when only one electron from a scattered pair hit a counter. The probability of both counters hit is around 20% of that of only one counter hit. The high rate of scattered electrons results in a high random coincidence rate.

Figure 5.a shows the sum of count rates during a depolarizer frequency scan. Because of the wide range of the count rate variation it is hard to recognize a depolarization jump. When the slope of the count rate is removed by a special fit in an assumption of no depolarization, the depolarization jump is seen. However, there are count rate instabilities, which may complicate the depolarization moment determination (Fig. 5.b). This issue is solved using the following compensation technique. Two polarized and unpolarized bunches are prepared. After injection into VEPP-4M their currents are aligned to a level of 1% by step by step kicking of the inflector plates. The value $\Delta = \dot{N}_{pol}/\dot{N}_{unpol} - 1$ of relative difference of count rate from polarized and unpolarized bunches is under observation. This effectively suppresses the beam orbit or beam size instabilities, as one can see in Figure 5.c.

7 Laser polarimeter at VEPP-4M

It is planned to use a laser polarimeter at VEPP-4M for polarization measurement at energies around Υ mesons. A general view of the measurement scheme is shown on Figure 6. A solid state Nd:YLF pulse laser with a wavelength of 527 nm is used as a source of initial photons. The circular polarization is prepared by the KD*P Pockels cell or via rotation of the $\lambda/4$ phase plate. The left-right polarization switching has a frequency of about 1 kHz for the Pockels and 1 Hz for the phase plate. The motorized expander and mirrors focus the laser beam on an electron bunch at the azimuth between the quadrupole lenses and the bending magnet where a minimum vertical angular spread of 60 μ rad at 5 GeV is expected. The Compton backscattered photons are detected by the two-dimensional coordinate detector based on

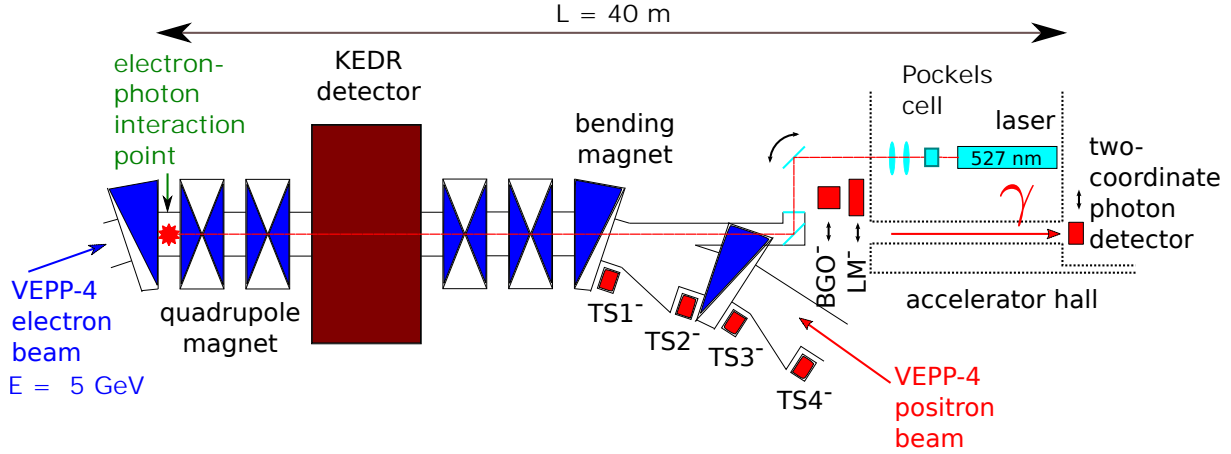


Fig. 6: Layout of the laser polarimeter at VEPP-4M

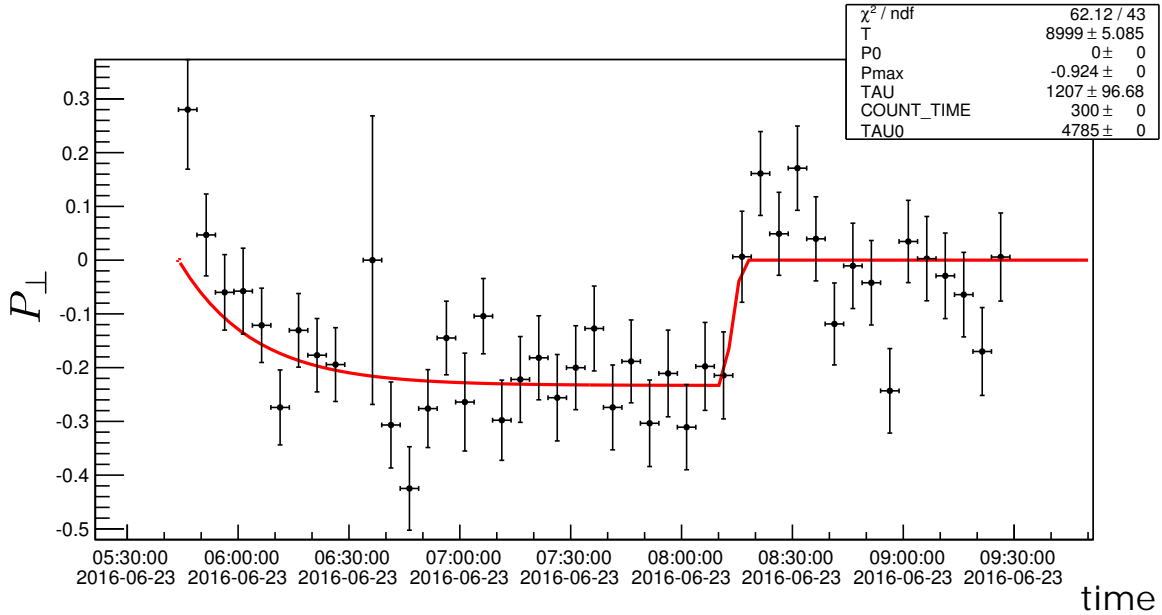


Fig. 7: Observation of the radiative polarization by the laser polarimeter at $E = 4.1$ GeV. P_{\perp} is the vertical electron polarization.

GEM [41] with a 12 mm thick lead photon converter. First experiments with this polarimeter were done in 2016. With a 2 kHz pulse repetition rate and a $180 \mu\text{J}$ pulse, the energy counting rate is about 600 Hz/mA. The radiative polarization measured is presented on Figure 7.

The polarization time measured is 36 minutes, and the polarization degree is $41 \pm 4\%$. The system requires improvement on the mirror quality and focusing. A new GEM detector is being designed and will be created. We expect the count rate to be about 16 kHz for a 10 mA beam current. It allows to measure the beam energy with an accuracy of 10^{-6} .

8 Energy calibration

During experiments on J/ψ , $\psi(2S)$ [3], $\psi(3770)$ [4], D^{\pm} , and D^0 [5] mass measurement, the following procedure is used. Energy calibration is performed *a*) at the beginning and at the end of the resonance energy scan point; *b*) after a VEPP-4M magnetic cycle; *c*) after a large ($\Delta H/H \gtrsim 10^{-4}$) change in

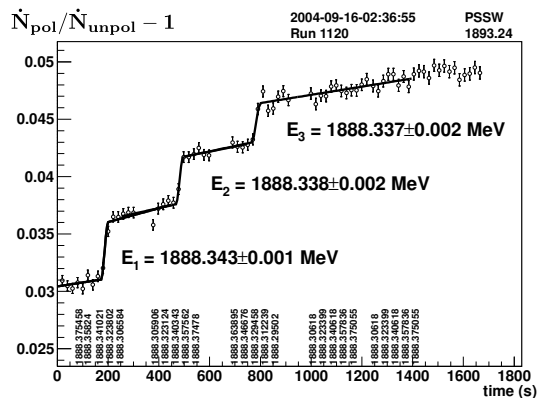


Fig. 8: Triple energy calibration on the same polarized bunch. The differences in energy calibrations are connected with the VEPP-4M energy drift and fluctuation.

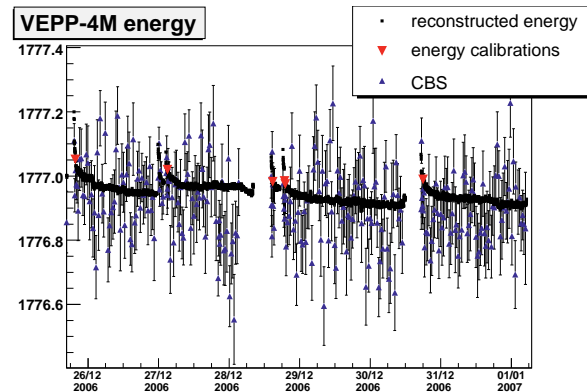


Fig. 9: Energy calibration by resonant depolarization method (red), by Compton backscattering method (blue) and interpolated energy via NMR and temperature parameters (black).

the magnetic field; *d*) after a large ($\gtrsim 1^\circ\text{C}$) change in the cooling water temperature. The magnetic field is measured by the nuclear magnetic resonance (NMR) method every two minutes. Power supply stabilization by NMR measurement feedback was done [42].

A single beam is prepared and polarized in VEPP-3 for 1.5 hours at 1.5 GeV and 1 hour at 1.85 GeV. Successful polarization requires control of the vertical and horizontal betatron tunes to avoid depolarizer resonances and depends on the working energy. After polarized beam injection into VEPP-4M and adjustment of the VEPP-4M betatron tunes, the second unpolarized beam is prepared and injected into VEPP-4M. Their currents are adjusted with an accuracy of 1%. The counters are moved to their working position to achieve a count rate of around 100 kHz per each counter. Final current alignment is done through count rate measurement from each bunch. An electrostatic separation in VEPP-4M should be turned off to satisfy beam orbit conditions during luminosity run.

In the τ mass measurement experiment in [6, 25], the polarized beam is prepared in a different way due to close vicinity to the $\nu = 4$ spin resonance. The beam is polarized at an energy of 1850 MeV in VEPP-3; after injection into VEPP-4M the beam energy is lowered to the τ threshold; after 30 minutes of magnetic field relaxation, resonant depolarization is done by common way. Between RD energy calibrations the energy is controlled by the alternative Compton backscattering edge method [43].

The beam energy uncertainty defines the depolarizer scan mode. At the beginning of the mass measurement scan we know the energy with an accuracy of around 1 MeV. The depolarizer has a 10 keV/s ($\sim 20 \text{ Hz/s}$) scan speed to cover the 4 MeV energy region. The subsequent energy calibration, already tied with the NMR measurement and energy can be predicted with accuracy $\lesssim 0.2 \text{ MeV}$ and thus the depolarizer scan speed is 0.3 keV/s and covers the 400 keV energy range. With a scan speed of 10 keV/s the energy calibration accuracy is about 10–20 keV, thus the energy calibration is repeated with a new polarized beam and a scan speed of 0.3 keV/s. The depolarizer amplitude is adjusted to get a depolarization time of about 1 s and partial beam depolarization that allows to perform two energy measurements with the same polarized bunch. The second scan is done in the opposite direction to determine the systematic error associated with the depolarization process for a finite spin line width. Another reason for the second opposite scan is to exclude depolarization on the side 50 Hz (25 keV) spin resonance caused by a 50 Hz magnetic field pulsation. The efficiency of the Touschek polarimeter and the method of partial depolarization is shown on Figure 8 via triple energy calibration on the same polarized bunch.

During and between energy calibration, the magnetic field is measured by the NMR method; the beam orbit is measured by beam position monitors; the temperatures of the cooling water, magnets

and wall of the tunnel where the ring is located are measured. This VEPP-4M parameters are used to interpolate the accelerator energy between energy calibrations [3]. An example of energy interpolation in the τ mass experiment is shown of Figure 9. The accuracy of interpolation depends on the energy calibration rate and the operation mode of the accelerator and was about 10–30 keV.

9 Conclusion

The resonant depolarization method for beam energy measurement is the most precise method of beam energy calibration. The high efficiency Touschek polarimeter at VEPP-4M is used in high precision mass measurement of J/ψ , $\psi(2S)$, $\psi(3770)$, $D^{+,0}$ mesons and τ lepton masses. More than three thousand energy calibrations were done. The Touschek polarimeter is used now for new D meson mass measurements with the KEDR detector. The VEPP-4M laser polarimeter will be used in new measurements of the mass of the Υ mesons. The resonant depolarization technique could also be applied in new τ mass measurements at the future Super Charm- τ factory [44].

10 Acknowledgment

This work is supported by the Russian Science Foundation under grant 14-50-00080. Part of the laser polarimeter equipment is provided by the Russian Foundation for Basic Research under grants 14-02-01011-a and 15-02-03114-a.

References

- [1] V. E. Blinov, *et al.*, *Phys.Part.Nucl.Lett.*, vol. 11, no. 5, pp. 620–631, 2014.
- [2] V. V. Anashin, *et al.*, *Phys.Part.Nucl.*, vol. 44, pp. 657–702, 2013.
- [3] V. M. Aulchenko, *et al.*, *Phys. Lett.*, vol. B573, pp. 63–79, 2003.
- [4] V. V. Anashin, *et al.*, *Physics Letters B*, vol. 711, no.4, pp. 292–300, 2012.
- [5] V. V. Anashin, *et al.*, *Phys. Lett. B*, vol. 686, no. 2-3, pp. 84–90, 2010.
- [6] V. V. Anashin, *et al.*, *JETP Lett.*, vol. 85, pp. 347–352, 2007.
- [7] V. N. Baier, *Physics-Usppekhi*, vol. 14, no. 6, pp. 695–714, 1972.
- [8] A. D. Bukin, *et al.*, *Yad. Fiz.*, vol. 27, pp. 976–984, 1978. [Sov. J. Nucl. Phys27,516(1978)].
- [9] L. M. Barkov *et al.*, *Nucl. Phys.*, vol. B148, pp. 53–60, 1979.
- [10] L. M. Barkov *et al.*, *Yad. Fiz.*, vol. 46, pp. 1088–1094, 1987. [Sov. J. Nucl. Phys46,630(1987)].
- [11] L. Barkov *et al.*, *JETP Let.*, vol. 46, no. 4, pp. 164–167, 1987.
- [12] A. A. Zholents *et al.*, *Yad. Fiz.*, vol. 34, pp. 1471–1481, 1981.
- [13] A. A. Zholents *et al.*, *Phys. Lett.*, vol. B96, pp. 214–216, 1980.
- [14] W. W. MacKay *et al.*, *Phys. Rev.*, vol. D29, p. 2483, 1984.
- [15] D. P. Barber *et al.*, *Phys. Lett.*, vol. B135, pp. 498–509, 1984.
- [16] L. Arnaudon *et al.*, *Phys. Lett.*, vol. B307, pp. 187–193, 1993.
- [17] K. P. Wootton, *et al.*, *Phys. Rev. ST Accel. Beams*, vol. 16, p. 074001, Jul 2013.
- [18] L. H. Thomas, *Nature*, vol. 117, p. 514, 1926.
- [19] V. Bargmann, *et al.*, *Phys. Rev. Lett.*, vol. 2, pp. 435–436, May 1959.
- [20] K. A. Olive *et al.*, *Chin. Phys.*, vol. C38, p. 090001, 2014.
- [21] A. S. Artamonov *et al.*, *Phys.Lett.*, vol. B474, pp. 427–429, 2000.
- [22] A. A. Sokolov and I. M. Ternov, *Sov. Phys. Dokl*, vol. 8, pp. 1203–1205, 1964.
- [23] I. Duff, *et al.*, *Proc. of III Int.Conf.Charged Part.Accel., Orsay*, pp. 4–73, 1973.
- [24] V. E. Blinov, *et al.*, *Nucl. Part. Phys. Proc.*, vol. 273-275, pp. 210–218, 2016.
- [25] A. Bogomyagkov, *et al.*, *Proc. of EPAC-06*, pp. 625–627, 26-30 Jun 2006.

- [26] C. Bernardini *et al.*, *Phys. Rev. Lett.*, vol. 10, pp. 407–409, 1963.
- [27] V. N. Baier and V. A. Khoze, *At. Energ.*, vol. 25, pp. 440–442, 1968.
- [28] S. Serednyakov, *et al.*, *JETP*, vol. 44, no. 6, p. 1063, 1976.
- [29] Baier, V.N. *et al.*, *Sov. Phys. Dokl.*, vol. 23, p. 573-575, 1978.
- [30] V. M. Strakhovenko, *Phys. Rev. ST Accel. Beams*, vol. 14, p. 012803, Jan 2011.
- [31] S. A. Nikitin and I. B. Nikolaev, *J.Exp.Theor. Phys.*, vol. 115, no. 1, pp. 36–47, 2012.
- [32] V. Blinov, *et al.*, *Proceedings of PAC-2011*, (New-York, USA), p. MOP182, april 2011.
- [33] V. N. Baier and V. A. Khoze, *Sov.J.Nucl.Phys.*, vol. 9, pp. 238–240, 1969.
- [34] D. B. Gustavson, *et al.*, *Nucl.Instr.Meth.*, vol. 165, no. 2, pp. 177–186, 1979.
- [35] P. Vorobiev *et al.*, *Proc. VII All-Union workshop on part. accel.*, vol. 1982, no. 2, pp. 272–276.
- [36] Y. S. Derbenev, *BINP Preprint*, vol. 112, 1976.
- [37] A. S. Artamonov *et al.*, *Phys. Lett.*, vol. B118, p. 225, 1982.
- [38] A. S. Artamonov *et al.*, *Phys. Lett.*, vol. B137, p. 272, 1984.
- [39] E. L. Saldin and Y. M. Shatunov, *Proc. VI All-Union workshop on part. accel.*, vol. 1, (Dubna), pp. 124–127, 1978.
- [40] P. Vorobiov *et al.*, *BINP preprint*, vol. 140, 1986.
- [41] L. I. Shekhtman, *et al.*, *J. Instr.*, vol. 9, 2014. INSTR-2014, BINP, Novosibirsk
- [42] V. Blinov, *et al.*, *ICFA Beam Dynamics Newsletter*, vol. 48, pp. 207–217, 2009.
- [43] N.Yu. Muchnoi, *et al.*, *European Particle Accelerator Conference (EPAC 06)* pp. 1181-1183, 2009.
- [44] V. V. Anashin, *et. al.*, *A project of Super c - τ factory in Novosibirsk.*. Conceptual design report.

Fast and Precise Beam Energy Measurement using Compton Backscattering at e^+e^- Colliders

V.V. Kaminskiy, M.N. Achasov, N.Yu. Muchnoi and V.N. Zhilich
Budker Institute of Nuclear Physics SB RAS, Novosibirsk, Russia
Novosibirsk State University, Novosibirsk, Russia

Abstract

The report describes a method for fast and precise beam energy measurement in the beam energy range of 0.5-2 GeV and its application at various e^+e^- colliders. Low-energy laser photons interact head-on with the electron or positron beam and produce Compton backscattered photons, whose energy is precisely measured by HPGe detector. The method allows measuring the beam energy with a relative accuracy of $\sim 2-5 \cdot 10^{-5}$. The method was successfully applied at VEPP-4M, VEPP-3, VEPP-2000 (BINP, Russia) and BEPC-II (IHEP, China).

Keywords

Compton effect; e^+e^- collider; beam energy measurement; HPGe detector; laser.

1 Motivation

For precise experiments on e^+e^- colliders an accurate beam energy measurement is needed. There are a number of beam energy measurement methods with different precision, time performance and energy range.

For instance, the resonant depolarisation technique is extremely precise; its uncertainty is 10^{-6} of the beam energy. It was applied at various colliders such as VEPP-2, VEPP-4M, LEP, etc., where it gave precise results in high-energy physics (e.g., masses of ω , J/ψ , Z). But the cost of such a precision is a long measurement time (e.g., hours to prepare transverse beam polarisation according to the Sokolov-Ternov mechanism at GeV energy range machines) and technical difficulties (polarisation is very sensitive to beam conditions).

Another method actually is not a beam energy measurement, but worth to be mentioned: collider energy scale calibration using narrow hadron resonances with well-known energy such as J/ψ , $\psi(2S)$, $\psi(3770)$, etc. The precision reaches 10^{-5} of the beam energy in particular points within hours of data-taking time.

Field measurement can be used for rough and very fast energy determination. Usually it is NMR. The energy is calculated: E_0 [MeV] ≈ 300 [MeV/T/m] B [T] ρ [m], where ρ is a bending radius in a field B . The intrinsic accuracy is 10^{-2} , though when calibrated with a more precise method (e.g., resonant depolarisation) and provided with magnet temperature and sextupole field corrections, the method can define the beam energy with a $10^{-3}-10^{-4}$ accuracy within some time.

In this report we discuss a fast and precise method based on measuring the energy of the spectrum edge of Compton backscattered photons. It is applicable at the beam energy range of 200–2000 MeV or even wider. This method has an accuracy of $2-5 \cdot 10^{-5}$ within 20–60 minutes of data-taking time.

2 Compton backscattering

Compton backscattering (CBS, or inverse Compton effect) in our context, is a head-on inelastic interaction of a low-energy photon and an ultra-relativistic electron (or positron). The scattered photon energy is

strictly coupled with the scattering angle θ_γ [1]. When $\theta_\gamma = 0$, the photon energy reaches the maximum:

$$\omega_{\max} = \frac{E_0 \lambda}{1 + \lambda} \approx 4\gamma^2 \omega_0, \quad \lambda = \frac{4E_0 \omega_0}{m^2}, \quad (1)$$

and the scattered electron energy reaches the minimum:

$$E_{\min} = \frac{E_0}{1 + \lambda}. \quad (2)$$

Here E_0 and γ are the energy and the Lorentz factor of the initial electron, respectively; ω_0 is the initial photon energy; m is the electron rest energy ($c = 1$).

So, the CBS photon spectrum looks like a plateau with a narrow edge at ω_{\max} , see Fig. 1 and Fig. 2, right upper corner.

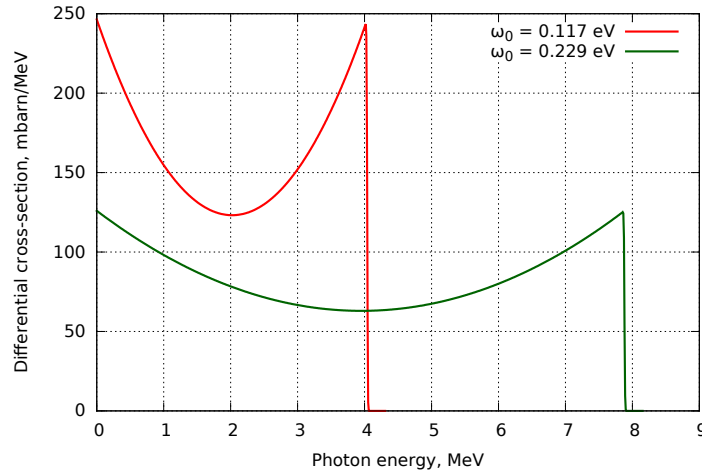


Fig. 1: Theoretical spectrum of Compton backscattered photons. The initial electron energy is 1500 MeV; initial photon energies are 0.117 eV and 0.229 eV (corresponding to particular lasers discussed in this paper).

3 Concept

The procedure of beam energy measurement looks as follows:

- A mid-IR laser beam interacts with an electron (or positron) beam. For this purpose an automated optical system is needed, providing proper focusing and transverse positioning of the laser beam at the interaction point.
- The high-purity germanium (HPGe) detector with an ultimate energy resolution (1–2 keV at 1 MeV, see Fig. 2, middle) registers MeV-range Compton backscattered photons.
- The HPGe detector energy scale is calibrated using monochromatic photons with well-known energies from gamma-emitting isotopes (see Fig. 2, left upper corner). Additionally, the HPGe detector is calibrated using a precision pulse generator to take into account its digital signal processor non-linearity (see Fig. 2, bottom). In Fig. 2 some detector characteristics are shown. For details see particular experiment papers referred in Section 4.
- The energy of the Compton spectrum edge (Fig. 2, right upper corner) is found and the beam energy is calculated according to equation 1:

$$E_0 = \frac{\omega_{\max}}{2} \left(1 + \sqrt{1 + \frac{m^2}{\omega_0 \omega_{\max}}} \right) \approx \frac{m}{2} \sqrt{\frac{\omega_{\max}}{\omega_0}}. \quad (3)$$

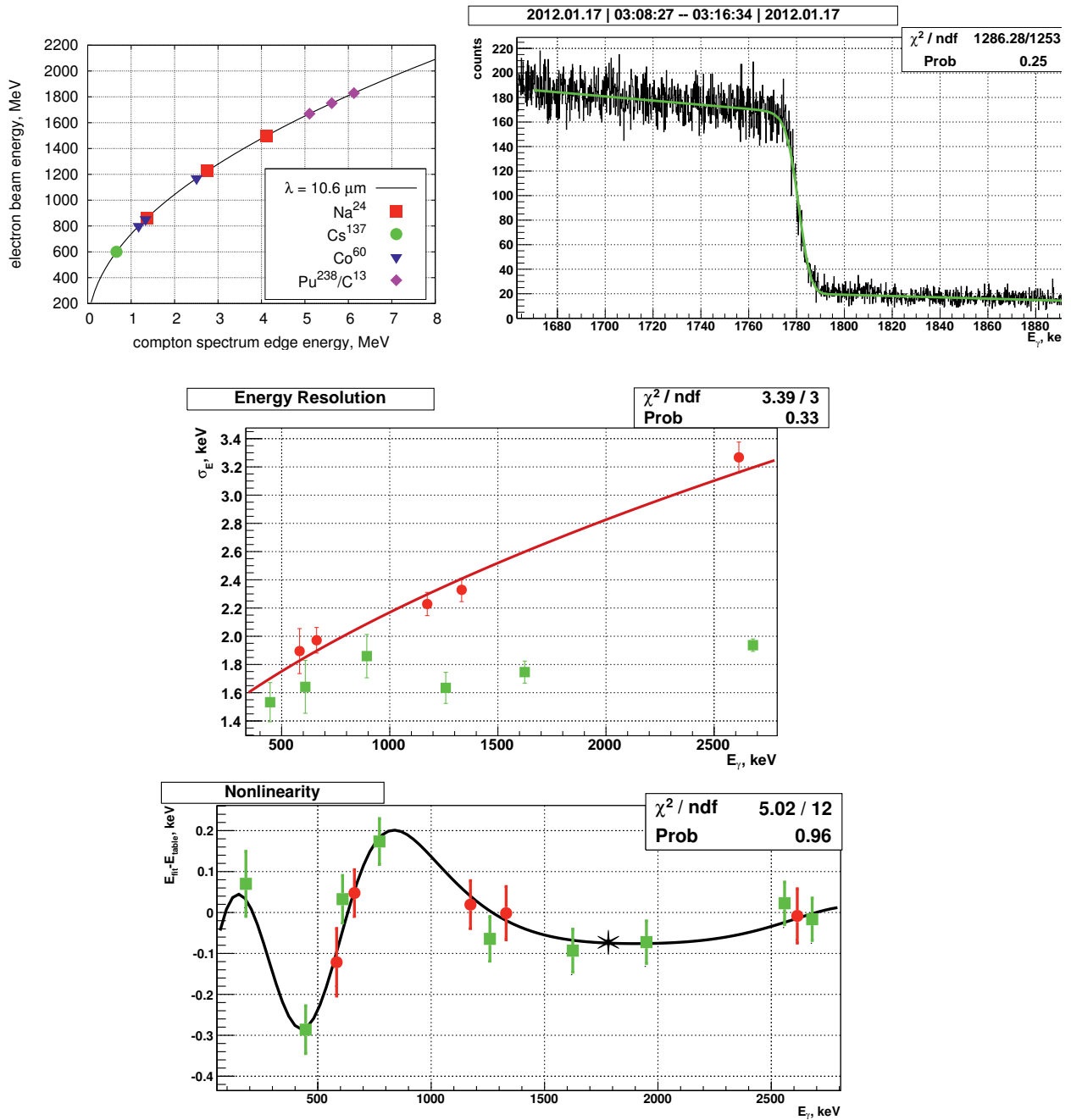


Fig. 2: HPGe detector characteristics and performance. Top left: energies of isotopes used for energy scale calibration vs. corresponding beam energy (CBS with $10 \mu\text{m}$ laser). Top right: CBS photon spectrum edge. Middle: detector energy resolution. Bottom: detector residual nonlinearity; solid curve: nonlinearity measured with a precision pulse generator; asterisk: ω_{max} with $10 \mu\text{m}$ laser and 1.0 GeV electron beam energy. In the latter two plots, red circles: isotopes photopeaks; green squares: precision pulse generator peaks. Source: Ref. [2].

- The uncertainty of the beam energy is

$$\frac{\Delta E_0}{E_0} \simeq \sqrt{\left(\frac{1}{2} \frac{\Delta\omega_{\max}}{\omega_{\max}}\right)^2 + \left(\frac{1}{2} \frac{\Delta\omega_0}{\omega_0}\right)^2 + \left(\frac{\Delta m}{m}\right)^2}. \quad (4)$$

The uncertainty is mostly defined by the first term. It comprises detector issues, such as energy scale calibration, response function, etc., and the beam energy spread. The second term is the uncertainty and stability of the laser photon energy; the third term is the extremely small uncertainty of the electron rest energy. Both of them do not exceed 10^{-7} . The total beam energy uncertainty is typically $5 \cdot 10^{-5}$.

- Additionally, the beam energy spread can be found with an accuracy of 10% through measuring the spectrum edge width and deconvolving the detector response function.

4 Implementation

At the first time the method under discussion was implemented at the «Taiwan Light Source» SR ring in 1996, see Ref. [3]. There a 0.1% precision was achieved at a beam energy 1300 MeV. At the end of the nineties the method was applied at the SR ring BESSY-I in Berlin, and later at the successor, BESSY-II, see Refs. [4, 5]. The accuracy achieved was $3 \cdot 10^{-5}$. The latter results showed that the method under discussion could be sufficient for colliders, especially for precise high-energy physics. It was decided to apply the method at BINP colliders and other installations. In this section the beam energy measurement facilities created by BINP team in 2005–2014 are discussed.

4.1 VEPP-4M

VEPP-4M at Budker Institute of Nuclear Physics (Novosibirsk, Russian Federation) is the e^+e^- collider with beam energies of 1.5 GeV to 5.5 GeV designed for precise experiments such as measurement of τ -lepton, J/ψ , $\psi(2S)$, $\psi(3770)$ masses and R (the ratio of total hadrons production cross-section to that of leptons) at the KEDR detector. For this purpose the beam energy is measured by resonant depolarisation technique at some energies. At the τ threshold and some other important points the beam polarisation is destroyed by the machine resonances, and thus another beam energy measurement method was needed. In 2005 the CBS installation was constructed at VEPP-4M. It was in operation until 2014. The layout of the installation is shown in Fig. 3. Since both electron and positron beams move in the same magnet system, only the electron beam energy was measured. A CO₂ laser with a wavelength of $10.56 \mu\text{m}$ ($\omega_0 = 0.117 \text{ eV}$), 50 W CW power was used.

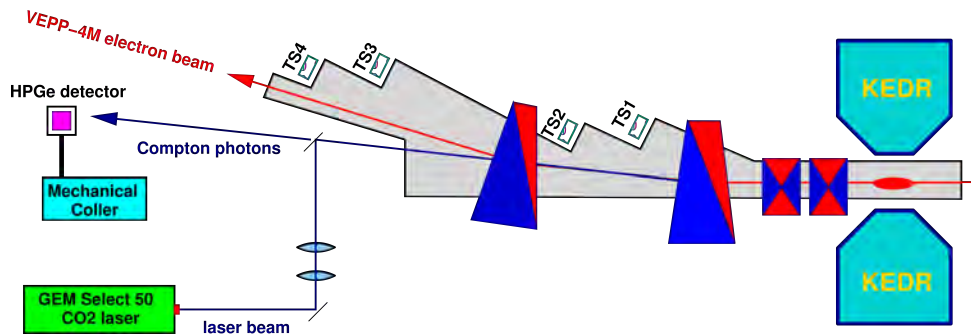


Fig. 3: Layout of the CBS facility at VEPP-4M

In this experiment the best accuracy of the method was $2 \cdot 10^{-5}$ (1.5 hours of data-taking); typical accuracy was $4 \cdot 10^{-5}$ (within 20 minutes). This accuracy was confirmed in simultaneous beam energy measurement by the resonant depolarisation technique. More details can be found in Ref. [6].

The method was used in a precise τ -lepton mass measurement, see Ref. [7].

4.2 VEPP-3

An experimental study of electromagnetic form factors of the proton was performed at the VEPP-3 storage ring at BINP in 2009–2012. The goal of the experiment was to measure the two-photon contribution in elastic ep scattering through comparison of the e^-p and e^+p scattering cross-sections. The electron and positron beams were scattered one by one on cold polarised protons. The beam energy was 1.0 GeV and 1.6 GeV. To reduce systematic errors, the e^+ and e^- beam conditions should be as identical as possible; for instance, the e^+ and e^- energy difference should be kept less than 1 MeV (10^{-3}). For this task the CBS method was applied for VEPP-3 beam energy measurement. A layout of the facility is shown in Fig. 4. The CO₂ laser mentioned above ($10.56 \mu\text{m}$, 50 W CW) was used.

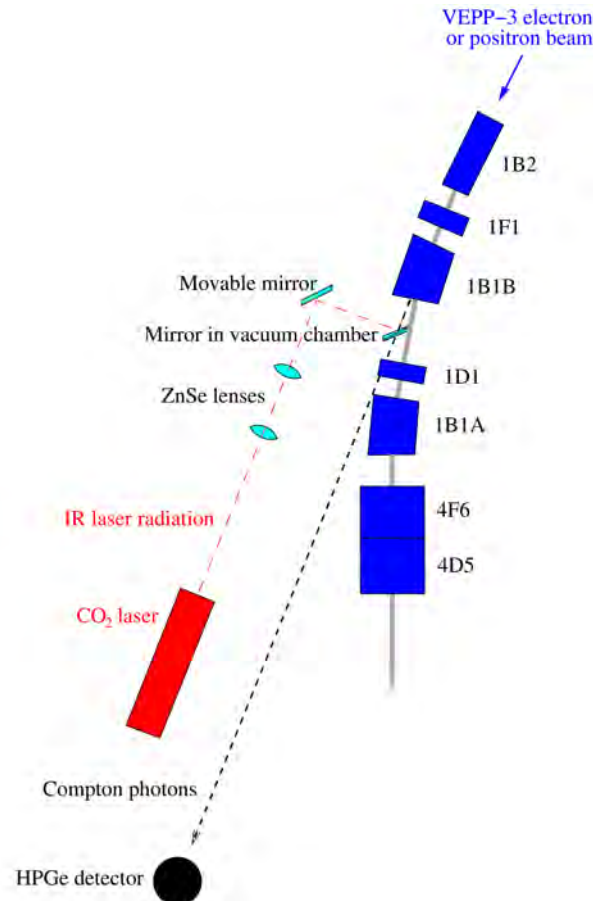


Fig. 4: Layout of the CBS facility at VEPP-3. Source: Ref. [2]

Here a precision pulse generator was applied for the first time for the detector energy scale calibration in the experiments under discussion. It allows measuring the nonlinearity of the HPGe detector multi-channel analyser (a digital signal processor for acquiring photon energies from the detector), which appeared to be a major source of integral nonlinearity. Fig. 2, bottom, shows this residual nonlinearity. These measures improved the calibration precision to a level of 10^{-4} or even better.

The typical accuracy of the beam energy measurement was $5 \cdot 10^{-5}$. See long-term energy behaviour in Fig. 5. More details of the experiment can be found in Ref. [8]; more details of the CBS method implementation can be found in Ref. [2].

4.3 BEPC-II

BEPC-II at IHEP (Beijing, China) is a high luminosity e^+e^- collider in the energy region of 1–2 GeV. Precise experiments on τ , J/ψ , $\psi(2S)$ with the BES-II detector required accurate beam energy mea-

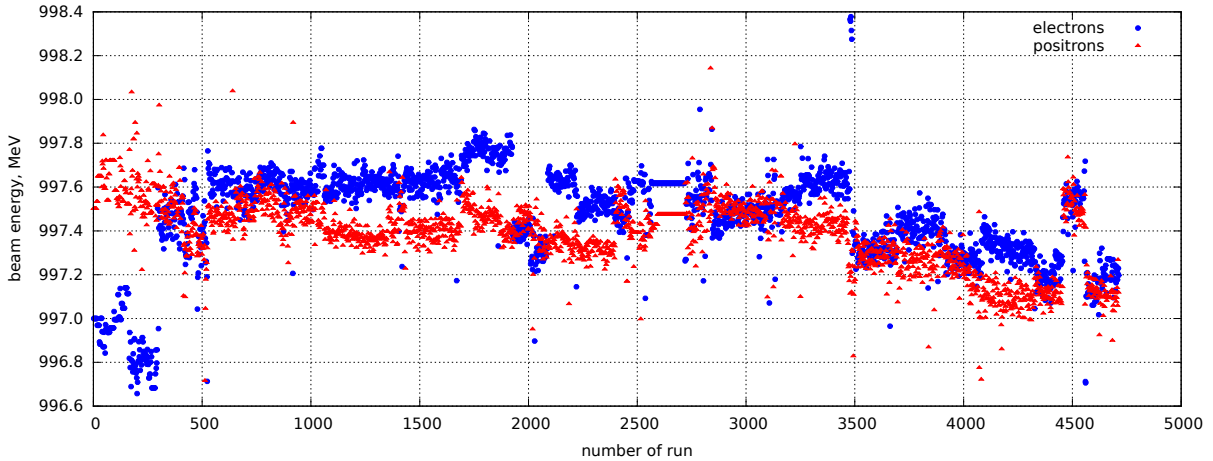


Fig. 5: VEPP-3 beam energy behavior. Source: Ref. [2]

surement. Because of the strong depolarization impact (due to the increased luminosity), the resonant depolarisation technique is not applicable. The CBS beam energy measurement system was installed in 2010. BEPC-II has two separate beamlines for positrons and electrons. It was decided to use one CO₂ laser ($\lambda_0 = 10.84 \mu\text{m}$, $\omega_0 = 0.114 \text{ eV}$, 50 W) and one HPGe detector for measuring the energies of both beams, as shown in Fig. 6.

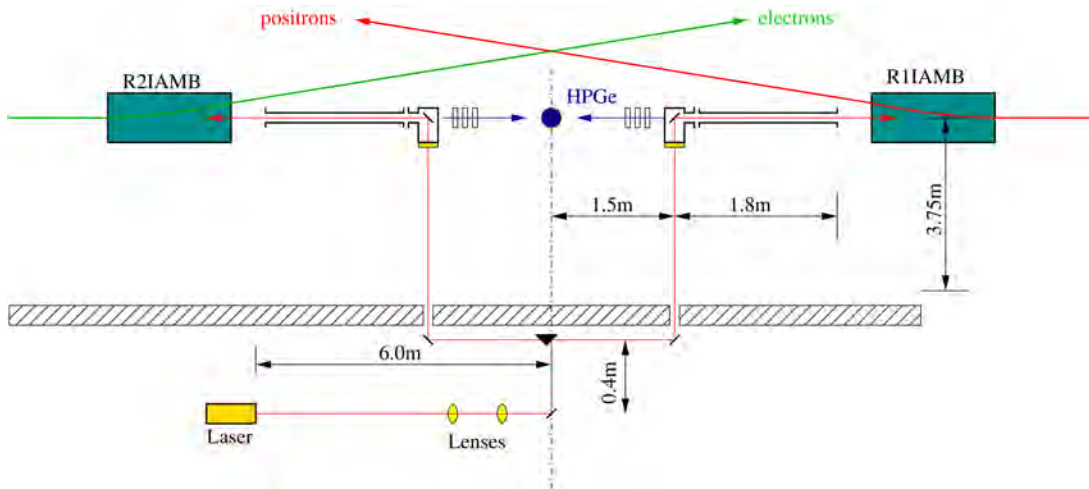


Fig. 6: Layout of the CBS facility at BEPC-II. Source: Ref. [9]

The typical accuracy of the beam energy measurement was $5 \cdot 10^{-5}$; the accuracy was measured using a scan of narrow hadron resonances. More details of the method can be found in Ref. [9]. Some precise results at the BES-III detector (e.g., τ lepton mass) are shown in Ref. [10].

4.4 VEPP-2000

In 2012 the CBS facility was constructed at VEPP-2000 (BINP), the e^+e^- collider operating in the beam energy range of 0.5–1.0 GeV for precise experiments with the SND and CMD-3 detectors. A CO₂ laser ($\lambda_0 = 10.56 \mu\text{m}$, $\omega_0 = 0.117 \text{ eV}$, 50 W) and CO laser ($\lambda_0 \sim 5 \mu\text{m}$, 2 W) were used. The Compton interaction occurs in the dipole magnet, see Fig. 7, top, unlike similar CBS facilities described in this paper. This fact led to an unusual Compton spectrum shape: a wider edge and distinguishable oscillations, see Fig. 7, bottom.

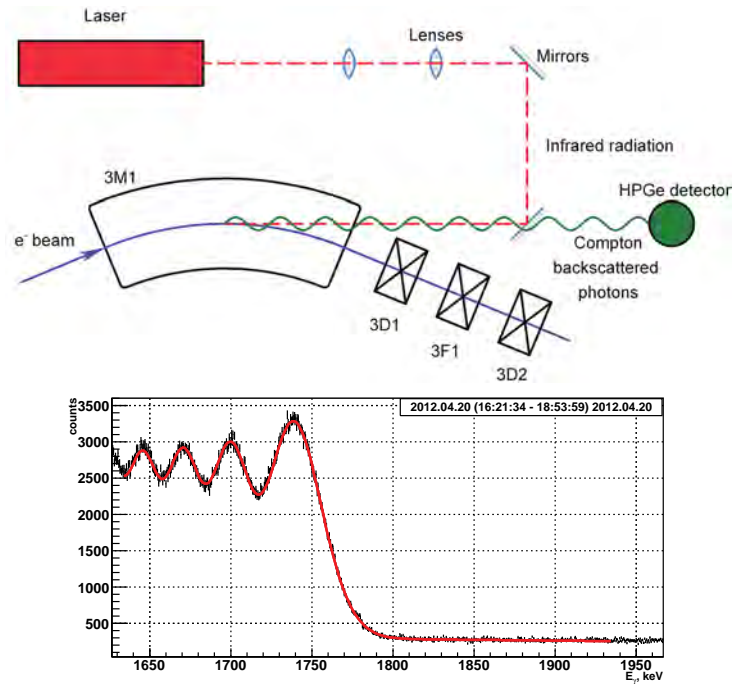


Fig. 7: Top: layout of the CBS facility at VEPP-2000. Bottom: observed spectrum of CBS photons. Source: Ref. [12].

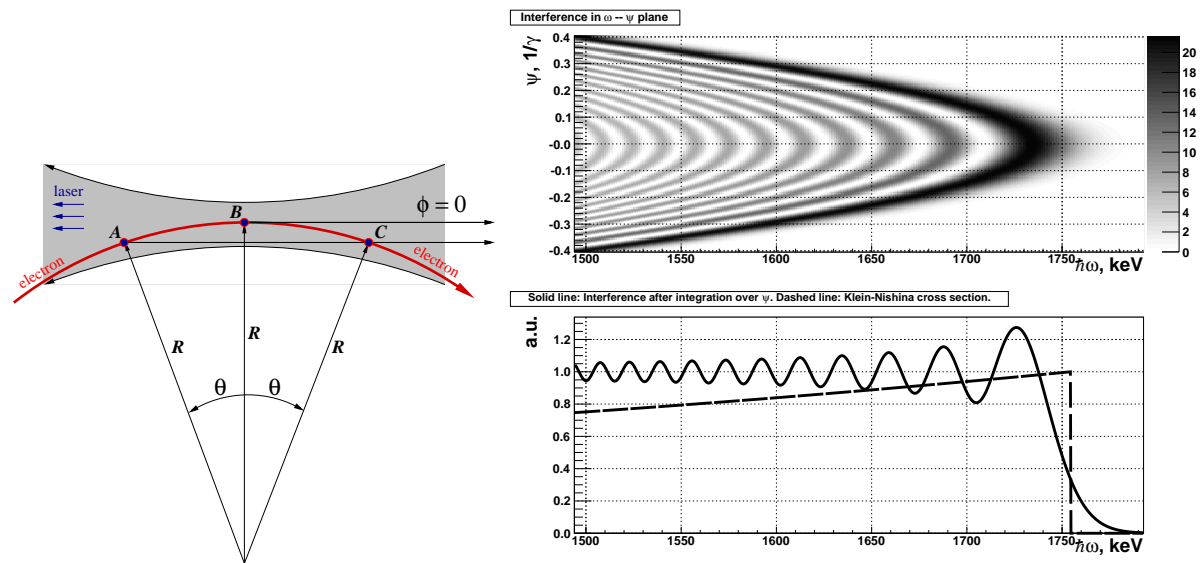


Fig. 8: Interference of MeV-range photons in CBS in magnetic field. Left: layout of formation of the interference. Right top: 2D view, angle vs. energy; right bottom: result of integration. Source: Ref. [12].

This unusual spectrum shape is indeed a newly observed phenomenon. Unlike previous experiments, here the photon interacts with the electron in a magnetic field, and thus the electron can be treated as a bound one. The phenomenon can be described both in QED and quasi-classical frameworks. The quantum solution is derived from the Dirac equation in Ref. [11]. In the quasi-classical approach the phenomenon can be treated as interference of MeV-range photons emitted in an arc electron trajectory (see Fig. 8 and Ref. [12], details of the experiment at VEPP-2000 can also be found there). Multiplied by the Klein-Nishina cross-section, a quasi-classical expression becomes similar to a quantum one with

a slight difference: the difference in energy is less than 10^{-6} . The theory is in a good agreement with the experiments, see the analytically defined function and the spectrum in Fig. 7, bottom. Some precise results obtained at the CMD-3 detector are given in Ref. [13]

5 Conclusion

- Beam energy measurement using the spectrum edge of Compton backscattering photons was successfully implemented at various accelerators and colliders: VEPP-4M, VEPP-3, VEPP-2000, and BEPC-II. The BINP team has a large experience.
- The method is fast, precise, and non-invasive and does not require special beam conditions.
- The method has an accuracy of $2-5 \cdot 10^{-5}$ of the beam energy, which can be achieved within 20–120 minutes of data-taking time.
- The method can be applied at various low-energy e^{\pm} accelerators, including the Super charm-tau Factory (project of a high-luminosity 1–5 GeV e^+e^- collider at BINP).
- Interference of MeV-range photons was observed.

References

- [1] F.R. Arutyunian, V.A. Tumanian, *Phys. Lett.* **3** (1963) 176, [https://doi.org/10.1016/0031-9163\(63\)90351-2](https://doi.org/10.1016/0031-9163(63)90351-2).
- [2] V.V. Kaminskiy *et al.*, *JINST* **9** (2014) T06006, <https://doi.org/10.1088/1748-0221/9/06/T06006>
- [3] I.C. Hsu, C.-C. Chu, and C.-I. Yu, *Phys. Rev.* **E54** (1996) 5, <https://doi.org/10.1103/PhysRevE.54.5657>.
- [4] R. Klein *et al.*, *J. Synchrotron Radiat.* **5** (1998) 392, <https://doi.org/10.1107/S090904959701532X>.
- [5] R. Klein *et al.*, *Nucl. Instrum. Methods Phys. Res.* **A486-3** (2002) 545, [https://doi.org/10.1016/S0168-9002\(01\)02162-3](https://doi.org/10.1016/S0168-9002(01)02162-3).
- [6] V.E. Blinov *et al.*, *ICFA Beam Dynamics Newsletter* **48** (2009) 195, http://icfa-usa.jlab.org/archive/newsletter/icfa_bd_nl_48.pdf.
- [7] S.I. Eidelman *et al.* (KEDR collaboration), *Nucl. Phys.* **B218-1** (2011) 155, <https://doi.org/10.1016/j.nuclphysbps.2011.06.026>
- [8] I.A. Rachek *et al.*, *Phys. Scr.* **T166** (2015) 014017, <https://doi.org/10.1088/0031-8949/2015/T166/014017>.
- [9] E.V. Abakumova *et al.*, *Nucl. Instrum. Methods Phys. Res.* **A659-1** (2011) 21, <https://doi.org/10.1016/j.nima.2011.08.050>.
- [10] M. Ablikim *et al.* (BESIII Collaboration), *Phys. Rev.* **D90** (2014) 012001, <https://doi.org/10.1103/PhysRevD.90.012001>.
- [11] V.C. Zhukovsky and I. Herrmann, *Sov. J. Nucl. Phys.* **14** (1971) 150.
- [12] E.V. Abakumova *et al.*, *Phys. Rev. Lett.* **110** (2013) 140402, <https://doi.org/10.1103/PhysRevLett.110.140402>.
- [13] E.A. Kozyrev *et al.*, *Phys. At. Nucl.* **78** (2015) 358, <https://doi.org/10.1134/S1063778815020192>.

High Field Studies for CLIC Accelerating Structures Development

I. Profatilova

CERN, Geneva, Switzerland

Institute of Applied Physics, National Academy of Sciences of Ukraine, Sumy, Ukraine

Abstract

Compact Linear Collider RF structures need to be able to achieve the very high average accelerating gradient of 100 MV/m. One of the main challenges in reaching such high accelerating gradients is to avoid vacuum electrical breakdown within CLIC accelerating structures. Accelerating structure tests are carried out in the klystron-based test stands known as the XBoxes. In order to investigate vacuum breakdown phenomena and its statistical characteristics in a simpler system and get results in a faster way, pulsed dc systems have been developed at CERN. To acquire sufficient breakdown data in a reasonable period of time, high repetition rate pulse generators are used in the systems for breakdown studies, so-called pulsed dc system. This paper describes the pulsed dc systems and the two high repetition rate circuits, which produce high-voltage pulses for it, available at CERN.

Keywords

CLIC; vacuum breakdown; pulsed dc system; breakdown rate.

1 Introduction

The Compact Linear Collider (CLIC) is one of the candidates for the next generation high-energy linear colliders. In order to reach up to the target 3 TeV and maintain an acceptable length, the accelerating gradient must be around 100 MV/m. This results in surface electric fields of more than 200 MV/m on the copper surface of accelerating structures. With such fields, vacuum breakdowns sometimes occur and these breakdowns disrupt the accelerated beam. Breakdowns are one of the main performance limitations for CLIC and other high-gradient linacs. Whenever a breakdown happens, it results in partial or full loss of luminosity for that pulse. The breakdowns have a certain probability of occurring and obtaining a low breakdown rate ($3 \cdot 10^{-7}$ breakdowns per pulse per meter) in CLIC accelerating structures is a critical requirement for a successful operation.

A vacuum breakdown is a sudden exchange of charge occurring between two electrodes with a high potential difference in vacuum conditions and results in large currents [1]. Vacuum breakdown is one of the main limitations to achieve the required accelerating gradient in CLIC. This effect can produce strong back reflection of the incident RF, reduction of the luminosity of the accelerator complex, surface damages and other undesirable effects [2].

For understanding breakdown phenomena in vacuum and for finding the best materials, treatment methods and study the conditioning process for accelerating structures of future colliders several pulsed dc systems have been developed at CERN. The first system, its opportunities and results are described in several publications [1–4]. The initial electrical circuit for the pulsed dc systems was based on a mechanical relay and gave possibilities to apply voltage at a maximum repetition rate of 0.5 Hz [3]. Breakdown field strengths, evolution of field enhancement factor for different materials and other measurements were done [5,6].

2 Pulsed dc systems

For studying values related to breakdown (breakdown rate, dark current, delay to breakdown and etc.), for finding better parameters of conditioning process with similar surface electric field as in RF structures

a pulsed dc system capable for much higher repetition rates was designed and built. This system helps to get results much faster than in RF measurements. For example, the same amount of data taken in RF measurements with 50 Hz in 1 months could be taken with a pulsed dc system at 1 kHz during about 2 days.

The pulsed dc system is used for studying breakdown phenomenon between two electrodes. It includes as main parts: a vacuum chamber with electrodes inside, an electrical circuit or generator, and a DAQ system.

2.1 Vacuum chamber for pulsed dc system

Currently the Large Electrodes System (LES) is used as a vacuum chamber for pulsed dc system (Fig. 1). It is a compact vacuum system which contains two plane electrodes. High voltage with a positive polarity is applied to one of them (an anode), while the second electrode is grounded (a cathode). They are held apart by a ceramic ring mounted away from the high-field area, which results in a gap between the electrodes, typically in the range of $60 \mu\text{m}$ for the experiments described in this report. As both electrodes are planar and the gap distance is small compared to the diameter of their working surfaces, 60 mm, they can be treated like a parallel plate capacitor. The electric field could be estimated as $E = V/d$, where V is applied voltage and d is gap distance.

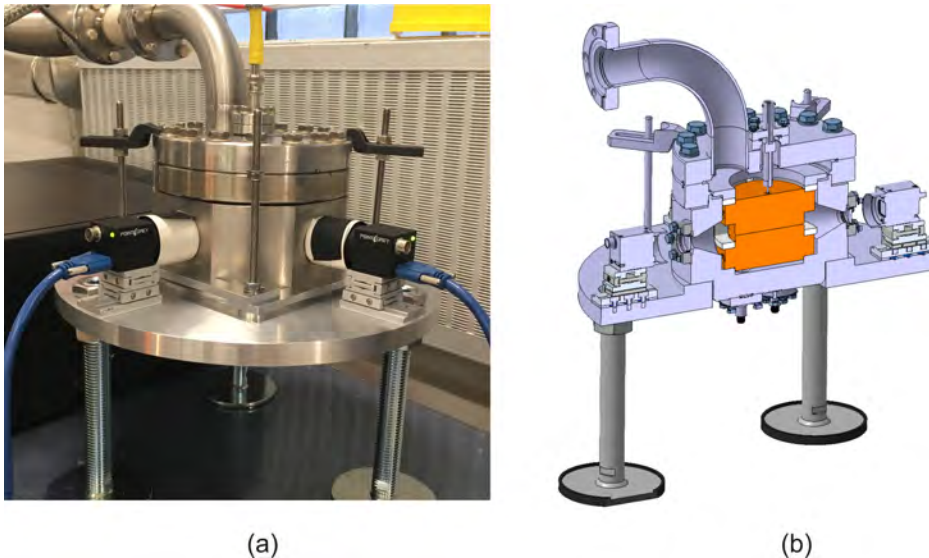


Fig. 1: Large Electrodes System: (a) photo, (b) 3D model

The vacuum level required for the tests is $10^{-8} - 10^{-10}$ mbar and is achieved by using two pumps: a roughening pump for initial pumping from atmospheric pressure to the mbar range, and turbo pump to reach a lower pressure.

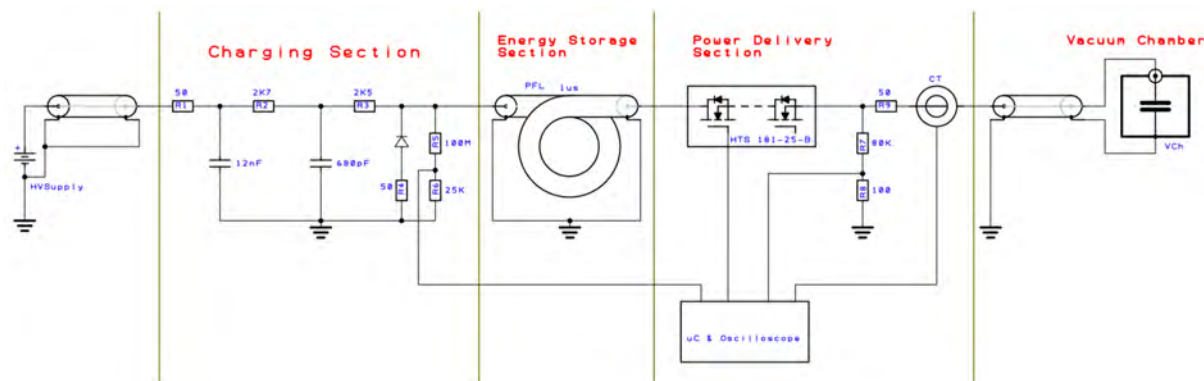
2.2 High repetition rate generators for pulsed dc system

In order to obtain data on the breakdown phenomenon in d.c. with a rate of about $1 \cdot 10^{-7}$ breakdown per pulse and in a reasonable period of time a high-voltage generator with high repetition rate is required.

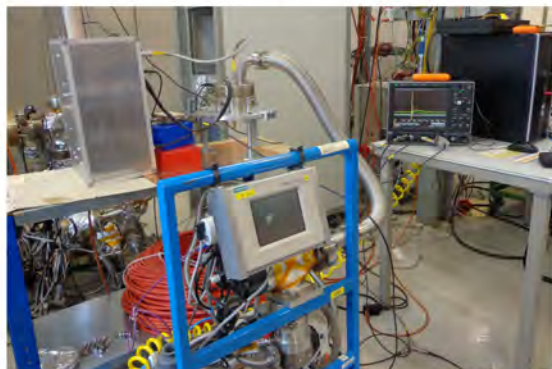
A first high-voltage pulse generator, so-called High Repetition Rate circuit (HRR circuit), for pulsed dc system was designed and built by R.H. Soares and M.J. Barnes [7]. The following performances were achieved: the circuit provides the possibility to apply pulses with voltage up to 12 kV with repetition rate up to 1 kHz across the samples in the pulsed dc system. Following the system specific features, the circuit has two modes:

- *Running mode* - without breakdown - during applying high voltage pulse, if breakdown doesn't happen, the voltage should not drop more than 1% of its maximum value.
- *Breakdown mode* - during applying high voltage pulse the increasing of current should be detected and pulsing should be stopped for several seconds. When breakdown occurs, the circuit should deliver a rectangular current pulse of several 10's of Amps and 2 μ s duration.

HRR circuit was build based on MOSFET switch technology and a BEHLKE HTS 181-25-B is used as a switch. The electrical circuit and a photo are shown in Fig. 2.



(a)



(b)

Fig. 2: HRR circuit: (a) schematic of electrical circuit; (b) photo together with Large Electrodes System

After few years of testing pulsed dc systems with the HRR circuit, a new generator started to be exploited. As in RF tests the pulse is roughly rectangular and has 200 ns length, the new generator had this additional requirement: a rectangular pulse shape and pulse length closer to range used in RF. This should make d.c. results more comparable with RF.

The new generator was produced by the Portuguese company "Energy Pulse Systems" [8]. A EPULSUS-FPM1-10 incorporates a positive-voltage Marx generator, with 15 stages, based on state of the art SiC MOSFET technology. The EPULSUS-FPM1-10 (hereinafter simply called as Marx generator) was designed especially for pulsed dc system.

The Marx generator circuit generates a high-voltage pulse from a low-voltage d.c. supply [9]. This is achieved by charging the 15 capacitors of the device which are connected in parallel, then discharging them in series using very fast switching devices. The simplified diagram of the generator is shown in Fig. 3.

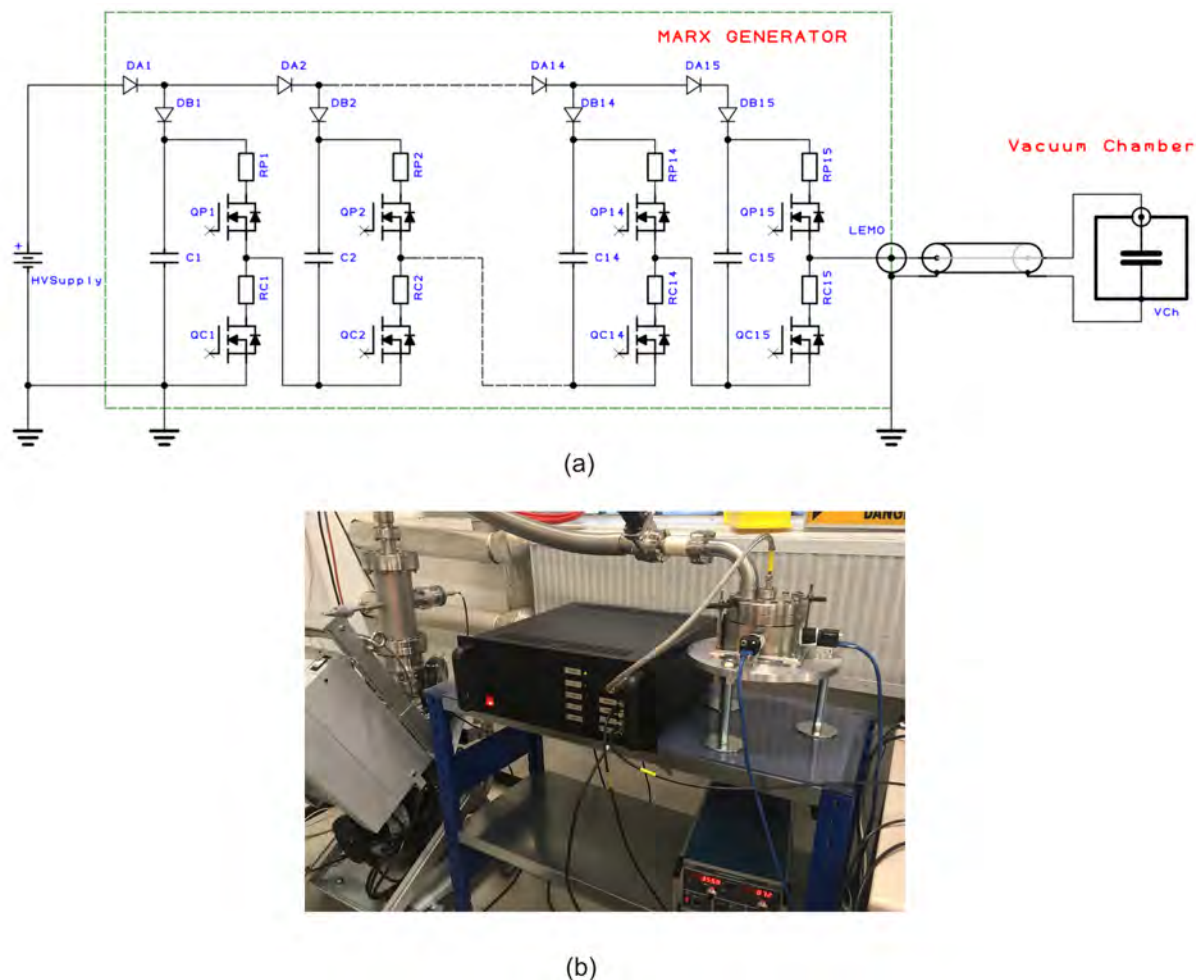


Fig. 3: The Marx generator for pulsed dc system: (a) the simplified positive solid-state Marx generator circuit, (b) a photo with Large Electrodes System.

The Marx generator can deliver up to 10 kV and 50 A square wave repetitive pulses with adjustable length. Small rise and fall times are provided square-shaped high-voltage pulses. The maximum frequency 6 kHz limited by the internal power dissipation. The d.c power supply in this circuit is external medium voltage power supply reaching up to 1250 V and 250 mA.

The typical waveforms taken with Large Electrodes System for both circuits are shown in Fig. 4. When the capacitor charges a current pulse is produced. If no breakdown occurs, in the HRR circuit the current is discharged slowly through the R7 and R8 resistors (Fig. 2 (a)), while for the Marx generator the discharge is shown by a negative current signal at the end of the pulse (Fig. 4 (d)). If a breakdown occurs, the current increases rapidly to several 10's of Amps (Figs. 4 (c) and (d)). This current increase is used for breakdown detection in both circuits. The current starts getting higher than usual charging current and breakdown is detected. The voltage drops almost to zero during breakdown. Both circuits (HRR circuit and Marx generator) have implemented, in different ways, a so-called "delay after breakdown", i.e. a period during which the current between the electrodes is sustained after a breakdown. The $2 \mu\text{s}$ delay after breakdown for both circuits is shown in Figs. 4 (c) and (d).

According to Fig. 4, if a $5 \mu\text{s}$ signal is sent to the controller, the HRR circuit will produce a pulse with effective pulse length $21.3 \mu\text{s} \pm 10\%$ (voltage signal higher than 90%), while the Marx generator's pulse will be $5 \mu\text{s} \pm 5\%$. Table 1 shows the main parameters for both generators. The big fall time for

the voltage signal generated with the HRR circuit (130 μs from 90% to 10% voltage signal amplitude at 4 kV from sending 5 μs signal to the switch) led to the requirement to change the circuit.

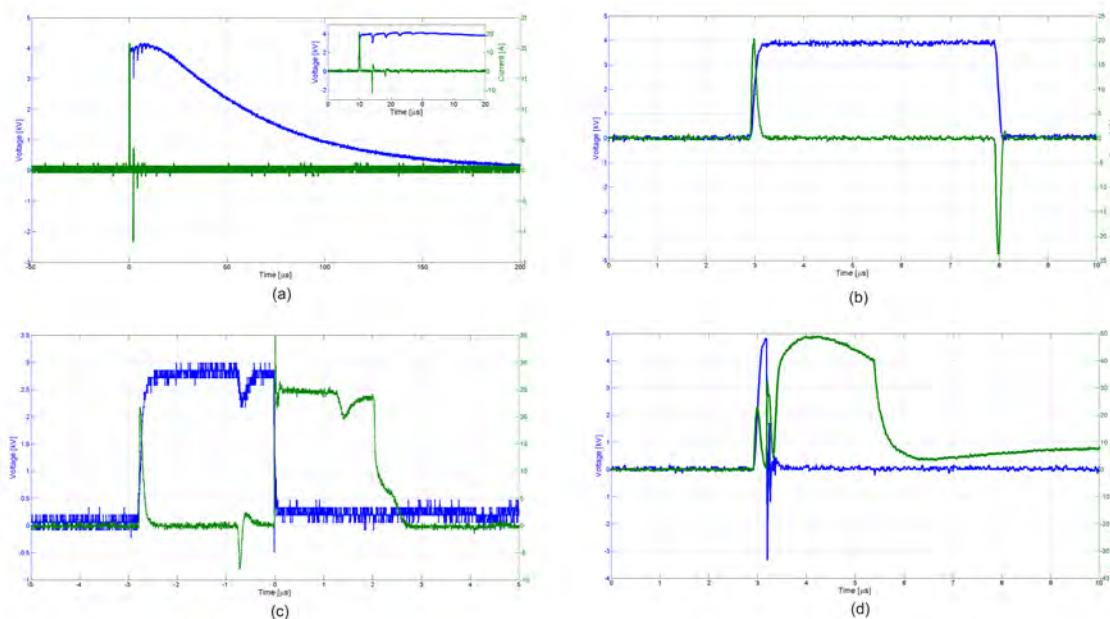


Fig. 4: Typical waveforms taken with the Large Electrodes System and: (a) HRR circuit without breakdown at 4 kV and 5 μs pulse signal sent to the controller, (b) Marx generator without breakdown at 4 kV and 5 μs pulse signal to the controller, (c) HRR circuit with breakdown at 2.9 kV; (d) Marx generator with breakdown at 5.12 kV. Current signals are shown in green, voltage signals are shown in blue.

Table 1: Comparison of main parameters HRR circuit and Marx generator.

Parameter	HRR circuit	Marx generator
Maximum voltage	12 kV	10 kV
Maximum frequency	1 kHz	6 kHz
Pulse length (switch control signal)	3 - 7 μs	400 ns - 100 μs
Delay after breakdown	2 μs	600 ns - 2.3 μs
Stored energy (for 10 kV)	~ 1.4 J	~ 1.4 J
Rise time (for 4 kV)	200 ns	180 ns
Fall time (for 4 kV)	130 μs	100 ns

3 Results and conclusions

Pulsed dc systems are being used at CERN for studying breakdown phenomenon. A comparison of data from RF and d.c. conditioning experiments is shown at Fig 5. The scaled gradient is the value taken for better comparison the results from pulsed dc system and RF measurements. It is:

$$E_{scaled} = \frac{E(MV/m) \cdot t_p^{1/6}(ns)}{BDR^{1/30}} \quad (1)$$

where E is the electric field in MV/m , t_p the pulse length taken in ns , BDR the breakdown rate (or breakdown probability) defined as:

$$BDR = \frac{Breakdowns}{Pulses} \quad (2)$$

For d.c. tests the copper electrodes followed the same heat treatment procedure as in RF accelerating structures. Also the algorithm for conditioning tests in a pulsed dc system was adapted to RF measurements to make it more similar [10]. The pulsed dc system's data shown in Fig. 5 were taken with the HRR circuit. Results from d.c. tests have similar behavior as from RF measurements. Experiment in the pulsed dc system with a pulse shape and length similar to the RF pulse will produce data for understanding the difference in magnitude of the scaled electrical field between RF and d.c. results.

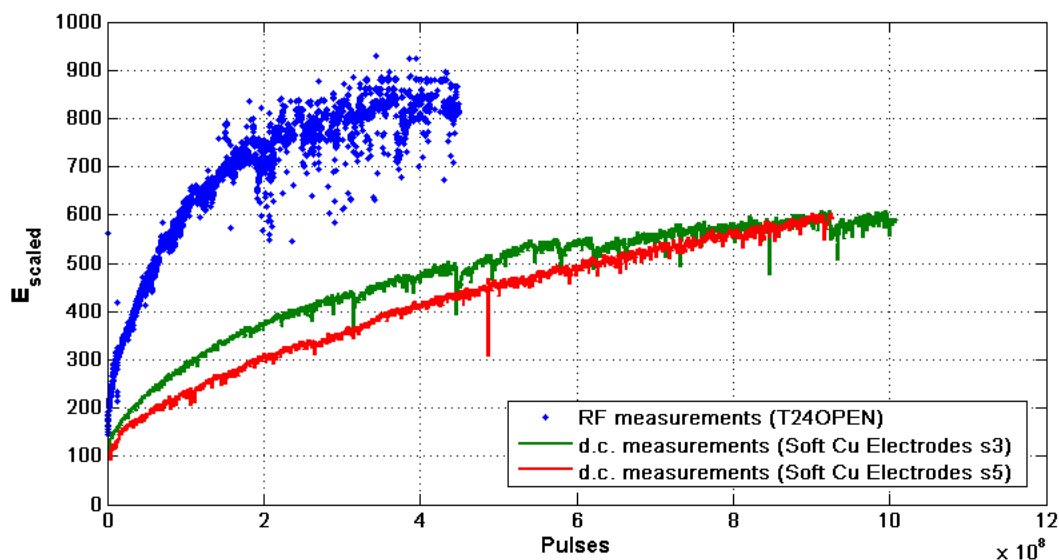


Fig. 5: Comparison of the scaled electric field versus the accumulated number of pulses for d.c and RF results [10]

Two high repetition circuits used as generators for applying high voltage pulses are described and compared in this paper. The Marx generator is a significant improvement of the system for studying breakdown phenomena. It produces a pulse shape and pulse length range closer to the RF case. Also the Marx generator provides more variables for possible future tests with pulsed dc systems.

4 Acknowledgements

The author would like to thank Walter Wuensch from CERN and Oleg Kondratiev from "Energy Pulse Systems" for their help and constructive feedback.

References

- [1] N. Shipman, Ph.D. thesis, Manchester University, 2014.
- [2] J. Kovermann, Ph.D. thesis, University of Aachen, 2010.
- [3] M. Kildemo, *Nucl. Instrum. Methods Phys. Res.* **A530** (2004) 596.
- [4] H. Timko, Ph.D. thesis, University of Helsinki, 2011.
- [5] A. Descoedres *et al*, *Phys. Rev. ST Accel. Beams* **12** (2009) 092001.
- [6] A. Descoedres *et al*, *Phys. Rev. ST Accel. Beams* **12** (2009) 032001.
- [7] R.H. Soares *et al*, A 12 kV, 1 kHz pulse generator for breakdown studies of samples for CLIC RF accelerating structures, Proceedings of IPAC2012 (3rd International Conference on Particle accelerator (IPAC 2012), New Orleans, USA, 2012), p.3431.
- [8] <http://energypulsesystems.pt/>, last accessed 15 February 2017.

- [9] L. M. Redondo, J. F. Silva, P. Tavares, and E. Margato, Solid-state Marx Generator Design with an Energy Recovery Reset Circuit for Output Transformer Association, 2007 IEEE Power Electronics Specialists Conference, 2007.
- [10] L. Mercadé Morales, M.Sc. thesis, University of Valencia, 2016.

Low Energy Electron Cooler for NICA Booster

A.P. Denisov and V.V. Parkhomchuk
BINP, Novosibirsk, Russia

Abstract

BINP has developed an electron cooler to increase the ion accumulation efficiency in the NICA (Nuclotron-based Ion Collider fAcility) heavy ion booster (JINR, Dubna). Adjustment of the cooler magnetic system provides a highly homogeneous magnetic field in the cooling section $B_{trans}/B_{long} \leq 4 \cdot 10^{-5}$, which is vital for efficient electron cooling. First experiments with an electron beam performed at BINP demonstrated the target DC current of 500 mA and electron energy of 6 keV.

Keywords

NICA; booster; electron cooling; solenoid; magnetic field shape.

1 Introduction

1.1 NICA project

The main goal of the NICA project is to study the properties of dense baryonic matter including strong interaction and transition between baryonic matter and QGP (Quark-Gluon Plasma) [1]. This is studied in collisions of high-energy heavy ion beams; however, the most sophisticated part is to provide such beams. NICA Nuclotron will accelerate fully stripped ions up to an energy 4.5 GeV per nucleon, but since the Nuclotron is not able to strip ions by itself, a Booster will be added.

The NICA Booster will accumulate ions and accelerate them up to an energy, at which the ion stripping is the most efficient, and then send them to the Nuclotron. The Booster will include the low energy electron cooling system performing two main functions: to increase the ion accumulation efficiency and to cool the ion beam before stripping.

1.2 The electron cooler for the NICA Booster

The electron cooler will operate with ions at two different energies: an injection energy of 3.2 MeV per nucleon and an intermediate energy of 65 MeV per nucleon. The electron cooler for the NICA Booster provides an electron beam with energy ranging from 1.5 keV to 60 keV, which is necessary to match the energies of the electron and ion beams. More information about electron cooling can be found in [2]. The schematic layout of the cooler is shown in Fig. 1.

The most important part of the cooler is the cooling section. The quality of the magnetic fields in this section determines the efficiency of the cooling process. To achieve cooling times around one second the straightness of the magnetic field in the cooling section should be better than 10^{-5} rad. However, many factors such as assembly errors and magnetization of the magnetic elements affect the magnetic field straightness. These factors can change during the electron cooler operation, so one needs to compensate for them. Therefore, this article emphasises on the methods of magnetic measurements and adjustments of the magnetic system.

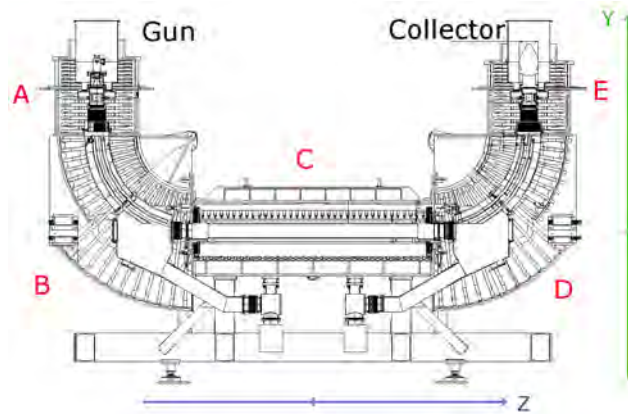


Fig. 1: The magnetic system of the electron cooler. A,E – solenoids of gun and collector; B,D – bending magnets and dipoles; C – the cooling section including the main solenoid.

2 Magnetic measurements

Magnetic measurements discussed in this section include only measurements of magnetic field on the main solenoid axis. Two different measuring devices were used: Hall sensor and compass. The Hall sensor is widespread, so it is not described in this article. Using the Hall sensor, we measured magnetic fields along the cooling section created by each individual magnetic element, providing a rough estimate of their magnetization (Fig. 2). The compass is actually the magnetic needle, so it can measure the direction of magnetic field force lines with an accuracy about 10^{-6} rad.

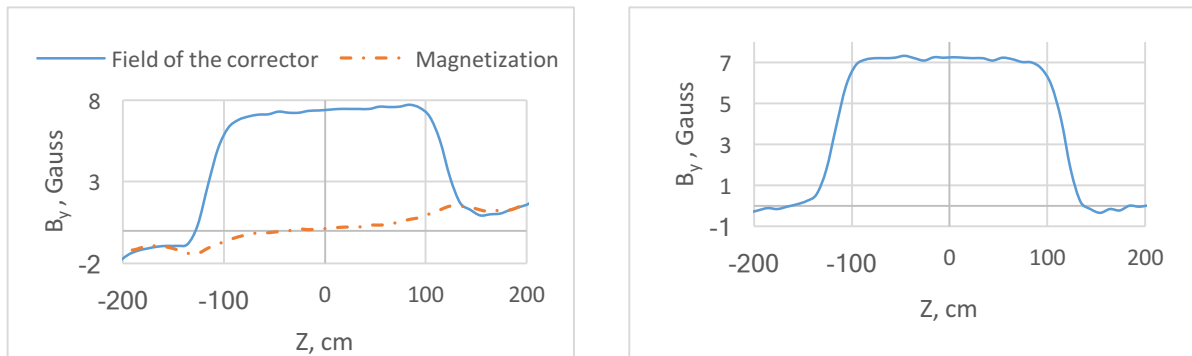


Fig. 2: Hall measurements of magnetic fields created by the vertical corrector in the cooling section. The graph on the left represents raw data, and on the right the processed response function of the corrector is shown. The corrector current is 5 A.

The scheme of magnetic measurements with the compass is shown in Fig. 3. The feedback system has laser optics whose optical axis aligns with the magnetic axis of the main solenoid. A laser beam propagates along the optical axis and reflects from a mirror placed on the compass. The reflected beam reaches a photo sensor that measures the displacement of the laser beam. In the presence of a transversal magnetic field in the cooling section, the compass is tilted from the solenoid axis. While it is tilted, the feedback system controls a compensating transverse magnetic field created by special coils placed near the compass to set the tilt of the compass to zero. By performing measurements with the compass along the cooling section the profile of the transverse magnetic field is measured.

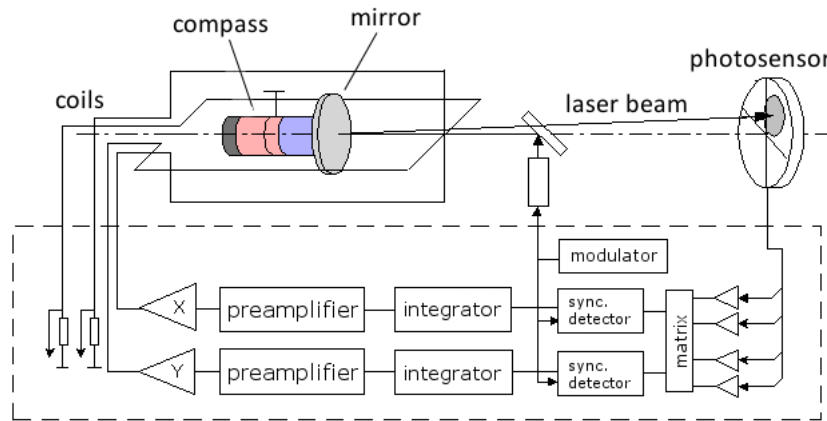


Fig. 3: The principal scheme of compass measurements

The ideal situation for the electron cooling is when there is no transverse magnetic field in the cooling section. However, due to assembly errors in magnetic elements and magnetization, the real magnetic profiles are always non-zero. In order to control the shape of the magnetic profiles the magnetic system of the electron cooler includes special correctors. Those correctors and methods of compensation of transverse magnetic fields are discussed in the next sections.

3 Magnetic field straightness

As noted in section 2, the magnetic profiles are always non-zero due to such factors as magnetization and solenoid assembly errors. However, these profiles can be corrected by using a special construction of the main solenoid.

The main solenoid consists of many independent coils, each of which can slightly rotate from its original position (Fig. 4). As a rotated coil contributes to the transverse magnetic profile, the right combination of coil rotations can reduce the magnetic profiles to zero.

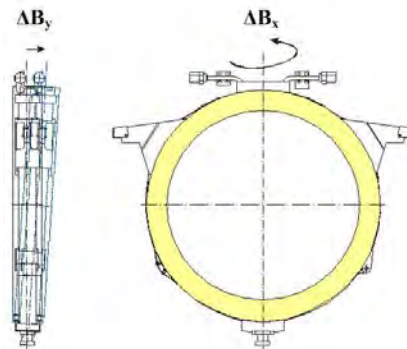


Fig. 4: One coil of the main solenoid. Moving the two upper handles, the coil can be rotated with respect to its pivot point, located at the bottom of the coil.

The procedure of compensation includes several steps. The initial profile is measured. Subsequently a correction to the position of one of the coils is applied and the profile is measured again. The difference between these two measurements, normalized to the correction value, gives the response function of the coil (Fig. 5). We assume that all corrections are small and the response functions have a linear dependence on these corrections. Assuming that the response functions are the same for all coils the compensating field is modeled (1).

$$B(\vec{a}, z) = \sum_j a_j f(z - \xi_j) \quad (1)$$

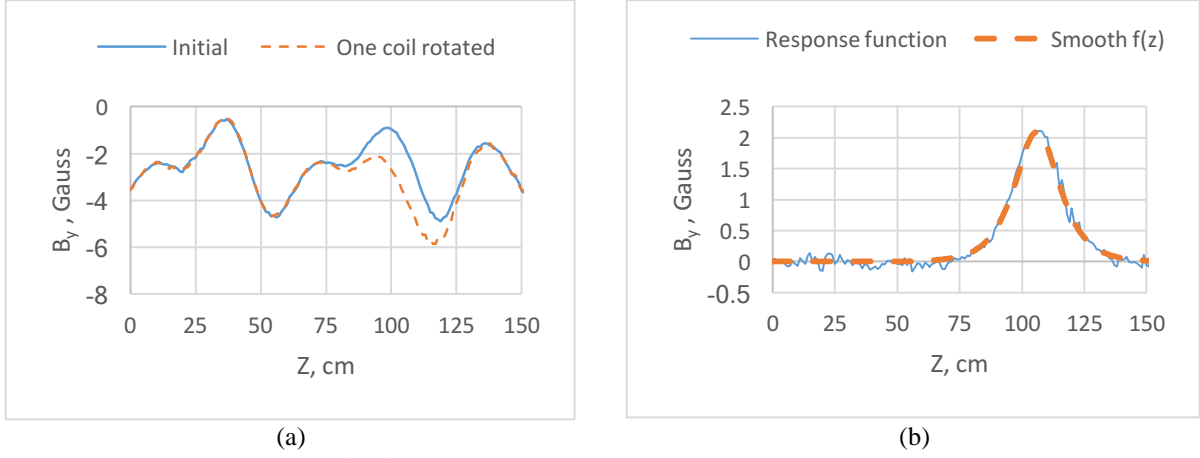


Fig. 5: Measurements of the coil response function

Values of the corrections can be calculated using the least squares method.

$$L(\vec{a}) = \sum_i (b_i - B(\vec{a}, z_i))^2 + g \cdot \sum_j a_j^2 \rightarrow \min, \quad (2)$$

where $f(z)$ is the response function of the coil, a_j is the value of the coil correction, b_i and z_i are values of the transverse magnetic field and the coordinates of the measurement location, g is the coefficient limiting the area of influence of each individual coil. $g = 0$ corresponds to the case when each coil affects unlimited area and the corrections with no limitation become too large (Fig. 6). However, if $g > 0$ the constructed field compensates the magnetic profile incompletely, and the procedure has to be iterated several times.

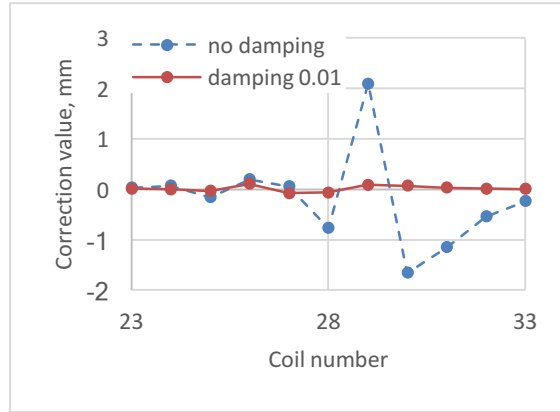


Fig. 6: Correction values for different given damping coefficients

After several iterations of applying corrections to the solenoid coils, the straightness of the magnetic field in the cooling section reached $4 \cdot 10^{-5}$ rad (Fig. 7). Nevertheless, it is not enough to adjust the coils of the main solenoid only once. During experiments with electron cooling the operational fields of the cooling system can change, thus the magnetization of those elements changes. Since the efficiency of the electron cooling strongly depends on the quality of the magnetic field, the changing magnetization must be compensated in real time. The scheme of compensation of the magnetization is discussed in the next section.

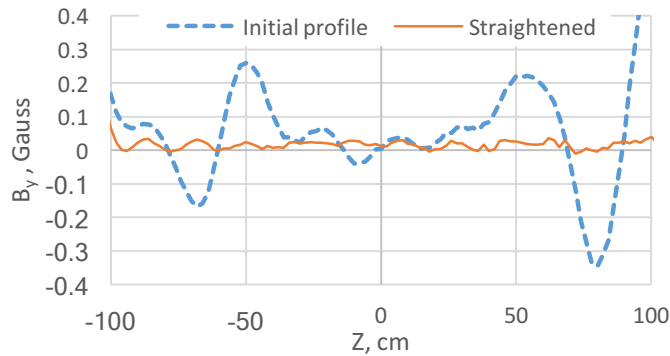


Fig. 7: Profiles of the vertical magnetic field in the cooling section

4 Magnetization

Magnetization of the magnetic elements contributes to the transversal magnetic field and depends on operational magnetic fields. In this section, the number of presented operational regimes is reduced, because the goal is to demonstrate the methodology rather than display all the results. The list of discussed operational regimes is presented in Table 1.

Table 1: Operational regimes used in measurements and corresponding operational currents of magnetic elements.

Regime name	Supply current of magnetic elements		
	Main solenoid	Bending magnets and vertical solenoids	Dipoles
Regime 1	167.4 A	500 A	221.2 A
Regime 2	134.4 A	400 A	178 A
Regime 3	100 A	300 A	132.7 A

The first well-known problem due to magnetization is non-repeatability of magnetic profiles (Fig. 8). However, this problem has a well known solution called cycling, which consists of ramping the magnets down and up to reduce hysteresis effects. To achieve repeatability, the cycling is applied every time the operational regime is changed, and thus, for the same regimes we get the same profile curves while the shape of curves related to different regimes can differ (Fig. 9).

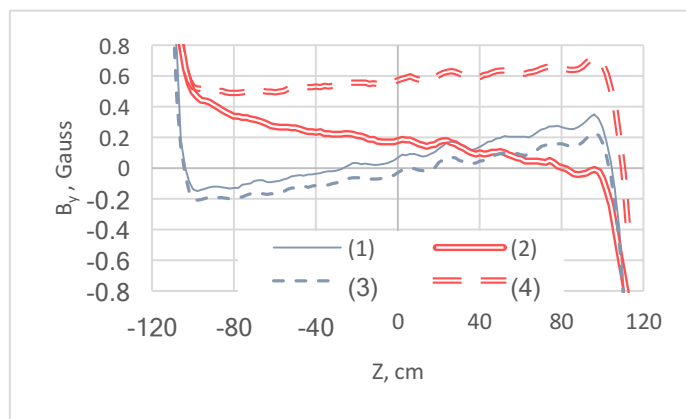


Fig. 8: Non-repeatability of measurements. Curves (1) and (3) correspond to Regime 2, (2) and (4) to Regime 3. Regimes were changed in the following order: from (1) to (2) without cycling, then to (3) and then to (4) with cycling. States (2) and (4) both correspond to Regime 3, but the profiles are different.

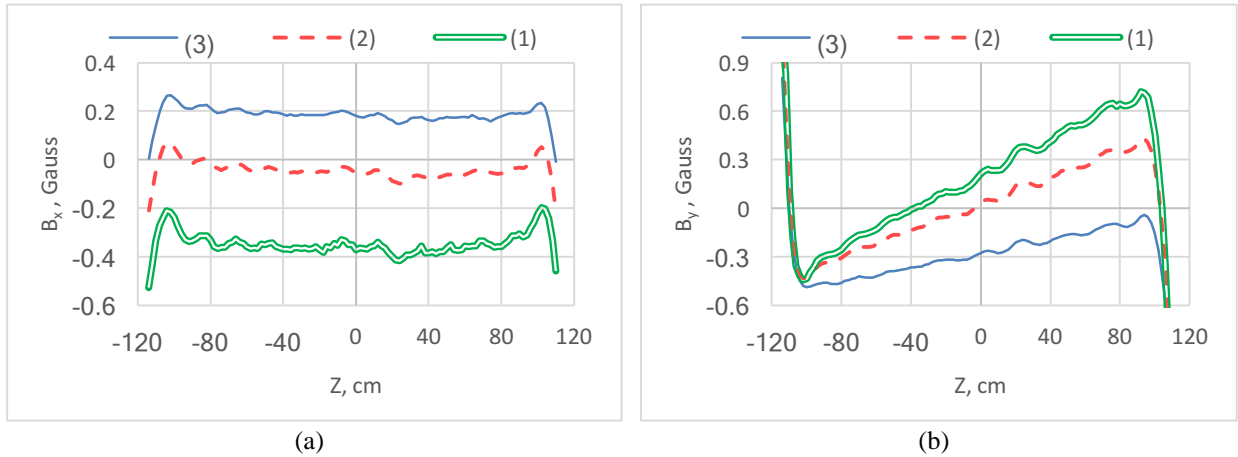


Fig. 9: Magnetic profiles at different operational regimes. (a) shows horizontal profiles, (b) shows vertical profiles. States 1,2 and 3 represent regime numbers which are described in Table 1.

For simplicity we assume that the longitudinal component of the magnetic field in the cooling section depends only on the operational current of the main solenoid. Now we can take into account the displacement of the measured profile curves. In Section 2, we noted that the optical axis of the compass feedback system is aligned with the magnetic axis of the main solenoid. If there is a tilt between these two axes, the longitudinal field contributes to the measured value of the transversal field (Fig. 10). The contribution is proportional to the longitudinal field, so it can be calculated by comparing several measurements at different operational regimes and then be excluded from further consideration.

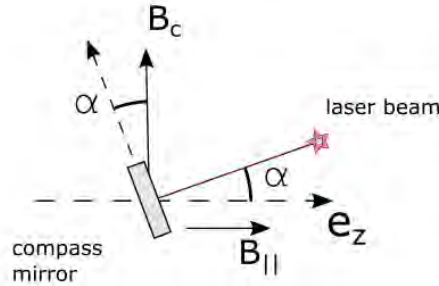


Fig. 10: Systematic measurement error due to the tilt between the optical axis and the axis of the main solenoid. $B_c^* = B_{\parallel} \cdot \sin \alpha$, where α is a tilt value, B_{\parallel} is the longitudinal magnetic field strength, B_c^* is an addition to the measured transverse component of the magnetic field.

Another issue is the slope of the magnetic profile changing with operational current (Fig. 9(b) and Fig. 11(a)). During magnetic measurements made at BINP the magnetic field strength in the cooling section was varied from 400 Gauss to 1 kGauss. Changing operational currents in all magnetic elements proportionally (with respect to the operational current of the bending magnets), the slope of the magnetic fields changes linearly with the operational current (Fig. 11(b)). Such profiles are compensated by special corrections of the coils of the main solenoid. As Figure 12 shows, as a result of such corrections, the slope of the magnetic field does not depend on the operational current anymore.

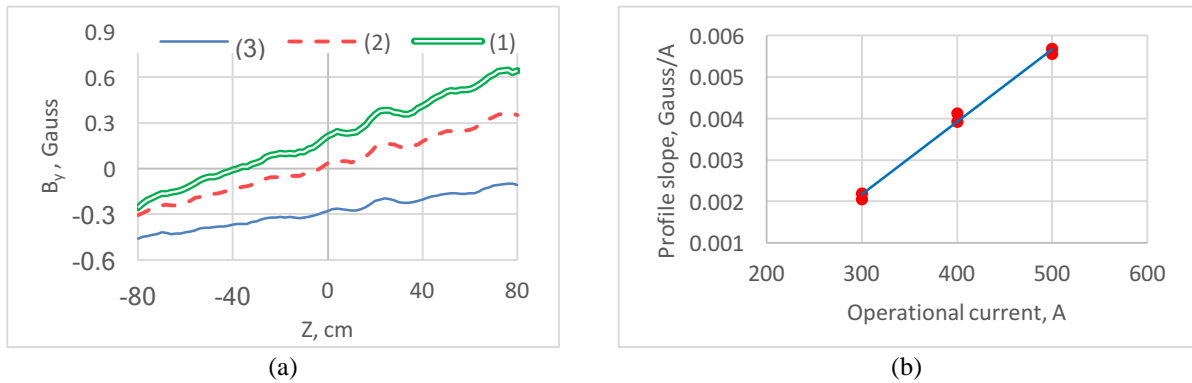


Fig. 11: Slope of the profile of the vertical magnetic field. Graph (a) is the profile limited by boundaries of the cooling site. Graph (b) demonstrates that if the operational currents are changed proportionally, the slope behaves according to a linear function of the operational current.

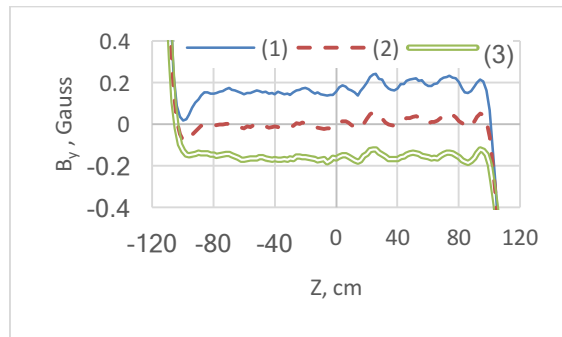


Fig. 12: By changing the operational current proportionally, a special correction to the coils of the main solenoid is applied, such that the shape of the vertical profile doesn't depend on the operational current.

The last question is how the magnetic profile changes, when the operational current is changed only in one symmetrical pair of the magnetic elements. In this case the measurements are similar to the previous ones. One varies only one operational current, measures the profiles and calculates the normalized difference, called the magnetization response function of the magnetic element. As shown in Fig. 13, the magnetization response function slightly depends on the operational current while the shape of the response function in the cooling section can be considered as constant. The total magnetization response is expected to be a linear function of all operational current deviations $\Delta B_y = k_1 \cdot \Delta I_1 + k_2 \cdot \Delta I_2 + k_3 \cdot \Delta I_3$, where $k_{1,2,3}$ are magnetization response functions of different pairs of elements.

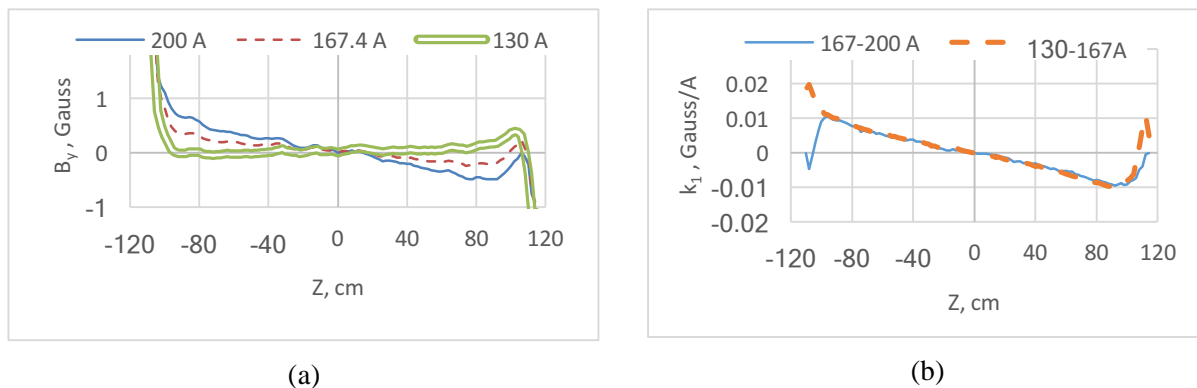


Fig. 13: Measurements of the magnetization response function of the main solenoid. (a) shows series of measurements, (b) shows the magnetization response functions for different combinations of the main solenoid operational current.

To prove this concept, we compared the measured profile curves and the curves calculated by Eq. (3) (Fig. 14(a)).

$$B_i = B_0 + k_1 \cdot \Delta I_1^i + k_2 \cdot \Delta I_2^i + k_3 \cdot \Delta I_3^i, \quad (3)$$

where B_0 is the original magnetic profile corresponding to regime 1, $\Delta I_{1,2,3}^i$ are deviations of operational currents of i -th regime from the currents corresponding to regime 1.

Going further one can say that the operational currents are just deviations from the zero-state corresponding to the residual magnetization. As a result, one can obtain the profile of the residual magnetization by simply subtracting the modelled curves of profiles from the measured ones using Eq. (4) (Fig. 14(b)).

$$B_i^{res} = B_i^{meas} - k_1 \cdot I_1^i - k_2 \cdot I_2^i - k_3 \cdot I_3^i \quad (4)$$

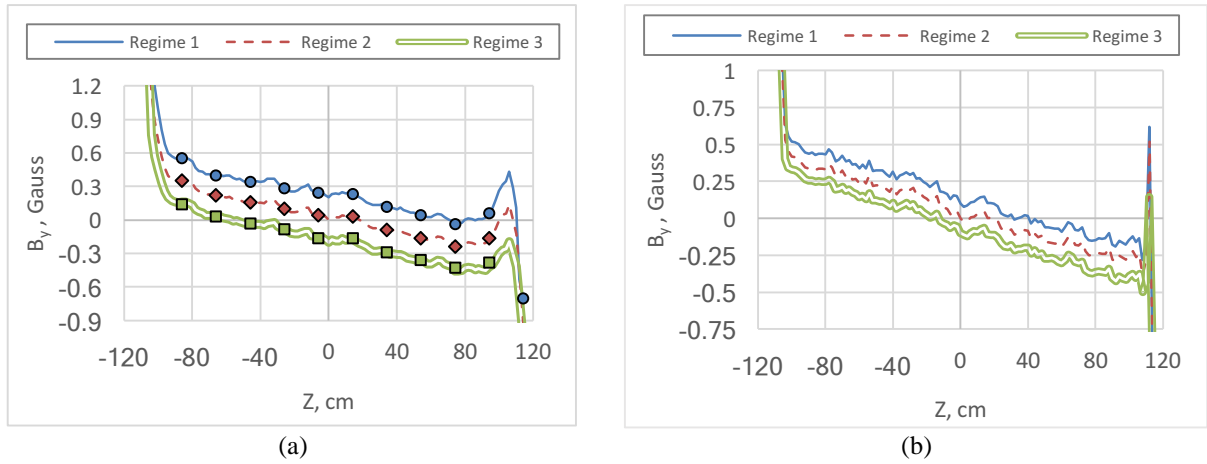


Fig. 14: Using magnetization response functions to recover the profile of the residual magnetization. (a) shows comparison of modelled and measured profiles, (b) shows calculated profiles of the residual magnetization. Presented curves are separated artificially.

As expected from the previous results, the residual magnetization does not depend on the operational currents.

With information about the residual magnetization and the magnetization response functions of magnetic elements one can predict changes of the magnetic profiles resulting from changes in operational magnetic regimes. Thus, such changes can be compensated by the magnetic correctors of the cooling section.

5 First experiments with an electron beam

Before disassembling the electron cooler and sending it to JINR (Dubna) we performed several experiments with an electron beam at an energy 6 keV. The most interesting parameters are the perveance of the cathode and the current losses (Fig. 15). After one week of cathode training, the electron beam DC current reached 500 mA and the current losses were less than 1 μ A. As Fig. 15(b) shows, initially current losses increase with increasing beam current. However, at some point a beam space charge creates a potential barrier near the suppressor that locks the secondary emission from the collector.

The subsequent increase of the beam current can lead to the opposite effect. If the potential barrier is too high and the electron beam is not able to reach the collector, in most cases the beam will die on the walls of vacuum chambers. In other words, it results in a rapid increase of current losses.

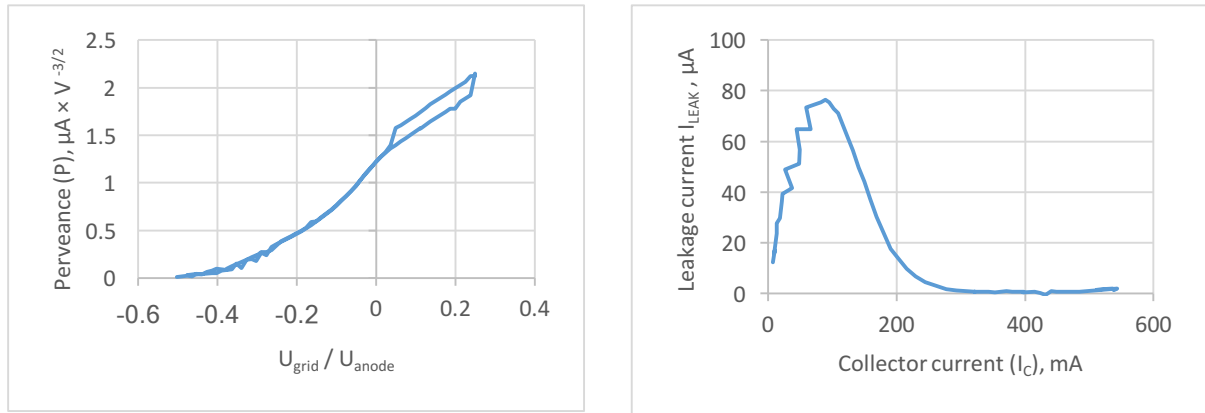


Fig. 15: Measurements of the perveance of the electron gun (a) and the electron beam current losses (b)

6 Conclusion

For efficient electron cooling it is vital to have high quality magnetic fields in the cooling section of the electron cooler system. This article covers basic aspects of measuring the magnetic fields and controlling the shape of the magnetic profile in the cooling section. However, obtained results are applicable for an operational field strength equal to or less than 1 kGauss. After the electron cooler is sent to JINR (Dubna), we will conduct further experiments with magnetic field strengths up to 2 kGauss and electron beam currents up to 3 A at an energy of 60 keV.

References

- [1] NICA – Nuclotron-based Ion Collider facility. Retrieved from <http://nica.jinr.ru>.
- [2] V.V. Parkhomchuk and A.N. Skrinski, Electron cooling: 35 years of development, Uspekhi Fizicheskikh Nauk, Russian Academy of Science (2000)

Design study of CEPC Alternating Magnetic Field Booster*

T. Bian^{*1}, J. Gao¹, Y. Cai², M. Koratzinos³, C. Zhang¹, X. Cui¹, Y. Wang¹, S. Bai¹, D. Wang¹, F. Su¹, M. Xiao¹

¹Institute of High Energy Physics, Beijing, China, ²SLAC National Accelerator Laboratory, CA, USA, ³University of Geneva, Geneva, Switzerland

Abstract

The CEPC is a next generation circular e^+e^- collider proposed by China. The design of the full energy booster ring of the CEPC is especially challenging. The ejected beam energy is 120 GeV, but that of the injected beam is only 6 GeV. In a conventional approach, the low magnetic field of the main dipole magnets creates problems. We propose operating the booster ring as a large wiggler at low beam energies and as a normal ring at high energies to avoid the problem of very low dipole magnet fields.

Keywords

CEPC; Booster; Alternating Magnetic Field; style.

1 Introduction

The CEPC (Circular Electron and Positron Collider) was proposed as an electron and positron collider ring with a circumference of 50-100 km to study the Higgs boson [1-3]. The CEPCB (the CEPC Booster) is a full energy booster ring of the same length, which ramps the beam from 6 GeV to 120 GeV. At the injected beam energy, the magnetic field of the main dipole is about 30 Gs; a low magnetic field will create problems for magnet manufacturing [4].

A preliminary design has been proposed in the Pre-CDR [5], but the problems of low field of the main dipole and dynamic aperture are not solved.

In this paper, we focus on these problems and find a reasonable solution. The wiggler scheme, which splits a normal dipole into several pieces with different magnet field direction, is adopted to avoid the problem of very low dipole magnet fields [6-8]. An analytic map method (Differential algebra) [9] is used to derive the Twiss functions of arbitrary order of the energy spread, such as β function, phase advance function or dispersion function. These functions are analytic functions dependent on the sextupole strength. First optimization of the high order chromaticities is done, and then a good dynamic aperture for both on-momentum and off-momentum particles is obtained.

2 Design goal

At present, the emittance of the CEPC is about $2.0 \times 10^{-9} m \cdot rad$, which is much lower than that in the Pre-CDR because of the crab waist. This makes the CEPCB harder to design because the emittance of the CEPCB at high energy is also reduced, which causes much stronger chromaticities and poses challenges to our design at the same time.

* Corresponding author: biantj@ihep.ac.cn

Figure 1 shows the x direction injection scheme. It assumes that the dynamic aperture of the CEPC at a 0.5% energy spread is 20-fold sigma and the beta function is 590 m.

The total space for injection:

$$\sqrt{2.0 \times 10^{-9} \times 590 \times 20} = 0.0217(\text{m})$$

8 sigma is retained for the circulating beam to get enough quantum life time:

$$\sqrt{2.0 \times 10^{-9} \times 590 \times 8} = 0.0087(\text{m})$$

6 sigma is retained for the injection beam to lose fewer particles:

$$\sqrt{3.5 \times 10^{-9} \times 590 \times 6} = 0.0086(\text{m})$$

Under this condition, 4 mm is retained for the septum. So, $3.5 \times 10^{-9} \text{ m} \cdot \text{rad}$ seems to be a reasonable option for the emittance of the CEPCB at 120 GeV.

Below are listed the design goals of the CEPCB:

The emittance of the CEPCB at 120 GeV is about $3.5 \times 10^{-9} \text{ m} \cdot \text{rad}$.

1% energy acceptance for enough quantum life time.

The dynamic aperture results must be better than 6 sigma (normalized by an emittance of $3 \times 10^{-7} \text{ m} \cdot \text{rad}$, which is determined by the beam from the linac) for both on-momentum and off-momentum (1%) particles.

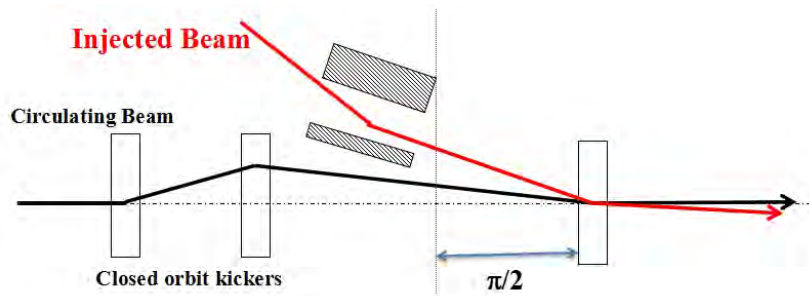


Fig. 1: Injection scheme

2.1 Linear lattice

The layout of the CEPCB is shown in Fig. 2. It is composed of 8 arcs and 8 straight sections with a total length of 63.8 km. The RF cavities are distributed in each straight section. The lattice for the CEPCB has been chosen to use the standard FODO cells with 90-degree phase advances in both transverse planes, which gives us a smaller emittance and a clear phase relationship between the sextupoles.

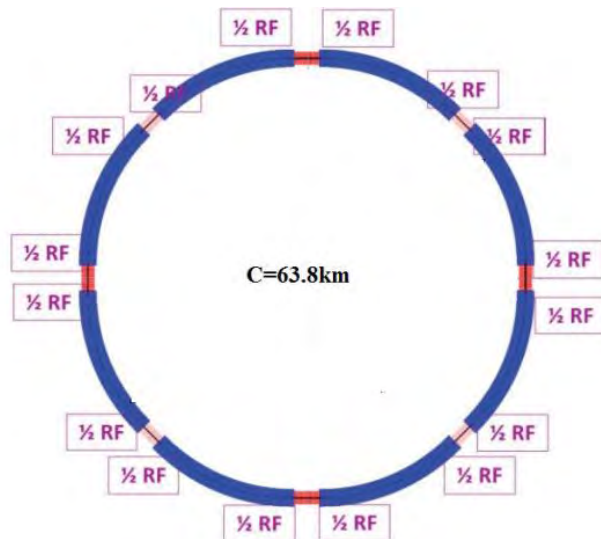


Fig. 2: Layout of CEPCB

A standard FODO cell with a 90-degree phase advance is shown in Fig. 3. The length of each bend is 30.4 m; the length of each quadrupole is 1.2 m, while the distance between each quadrupole and the adjacent bending magnet is 1.7 m. The total length of each cell is 70 m.

In order to make the main dipole stronger to avoid the problem of low magnetic field, we split the 30.4 m bend into 8 pieces. Adjacent dipoles in the pieces have different magnetic field directions, but the integral field strength of dipoles is the same as that of the normal dipole. We call this scheme the “wiggler scheme”, as shown in Fig. 4. The orbit off-set (the red curve in Fig. 4) in the dipoles decreases during the beam ramp up until the negative dipole changes the sign of the field and all the dipoles become normal bending magnets at 120 GeV. Figure 5 shows the bending angle of positive and negative magnets as a function of the ramping time.

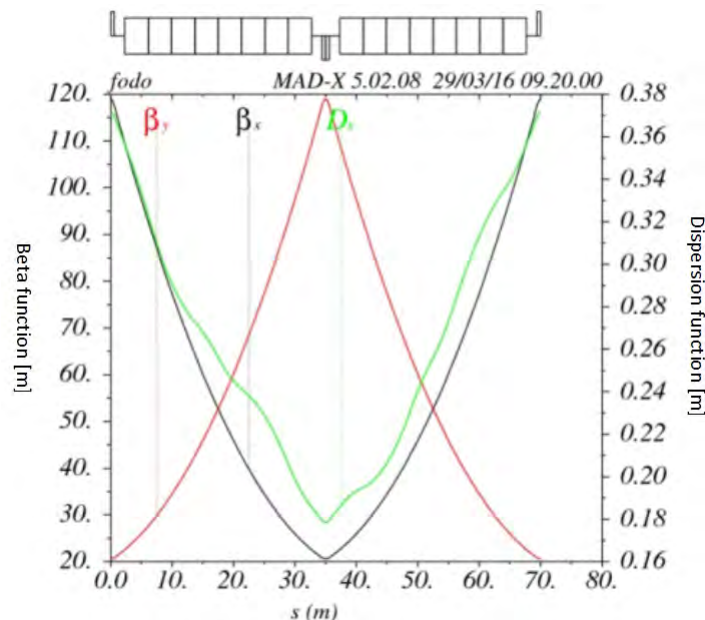


Fig. 3: Beta functions and dispersion function of a standard FODO cell with a 90/90-degree phase advance in the CEPCB.

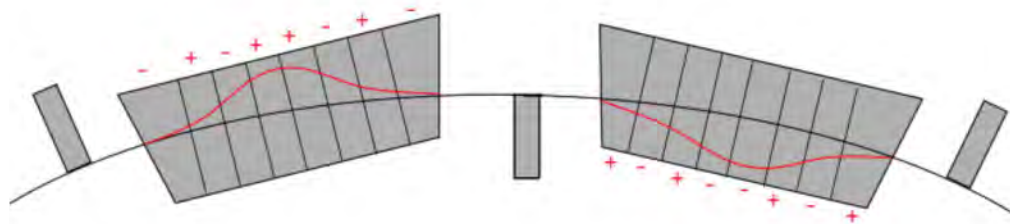


Fig.4: Twisted orbit in a FODO cell

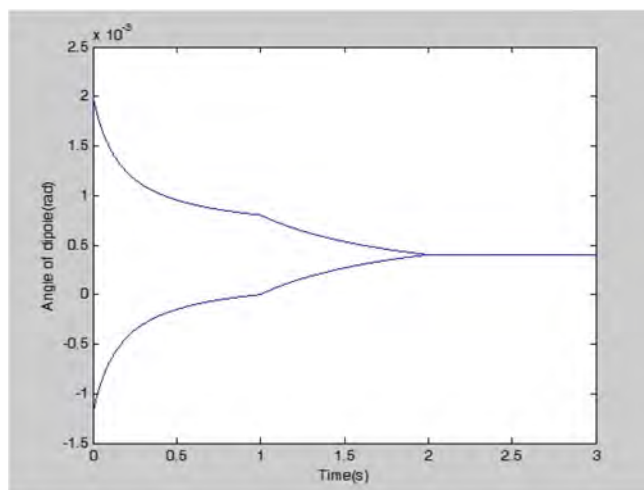


Fig. 5: Bending angle of the positive and negative magnet as a function of the ramping time

3 Sextupole scheme

The sextupole scheme of the CEPCB is shown in Fig. 6. “SF” and “SD” means focusing and defocusing sextupole. The long space means a 180-degree phase advance and the short space means a 90-degree phase advance. The “--” indicates a 45-degree phase advance between the focusing and defocusing sextupole. The FODO in Fig. 6 means that a FODO cell is inserted between two repeated sextupole arrangements. In total, 8 families of sextupoles are used.

SF1 SF1 SF2 SF2 SF3 SF3 SF4 SF4 -- SD1 SD1 SD2 SD2 SD3 SD3 SD4 SD4
FODO
SF1 SF1 SF2 SF2 SF3 SF3 SF4 SF4 -- SD1 SD1 SD2 SD2 SD3 SD3 SD4 SD4

Fig. 6: Sextupole scheme of CEPCB

In this scheme, the geometric terms are minimized because of the non-interleaved sextupole scheme. Two identical sextupoles stand apart by a 90-degree phase advance to cancel the beta-beat effect of off-momentum particles. Our goal is reducing the 2nd and 3rd order chromaticities to enlarge the energy acceptance. The analytic map method (Differential algebra) [9] is used to derive the 2nd and 3rd order chromaticities analytically, which contain the information of the 8 sextupole families.

When we optimize the 8 sextupole families using the 2nd and 3rd order chromaticities we have derived, we find that it is not enough to make the 2nd and 3rd order chromaticities as small as we expect. So, a tune shift between ARCs is considered. The analytic map method is also used in finding a right

phase advance between two ARCs, and we find the 43.3 degree is a good choice [7]. Figure 7 shows the tune as a function of the energy spread.

4 Dynamic aperture results and CEPCB parameters

To make the CEPCB more real, multi-pole errors are added. We estimate that the error of the CEPCB is at the same level as that of the LEP [10]; Table 1 shows the error estimation.

The tune we are using is 0.61/0.88, because it avoids some strong resonance lines. This tune is a rough estimation; tune scanning is needed to find a better tune.

With the error, cavity on and 0% and 1% energy spread, the dynamic aperture result is shown in Figs. 8 and 9. In the x direction, the dynamic aperture is 0.06 m and 0.04 m, and in the y direction, the dynamic aperture is 0.023 m and 0.016 m for on-momentum and 1% off-momentum particles. Figures 8 and 9 also show the tune shift depending on the amplitude, which is also constrained in a reasonable range. The parameters of the CEPCB are listed in Table 2.

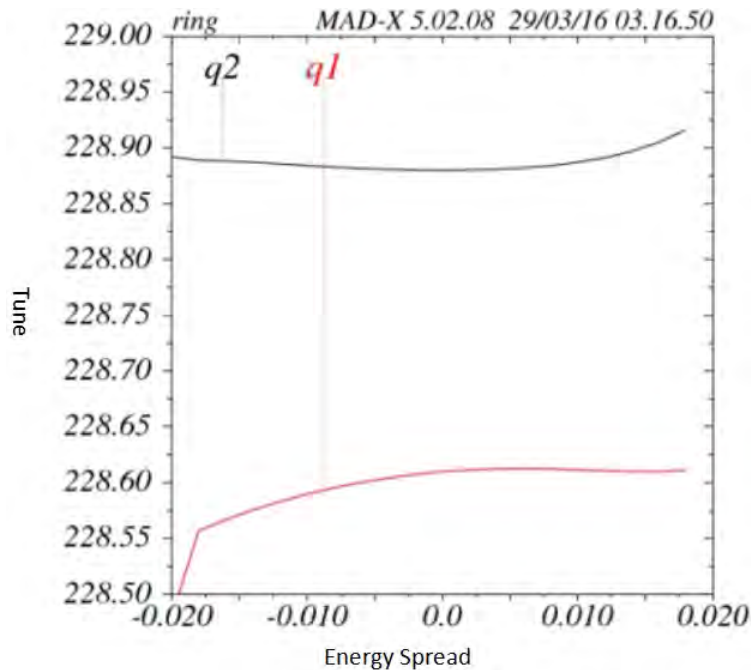


Fig. 7: Tune as a function of energy spread

Table 1: CEPCB multi-pole error estimate

	Bend	Quad	Sext
Quadrupole	8×10^{-4}		
Sextupole	2×10^{-4}	6×10^{-4}	
Octupole	7×10^{-5}	5×10^{-4}	1.7×10^{-3}

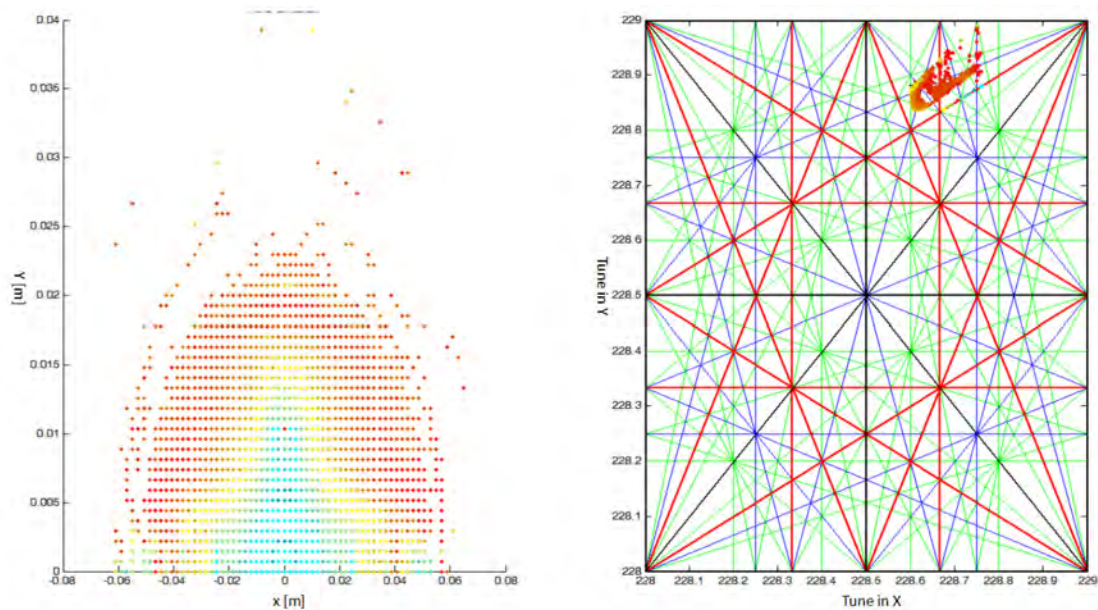


Fig. 8: Dynamic aperture and tune shift for the on-momentum particles

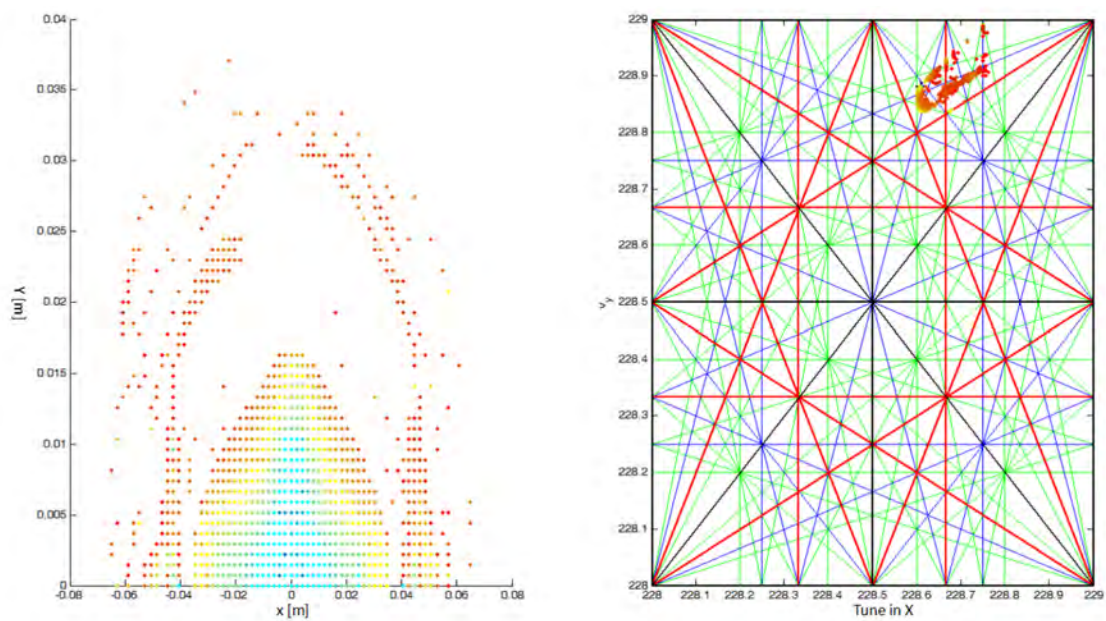


Fig. 9: Dynamic aperture and tune shift for the 1% off-momentum particles

Table 2: CEPCB parameters

6 GeV	Unit	Value	120 GeV	Unit	Value
Beam off-set in bend	cm	1.20	Beam off-set in bend	cm	0
Momentum compaction factor		2.33×10^{-5}	Momentum compaction factor		2.54×10^{-5}
Strength of dipole	Gs	-129/180	Strength of dipole	Gs	516.71
NB/beam		50	NB/beam		50
Beam current / beam	mA	0.92	Beam current / beam	mA	0.92
Bunch population		2.0×10^{10}	Bunch population		2.0×10^{10}
RF voltage	GV	0.21	RF voltage	GV	6
RF frequency	GHz	1.3	RF frequency	GHz	1.3
Synchrotron oscillation tune		0.21	Synchrotron oscillation tune		0.21
Energy acceptance RF	%	5.93	Energy acceptance RF	%	4.57
SR loss / turn equilibrium	GeV	5.42×10^{-4}	SR loss / turn equilibrium	GeV	2.34
Energy spread	%	0.0147	Energy spread	%	0.12
Horizontal emittance equilibrium	m*rad	6.38×10^{-11}	Horizontal emittance equilibrium	m*rad	3.61×10^{-9}

5 Summary

In this paper, a possible implementation for the CEPCB is proposed. The low field problem is solved by the wiggler scheme. The strength of the main dipole increases from 30 Gs to -129.18/+180.84 Gs. The damping times are much shorter, 4.7 seconds.

With the error, cavity on and 0% and 1% energy spread, the dynamic aperture is 9.2 sigma and 6.6 sigma in the x direction and 9.6 sigma and 6.4 sigma in the y direction.

In contrast to the design goal we proposed in the second section, this design is reasonable and meets the requirements. Further studies are required to include the effect of the earth magnetic field; shielding or correcting is needed.

References

- [1] G. Jie, Review of some important beam physics issues in electron–positron collider designs, *Modern Physics Letters A* **30** (11) (2015) 1530006.
- [2] W. Dou *et al.*, Optimization parameter design of a circular e+ e- Higgs factory. *Chinese Physics C* **37** (9) (2013) 097003.
- [3] S. Feng *et al.*, Method study of parameter choice for a circular proton-proton collider. *Chinese Physics C* **40** (1) (2015) 17001-017001.
- [4] K. Wen, Some Design Considerations and R&D of CEPCB Dipole Magnet, IHEP, Beijing, Apr. 2016.
- [5] The CEPC-SPPC Study Group, CEPC-SPPC Preliminary conceptual Design Report, IHEP, Beijing, IHEP-AC-2015-01, March. 2015.
- [6] M. Koratzinos, private communication, Dec. 2015.
- [7] Y. Cai, private communication, Feb. 2016.
- [8] G. Xu, private communication, Feb. 2016.
- [9] Y. Cai, Symplectic maps and chromatic optics in particle accelerators, *Nucl. Instr. Meth.* **797** (2015) 172-181.
- [10] S. Bai, CEPC magnet error study summary, IHEP, Beijing, Dec. 2015.

Application of a Low-Energy Electron Beam as a Tool for Ultrashort Bunch Length Measurement in Circular Machines

D.A. Nikiforov, A.A. Starostenko, P.V. Logatchov, K. Rusinov
Budker Institute of Nuclear Physics, Novosibirsk, Russia
D. Malyutin, A. Matveenko
Helmholtz-Zentrum Berlin, Berlin, Germany

Abstract

A new diagnostic device designed for non-destructive ultrashort bunch length measurement is described. The operating principle of the device and the measuring technique are described. The possible scheme of arrangement of the device elements is described. The results of simulations of Electron Beam Probe application for different beams under investigation are presented. The quality requirements of the low-energy testing beam are considered and the resolving detector ability is determined.

Keywords

Bunch length; electron beam probe; low energy electron beam.

1 Introduction

The experiments in particle physics and high-energy physics and the commissioning of new generation facilities for applied research and experiments with synchrotron radiation require continuous improvement of parameters of charged particle beams (particularly their intensity and luminosity). Such an improvement can be realised by means of advancement of techniques for diagnostics of charged particle beams. Ideally, these diagnostics methods should not affect the quality of the studied beam. Non-destructive methods for diagnostics are based on the measurement of electromagnetic fields that are generated by the beam under investigation. These techniques use electromagnetic interaction of the studied beam with various “probing elements” such as the vacuum chamber of accelerators, the residual gas or gas flow, a testing laser beam or the external low energy electron beam. Synchrotron radiation, which is generated in bending magnets, is also widely used for nondestructive diagnostics [1].

In this study, a low energy electron beam is considered as the possible instrument for ultra-short bunch length measurement for two accelerator facilities [2]: BESSY VSR [3] and ERL bERLinPro [4]. The main parameters of such a facilities are presented in Table 1. The device that uses low-energy electron beam is called electron beam probe (EBP) [5]. Besides length measurements this device can be used for the reconstruction of transverse and longitudinal charge distributions in a bunch under investigation.

Table 1. BESSY VSR and bERLinPro main parameters

Parameter	Unit	BESSY VSR	bERLinPro
Beam energy	MeV	1700	50
Max. average current	mA	300	100
Bunch charge	pC	100-8000	< 77
Bunch length	ps	0.3 – 15	0.1-2
Emittance (normalised)	π mm mrad		< 1

In the case of BESSY VSR, it is possible to carry out a bunch length measurement by means of streak camera, but for bERLinPro with energy 50 MeV and low current, it will be hard to detect synchrotron radiation from a single bunch. Thus, EBP can be used as an alternative diagnostics method.

2 Basic operational principles of the EBP

A very thin electron beam with low current moves across the trajectory of an intense ultra-relativistic bunch with offset parameter ρ (see Fig. 1). An ultra-relativistic bunch moves in Z direction with the velocity of light c ($\beta=1$). A probe electron beam (PB) moves in X direction, perpendicularly to the Z axis, with the velocity βc . The particles of a probe electron beam suffer the deflection in the electromagnetic fields of an ultra-relativistic bunch. Each particle of a probe beam has θ_y and θ_x deflection angles after passing the interaction region. The transverse sizes of both beams are much smaller than the offset parameter ρ . The longitudinal distribution of charge density in an ultra-relativistic beam under investigation is given as a function $n(z)$ at the time moment $t=0$. At the same time ($t=0$) each particle of a probe beam has its own value of coordinate x . As a result of scattering in the electromagnetic fields of the beam under investigation, PB describes a closed curve on detection screen (see Fig. 1). The detection screen is placed in a plane parallel to the Y-Z plane at distance L from the Z axis.

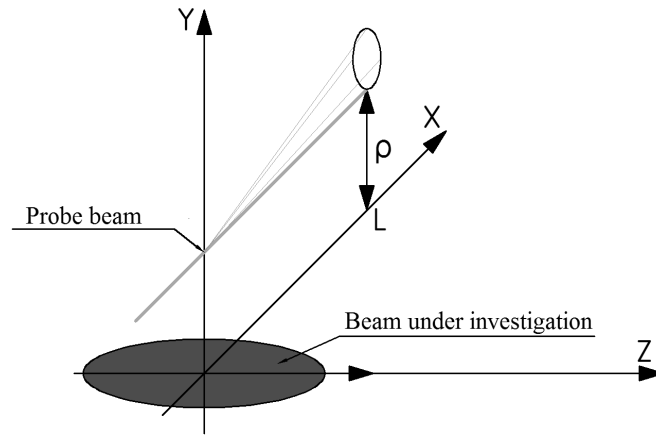


Fig. 1: Diagram illustrating the operating principle of the EBP

A small kick for the probe beam electron can be expressed as:

$$\begin{aligned} d\theta_z &= \frac{dP_z}{P_x} = \frac{1}{\gamma mc\beta} \cdot \frac{e^2 2n(z)\beta}{\sqrt{\rho^2 + (x + \beta ct)^2}} \cdot \frac{x + \beta ct}{\sqrt{\rho^2 + (x + \beta ct)^2}} \cdot dt = \\ &= \frac{2r_e}{\gamma} \cdot \frac{n(z)(x + \beta z)}{\rho^2 + (x + \beta z)^2} \end{aligned}$$

One can use also the simple correlation between t and z for an ultra relativistic bunch ($z=ct$). For Z direction it is easy to find:

$$\begin{aligned}
 d\theta_y &= \frac{dP_y}{P_x} = \frac{1}{\gamma mc\beta} \cdot \frac{e^2 2n(z)}{\sqrt{\rho^2 + (x + \beta ct)^2}} \cdot \frac{\rho}{\sqrt{\rho^2 + (x + \beta ct)^2}} \cdot dt = \\
 &= \frac{2\rho r_e}{\gamma\beta} \cdot \frac{n(z)}{\rho^2 + (x + \beta z)^2}
 \end{aligned}$$

Finally the dependencies **Error! Bookmark not defined.** can be written as:

$$\theta_z(x) = \frac{2r_e}{\gamma} \int_{-\infty}^{+\infty} \frac{(x + \beta z)n(z)dz}{\rho^2 + (x + \beta z)^2} \quad (1)$$

$$\theta_y(x) = \frac{2\rho r_e}{\beta\gamma} \int_{-\infty}^{+\infty} \frac{n(z)dz}{\rho^2 + (x + \beta z)^2} \quad (2)$$

where r_e is the classical electron radius, ρ is the impact parameter, $\beta = \frac{v}{c}$ is the ratio of the probe beam (PB) velocity to the velocity of light, $\gamma = \frac{1}{\sqrt{1 - \beta^2}}$ is the relativistic factor of the PB, x is the coordinate of the PB particle at moment $t = 0$ and $n(z)$ is the dependence of the linear electron density in the relativistic bunch on longitudinal coordinate z .

2.1 Determining the length of a Gaussian relativistic bunch

In the case of an exact collision ($\rho=0$) of the beams, when their trajectories intersect at a right angle (see Fig. 2) and the transverse size of the PB is larger than that of the beam under investigation, quite pronounced peaks in the vertical and horizontal deflection angles of the probing particles are observed. These maxima are determined from maximum horizontal and vertical sizes of the image on the detection screen (see Fig. 3).

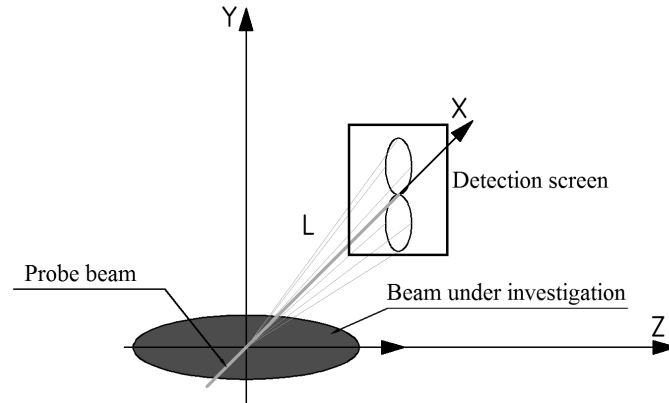


Fig. 2: Diagram illustrating of an exact collision of the beams

In this case, the total maximum deflection angles may be expressed as:

$$\theta_y(\rho, x, \sigma_l, \sigma_r) = \frac{2\rho r_e}{\beta\gamma} \int_{-\infty}^{+\infty} \frac{n(z)dz}{\rho^2 + (x + \beta z)^2} \left(1 - e^{-\frac{\rho^2 + (x + \beta z)^2}{2\sigma_r^2}}\right) \quad (3)$$

$$\theta_z(\rho, x, \sigma_l, \sigma_r) = \frac{2r_e}{\gamma} \int_{-\infty}^{+\infty} \frac{(x + \beta z)n(z)dz}{\rho^2 + (x + \beta z)^2} \left(1 - e^{-\frac{\rho^2 + (x + \beta z)^2}{2\sigma_r^2}}\right) \quad (4)$$

where σ_r is the transverse RMS size of the studied bunch and σ_l is the longitudinal RMS size of the studied bunch and $n(z)$ is a Gaussian distribution.

In this way, measuring the vertical θ_y (horizontal θ_z) deflection angle of the PB, and the charge and the transverse sizes of the studied beam it is possible to restore the bunch length. In this analytical model (Eq.3) only PB particles with coordinate $x = 0$ will have the maximum vertical deflection [2]. An example of maximal vertical deflection angle on impact parameter ρ for electrons with coordinate $x = 0$ and different transverse sizes of the studied beam is shown in Fig.4. Dependence of the maximal deflection angle versus the bunch length (Eq.3) is shown in Fig.5.

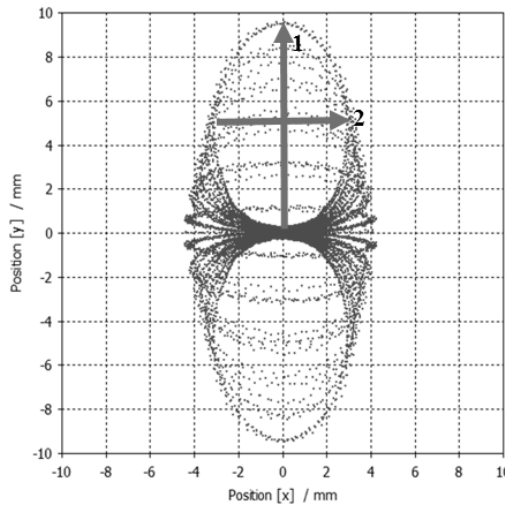


Fig. 3: Numerical simulations of the image on the EBP screen: 1 – maximum vertical deflection, 2 – maximum horizontal deflection. $L = 40$ cm. Simulations were performed by means of CST Particle studio.

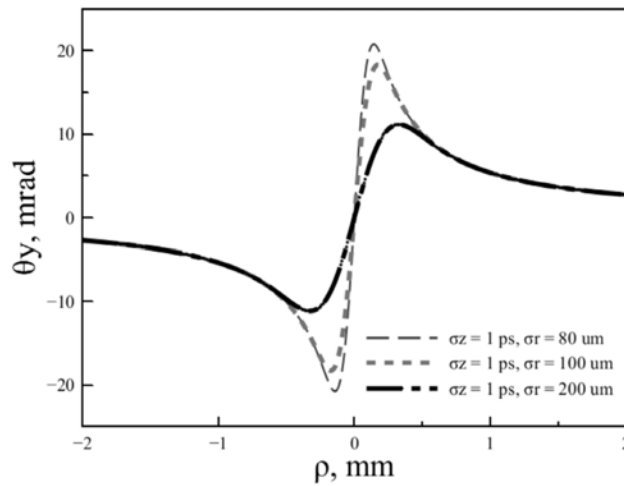


Fig. 4: Deflection angle θ_y as a function of the impact parameter ρ . RMS bunch length is equal to 1 ps

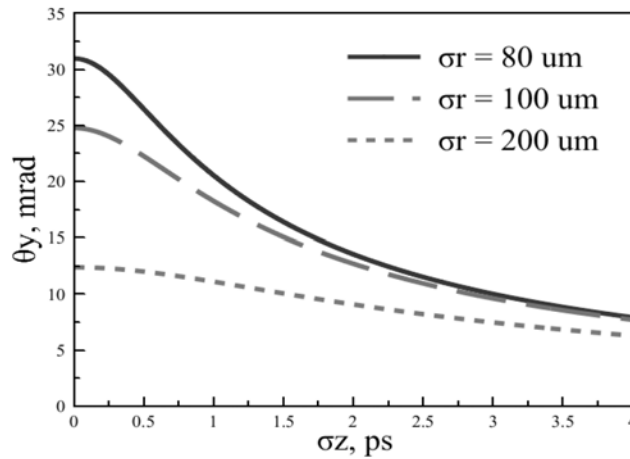


Fig. 5: Maximal vertical deflection angle θ_y as a function of the bunch length for different transverse RMS sizes (σ_r) of a studied beam. The charge of the studied beam is equal to 100 pC.

As can be seen in Fig.5, the dependence is quite significant, particularly between 0.5 ps and 3 ps. It means that it is possible to achieve a good time resolution for such a method. For example for a bunch length of 1 ps and transverse size of 80 μm the time resolution will be around ± 0.4 ps, (see Fig.5) [2].

3 Typical experimental setup of EBP

The schematic diagram of the EBP layout is shown in Fig. 6. A probe electron beam is generated and accelerated in an electron gun (1) with energy up to 100 kV. An axial magnetic focusing lens (3) forms a minimal probe beam size in interaction region (5); also, the PB can be adjusted by means of two-coordinate magnetic correctors (2). The detection system (9) consists of a micro channel plate (MCP) (6), a phosphor screen (7) and a CCD camera (8).

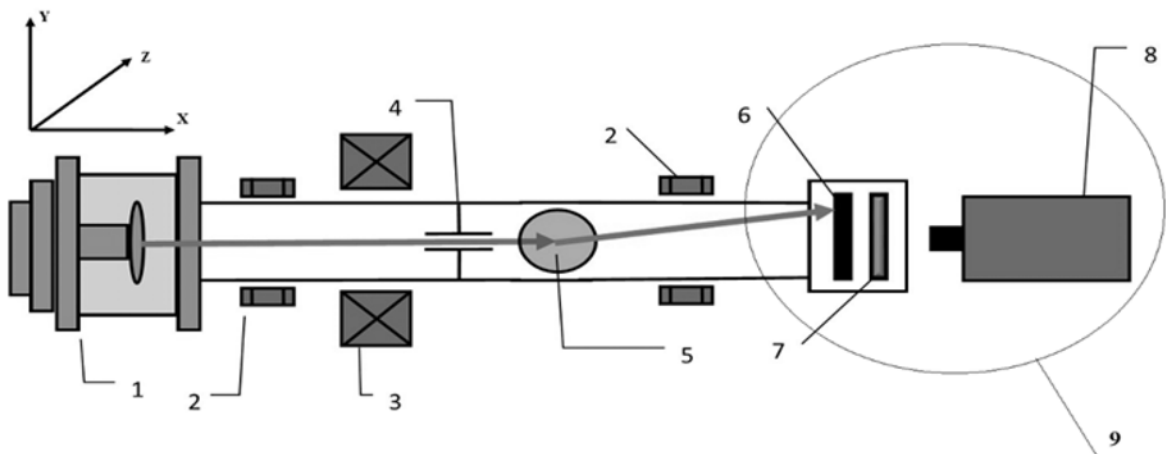


Fig. 5: The scheme of installation of EBP: 1 – electron gun, 2 – magnetic corrector, 3 – axial magnetic lens, 4 – sweep plate, 5 – interaction region, 6 – MCP, 7 – phosphor screen, 8 – CCD camera, 9 – detection system.

4 Simulations

Particle tracking simulations were performed by means of CST Particle studio [6]. The studied bunch has 100 pC charge, transverse and longitudinal Gaussian distributions and a 100 μm transverse RMS size. The probe beam has an energy of 100 keV, 120 μm radius and a uniform longitudinal distribution. The results of the numerical simulations are presented in Fig. 6: the dashed line corresponds to Eq.3, the solid line corresponds to CST simulations for different bunch lengths.

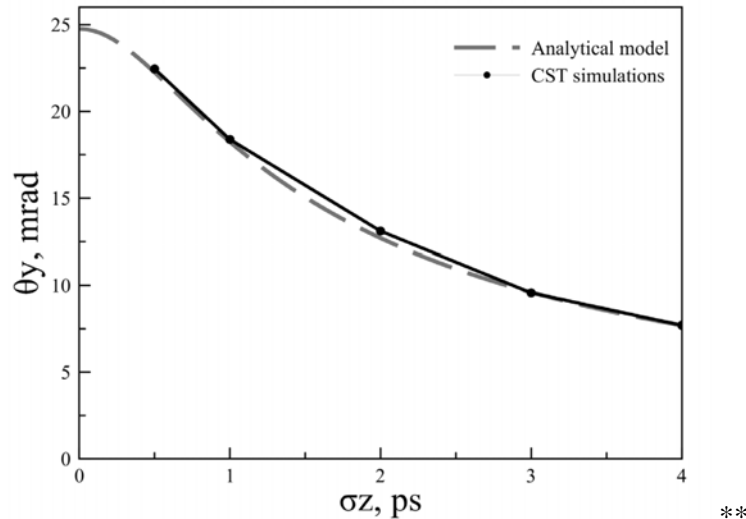


Fig. 6: Maximum vertical deflection angle as a function of the studied bunch length: the dashed line corresponds to Eq.3, the solid line corresponds to particle-tracking simulations.

The particle tracking results are in good agreement with the analytical model.

References

- [1] L.N. Vyacheslavov, M.V.Ivantsivskii, O.I. Meshkov, S.S.Popov and V.V. Smaluk, *Phys.Part.Nucl.* **43** (2012) 231. <https://doi.org/10.1134/S1063779612020074>
- [2] D.Malyutin, A. Matveenko, Electron beam probe for the bunch length measurements at bERLinPr, in Proc. of IPAC 16, Busan, Korea, paper MOPMB009, p. 92. <http://accelconf.web.cern.ch/AccelConf/ipac2016/papers/mopmb009.pdf>
- [3] A. Vélez et al., BESSY VSR: A novel application of SRF for synchrotron light sources, in Proc. of SRF '15, Whistler, BC, Canada, paper TUAA03, p. 462. <http://accelconf.web.cern.ch/AccelConf/SRF2015/papers/tuaa03.pdf>
- [4] M. Abo-Bakr and A. Jankowiak Status Report of the Berlin Energy Recovery Project bERLinPro, in Proc. of IPAC'16, Busan, Korea, paper TUPOW034, p. 1827. <http://accelconf.web.cern.ch/AccelConf/ipac2016/papers/tupow034.pdf>
- [5] P. V. Logachev, D. A. Malyutin, and A. A. Starostenko, *Instruments and Experimental Techniques* **51** (1) (2008) 1. <https://doi.org/10.1134/S0020441208010211>
- [6] <https://www.cst.com/products/cstps>

Kaon Identification using the Tracking System of the CMD-3 Detector

R.R. Akhmetshin, A.N. Amirkhanov, A.V. Anisenkov, V.M. Aulchenko, V.Sh. Banzarov, N.S. Bashtovoy, A.E. Bondar, A.V. Bragin, S.I. Eidelman, D.A. Epifanov, L.B. Epshteyn, A.L. Erofeev, G.V. Fedotov, S.E. Gayazov, A.A. Grebenuk, S.S. Gribov, D.N. Grigoriev, F.V. Ignatov, V.L. Ivanov, S.V. Karpov, V.F. Kazanin, O.A. Kovalenko, A.A. Korobov, A.N. Kozyrev, E.A. Kozyrev, P.P. Krokovny, A.E. Kuzmenko, A.S. Kuzmin, I.B. Logashenko, P.A. Lukin, K.Yu. Mikhailov, V.S. Okhapkin, Yu.N. Pestov, A.S. Popov, G.P. Razuvaev, A.A. Ruban, N.M. Ryskulov, A.E. Ryzhenkov, V.E. Shebalin, D.N. Shemyakin, B.A. Shwartz, A.L. Sibidanov, E.P. Solodov, V.M. Titov, A.A. Talyshev, A.I. Vorobiov, Yu.V. Yudin*
Budker Institute of Nuclear Physics, SB RAS, Novosibirsk, 630090, Russia

Abstract

This paper describes the K/π separation technique based on ionisation losses in the drift chamber of the CMD-3 detector. First the procedure of the ionisation-loss calibration is described. Then methods of K/π separation are discussed for the example process $e^+e^- \rightarrow K^+K^-\pi^+\pi^-$.

Keywords

Drift chamber; Ionisation losses calibration; VEPP-2000; CMD-3 detector.

1 Introduction

The electron-positron collider VEPP-2000 [1] was commissioned at the Budker Institute of Nuclear Physics (BINP) in 2010. The machine covers a center-of-mass energy range from $E = 0.32$ GeV to 2 GeV and employs a novel so-called round beam technique to reach luminosities of up to $10^{32} \text{ cm}^{-2}\text{s}^{-1}$ at 2 GeV.

The CMD-3 [2] detector occupies one of two interaction regions of VEPP-2000. The detector layout is shown in Fig. 1. The tracks of charged particles are detected by the cylindrical drift chamber (DC) with hexagonal cells. The fiducial volume for charged tracks is precisely determined by the Z-chamber, a Multi Wire Proportional Chamber (MWPC) with dual anode and cathode readout. The barrel electromagnetic calorimeter, placed outside of the superconducting solenoid ($0.08 X_0$, 13 T), consists of two systems: the Liquid Xenon (LXe) calorimeter (about $5.4 X_0$) and the Cesium Iodine (CsI) crystal calorimeter (about $8.1 X_0$) that surrounds the LXe calorimeter. The LXe calorimeter has 7 layers and utilizes dual readout: the anode signals are used for measurement of the total energy deposition while signals from the cathode strips provide information about the shower profile. Also they are used for the measurement of the coordinates of photons with high precision (about 1-2 mm). The endcap Bismuth Germanate (BGO) crystal calorimeter (about $13.4 X_0$) operates in the main magnetic field. The Time-Of-Flight (TOF) system, designed to identify the particle species, is placed between the two layers of the barrel calorimeter. The calorimeters are surrounded by the so-called muon range system based on scintillation counters. The full detector has a radius of 1.5 m and a length of 2 m.

During the first experimental run from 2010 to 2013, the detector has collected about 60 pb^{-1} of integrated luminosity. An average luminosity above $10^{31} \text{ cm}^{-2}\text{s}^{-1}$ was reached at VEPP-2000, which is still below the design luminosity. The main limitation at high energies was a deficit of positrons. After the VEPP-2000 upgrade, started in 2013, which included the commissioning of the new positron injection facility and an increase of the maximum energy of the booster ring, one of the pre-accelerators, a gain in the maximum luminosity of up to a factor of 10 is expected.

The main task of the CMD-3 detector is the measurement of the exclusive cross sections of the electron-positron annihilation into hadrons. For the measurement of events including charged kaons

*Corresponding author. Email: dimnsh@yandex.ru

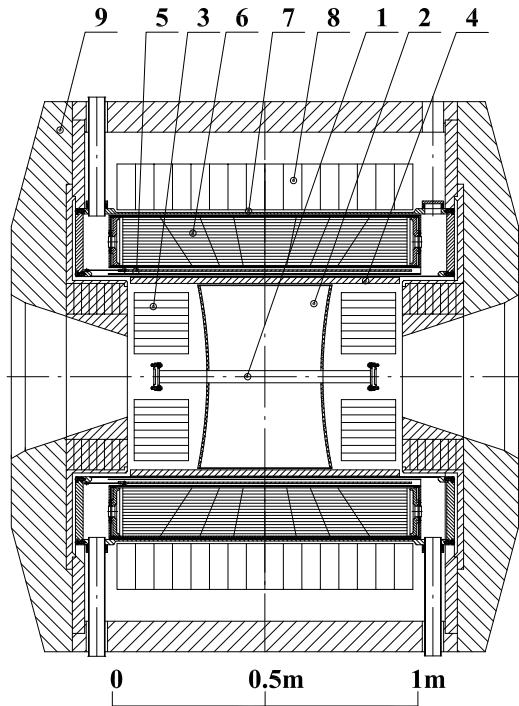


Fig. 1: CMD-3 detector: 1 – beam pipe, 2 – drift chamber, 3 – BGO calorimeter, 4 – Z-chamber, 5 – SC solenoid (0.08X₀, 13 T), 6 – LXe calorimeter, 7 – TOF system, 8 – CsI calorimeter, 9 – yoke. Outer muon range system is not shown.

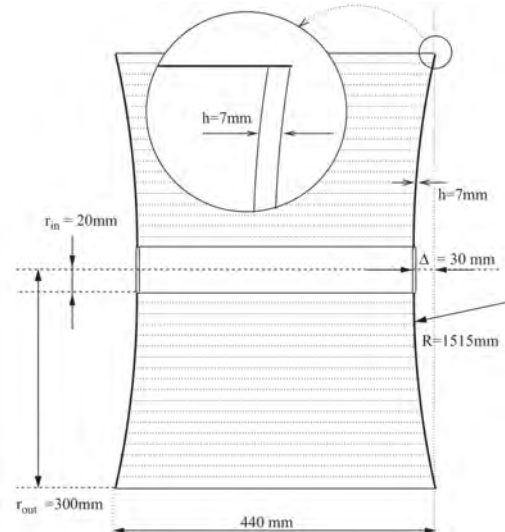


Fig. 2: Drift chamber layout.

a kaon identification procedure is needed, where pions represent the largest background. This paper describes the method of K/π separation using ionisation losses (dE/dx) in the DC and the calibration of the dE/dx measurement with the DC.

2 Drift chamber

The drift chamber is the main tool of the CMD-3 detector for charged particle reconstruction. A sketch of the DC is shown in Fig. 2. 1218 identical hexagonal cells of a cell side of 9 mm and a sense to field wires ratio of 1:2 cover the full sensitive volume of the chamber. The charge division technique is used to measure the coordinate along the sense wires which have 15 mm diameter and are made of gold plated tungsten-rhenium alloy with a resistance of 1 k Ω m. The field wires have a diameter of 100 μ m and they are made of titanium. The DC end plates are 7 mm thick spherical segments made of carbon fibers. As gas mixture Ar:C₄H₁₀ is used with a proportion of 80:20. A simulation with Garfield [3] has shown a maximum drift time in the 1.3 T magnetic field of about 600 ns while the beam revolution time is 80 ns. The mixture is prepared using two Bronkhorst gas flow controllers. Direct measurements of the magnetic field in the DC volume have shown an agreement with calculations: the maximum deviation of the magnetic field does not exceed 1% along the beam axis and 0.2% from the interaction point to the outer shell.

3 Ionisation losses calibration

Cosmic muon events are used for the estimation of the DC gain for each wire. Also the reconstructed track parameters allow one to know the position at which a particle crosses a cell and calculate a geometrical amendment for the collected ionization. The calibration includes corrections on the following

parameters:

- distance from track to the wire ρ ,
- polar angle of track θ ,
- longitudinal position of the track z ,
- amplitude difference between wires.

As shown in Fig. 3, the ionisation losses is constant for central values of z while at the borders of the DC it shows a linear dependence on the longitudinal track position. The dE/dx dependence on the distance between track and wire (ρ) is different for different polar angles (see Fig.4). Hence, the mean ionisation loss as a function of the polar angle (see Fig. 5) are approximated for different values of ρ . These approximations are then used for the detector calibration.

For the calibration of the dE/dx scale, we use "one-proton" events with a momentum of 350 MeV/c and cosmic muon events with a momentum of higher than 500 MeV/c. The mean dE/dx measured with the wires of DC is presented in Fig. 6. Red points correspond to protons, blue points correspond to cosmic muon events. We set mean ionisation losses value on 10000 arbitrary units for protons and 2000 arbitrary units for cosmic muon events. The final dE/dx measurement resolution is 10%-13% for minimum ionisation particles.

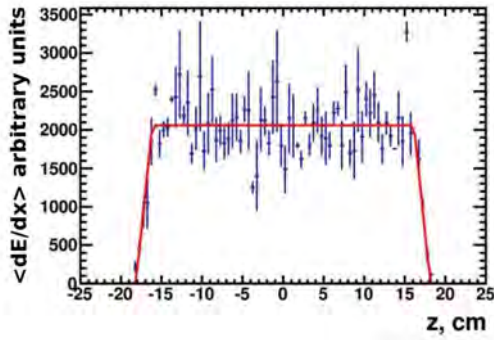


Fig. 3: Dependence of the mean dE/dx on the longitude position of track z .

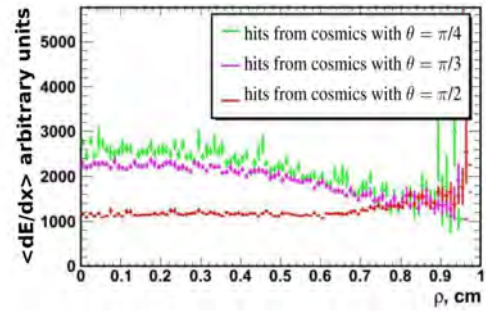


Fig. 4: Dependence of the mean dE/dx on the distance between track and wire ρ for three different polar angles.

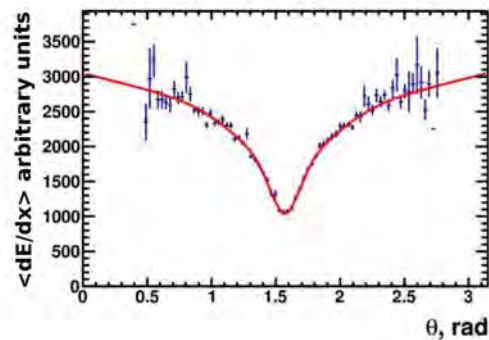


Fig. 5: Dependence of the mean dE/dx on the polar angle of track θ .

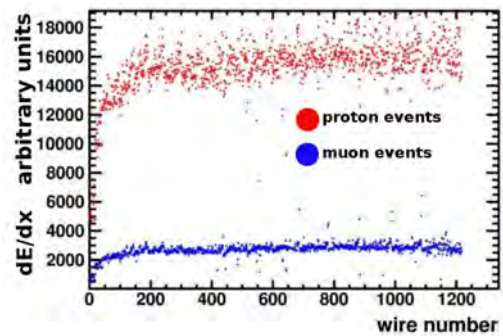


Fig. 6: dE/dx for all wires of the DC for proton events and cosmic muon events.

4 Kaon identification

The dE/dx distribution for collinear events (two tracks with $\Delta\theta = 0.15$ rad and $\Delta\phi = 0.1$ rad) at $E = 1.019$ GeV is presented in Fig. 7. The momentum of kaons are about 110 MeV/c. A cut based event selection shown as black lines allows to identify events of the process $e^+e^- \rightarrow K^+K^-$ with less than 0.5% background [4].

The dE/dx in the DC versus the particle momentum for $e^+e^- \rightarrow K^+K^-\pi^+\pi^-$ events is presented in Fig. 8 for $E = 1.8$ GeV. For the K/ π separation for particles with a momentum of larger than 400 MeV/c, a probability density function (PDF) with momentum and dE/dx dependence is used to extract the number of pions and kaons in the event. It is constructed for kaons $f_K(p, dE/dx)$ and pions $f_\pi(p, dE/dx)$ as

$$f_{K,\pi}(p, dE/dx) = N_G \times G(\langle dE/dx \rangle, \sigma_G) + N_{Gl} \times Gl(\langle dE/dx \rangle, \sigma_{Gl}, \eta). \quad (1)$$

where $G(\langle dE/dx \rangle, \sigma_G)$ is the Gaussian function, $Gl(\langle dE/dx \rangle, \sigma_{Gl}, \eta)$ is the logarithmic Gaussian function. The latter is necessary to describe the tails of the distribution of the ionization losses. The average ionization losses $\langle dE/dx \rangle$, standard deviations σ_G and σ_{Gl} , asymmetry η , amplitudes N_{Gl} and N_G depend only on the particle momentum. The PDF parameters are extracted from the dE/dx dependence on the particle momentum using a 7-dim. fit. First the $f_\pi(p, dE/dx)$ is determined using a sample of $e^+e^- \rightarrow \pi^+\pi^-\pi^+\pi^-$ events, then the $f_K(p, dE/dx)$ is determined using a sample of $e^+e^- \rightarrow K^+K^-\pi^+\pi^-$ events with fixed $f_\pi(p, dE/dx)$. This procedure was performed for simulated and experimental data at each energy point. An example of a PDF is shown in Fig. 9 for momenta of 400 - 450 MeV/c.

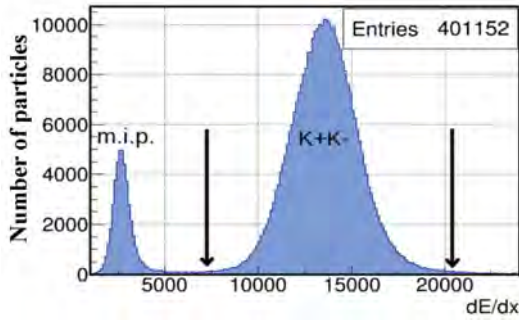


Fig. 7: Particle ionization losses in DC for collinear events at $E = 1.019$ GeV.

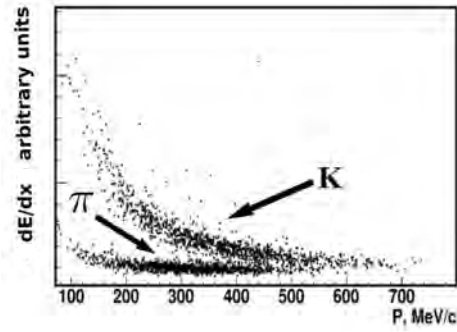


Fig. 8: Pion and kaon ionization losses in DC as a function of the particle momentum in simulation.

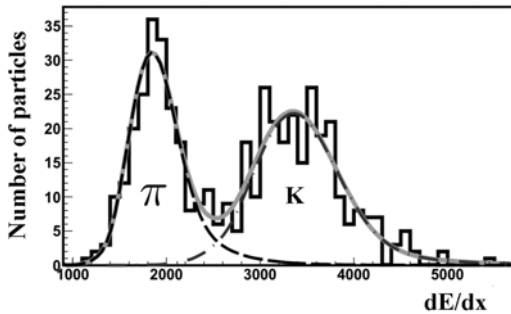


Fig. 9: Pion and kaon ionization losses in DC for the momentum interval from 400 to 450 MeV/c in simulation.

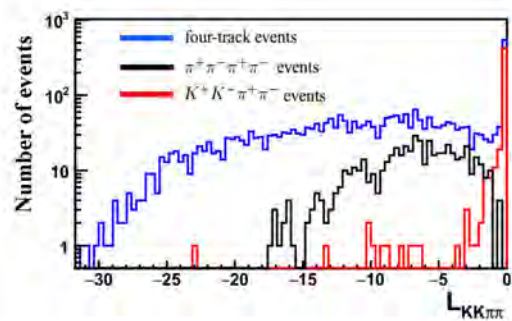


Fig. 10: Distribution of the likelihood function ($L_{KK\pi\pi}$) for the four-track events in simulation. The blue histogram corresponds to all four-track events, the black one to $\pi^+\pi^-\pi^+\pi^-$ events and the red one to $K^+K^-\pi^+\pi^-$ events.

In the analysis of the process $e^+e^- \rightarrow K^+K^-\pi^+\pi^-$ the likelihood function ($L_{KK\pi\pi}$) is defined as

$$L_{KK\pi\pi} = \log\left(\frac{\prod_i f_{\alpha_i}^i(p, dE/dx)}{\prod_i [f_{\pi}^i(p, dE/dx) + f_K^i(p, dE/dx)]}\right), \quad (2)$$

where i is the track index, α_i is the supposed type (K or π) of the particle corresponding to the i th track. The $L_{KK\pi\pi}$ is constructed for events with three or four tracks in the DC, so the track index changes from 1 to 3 or 4, respectively. $L_{KK\pi\pi}$ is constructed under the assumption that each event is a $K^+K^-\pi^+\pi^-$ event, so two tracks are identified as kaons and two as pions. Therefore, taking into account all the permutations and charges of the particles, $L_{KK\pi\pi}$ receives four different values for each event. The most probable combination of particle types provides a maximum of this function. The distribution of $L_{KK\pi\pi}$ for simulated data at a center-of-mass energy of 2 GeV is shown in Fig. 10. The blue histogram corresponds to all four-track events while the black and red ones correspond to $\pi^+\pi^-\pi^+\pi^-$ and $K^+K^-\pi^+\pi^-$ events respectively. It is seen that the likelihood function value also is a good parameter to select $e^+e^- \rightarrow K^+K^-\pi^+\pi^-$ events from background. The condition for the $L_{KK\pi\pi}$ value to be larger than -2 was chosen as a selection condition, which allows to suppress background events by a factor of 20 and it preserves more than 99% of signal events, according to simulation as extracted from Fig. 10. Similar likelihood functions were used for analyses of the processes $e^+e^- \rightarrow K^+K^-\omega$, $K^+K^-\pi$ and $K^+K^-\eta$ [6].

5 Conclusion

The CMD-3 tracking system based on the DC and Z-chamber participated in the data taking since 2010. Calibration procedures of the dE/dx measurement have been developed and they were used during all data taking periods. The DC ionisation losses resolution is 10%-13%. Information about ionisation losses in the DC is successfully used in analyses of processes $e^+e^- \rightarrow K^+K^-\omega$, $K^+K^-\pi$, $K^+K^-\pi^+\pi^-$ and $K^+K^-\eta$.

Acknowledgements

We wish to thank the VEPP-2000 personnel for the excellent machine operation. This work is supported in part by Russian Science Foundation (grant No. 14-50-00080), by the Russian Foundation for Basic Research grants RFBR 14-02-00580-a, RFBR 14-02-91332, RFBR 15-02-05674-a, RFBR 16-02-00160-a, RFBR 17-02-00897-a.

References

- [1] Y.M. Shatunov *et al.*, *Conf. Proc. C* 0006262 (2000) 439. <http://accelconf.web.cern.ch/accelconf/e00/PAPERS/MOP4A08.pdf>
- [2] B.I. Khazin *et al.*, *Nucl. Phys. Proc. Suppl.* 181-182 (2008) 376. <https://doi.org/10.1016/j.nuclphysbps.2008.09.068>
- [3] Garfield - simulation of gaseous detectors. <http://garfield.web.cern.ch/garfield/>, last accessed April 21st 2017
- [4] E.A. Kozyrev *et al.*, *Phys. Atom. Nucl.* 78 (2015) 358-362. <https://doi.org/10.1134/S1063778815020192>
- [5] D.N. Shemyakin *et al.*, *Phys. Lett. B*756 (2016) 153-160. <https://doi.org/10.1016/j.physletb.2016.02.072>
- [6] V.L. Ivanov *et al.*, *Phys. Atom. Nucl.* 79 (2016) 251-259. <https://doi.org/10.1134/S1063778816020083>

Vertex and Tracker Research and Development for CLIC *

M. Munker (on behalf of the CLICdp collaboration)
CERN, University of Bonn

Abstract

Challenging detector requirements are imposed by the physics goals at the future multi-TeV e^+e^- Compact Linear Collider (CLIC). A single point resolution of $3\ \mu\text{m}$ for the vertex detector and $7\ \mu\text{m}$ for the tracker is required. Moreover, the CLIC vertex detector and tracker need to be extremely light weighted with a material budget of $0.2\% X_0$ per layer in the vertex detector and $1-2\% X_0$ in the tracker. A fast time slicing of $10\ \text{ns}$ is further required to suppress background from beam-beam interactions. A wide range of sensor and readout ASIC technologies are investigated within the CLIC silicon pixel R&D effort. Various hybrid planar sensor assemblies with a pixel size of $25 \times 25\ \mu\text{m}^2$ and $55 \times 55\ \mu\text{m}^2$ have been produced and characterised by laboratory measurements and during test-beam campaigns. Experimental and simulation results for thin ($50\ \mu\text{m} - 500\ \mu\text{m}$) slim edge and active-edge planar, and High-Voltage CMOS sensors hybridised to various readout ASICs (Timepix, Timepix3, CLICpix) are presented.

Keywords

Solid state detectors; hybrid detectors; electronic detector readout concepts (solid-state).

1 Introduction

The Compact Linear Collider CLIC [1–4] is a proposed linear e^+e^- collider at CERN, with centre-of-mass energies up to $3\ \text{TeV}$. Precision measurements of Standard Model parameters and possibly of BSM phenomena discovered by the LHC are one important part of the CLIC physics goals. In addition, CLIC has a great potential to discover new physics, both through direct production and indirectly via the high precision achievable to measure electroweak observables [2, 5]. The requirements for high precision measurements at CLIC impose challenging constraints on the CLIC vertex detector and tracker. A single point tracking resolution of $3\ \mu\text{m}$ in the vertex detector and $7\ \mu\text{m}$ in the tracker needs to be achieved. In addition, the vertex detector and the tracker have to be low mass detectors, with a material budget of only $0.2\% X_0$ per layer in the vertex detector and $1-2\% X_0$ in the tracker. This demand of a very low material budget does not allow for a liquid cooling system in the vertex detector. Forced air flow cooling is feasible only for a low power dissipation and is currently under investigation for the CLIC vertex detector. To reach this, a pulsed power operation of the front end electronics is foreseen, taking advantage of the train repetition of the CLIC machine operating at $50\ \text{Hz}$ and the low duty cycle. The strong focusing of the beam at the interaction point, as well as the high centre-of-mass energy at CLIC, result in a high rate of background particles from beam-beam interactions. To suppress this beam-induced background, a time slicing of $10\ \text{ns}$ needs to be achieved for the vertex detector and tracker. The compatibility of different sensor and readout technologies has been studied in various test-beam campaigns, performed at DESY with a beam of $5.6\ \text{GeV}$ electrons and at the CERN SPS with $120\ \text{GeV}$ pions. As a reference system for the particle track reconstruction, either the AIDA telescope [6] or the CLICdp Timepix3 telescope have been used.

*This article is also published in JINST for the proceedings of the IWORID2016: M. Munker, *Silicon pixel R&D for CLIC*, <http://dx.doi.org/10.1088/1748-0221/12/01/C01096> (2017).

2 Planar sensor assemblies

To achieve the required low material budget and single point resolution in the vertex detector and tracker, very thin planar sensors with small pixel sizes are investigated. In the following sections test-beam and simulation results from Timepix and Timepix3 ASICs with a pixel size of $55 \times 55 \mu\text{m}^2$, as well as CLICpix ASICs with a pixel size of $25 \times 25 \mu\text{m}^2$ are presented.

2.1 Timepix and Timepix3 assemblies

Timepix [7] and Timepix3 [8] readout ASICs are used as test vehicles due to their excellent performance in terms of timing and analogue charge measurement. Planar sensors from Micron [9] and Advacam [10] with different thicknesses ranging from $500 \mu\text{m}$ down to $50 \mu\text{m}$ and various edge designs have been bump-bonded to Timepix and Timepix3 readout ASICs.

2.1.1 Sensor performance for different sensor thicknesses

Since the particles passing thin sensors create only small signals, the detection threshold needs to be low in order to operate these thin planar assemblies at full efficiency. This, in turn, requires a low noise level of the readout ASICs. The noise level of the Timepix and Timepix3 assemblies can be sufficiently suppressed with a threshold of $\sim 1000 e^-$. The efficiency of the charge collection as a function of the detection threshold has been investigated in test-beams. Figure 1 shows, that the low noise of the Timepix3 assemblies allows to set the detection threshold below $1000 e^-$, where thin planar sensor assemblies with a thickness of $50 \mu\text{m}$ can be operated with an efficiency higher than 99 %.

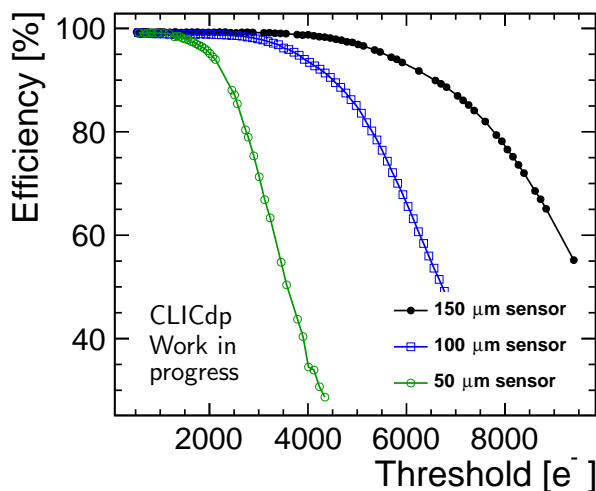


Fig. 1: Charge collection efficiency versus threshold for Timepix3 planar sensor assemblies with different thicknesses (from [11]).

The low signal in the thinnest assemblies indirectly also affects the position resolution: larger cluster sizes provide better position resolution, but in thinner sensors generally smaller cluster sizes are observed. This has been studied in detail with a series of sensors coupled to Timepix ASICs [12]. Results are shown in Fig. 2, where the fraction of matched clusters as a function of sensor thickness is presented. A cluster is considered to be matched if the distance between the reconstructed cluster position and the interpolated telescope track position on the Device Under Test (DUT) is smaller than $100 \mu\text{m}$. The lower fraction of matched clusters with size larger than 1 for thin sensors results in a loss of information in the reconstruction of the spacial position, as shown in Fig. 3, where the position resolution is presented as a function of the sensor thickness.

The position resolution is defined as the difference between the position of the interpolated telescope track and the hit position on the DUT. The hit position on the DUT was determined by charge interpolation between the pixels in a matched cluster, applying an η -correction to correct for non linear charge sharing effects [12].

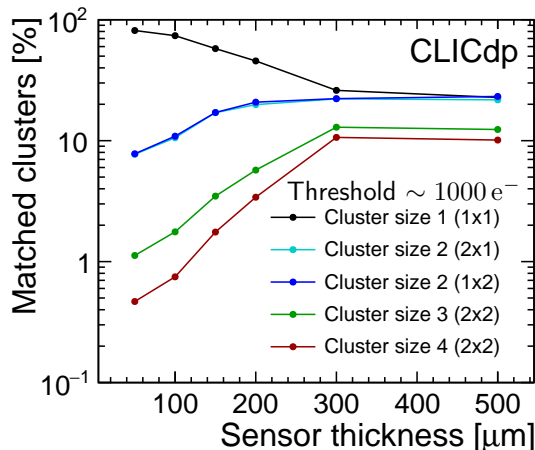


Fig. 2: Matched cluster fraction versus sensor thickness for Timepix planar sensor assemblies (from [12]).

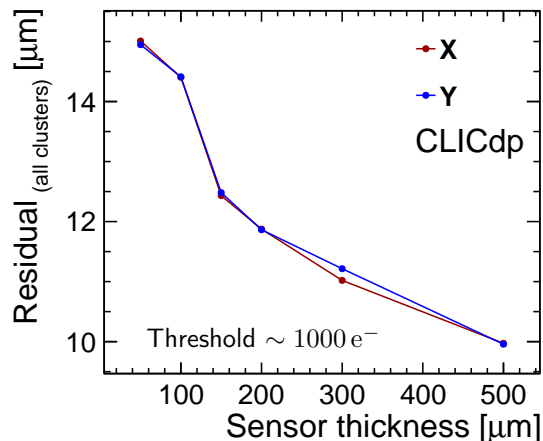


Fig. 3: Position resolution versus sensor thickness for Timepix planar sensor assemblies (from [12]).

2.1.2 Edge efficiency

Active-edge sensors involve an extension of the backside potential to the edge of the sensor, to reduce inactive sensor regions and provide for the possibility of seamless tiling. This reduces the fraction of dead material and is thus an interesting technology to avoid the need for overlap due to inactive regions. It therefore helps to reduce the overall material budget of the detector.

The active-edge sensors tested were produced by Advacam. The Deep Reactive Ion Etching (DRIE) process was used to cut the sensors and extend the backside implant to this cut edge, resulting in a continuation of the electric field lines to the sensor edge. Charge created in the edge region gets collected by the closest pixel at the edge, leading to efficient charge collection up to the sensor edge. The closest pixel at the edge is in the following referred to as the last pixel. A very high potential gradient between the cut edge and the last pixel may lead to an earlier breakdown of the sensor and has been observed for a $50\ \mu\text{m}$ thin planar active-edge sensor without a guard ring. To smoothen the potential gradient in this region, different guard ring designs are placed on the sensor surface between the active-edge and the last pixel. Results using sensors with a thickness of $50\ \mu\text{m}$ without a guard ring, a floating guard ring and a grounded guard ring are presented. For the layout with a grounded guard ring different distances between the last pixel cell and the sensor edge are studied. The efficiency close to the edge of the sensor for the different guard ring layouts is shown in Fig. 4. The design without a guard ring as well as the design with a floating guard ring are fully efficient up to the cut edge of the sensor. For the designs with a grounded guard ring the efficiency drops at the cut sensor edge. This can be understood using a finite element TCAD [14] simulation of the described technology, as shown in Fig. 5. The figure shows the electric field lines for various active-edge planar sensors tested. As can be seen, most of the electric field lines are bent from the active-edge to the last pixel implant for the layout without a guard ring as well as for the one with a floating guard ring. In this case, charge created in this region will be collected by the last pixel at the sensor edge, leading to a fully efficient operation of the sensor right up to the cut sensor edge. For the design with a grounded guard ring the electric field lines reach from the active-edge to the grounded guard ring. Charge created in this region is thus directed away from the last pixel, leading to a drop in efficiency at the cut sensor edge.

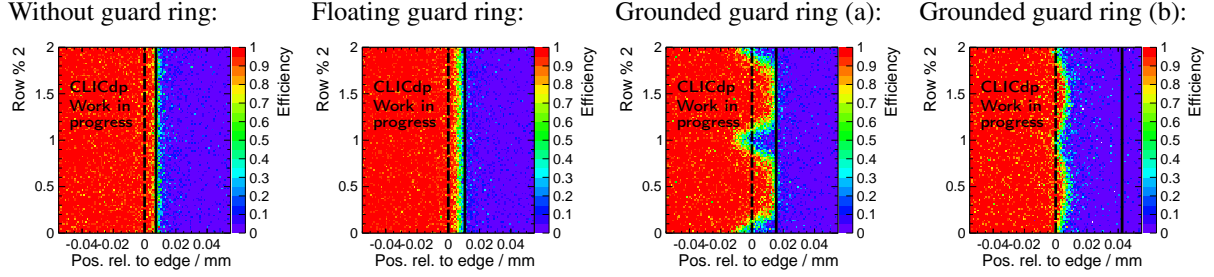


Fig. 4: Charge collection efficiency close to the edge of the Timepix3 active-edge planar sensor assemblies with a thickness of $50\ \mu\text{m}$ for different guard ring layouts. The dashed line marks the edge of the last pixel cell, whereas the solid line marks the cut edge of the sensor. For the design with a grounded guard ring two layouts (a) and (b) with different distances between the edge of the last pixel and the cut sensor edge have been investigated (from [13]).

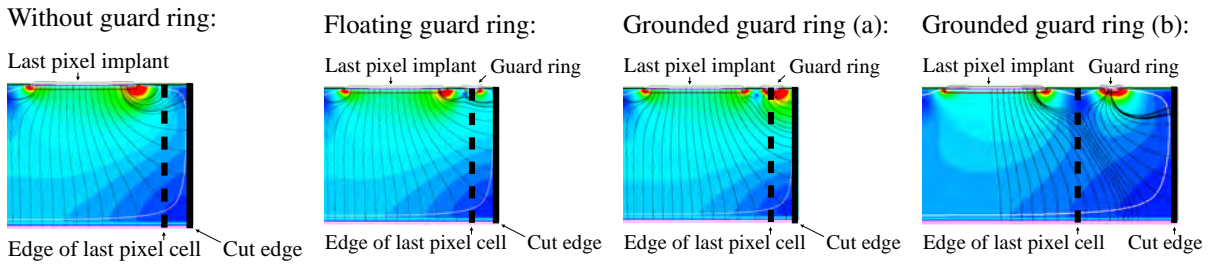


Fig. 5: Electric field map (colour scheme) from a TCAD simulation of the active-edge planar sensor designs with different guard ring layouts. The red colours indicate high electric field regions whereas the blue colours indicate low electric field regions. The electric field lines are shown in black.

In conclusion of these studies, the active edge planar sensor design with a floating guard ring was found to be a good compromise between operation stability up to higher bias voltages and efficient charge collection up to the sensor edge.

2.2 CLICpix assemblies

The pixel size of $55 \times 55\ \mu\text{m}^2$ of the Timepix and Timepix3 assemblies is not expected to allow for the $3\ \mu\text{m}$ single point resolution needed for the CLIC vertex detector (see also figure 3). Therefore, a CLICpix readout ASIC with a pixel size of $25 \times 25\ \mu\text{m}^2$ was designed to meet the specific CLIC requirements [15]. Planar sensors with different thicknesses were bump-bonded to CLICpix readout ASICs, using a single chip bump-bonding process developed at SLAC [16]. Figure 6 shows the position resolution for different bias voltages of a $200\ \mu\text{m}$ thick CLICpix planar sensor assembly. The position resolution improves with increasing bias voltage up to the depletion voltage at $\sim 35\ \text{V}$. A degradation of the position resolution for higher bias voltages can be observed. The fraction of matched clusters between 1 and 3 for different bias voltages is shown in Fig. 7. The fraction of clusters with a size larger than 1 increases with increasing bias voltage up to the depletion voltage and decreases for higher voltages. For a bias voltage below the depletion voltage the active thickness of the sensor increases with the bias voltage, explaining the increase of the cluster size and the improvement of the position resolution up to the depletion voltage. For a bias voltage larger than the depletion voltage the electric field in the sensor increases and gets more homogeneous around the pixel implants, leading to less charge sharing and a degradation of the position resolution, as observed in Figs. 6 and 7. Overall, a position resolution of $3\text{--}4\ \mu\text{m}$ has been achieved for CLICpix planar sensor assemblies with a thickness of $200\ \mu\text{m}$. To further explore the feasibility of this technology with respect to the CLIC requirements, $50\ \mu\text{m}$ thin planar sensors meeting the requirement of a low material budget are currently under investigation.

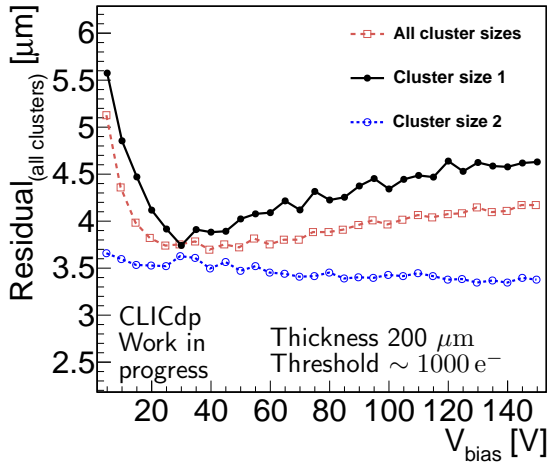


Fig. 6: Position resolution versus bias voltage for CLICpix planar sensor assemblies (from [11]).

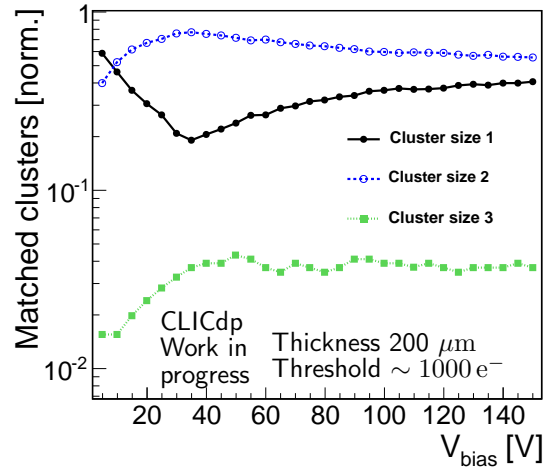


Fig. 7: Cluster fraction versus bias voltage for CLICpix planar sensor assemblies (from [11]).

2.3 Simulation of planar sensors

To gain a detailed understanding as well as a validation of the results presented in Sections 2.1 and 2.2 a simulation chain has been developed to simulate the performance of tracking sensors. This simulation chain consists of four steps. First, a GEANT4 [17] simulation is performed to obtain the spacial energy deposit of a specific particle in the bulk silicon of the sensor. Secondly, the sensor response is simulated with a finite element TCAD simulation, using the obtained distribution of the spacial energy deposit from the GEANT4 simulation to model the track of the particle in the sensor. In the next step, the impact of the digitisation, noise and energy fluctuation on the readout signal is simulated using a fast parametric model. Finally, a reconstruction is performed, including an η -corrected position reconstruction and a model of the resolution of the reference tracks from the telescope. A comparison of the simulation to Timepix planar sensor test-beam results is presented in Figs. 8 and 9. A good agreement can be observed for the spacial residual distribution and the dependence of the mean cluster size on the incident angle of the particle track. The Root Mean Square (RMS) from the simulated residual distribution of $13 \mu\text{m}$ reproduces well the RMS of $14 \mu\text{m}$ of the residual distribution from the test-beam data.

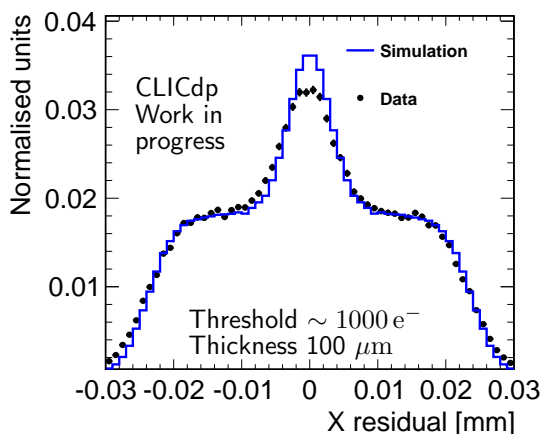


Fig. 8: Spacial residual distribution for a Timepix assembly with a $100 \mu\text{m}$ thick sensor operated at 30 V for simulation (solid line) and data (solid points).

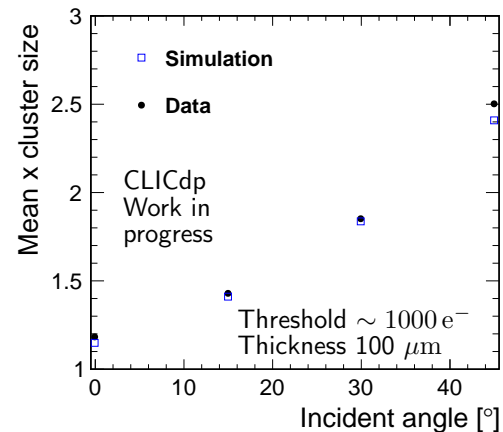


Fig. 9: Mean cluster size for different incident angles of the particle track for a Timepix assembly with a $100 \mu\text{m}$ thick sensor operated at 30 V for simulation (open squares) and data (solid points).

The good agreement between simulation and test-beam data confirms the results from the planar sensor test-beam analysis and validates the developed simulation chain, which can be further used to explore other sensor designs.

3 HV-CMOS active sensors and capacitive coupling to CLICpix readout ASICs

Alternatives to the technology of planar sensor assemblies are investigated in the framework of the CLIC silicon pixel R&D programme. As an example, studies of active HV-CMOS sensors with capacitive coupling to the readout ASICs are presented in the following sections.

3.1 CLICpix assemblies

Capacitively Coupled Pixel Detectors (CCPDs), are used as active sensors and are capacitively coupled via a layer of glue to the CLICpix readout ASICs [18]. Sensors matching the CLICpix footprint (CCPDv3) were produced in a 180 nm HV-CMOS process. Deep N-wells are implanted in the pixel structure to shield the electronics from the substrate bias of ~ 60 V. A fast signal collection is obtained by the drift of the created charges in the depleted region. The schematic of the CCPDv3 and CLICpix pixels is presented in Fig. 10. The collected charge is amplified by a two stage amplifier implemented in the CCPDv3. The amplification of the signal within the pixel allows for a capacitive coupling of the CCPDv3 output signal to the CLICpix readout ASIC via a layer of glue with a thickness of $\sim 1 \mu\text{m}$.

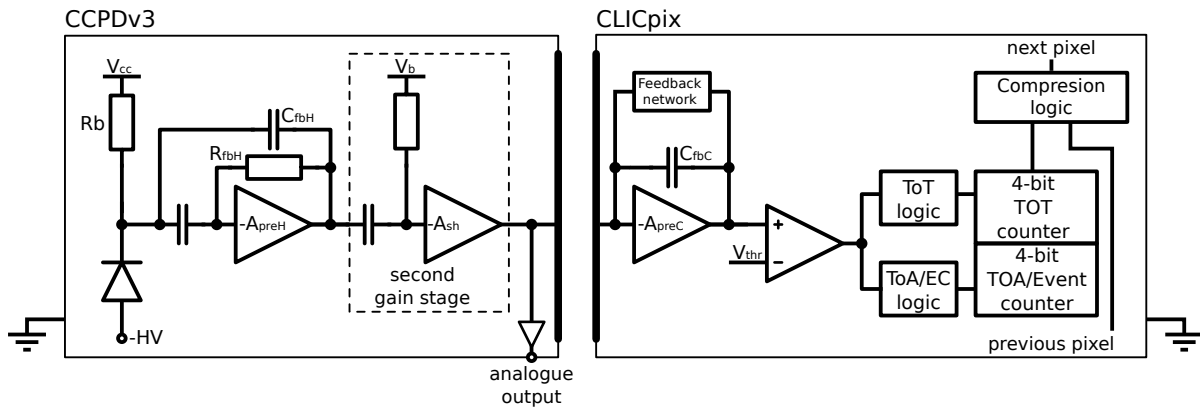


Fig. 10: Pixel schematic of the CCPDv3 and CLICpix assemblies. The interconnection between the CCPDv3 and the CLICpix ASIC has been realised by capacitive coupling through a layer of glue (from [18]).

As presented in Fig. 11, a position resolution of $6 \mu\text{m}$ can be achieved, which is limited by the small amount of charge sharing due to the thin depletion layer. Moreover, Fig. 12 shows that the assembly can be operated at close to 100 % efficiency. These first results of active HV-CMOS sensors with capacitive coupling to the CLICpix ASICs serve as a proof of principle of this technology. More work is needed to reach the required single point resolution of $3 \mu\text{m}$ for the vertex detector.

3.2 Simulation of HV-CMOS sensors

A two dimensional finite element TCAD simulation of the HV-CMOS sensor has been performed by implementing the detailed CCPDv3 structure in TCAD [19].

The calculated leakage current for different substrate resistivities as a function of the applied voltage is shown in Fig. 13. A breakdown of the CCPDv3 at ~ 90 V can be seen, which has been reproduced by laboratory measurements of the CCPDv3 [18]. The simulation of the CCPDv3 has been used to identify the pixel layout as the reason for the breakdown at ~ 90 V and is improved in next generations of CCPDs.

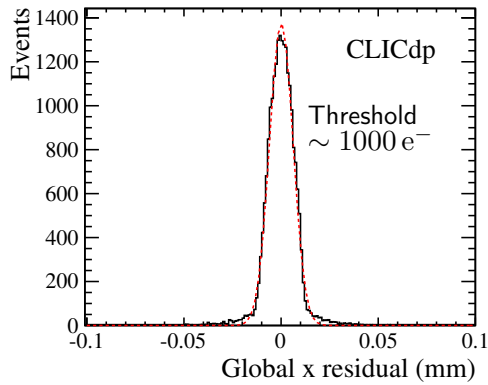


Fig. 11: Spatial residual distribution for a CCPDv3 sensor capacitively coupled to the CLICpix ASIC. A Gaussian fit with a width of $6\mu\text{m}$ is indicated by the red dashed line (from [18]).

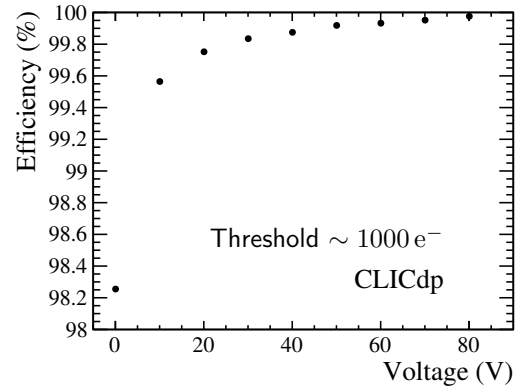


Fig. 12: Efficiency versus bias voltage for a CCPD sensor capacitively coupled to the CLICpix ASIC (from [18]).

To gain further understanding of the charge collection time with respect to depleted and non-depleted regions of the CCPDv3, a transient simulation of particles entering the CCPDv3 sensor at the centre position of the pixel has been performed separately in the depleted and the non-depleted regions of the sensor. The collected charge versus time is shown in Fig. 14 separately for particles passing through the depleted region (drift) and the non-depleted region (diffusion), as well as the combination of both (sum).

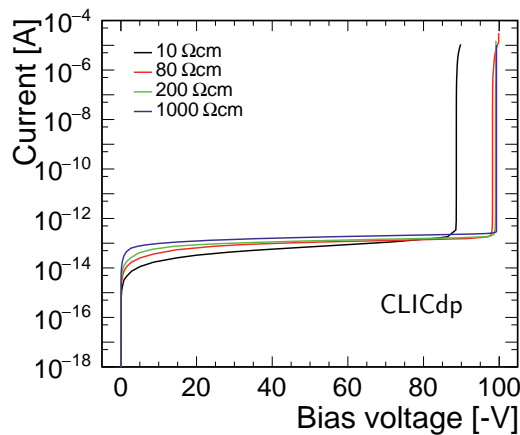


Fig. 13: Leakage current versus bias voltage obtained from a finite element TCAD simulations of the CCPDv3 sensor (from [19]).

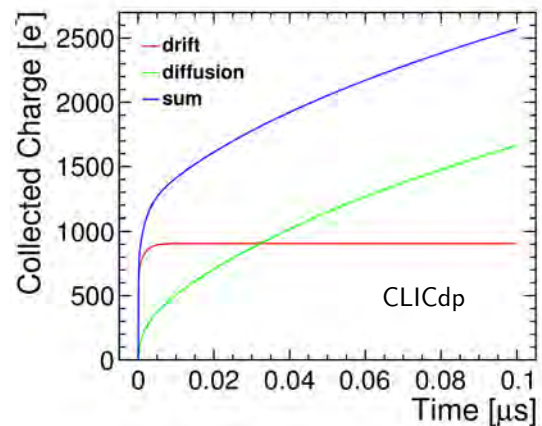


Fig. 14: Collected charge versus collection time for particles passing different parts of the CCPDv3. Results obtained through a simulation of the CCPDv3 sensor using TCAD (from [19]).

The charge created in the depleted region of the sensor is collected by the drift in the high electric field within ~ 10 ns, whereas charge created outside the depleted region is collected by diffusion over a much longer timescale.

4 Summary

To address the challenging requirements for the CLIC vertex detector and tracker, various sensor and readout technologies have been investigated.

Test-beam results for thin planar sensors with a thickness as small as $50\ \mu\text{m}$, read out by the Timepix and Timepix3 ASICs with a pixel size of $55 \times 55\ \mu\text{m}^2$ are presented. Hybrid technologies with a pixel size of $25 \times 25\ \mu\text{m}^2$ have been studied with planar sensors bump-bonded to the CLICpix ASICs. The obtained results are well reproduced by simulation. Further, the feasibility of active HV-CMOS sensors with capacitively coupling to the CLICpix ASICs has been demonstrated and a simulation of the CCPDv3 pixel structure has been performed.

Acknowledgements

This project has received funding from the European Union's Horizon 2020 research and innovation programme under grant agreement No 654168.

Work sponsored by the Wolfgang Gentner Programme of the Federal Ministry of Education and Research.

References

- [1] A Multi-TeV linear collider based on CLIC technology: CLIC Conceptual Design Report, edited by M. Aicheler *et al.*, CERN-2012-007 (CERN, Geneva, 2012).
<https://doi.org/10.5170/CERN-2012-007>
- [2] Physics and Detectors at CLIC: CLIC Conceptual Design Report, edited by L. Linssen *et al.*, CERN-2012-003 (CERN, Geneva, 2012).
<https://doi.org/10.5170/CERN-2012-003>
- [3] The CLIC Programme: towards a staged e^+e^- Linear Collider exploring the Terascale, CLIC Conceptual Design Report, edited by P. Lebrun *et al.*, CERN-2012-005 (CERN, Geneva, 2012).
<https://doi.org/10.5170/CERN-2012-005>
- [4] CLIC and CLICdp Collaborations, Updated baseline for a staged Compact Linear Collider, edited by M. J. Boland *et al.*, CERN-2016-004 (CERN, Geneva, 2016).
<https://doi.org/10.5170/CERN-2016-004>. arXiv: <http://arxiv.org/abs/1608.07537>
- [5] H. Abramowicz *et al.*, Higgs Physics at the CLIC Electron-Positron Linear Collider, CLICdp-Pub-2016-001 (2016). arXiv: <http://arxiv.org/abs/1608.07538>
- [6] H. Jansen *et al.*, Performance of the EUDET-type beam telescopes (2016).
arXiv: <http://arxiv.org/abs/1603.09669v2>
- [7] X. Llopard *et al.*, Timepix, a 65k programmable pixel readout chip for arrival time, energy and/or photon counting measurements, *Nuclear Instrumentation Methods A* **581** (2007) 485.
<https://doi.org/10.1016/j.nima.2007.08.079>
- [8] T. Poikela *et al.*, Timepix3: a 65k channel hybrid pixel readout chip with simultaneous toa/tot and sparse readout, *Journal of Instrumentation* **9** (2014) C05013.
<https://doi.org/10.1088/1748-0221/9/05/C05013>
- [9] Micron Semiconductor Ltd., England, <http://www.micronsemiconductor.co.uk/>
- [10] X. Wu *et al.*, Recent advances in processing and characterization of edgeless detectors, *Journal of Instrumentation* **7** (2012) C02001.
<https://doi.org/10.1088/1748-0221/7/02/C02001>
- [11] A. Nürnberg on behalf of the CLIC detector and physics (CLICdp) collaboration, Silicon pixel-detector R&D for CLIC, *Journal of Instrumentation* **11** (2016) C11039.
<https://doi.org/10.1088/1748-0221/11/11/C11039>
- [12] N. Alipour Tehrani *et al.*, Test beam analysis of ultra-thin hybrid pixel detector assemblies with Timepix readout ASICs, CLICdp-Note-2016-001 (2016).

- [13] N. Alipour Tehrani on behalf of the CLIC detector and physics (CLICdp) collaboration, Recent results with HV-CMOS and planar sensors for the CLIC vertex detector, *Nuclear Instrumentation Methods A* (2016), in press.
<https://doi.org/10.1016/j.nima.2016.05.133>
- [14] Sentaurus Device - An advanced multidimensional (1D/2D/3D) device simulator, <http://www.synopsys.com/Tools/silicon/tcad/Pages/default.aspx>
- [15] P. Valerio *et al.*, Design of the 65 nm clicpix demonstrator chip, LCD-Note-2012-018 (2012).
- [16] A. Tomada *et al.*, Flip Chip Assembly of Thin Substrates, Fine Bump Pitch, and Small Prototype Die, SLAC-PUB-16168 (2015).
- [17] S. Agostinelli *et al.*, Geant4 – a simulation toolkit, *Nuclear Instrumentation Methods A* **506** (2003) 250-303.
[https://doi.org/10.1016/S0168-9002\(03\)01368-8](https://doi.org/10.1016/S0168-9002(03)01368-8)
- [18] N. Alipour Tehrani *et al.*, Capacitively coupled hybrid pixel assemblies for the CLIC vertex detector, CLICdp-Pub-2015-003 (2015), *Nuclear Instrumentation Methods A* **823** (2016) 1-8.
<https://doi.org/10.1016/j.nima.2016.03.072>
- [19] M. Buckland, TCAD simulations of High-Voltage-CMOS Pixel structures for the CLIC vertex detector, CLICdp-Note-2016-004 (2016).

GEM Detectors in Experiments at e^+e^- Colliders in BINP

T.V. Maltsev

Budker Institute of Nuclear Physics SB RAS, Novosibirsk, Russia
Novosibirsk State University, Novosibirsk, Russia

Abstract

Micro-pattern gaseous detectors possess a high spatial resolution in the tens of microns, together with a high rate capability of up to $10^7 \text{ cm}^{-2} \text{ s}^{-1}$. In addition, they have all the advantages of gaseous detectors, such as relatively low cost per unit area and the possibility of equipping a large area, as well as high uniformity. Detectors based on cascaded gas electron multipliers (GEMs) are used in the collider experiments at the Budker Institute of Nuclear Physics (BINP), and are being developed for a number of new projects. In this article, a review of GEM-based detectors for the tagging system of the KEDR experiment at the VEPP-4M collider and for the DEUTERON facility at the VEPP-3 storage ring is presented. The GEM detector application of the CMD-3 detector upgrade at the VEPP-2000 collider and the Super $c\text{-}\tau$ Factory detector are discussed.

Keywords

KEDR experiment; DEUTERON facility; CMD-3 detector; Super $c\text{-}\tau$ Factory; gas electron multiplier.

1 Introduction

Cascaded gas electron multipliers (GEMs) [1] provide an opportunity to create large area detectors that are characterized by good spatial resolution and high rate capability [2–6]. Spatial resolution at the range of 50–70 μm can be achieved for relativistic charged particles with triple-GEM cascades operating with argon gas with a CO_2 admixture of 25% [2, 6]. Tracking detectors based on triple-GEM cascades are being developed and used in several experiments at the Budker Institute of Nuclear Physics (BINP).

In this paper, we will review the current status of the triple-GEM detectors for the tagging system (TS) of the KEDR detector [7–9] at the VEPP-4M [10, 11] collider and the light triple-GEM detectors for the photon tagging system (PTS) of the DEUTERON facility [12, 13] at the VEPP-3 storage ring [14]. The KEDR detector is a general-purpose detector installed at the VEPP-4M collider for experiments with electron–positron beams in the energy range 2–10 GeV in the centre-of-mass energy frame. The VEPP-4M is the electron–positron collider at BINP, working in the energy range 1–5 GeV per beam. The DEUTERON facility is a facility with an internal target at the VEPP-3 storage ring, intended for experiments with electrons or positrons, interacting with protons and deuteron nuclei. The VEPP-3 is the injection storage ring for the VEPP-4M collider; it can operate as a storage ring for electrons and positrons up to 2 GeV. Also, the VEPP-3 can operate as a synchrotron radiation source and as a beam source for the DEUTERON facility. We will discuss future GEM applications, including the large cylindrical triple-GEM detector for the cryogenic magnetic detector (CMD-3) at the VEPP-2000 collider and GEMs for a vertex detector of the future Super $c\text{-}\tau$ Factory [15, 16].

The TS is designed for the detection of electrons and positrons scattered after two-photon interaction. It consists of a magnet system and eight so-called co-ordinate stations—four stations at the electron side and four stations at the positron side. Each co-ordinate station includes a hodoscope of drift tubes and a triple-GEM two-dimensional detector. The TS is described in detail in Ref. [6].

The DEUTERON facility with internal target at the VEPP-3 storage ring [12, 13] is focused on experiments for the study of interactions of electrons, positrons, and photons with light nuclei. A major part

of the experimental programme at DEUTERON is devoted to the measurement of polarized observables in electro- and photo-nuclear reactions. Further progress in these experiments at VEPP-3 is associated with the development of the ‘almost-real PTS’ [4, 17]. Here, an ‘almost-real photon’ is a virtual photon with a virtuality $Q^2 = 8\text{--}15 \text{ fm}^{-2}$. The PTS includes a set of magnets and high-resolution tracking detectors that measure the momentum of an electron that has lost a large fraction of its energy via photon radiation, producing a photo-nuclear reaction in the target. The results of spatial resolution measurements of the triple-GEM detector for the DEUTERON facility are presented in this article.

The CMD-3 is installed at the VEPP-2000 collider [15, 18, 19] and is used for measurements of the total cross-section of electron–positron annihilation to hadrons in the operating energy range from 0.32 GeV to 2.00 GeV. The CMD-3 enables the study of light vector mesons as well as $n\bar{n}$ and $p\bar{p}$ production cross-sections near the threshold of the reactions in the energy range from 0.32 GeV to 2.00 GeV in the centre-of-mass frame. Among other subsystems, the CMD-3 has a so-called Z -chamber, a thin cylindrical multiwire proportional chamber (MWPC) surrounding the drift chamber. It measures a co-ordinate position along the beam of tracks and provides a signal for the first-level trigger. This chamber is about 20 years old and needs to be replaced. A new GEM-based cylindrical chamber was proposed for this purpose with improved parameters, which include better spatial resolution, trigger segmentation, and rate capability. Together with a new Z -chamber, new endcap GEM-based tracking detectors were proposed. They will be installed between the flanges of the drift chamber and the endcap BGO ($\text{Bi}_4\text{Ge}_3\text{O}_{12}$) crystal-based calorimeters. These detectors will provide precise track angle determination and trigger signals. The endcap tracker will significantly improve detection efficiency for multihadron events.

The Super $e\text{--}\tau$ Factory [16] is expected to be built at BINP. The electron–positron collider will operate in the centre-of-mass energy range 2–5 GeV with a peak luminosity of about $10^{35} \text{ cm}^{-2} \text{ s}^{-1}$ and longitudinally polarized electrons. The study of rare decays of D-mesons and τ -lepton decays requires a general-purpose magnetic detector. It is anticipated that the detector will comprise standard subsystems. GEM-based co-ordinate detectors are proposed for the time projection chamber (TPC) because GEMs are considered to provide an acceptable rate capability ($10^6 \text{ cm}^{-2} \text{ s}^{-1}$) as well as spatial resolution in the scale of tens of microns.

2 Triple-GEM detectors for the tagging system of the KEDR experiment at the VEPP-4M collider

The TS of the KEDR detector at the VEPP-4M electron–positron collider [7, 20] is intended for the study of two-photon processes in electron–positron interactions [8]. The TS uses the accelerator magnets as a spectrometer, as shown in Fig. 1. Electrons and positrons leave the interaction point at a very small polar angle after losing a fraction of their energy in photon–photon interactions. These particles pass through an area with a vertical magnetic field and are deflected at a larger angle than the particles of the initial energy (which have not interacted). Thus, electrons and positrons that participated in the photon–photon interaction are taken away from the equilibrium orbit and are detected in one of four TS stations (TS₁–TS₄). These particles will be referred to as scattered electrons in this paper. Particles of the initial energy remain at the equilibrium orbit. The quadrupoles focus scattered electrons in such a way that their transverse co-ordinates in the detector planes depend weakly on their emission angle. Thus, by measuring the co-ordinates, one can determine the scattered electron energy with a resolution of better than 10^{-3} (r.m.s.) of the beam energy.

The TS includes eight stations based on drift tube hodoscopes combined with high-resolution two-co-ordinate detectors based on triple-GEMs placed in front of each station. The GEM detectors improve the spatial resolution from 300 μm to 65 μm in the orbit plane and provide the possibility of single bremsstrahlung background rejection [6, 21, 22].

Each GEM detector comprises a cascade of three GEMs with a spacing of 1.5 mm. Each GEM has a hexagonal structure of holes of 80 μm in diameter with a pitch of 140 μm . The GEM thickness is

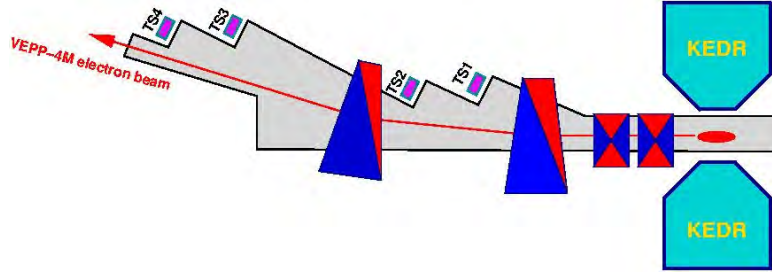


Fig. 1: KEDR tagging system

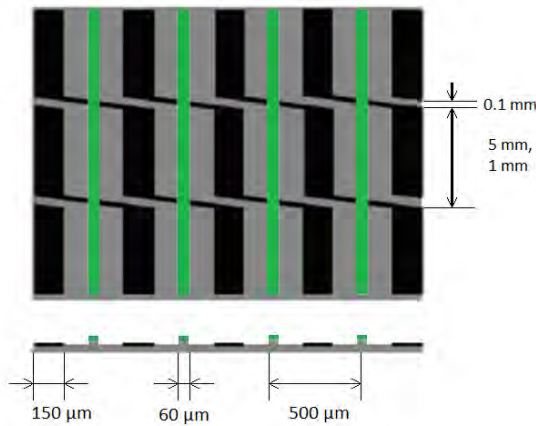


Fig. 2: PCB with small angle stereo readout. Straight strips are marked in green, stereo strips in black. Straight sections of the stereo strips have different lengths, depending on their positions in the detector. This is marked as 1 mm and 5 mm pointing at the straight section.

50 μm . The distance between the bottom GEM and the readout printed circuit board (PCB) is 2 mm and the distance between the top GEM and the drift electrode is 3 mm.

The PCB contains two layers, shown schematically in Fig. 2. The top layer contains straight, 60 μm wide strips. The bottom layer consists of 150 μm wide strips that are divided into straight sections and bridges connecting neighbouring sections so that this strip is, on average, inclined at a certain angle relative to the straight strips. The resulting inclined strips are called stereo strips. Such a configuration of the bottom layer provides uniform charge induction that does not depend on the position along a strip. Straight sections of the stereo strips have different lengths depending on their position in the detector. In the central area, up to 1 cm from the central plane of the detector, the straight sections are 1 mm long; this makes the angle between the stereo and straight strips equal to 30°. Outside this area, the straight sections are 5 mm long and the angle between the stereo and straight strips is close to 11°. Such a layout provides better spatial resolution in the vertical direction in the central area (than outside the central area), which corresponds to the region where electrons and positrons hit the detector. In both layers, the strip pitch is 0.5 mm. The strips in the bottom layer are shifted with respect to the strips in the top layer by 250 μm . The GEMs and PCBs were produced by the CERN PCB workshop.

A detailed discussion of the performance of the TS GEM detectors is presented in Ref. [6], as well as the results from the first long run within the KEDR detector in 2010–2011. During the first run with the KEDR detector, all the TS detectors demonstrated efficiencies between 95% and 98% at a gain between 20 000 and 40 000 [4, 6]. The determined spatial resolution of the detectors for TS KEDR was equal to (65 ± 3) μm for orthogonal electron tracks.

3 Light triple-GEM detectors for the DEUTERON facility at the VEPP-3 storage ring

The DEUTERON facility uses an internal gas target in the VEPP-3 electron storage ring for nuclear physics experiments. This method was proposed and first used in the late 1960s at BINP [12, 13]. The DEUTERON internal gas target [23] consists of polarized deuterium atoms injected in the form of a jet with an intensity of 8×10^{16} atoms/s into a thin-walled T-shaped storage cell with open edges. A series of experiments has been completed during the last decades, all utilizing the tensor-polarized deuterium target to measure tensor asymmetries in fundamental nuclear reactions, such as elastic electron–deuteron scattering and two-body deuteron photo-disintegration.

Further progress of the experiments focusing on the study of photo-nuclear processes can be achieved with the ‘almost-real PTS’ [13]. The PTS will provide the possibility of performing new measurements of the polarized observables in photo-nuclear reactions with higher photon energies—up to 1.5 GeV—and with higher precision than was achievable before. For example, measurement of tensor target asymmetry and photon beam asymmetry in the deuteron photo-disintegration experiment at large photon energies becomes feasible. Such data are of special interest after the Jefferson Lab has demonstrated that for unpolarized measurements the transition from a meson–nucleon to a quark–gluon description of the reaction has already been observed at an energy of approximately 1 GeV [17].

The PTS is located inside the experimental straight-line section and does not disrupt the storage ring beam optics (Fig. 3). It has three ‘warm’ dipole magnets (D1, D2, D3) building a chicane, with magnetic field integrals of 0.248 T m, 0.562 T m, and 0.314 T m, respectively. The internal target storage cell is placed between the first and second magnets. The second dipole magnet, together with the tracking system, serves as a magnetic spectrometer for those electrons that lost a fraction of their energy through radiation of an energetic photon producing a photo-reaction on the target. Such electrons are deflected from the beam trajectory by the strong field (1.7 T for a 2 GeV electron beam) of the second magnet, such that they leave through a thin beryllium window from the vacuum chamber of the storage ring. The system of position-sensitive detectors based on cascaded GEMs determines the tracks of these electrons. The trigger sandwich scintillator S2 is located behind the position-sensitive detectors. The main background process for the reaction of a virtual photon exchange reaction is the bremsstrahlung of electrons or positrons on the target nuclei. The veto sandwich scintillator (S1) detects photons from bremsstrahlung processes on the target, which allows most of such background events to be rejected. Three triple-GEM detectors have been planned for installation at the PTS. The first detector for the PTS was mounted with new electronics and tested in the first half of 2013. In general, the detector design is very similar to that of the detectors for the KEDR TS. The detector sensitive area is 160 mm \times 40 mm. The readout board contains two layers: the inclined and the straight strips. The inclination angle is 30°. Multiple scattering in the detector material affects the angular resolution in the PTS, unlike the KEDR TS, where only one high-resolution detector is installed just after the outlet window at each station. To minimize multiple scattering due to the detector elements, the thickness of copper on the electrodes at each GEM side was reduced with respect to the regular GEM-based detector layout, to 1–2 μm . Such an approach was investigated previously [24] and it was found that the thinning of copper layers does not affect the detector performance.

The amount of material in the detector was measured, using 100 MeV electrons in the experimental set-up shown in Fig. 4. The angular distribution of the tracks after multiple scattering in the detector under study showed that the amount of material in the detector corresponds to $X/X_0 = (2.4 \pm 0.5) \times 10^{-3}$. This value in turn means that the copper thickness in the GEMs and the PCB is approximately

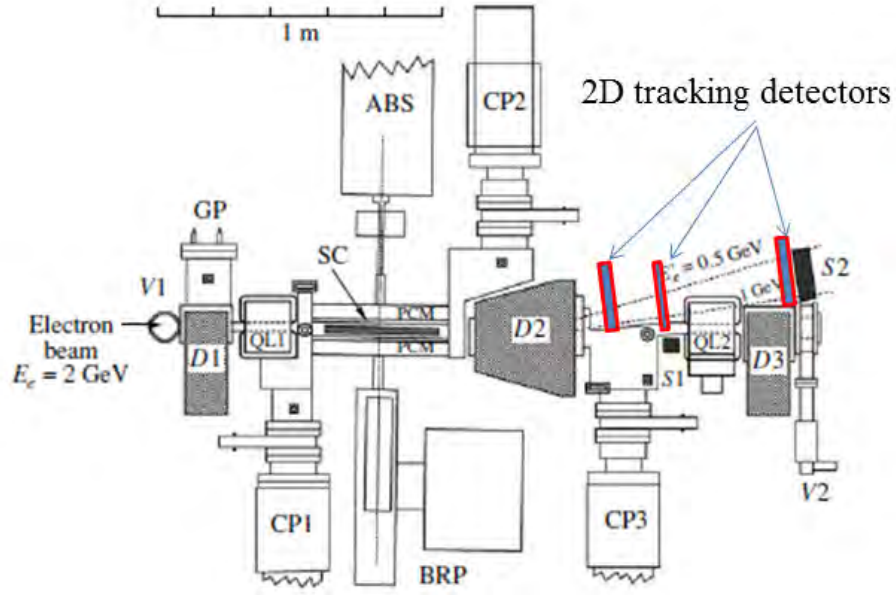


Fig. 3: ‘Almost-real photon tagging system’ (view from top). D1, D2, D3: three dipole magnets; QL1, QL2: quadrupole lenses; PCM: target polarization control magnet; S1, S2: trigger sandwich scintillators; ABS: polarized atomic beam source; SC: target storage cell; BRP: Breit–Rabi polarimeter for ABS jet atoms; CP1, CP2, CP3, GP: cryogenic and getter pumps; V1, V2: gate valves of the experimental section.

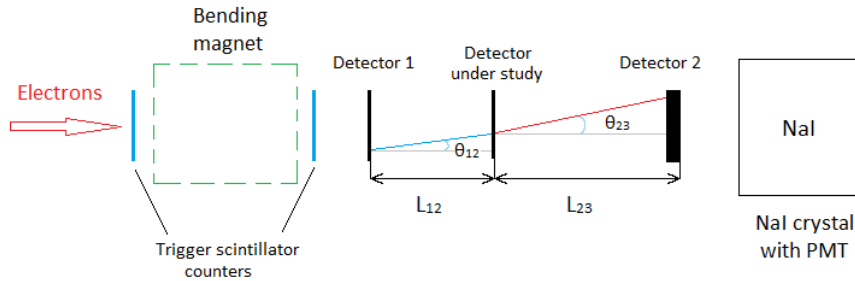


Fig. 4: Set-up for measurement of the material budget and the spatial resolution of the detector

3 μm . The spatial resolution of the detector under study was measured with the same set-up (Fig. 4), but the distances between the detectors were reduced to approximately 75 mm and the beam energy was increased to 1 GeV (Fig. 5) to reduce multiple scattering. The uncertainties in Fig. 5 represent the statistical errors. The curve in Fig. 5 was calculated using the formula of the quadratic sum of the resolution for orthogonal tracks and track projection to the detector plane,

$$\sigma = \sqrt{\sigma_0^2 + (L \times \tan(\alpha))^2/12}, \quad (1)$$

where σ_0 is chosen near the minimum value of the spatial resolution, L is the width of the drift gap, which is equal to 3 mm, and α is a track angle. The effects of multiple scattering and limited spatial resolution

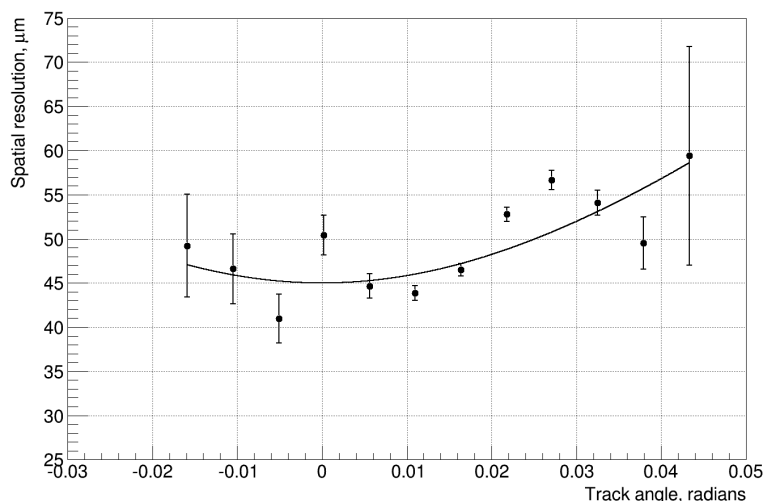


Fig. 5: Spatial resolution of GEM detector at the DEUTERON facility as a function of track angle, determined with 1 GeV electrons [25, 26]. Data are corrected for multiple scattering and the limited resolution of the tracking detectors (details in the text). Only statistical uncertainties are shown.

of the tracking detectors were corrected. The contribution of the multiple scattering to the determined spatial resolution was calculated, based on the value of material budget of the studied detector and the distances between the detectors. This contribution was then quadratically subtracted from the resolution and extracted from the primary co-ordinate residual distributions. The resulting value was divided by $\sqrt{3/2}$ to correct the value of the determined spatial resolution for the limited spatial resolution of the detectors in the experiment. The value $\sqrt{3/2}$ has a statistical origin and is based on the assumption that the tracking detectors in the experiment have the same spatial resolution. The measured spatial resolution of the studied GEM-based detectors for the DEUTERON PTS was extracted as (45 ± 3) μm for electron tracks hitting the detector orthogonally.

4 Large cylindrical triple-GEM for the CMD-3 detector at the VEPP-2000 collider

Large cylindrical triple-GEM detectors (CGEMs) and flat triple-GEM endcap discs are proposed for the upgrade of the CMD-3 detector at the VEPP-2000 electron–positron collider. The CMD-3 is a general-purpose detector intended for studies of light vector mesons in the energy range between 0.3 GeV and 2.0 GeV [15]. Its structure is shown schematically in Fig. 6. The Z -chamber (ZC) has operated for about 10 years at the VEPP-2M collider [27] and 4 years at the VEPP-2000. Its main purpose is to measure the track co-ordinates precisely along the beam axis (Z co-ordinate) and provide a trigger signal. Some of the ZC parameters have degraded with time. The high-voltage plateau width was reduced from a starting value of 250 V to 50 V, resulting in a decreased efficiency. Therefore, it is necessary to build a new chamber with improved parameters. The CGEM was chosen as utilizing the best technique for this purpose. The inner tracker of the KLOE-II experiment [28], with similar geometrical dimensions, has been constructed, representing a good showcase for the ZC upgrade.

The CGEM is planned to be constructed with a digital readout. The front-end electronics will be situated at the ends of the chamber. A fine segmentation of the anode readout structure can be implemented with modern electronics, using multiplexing (Fig. 7). The double layer of the chamber with a common cathode will allow for a reduction of the systematic errors in the Z co-ordinate determination, owing to the magnetic field and the polar angle of the tracks. One of the most important advantages of the CGEM is the absence of wires, which excludes possible mechanical damage of the wires, such as

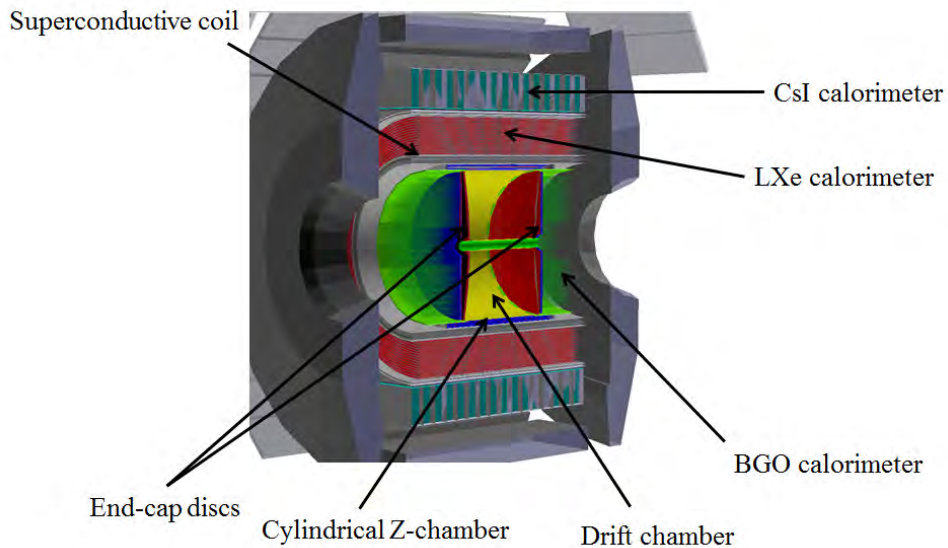


Fig. 6: CMD-3 detector with all subsystems indicated

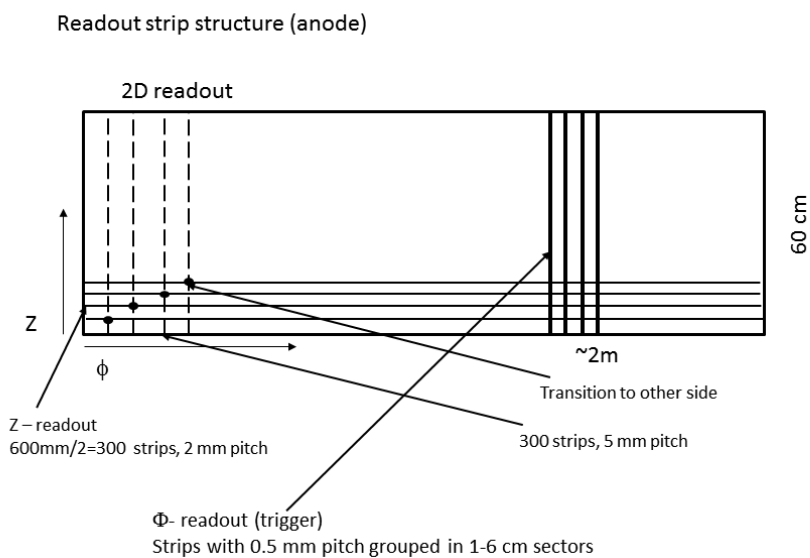


Fig. 7: Structure of readout board of CGEM Z-chamber

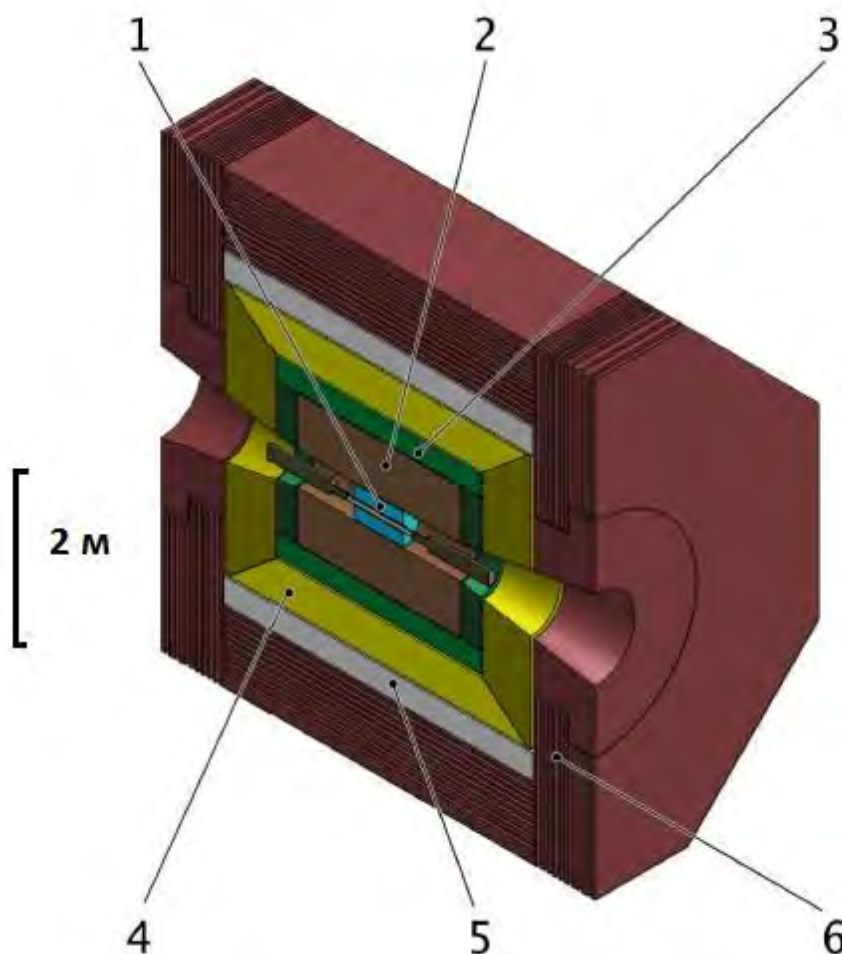


Fig. 8: General-purpose magnetic detector for Super c - τ Factory with general subsystems indicated. 1: vertex detector; 2: drift chamber; 3: identification system based on FARICH; 4: calorimeter; 5: superconducting coil; 6: yoke with muon system.

breakage or sagging. Another advantage is that the GEM structure has a counting rate capability more than two orders of magnitude higher than the wire chambers. The GEM segmentation allows a part of the chamber to be disconnected in case of damage and high-voltage short circuits after a breakdown; this is impossible with the current ZC. An advantage of the CGEM is the smaller dependence of the effective gain of the GEM cascade on the geometrical accuracy of the chamber than is achieved for the MWPC.

The chamber consists of two concentric triple-GEM detectors with common drift cathode and strip readout boards on the inner and outer cylinders. The chamber diameter and length are both about 60 cm. These dimensions allow one to fabricate each GEM from one piece, approximately $60 \text{ cm} \times 200 \text{ cm}$ rather than gluing several GEM pieces together, as used to be done in the case of the KHLOE-II Inner Tracker [28].

Both the inner and outer readout boards have the same structure as shown schematically in Fig. 7. The PCB has two layers with perpendicular strips, as in the triple-GEM detectors of the COMPASS experiment at CERN [29]. The bottom layer is segmented into 1.9 mm wide strips with a pitch of 2 mm, which provide a measurement of the Z co-ordinate. Each strip is connected through a metallized hole to the opposite side of the PCB, where strips in the perpendicular direction provide signal outputs to the cylinder end. The top layer of the readout board provides trigger signals. It is segmented in strips parallel

to the cylinder axis (Z direction) that are 100–150 μm wide and have a pitch of 500 μm . The trigger strips are connected to each other in groups of 1 cm to 6 cm in size, which will be divided into two halves by the plane at $Z = 0$ mm. The total number of channels used to measure the Z co-ordinate is 300, while the maximum number of trigger channels is 400. The effective pitch of the electronics channels at the cylinder ends will be about 4 mm in this case.

To increase the solid angle coverage of the CMD-3 tracker we propose to set a two-co-ordinate thin (approximately 15 mm) triple-GEM disc detector between the BGO calorimeter and the drift chamber flanges. In this case, the tracker will cover polar angles down to 0.1 rad.

The endcap tracker will provide measurements of the charge asymmetry for the $e^+e^- \rightarrow \mu^+\mu^-$ process, which has maximal cross-section at small angles. The high luminosity of the VEPP-2000 and the endcap tracker will enable measurement of the pion form factor over a wide energy range using initial state radiation—a new technique developed at BINP. These disc triple-GEM detectors will look like the detectors built for the TOTEM experiment at CERN [30].

5 GEMs at a vertex detector of the Super $c\text{-}\tau$ Factory

The conceptual project of the Super $c\text{-}\tau$ Factory [16] was accepted by BINP in 2013. A study of rare D-mesons and τ -lepton decays, as well as $D^0\bar{D}^0$ oscillations, is the main aim of the Super $c\text{-}\tau$ Factory physics programme. Another important aim is the search for lepton-flavor-violating decays of the τ -lepton, particularly the $\tau \rightarrow \mu\gamma$ decay, which has not yet been observed. The Super $c\text{-}\tau$ Factory is expected to have a peak luminosity of $10^{35} \text{ cm}^{-2} \text{ s}^{-1}$ in the energy region from 2 GeV to 5 GeV in the centre-of-mass energy frame. A universal collider detector with a magnetic field of approximately 1 T will be mounted in the interaction point of the electrons and positrons. The detector comprises standard subsystems, including a vacuum chamber, a vertex detector, a drift chamber, a particle identification system, an electromagnetic calorimeter, a superconducting coil, and an iron yoke with a muon system (Fig. 8).

Here, the TPC based on GEM detectors is proposed as a vertex detector. The reason for using the GEM detectors for the TPC of the vertex detector is the high rate capability and the possibility of operation in continuous mode, which is not possible for TPCs based on MWPCs. A modern example of the GEM is the development, by ILC Collaboration [31], of a TPC with a continuous readout with GEMs. Also, the ALICE TPC upgrade will utilize GEMs [32]. The continuous readout mode is achieved by a reduction of the ion backflow by more than three orders of magnitude. The first prototypes were tested with a gas mixture of Ar (95%), CF_4 (3%), and C_4H_{10} (2%) in a 5 T magnetic field, parallel to electric field lines up to 15 cm from the readout plane. The spatial resolution in the tests was determined to be approximately 50 μm , with sensitive pads with a surface of 2 mm \times 6 mm. It is worth noting that TPCs can implement particle identification based on energy measurements in gas, with dE/dx resolution of a few per cent [31].

6 Conclusions

Tracking detectors based on triple-GEM cascades are being developed and applied in a number of experiments at BINP. GEM detectors have operated at the TS of the KEDR experiment since 2010. The efficiency of these detectors is between 95% and 98% at a gain of 20 000–40 000. The spatial resolution is equal to $(65 \pm 3) \mu\text{m}$ for orthogonal electron tracks. The PTS of the DEUTERON facility includes three tracking GEM-based detectors. The detectors are characterized by a low material budget corresponding to $X/X_0 = (2.4 \pm 0.5) \times 10^{-3}$. The spatial resolution of the detectors measured with a 1 GeV electron beam is $(45 \pm 3) \mu\text{m}$ for orthogonal tracks.

Large cylindrical triple-GEM detectors and flat triple-GEM endcap discs are proposed for the upgrade of the CMD-3 detector at the VEPP-2000 electron–positron collider. For the upgrade application, the tracker will cover down to polar angles of 0.1 rad, and it will improve the sensitivity of the detector to

processes with small characteristic angles. It is proposed that the vertex detector of the general-purpose magnetic detector for the future Super c - τ Factory at BINP be based on a TPC with GEM detector readout. The experience of the International Linear Collider Collaboration gives reasons to expect that a vertex detector spatial resolution of 50 μm can be achieved.

Acknowledgement

This study was supported by the Russian Foundation for Basic Research (project number 15-02-09016).

References

- [1] F. Sauli, *Nucl. Instrum. Methods Phys. Res. A* **386** (1997) 531, [http://dx.doi.org/10.1016/S0168-9002\(96\)01172-2](http://dx.doi.org/10.1016/S0168-9002(96)01172-2)
- [2] B. Ketzer *et al.*, *IEEE Trans. Nucl. Sci.* **49** (2002) 2403, <http://dx.doi.org/10.1109/TNS.2002.803891>
- [3] A. Bressan *et al.*, *Nucl. Instrum. Methods Phys. Res. A* **425** (1999) 262, [http://dx.doi.org/10.1016/S0168-9002\(98\)01406-5](http://dx.doi.org/10.1016/S0168-9002(98)01406-5)
- [4] L.I. Shekhtman *et al.*, *J. Instrum.* **7** (2012) C03021, <http://dx.doi.org/10.1088/1748-0221/7/03/C03021>
- [5] L.I. Shekhtman *et al.*, *J. Instrum.* **8** (2013) C12035, <http://dx.doi.org/10.1088/1748-0221/8/12/C12035>
- [6] V.M. Aulchenko *et al.*, *J. Instrum.* **6** (2011) P07001, <http://dx.doi.org/10.1088/1748-0221/6/07/P07001>
- [7] V.V. Anashin *et al.*, *Nucl. Instrum. Methods Phys. Res. A* **478** (2002) 420, [http://dx.doi.org/10.1016/S0168-9002\(01\)01789-2](http://dx.doi.org/10.1016/S0168-9002(01)01789-2)
- [8] V.M. Aulchenko *et al.*, *Nucl. Instrum. Methods Phys. Res. A* **355** (1995) 261, [http://dx.doi.org/10.1016/0168-9002\(94\)01093-5](http://dx.doi.org/10.1016/0168-9002(94)01093-5)
- [9] V.V. Anashin *et al.*, *Phys. Part. Nucl.* **44** (2013) 657, <http://dx.doi.org/10.1134/S1063779613040035>
- [10] V.V. Anashin *et al.*, VEPP-4M collider: status and plans, Proc. EPAC'98, Stockholm, 1998, p. 400.
- [11] V. Smaluk *et al.* (VEPP-4 Team), Accelerator physics issues of the VEPP-4M at low energy, Proc. of EPAC 2004, Luzern, 2004, p. 749.
- [12] S.G. Popov, *Phys. At. Nucl.* **62** (1999) 256.
- [13] D.M. Nikolenko *et al.*, *Phys. At. Nucl.* **73** (2010) 1322, <http://dx.doi.org/10.1134/S1063778810080065>
- [14] M.V. Dyug *et al.*, *Nucl. Instrum. Methods Phys. Res. A* **536** (2005) 338, <http://dx.doi.org/10.1016/j.nima.2004.08.096>
- [15] B.I. Khazin *et al.*, *Nucl. Phys. B (Proc. Suppl.)* **181–182** (2008) 376, <http://dx.doi.org/10.1016/j.nuclphysbps.2008.09.068>
- [16] http://ctd.inp.nsk.su/c-tau/Project/CDR_en_ScTau.pdf, September 9th 2016.
- [17] P. Rossi *et al.*, *Phys. Rev. Lett.* **94** (2005) 012301, <http://dx.doi.org/10.1103/PhysRevLett.94.012301>
- [18] I.A. Koop *et al.*, *Nucl. Phys. B (Proc. Suppl.)* **181–182** (2008) 371, <http://dx.doi.org/10.1016/j.nuclphysbps.2008.09.067>
- [19] D. Berkaev *et al.*, *Nucl. Phys. B (Proc. Suppl.)* **225–227** (2012) 303, <http://dx.doi.org/10.1016/j.nuclphysbps.2012.02.063>
- [20] E.B. Levichev *et al.*, *Phys. Part. Nucl. Lett.* **13** (2016) 7, <http://dx.doi.org/10.1134/S154747711607044X>

- [21] V.M. Aulchenko *et al.*, *Nucl. Instrum. Methods Phys. Res. A* **494** (2002) 241, [http://dx.doi.org/10.1016/S0168-9002\(02\)01474-2](http://dx.doi.org/10.1016/S0168-9002(02)01474-2)
- [22] V.M. Aulchenko *et al.*, *Nucl. Instrum. Methods Phys. Res. A* **598** (2009) 112, <http://dx.doi.org/10.1016/j.nima.2008.08.115>
- [23] M.V. Dyug *et al.*, *Nucl. Instrum. Methods Phys. Res. A* **495** (2002) 8, [http://dx.doi.org/10.1016/S0168-9002\(02\)01572-3](http://dx.doi.org/10.1016/S0168-9002(02)01572-3)
- [24] A. Bondar *et al.*, *Nucl. Instrum. Methods Phys. Res. A* **556** (2006) 495, <http://dx.doi.org/10.1016/j.nima.2005.11.098>
- [25] V.S. Bobrovnikov *et al.*, *J. Instrum.* **9** (2014) C08022, <http://dx.doi.org/10.1088/1748-0221/9/08/C08022>
- [26] G.N. Abramov *et al.*, *J. Instrum.* **11** (2016) P03004, <http://dx.doi.org/10.1088/1748-0221/11/03/P03004>
- [27] E.V. Anashkin *et al.*, *Instrum. Exp. Tech.* **6** (2006) 798, <http://dx.doi.org/10.1134/S0020441206060066>
- [28] A. Balla *et al.*, *Nucl. Instrum. Methods Phys. Res. A* **628** (2011) 194, <http://dx.doi.org/10.1016/j.nima.2010.06.315>
- [29] B. Ketzer *et al.*, *IEEE Trans. Nucl. Sci.* **48** (2001) 1065, <http://dx.doi.org/10.1109/23.958724>
- [30] G. Antchev *et al.*, *Nucl. Instrum. Methods Phys. Res. A* **617** (2010) 62, <http://dx.doi.org/10.1016/j.nima.2009.08.083>
- [31] M. Dixit *et al.*, *Nucl. Instrum. Methods Phys. Res. A* **581** (2007) 254, <http://dx.doi.org/10.1016/j.nima.2007.07.099>
- [32] ALICE Collaboration. Technical design report for the upgrade of the ALICE time projection chamber. ALICE-TDR-016, CERN-LHCC-2013-020, (CERN, Geneva, 2013), <http://cds.cern.ch/record/1622286/files/ALICE-TDR-016.pdf>

Aerogel Cherenkov Counters of the KEDR Detector

*I.V. Ovtin,^{1,2} A.Y. Barnyakov,^{1,2} M.Y. Barnyakov,^{1,2} V.S. Bobrovnikov,^{1,2} A.R. Buzykaev,^{1,2}
A.F. Danilyuk,^{2,3} A.A. Katcin,^{1,2} S.A. Kononov,^{1,2} E.A. Kravchenko,^{1,2} I.A. Kuyanov,^{1,2}
A.P. Onuchin,^{1,2,4} and V.A. Rodiakin¹*

¹Budker Institute of Nuclear Physics, Novosibirsk, Russia

²Novosibirsk State University, Novosibirsk, Russia

³Boreskov Institute of Catalysis, Novosibirsk, Russia

⁴Novosibirsk State Technical University, Novosibirsk, Russia

Abstract

The particle identification system of the KEDR detector is based on aerogel threshold Cherenkov counters called ASHIPH counters. The system consists of 160 counters arranged in two layers. An event reconstruction program for the ASHIPH system was developed. The position of each counter relative to the tracking system was determined using cosmic muons and Bhabha events. The geometric efficiency of the ASHIPH system was verified with Bhabha events. The efficiency of relativistic particle detection was measured with cosmic muons. A π/K separation of 4σ in the momentum range $0.95 - -1.45$ GeV/ c was confirmed. A simulation program for the ASHIPH counters has been developed.

Keywords

Particle identification; ASHIPH; aerogel.

1 Introduction

The ASHIPH (Aerogel, SHifter, PHotomultiplier) method of Cherenkov light collection was suggested in 1992 [1–3]. Cherenkov light produced by traversing charged particles in the aerogel is transported by a wavelength shifter (WLS) placed in the middle of the counter to a photomultiplier (PMT). This method, compared with direct light collection, helped us to significantly decrease the PMT photocathode area and thus the cost of the system.

In 2014, the fully installed particle identification system of ASHIPH counters began operation in the KEDR experiment at the VEPP-4M e^+e^- -collider. The system consists of 160 counters arranged in two layers (80 barrel counters and 80 endcap counters) and covers 96% of the total solid angle (Fig. 1). The counters are arranged in such a way that a particle travelling from the beam interaction point with a momentum larger than 0.6 GeV/ c passes through at least two layers of counters. Constructions of the endcap and barrel counters are shown in Figs. 2 and 3, respectively. The total volume of the aerogel is 1000 litres. It has a refractive index $n = 1.05$. The system permits π/K separation for particles with momenta from 0.6 to 1.5 GeV/ c [4]. A total of 160 microchannel plate PMTs with a multi-alkali photocathode with a diameter of 18 mm capable of working in a magnetic field of 2 T are used as the photon detectors.

2 Operation of the ASHIPH system in the KEDR experiment

2.1 High voltage supply

The high voltage (HV) source for microchannel plate PMTs consists of six HV converters H40N (EMCO: 4000 V, 3.75 mA, 15 W) in one standard CAMAC 4M module and was developed at BINP. Ten HV modules (PNPI, St. Petersburg) of 16-channel active HV dividers provide tuning of voltage for each counter from 2500 to 4000 V [5].

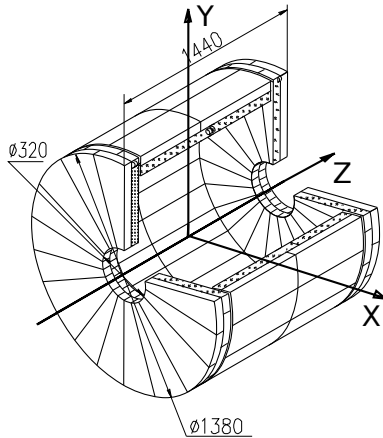


Fig. 1: Layout of the ASHIPH system of the KEDR detector.

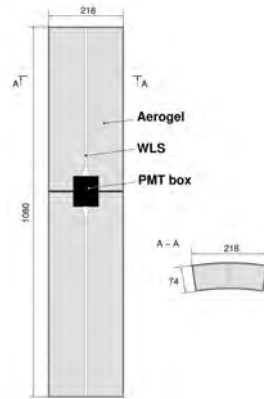


Fig. 2: Two barrel counters in a single housing.

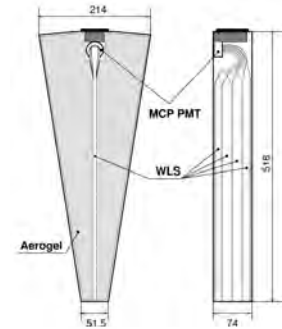


Fig. 3: Endcap counter.

2.2 Electronics

A charge from the photomultiplier anode is converted by the charge-sensitive preamplifier to the parase (bipolar) signal that is brought out of the detector. It is then supplied to inputs of digitizing boards via a long cable (40 m).

The data acquisition system of the KEDR detector is based on the KLUKVA electronic standard developed at BINP [6]. The counters are read out by 28 dedicated A6 electronics boards, which work in the pipeline mode. An A6 board has six channels. Basic elements of the circuit are a 10 bit flash analogue-to-digital converter (ADC) and a shift register. The ADC measures an instantaneous voltage value with a period of 55 ns. The shift register serves as data storage for the trigger-operation time. Five values of voltage are read out for each pulse. There is a discriminator in the circuit to monitor the dark count rates of the PMTs [5, 7].

2.3 Slow control system

The slow control system monitors the dark count rates of the PMTs and provides HV power control. In an emergency, each counter is switched off by an active HV divider individually. The gain stability and counter efficiency are monitored twice per week during calibration runs with LEDs and cosmic particles [5].

3 Event reconstruction and alignment of the ASHIPH system

The event reconstruction program of the ASHIPH system consists of two stages. In the first stage, the recorded pulse shape of five hit amplitudes is fitted to determine the amplitude and the time of arrival of the signal. In the second stage, a track extrapolated into the ASHIPH system and intersections with different parts of the counters are determined.

For the event reconstruction, the ASHIPH system needs to be aligned to the tracking system, which consists of a drift chamber and a vertex detector. The directions of the co-ordinate axes X , Y , and Z are presented in Fig. 1. For the alignment of the systems with each other, cosmic muons and Bhabha events (for the endcap) with at least one particle with a momentum of more than 1 GeV/c are used. The amplitude of the signal created by a particle that crosses the WLS is several times larger than from particles traversing the aerogel. We also know that the WLSs are each located at approximately 18° over the full azimuthal angle coverage (Fig. 4). This allows us to determine the position of each counter relative to the tracking system with 0.5–1.0 mm accuracy. This accuracy is determined by the

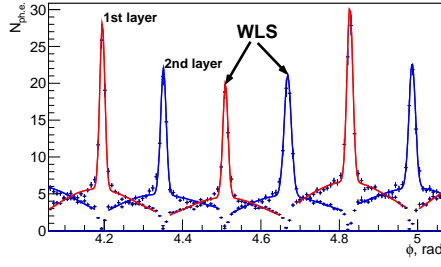


Fig. 4: Dependence of the signal amplitude of the cosmic muons (in number of photoelectrons) on the azimuthal angle φ .

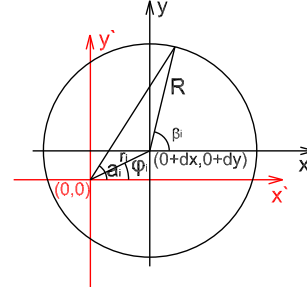


Fig. 5: Relationship between the co-ordinates of the KEDR tracking system (x', y') and the co-ordinates of the ASHIPH system (x, y) .

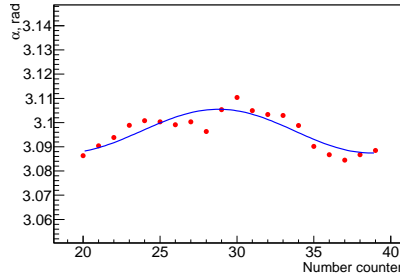


Fig. 6: Position of the WLSs in the azimuthal angle of the tracking system (x', y') normalized to the position of the WLS for one counter, together with a fit of the experimental data for determining β_i , φ_i , and r_i .

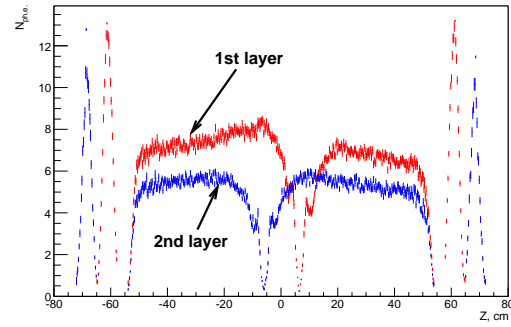


Fig. 7: Dependence of the amplitude from the cosmic muons on the Cartesian co-ordinate Z .

WLS geometry and co-ordinate resolution of the detector's drift chamber. The position of the WLS could be described by the relation between the co-ordinates of the tracking system and the geometric centre of the ASHIPH system (Fig. 5):

$$\alpha_i = \arctan \left(\frac{R \cdot \sin(\beta_i - i \cdot \pi/10) + r_i \cdot \sin(\varphi_i)}{R \cdot \cos(\beta_i - i \cdot \pi/10) + r_i \cdot \cos(\varphi_i)} \right) + (\pi/10) \cdot i, \quad (1)$$

where i is number of the counter, from 0 to 159 and β_i , φ_i , r_i are parameters determined in the fit to the experimental data (Fig. 6). R is the radius of the ASHIPH system, and was measured during the installation of the system to the KEDR detector. The experimental data were fitted independently for eight geometric parts of the ASHIPH system.

The displacement along the Z co-ordinate between the ASHIPH and the tracking system was determined using the position of the midpoints of the barrel counters (Fig. 7). The rotation angle φ is determined by the displacement of the WLS relative to zero in local co-ordinates. Displacement along the angles θ and ψ of the ASHIPH system is not visible; therefore, these angles were fixed to zero. The final shifts and rotations of the ASHIPH system after alignment relative to the tracking system are presented in Table 1.

4 ASHIPH system efficiency

4.1 Geometric efficiency on Bhabha events

To measure the geometric efficiency of the system, $e^+e^- \rightarrow e^+e^-$ events called Bhabha events were selected from the experimental data using information from the tracking system (two collinear tracks

Table 1: Shifts and rotation of the ASHIPH system

	Δx , mm	Δy , mm	Δz , mm	$\Delta\varphi$, rad
Barrel	2.30 ± 0.18	-4.10 ± 0.10	2.50 ± 0.20	0.046 ± 0.001
Left endcap	1.42 ± 0.16	0.27 ± 0.06	6.00 ± 0.23	0.035 ± 0.001
Right endcap	4.28 ± 0.02	6.18 ± 0.11	0.00 ± 0.20	0.035 ± 0.001

Table 2: Geometric efficiency for the case when at least one layer is fired.

Area of counter with offset from walls	ε , %
1)'Aerogel'-0 mm	$95.7 \pm 0.6\%$
2)'Aerogel'-5 mm	$86.1 \pm 0.6\%$
3)'Aerogel'-10 mm	$76.2 \pm 0.6\%$
4)'All counter'-0 mm	$99.5 \pm 0.5\%$
5)'All counter'-5 mm	$99.1 \pm 0.6\%$
6)'All counter'-10 mm	$98.4 \pm 0.6\%$

Table 3: Geometric efficiency for the case when both layers are fired.

Area of counter with offset from walls	ε , %
1)'Aerogel'-0 mm	$84.6 \pm 0.6\%$
2)'Aerogel'-5 mm	$74.4 \pm 0.6\%$
3)'Aerogel'-10 mm	$64.5 \pm 0.5\%$
4)'All counter'-0 mm	$86.4 \pm 0.6\%$
5)'All counter'-5 mm	$76.5 \pm 0.6\%$
6)'All counter'-10 mm	$66.5 \pm 0.5\%$

from the interaction point) and the calorimeter system (total released energy tracks should be more than 2 GeV). The geometric efficiency was determined by the expression:

$$\varepsilon = \frac{N_{\text{ashiph_tracks}}}{N_{\text{tracks}}}, \quad (2)$$

where N_{tracks} is the number of charged particle tracks and $N_{\text{ashiph_tracks}}$ is the number of charged particle tracks that hit in the ASHIPH system. The events were selected by the calorimeter in a polar angle range covering $20^\circ < \theta < 160^\circ$ (corresponding to 94% of the full sphere surrounding the interaction point).

Two area types of the counter are considered in the following, called 'Aerogel' and 'All counter'. 'Aerogel' is the area of the aerogel with cut-offs for the electronics and WLS and offset from the walls. 'All counter' is the area of the aerogel and WLS with cut-offs for the electronics and offset from the walls. Tables 2 and 3 present the results for two different intersections of the track of the system. At least one layer fired is the case when a particle hits at least one layer of the system. Both layers fired is the case when a particle hits both layers of the system.

4.2 Efficiency of charged particle detection

The momentum dependence of the amplitude sum of the number of photoelectrons on cosmic muons for both layers in the barrel part of the system is shown in Fig. 8 [5, 8]. The data in Fig. 8 are fitted by the function:

$$\mu = \mu_0 + \mu_{\text{max}} \cdot \frac{p^2 - p_{\text{thr}}^2}{p^2}, \quad (3)$$

where p is momentum of the muon, p_{thr} is the momentum corresponding to the Cherenkov emission threshold ($p_{\text{thr}} = 322 \text{ MeV}/c$ for $n = 1.05$), μ_0 is the amplitude for subthreshold particles, and μ_{max} is the amplitude for relativistic particles.

The average amplitude of cosmic muons crossing the barrel counters for the first layer is 5.7 ± 0.1 photoelectrons, for the second layer, it is 4.0 ± 0.1 photoelectrons, and for the sum of both layers, it is 9.3 ± 0.4 photoelectrons. The inefficiency for a single layer is $(1 \pm 2)\%$ if the threshold is 0.1 photoelectrons while for two layers in OR mode, it is $(1 \pm 2) \cdot 10^{-2}\%$.

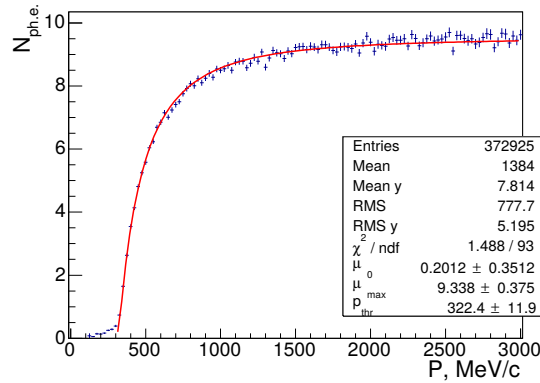


Fig. 8: The amplitude dependence of the barrel counters on the momentum of the cosmic muons which crossed two layers of aerogel in the KEDR ASHIPH system.

4.3 Investigation of detection efficiency

To evaluate the kaon identification efficiency and pion misidentification, a data set with muons of corresponding momentum were chosen from cosmic muons [5]. Muons with a momentum from 200 to 300 MeV/c were chosen as the under-threshold particles. They have the same velocities as kaons with a momentum range of $940 < P_K < 1430$ MeV/c. Muons with a momentum range of 700 to 1100 MeV/c were chosen as the relativistic particles. They correspond to pions with the same momentum, $940 < P_\pi < 1430$ MeV/c. Several approaches for particle registration with two layers of the system were investigated:

- ‘AND’—a relativistic particle gives a signal in both layers of the system;
- ‘OR’—a relativistic particle gives a signal in at least one layer of the system;
- ‘THICK’—the sum of the amplitudes in both layers exceeds the threshold.

For the approaches ‘THICK’, ‘OR’, and ‘AND’, the momentum dependencies of kaon registration efficiency and pion misidentification are presented in Fig. 9. For the ‘THICK’ option, the threshold is equal to 2.0 photoelectrons; for the two other approaches, the threshold is equal to 0.5 photoelectrons. The working momentum region is shown by vertical dashed lines. From these data it is possible to determine the separation power in terms of σ :

$$K[\sigma] = \text{erf}^{-1}(-1 + 2\varepsilon_K) + \text{erf}^{-1}(-1 + 2\varepsilon_\pi), \quad (4)$$

where ε_K is the identification efficiency for kaons and ε_π is the identification efficiency for pions. In the momentum range 0.95–1.45 GeV/c, π/K separation of better than 4σ can be extracted.

5 Simulation of ASHIPH counters

The simulation is performed using a Monte Carlo code based on the Geant3.21 package. The Geant3.21 description of the ASHIPH counters is integrated into the KEDR full detector simulation, which is used for KEDR performance studies and the production of simulated event data, needed for the data analysis. The simulation of the ASHIPH system includes a realistic geometric description of all 160 counters (three active media—aerogel, shifter, Teflon; electronics boxes; and HV outputs). For all counters, a realistic aerogel refractive index was used and measured inhomogeneities in the light collection are taken into account. The digitized amplitudes from calibrated single-photon spectra and pulse shapes are generated.

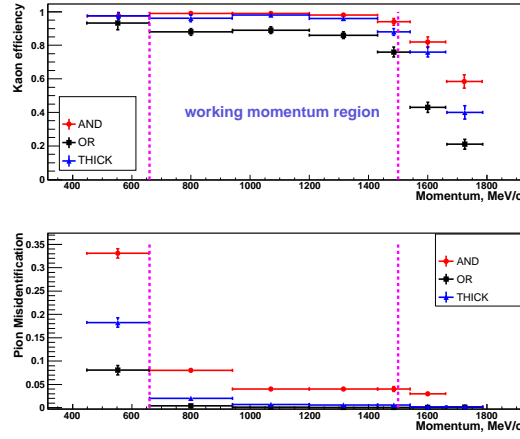


Fig. 9: Momentum dependence of kaon identification efficiency and pion misidentification (obtained from cosmic muons with corresponding velocity).

The full signal from a particle in the ASHIPH counter is the sum of the Cherenkov signal and the scintillation signal in aerogel, shifter, and Teflon:

$$I = I_{\text{ch_aer}} + I_{\text{ch_sh}} + I_{\text{ch_tef}} + I_{\text{sc_aer}} + I_{\text{sc_sh}} + I_{\text{sc_tef}} . \quad (5)$$

The magnitude of scintillation is proportional to the energy loss in matter:

$$I_{\text{sc}_i} = \alpha_i \Delta E_i , \quad (6)$$

where α_i is the proportionality factor and i is the index of the geometric volume (aerogel, shifter, or Teflon).

The number of Cherenkov photoelectrons from relativistic particles above the threshold is determined as:

$$I_{\text{ch}_i} = \frac{dN_i}{dx_i} = K_i \cdot z^2 \left(1 - \frac{1}{(n_i \beta)^2} \right) , \quad (7)$$

where n_i is the refraction index and K_i is the proportionality factor, taking into account the inhomogeneity of light collection, $\beta = v/c$.

The proportionality factor from experimental data is determined as:

$$K_i = \frac{\frac{N_{\text{ph.e.}}}{L_{\text{track}}}}{z^2 \left(1 - \frac{1}{(n_i \beta)^2} \right)} , \quad (8)$$

where $N_{\text{ph.e.}}$ is the number of photoelectrons and L_{track} is the track length in counter. To account for the inhomogeneity of the light collection in the counter, partition of aerogel and WLS was done for five different types of counter. The proportionality factor for each area was determined using cosmic muons with momentum more than 1 GeV/c (Figs. 10 and 11) and used in the simulation program. The results of the inhomogeneity of the light collection are presented in Table 4.

The amplitude distribution of the number of photoelectrons is not described by the Poisson distribution, owing to fluctuations in the gain. To generate a real amplitude, the function distribution is used, which is obtained by a convolution of single-electron spectrum with a Poisson distribution:

$$F(x) = \sum_{n=0}^{n=25} P_n f_n(x) , \quad (9)$$

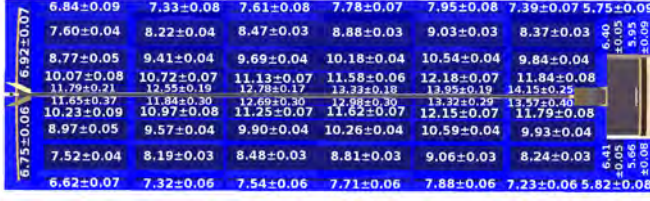


Fig. 10: Distribution of proportionality factor averaged over all long barrel counters of the first layer.

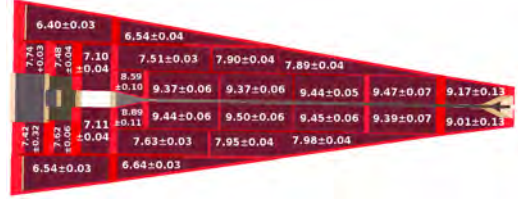


Fig. 11: Distribution of the proportionality factor averaged over all endcap counters.

Table 4: Inhomogeneity of light collection (relative error) for five types of counter

Type of counter	Inhomogeneity of light collection
Short counter of first layer	±26%
Long counter of first layer	±25%
Short counter of second layer	±32%
Long counter of second layer	±36%
Endcap counter	±19%

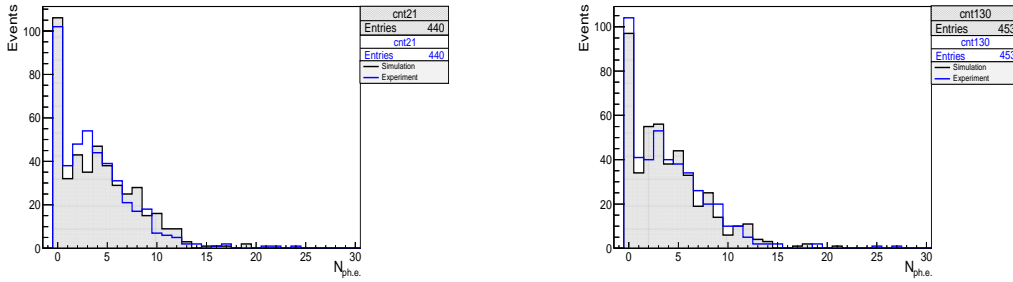


Fig. 12: Distribution of the number of photoelectrons from cosmic muons in simulation and data

where $f_n(x)$ is given by

$$f_n(x) = \int f_1(y) f_{n-1}(x - y) dy, \tag{10}$$

P_n is the Poisson distribution, and $f_1(x)$ is the single-photoelectron spectrum.

Figure 12 presents a comparison of the distribution of the number of photoelectrons from cosmic muons obtained in simulation with experimental data. The comparison of histograms was achieved using the χ^2 criterion. For example, the 21 counter has $\chi^2/ndf = 1.06$ and the 130 counter has $\chi^2/ndf = 0.99$. The integral of the efficiency for these amplitude spectra is presented in Fig. 13. The detection efficiency at a threshold of 0.5 photoelectrons is greater than 98%.

6 Summary

The ASHIPH technique of Cherenkov light collection was developed at BINP. It allowed us to decrease significantly the necessary photocathode area and production costs. An event reconstruction program for the ASHIPH system was developed. Alignment of the ASHIPH counters was performed. The average number of photoelectrons for relativistic cosmic muons ($> 1 \text{ GeV}/c$) that cross both counter layers is 9.3 ± 0.4 . The detection efficiency for muons with ($700 < p_\mu < 1100 \text{ MeV}/c$) is $99.3 \pm 0.1\%$ for a threshold at an amplitude sum equal to 2.0 photoelectrons. The detection efficiency for under-threshold muons ($200 < p_\mu < 300 \text{ MeV}/c$) using the same approach is $3 \pm 1\%$. These data correspond to a π/K

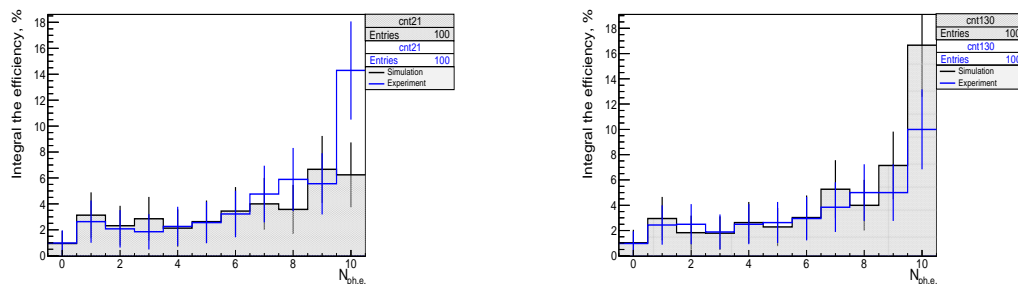


Fig. 13: Integral of the efficiency for amplitude spectra from simulation and data

separation better than 4σ in the momentum range 0.95–1.45 GeV/c. The geometric efficiency for Bhabha events was measured. In the case when a particle hits at least one layer of the system, the geometric efficiency is 96%. The inhomogeneity of the light collection of the ASHIPH counters with cosmic muons was measured. The inhomogeneity of light collection for barrel and endcap counters is $\pm 30\%$ and $\pm 19\%$ respectively. A simulation program for the ASHIPH counters was developed.

References

- [1] A. Onuchin *et al.*, *Nucl. Instrum. Methods* **A315** (1992) 517. [https://doi.org/10.1016/0168-9002\(92\)90757-U](https://doi.org/10.1016/0168-9002(92)90757-U)
- [2] M.Y. Barnykov *et al.*, *Nucl. Instrum. Methods* **A419** (1998) 584. [https://doi.org/10.1016/S0168-9002\(98\)00871-7](https://doi.org/10.1016/S0168-9002(98)00871-7)
- [3] A.Y. Barnyakov *et al.*, *Nucl. Instrum. Methods* **A494** (2002) 424. [https://doi.org/10.1016/S0168-9002\(02\)01513-9](https://doi.org/10.1016/S0168-9002(02)01513-9)
- [4] A.Y. Barnyakov *et al.*, *Nucl. Instrum. Methods* **A478** (2002) 353. [https://doi.org/10.1016/S0168-9002\(01\)01828-9](https://doi.org/10.1016/S0168-9002(01)01828-9)
- [5] A.Y. Barnyakov *et al.*, *Nucl. Instrum. Methods* **A824** (2016) 79. <https://doi.org/10.1016/j.nima.2015.10.105>
- [6] V.M. Aulchenko *et al.*, *Nucl. Instrum. Methods* **A409** (1998) 639. [https://doi.org/10.1016/S0168-9002\(98\)00088-6](https://doi.org/10.1016/S0168-9002(98)00088-6)
- [7] V.V. Anashin *et al.* (KEDR collaboration), *Phys. Part. Nucl.* **44** (2013) 657. <https://doi.org/10.1134/S1063779613040035>
- [8] A.Y. Barnyakov *et al.*, *J. Instrum.* **9** (2014) C08010. <https://doi.org/10.1088/1748-0221/9/09/C09005>

Dynamical Aperture Control in Accelerator Lattices with Multipole Potentials

I. Morozov and E. Levichev

Budker Institute of Nuclear Physics, Novosibirsk, Russia

Abstract

We develop tools for symbolic representation of a non-linear accelerator model and analytical methods for description of non-linear dynamics. Information relevant to the dynamic aperture (DA) is then obtained from this model and can be used for indirect DA control or as a complement to direct numerical optimization. We apply two analytical methods and use multipole magnets to satisfy derived analytical constraints. The accelerator model is represented as a product of unperturbed and perturbed exponential operators with the exponent of the perturbed operator given as a power series in the perturbation parameter. Normal forms can be applied to this representation and the lattice parameters are used to control the normal form Hamiltonian and normal form transformation. Hamiltonian control is used to compute a control term or controlled operator. Lattice parameters are then fitted to satisfy the imposed control constraints. Theoretical results, as well as illustrative examples, are presented.

Keywords

Non-linear dynamics; dynamic aperture; analytical methods; optimization.

1 Introduction

The dynamic aperture (DA) is an important parameter for circular accelerators; it can be defined as a stable area in phase space or, more practically, as an area stable for a fixed number of turns in co-ordinate space. Reduction of DA is mainly caused by non-linear effects, which manifest themselves through frequency dependence on the amplitude, appearance of resonances, and chaos. For DA optimization, usually sophisticated numerical algorithms are used [1]. In this case, the DA is computed directly via particle tracking. In this study, we try to increase the DA by constructing symbolic constraints with analytical tools, such as normal forms [2–4] and Hamiltonian control [5, 6]. Thus, analytical results can be used as a complement to direct DA optimization by providing good initial values for system parameters and additional constraints; it can also be used for indirect optimization. We use a simple FODO cell as an example for which a symbolic model is computed and analytical methods are applied (Fig. 1).

2 Non-linear accelerator model

To study DA, one first needs to build a non-linear model of an accelerator lattice. Here, we use the framework of single-particle Hamiltonian (or symplectic) dynamics. Relevant information about DA can be extracted from the accelerator one-turn map:

$$x_2 = f(x_1), \quad (1)$$

where f is a one-turn map that describes propagation of a particle for one turn in an accelerator, x_1 are the initial co-ordinates, and x_2 are the co-ordinates after one turn. It is well known [2,3,7] that single-particle dynamics can be described in terms of compositional operators $(\mathcal{M}_f g)(x) := (g \circ f)(x) = g(f(x))$; then the lattice operator is given by

$$x_2 = (\mathcal{M}I)(x_1), \quad (2)$$

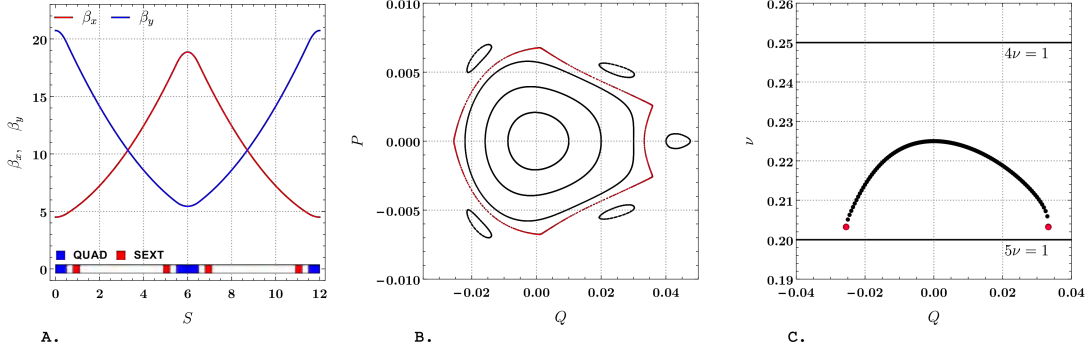


Fig. 1: FODO lattice with sextupole perturbation: (A) layout and lattice functions; (B) phase space trajectories (black) and dynamic aperture (red); (C) frequency dependence on amplitude.

where \mathcal{I} is an identity function and the reference to the associated one-turn map f is dropped from now on.

For analytical (symbolic) calculations, we want to factorize the lattice operator \mathcal{M} . Our goal is to express \mathcal{M} as a product of unperturbed and perturbed parts and to obtain their exponential representations:

$$\mathcal{M} = \mathcal{M}_L \mathcal{M}_N = \exp([F_L]) \exp([F_N]), \quad (3)$$

where \mathcal{M}_L is the unperturbed part, \mathcal{M}_N is the perturbed part, $[F_L]$ and $[F_N]$ are Lie operators, and the Poisson bracket operator is defined as $[f]g := [f, g] = \partial_q f \partial_p g - \partial_p f \partial_q g$. The non-linear perturbation generator $F_N = F_N^{(1)}\varepsilon + F_N^{(2)}\varepsilon^2 + \dots$ is computed up to some order of the formal perturbation parameter ε .

Often, the unperturbed part is associated with linear motion and the perturbed part with non-linear motion. For multipole perturbations, it is common to associate perturbation with homogeneous polynomials, e.g., for 2D phase space with co-ordinates (q, p) , one has

$$F_N^{(k-2)} = F^{(k,0)}q^k + F^{(k-1,1)}q^{k-1}p + \dots + F^{(0,k)}p^k.$$

In the case of accelerators, it is convenient to express the lattice operator as a product of functionally independent parts, e.g., each part describes propagation through a certain accelerator element:

$$\mathcal{M} = \mathcal{M}_1 \mathcal{M}_2 \dots \mathcal{M}_n, \quad (4)$$

where $\mathcal{M}_\alpha = \mathcal{M}_{\alpha,L} \mathcal{M}_{\alpha,N} = \exp([F_{\alpha,L}]) \exp([F_{\alpha,N}])$ is an element operator that satisfies [2]

$$\mathcal{M}_\alpha' = \mathcal{M}_\alpha[-H_\alpha] = \mathcal{M}_\alpha[-H_{\alpha,L} - H_{\alpha,N}], \quad (5)$$

where H_α is the element's Hamiltonian function, and $H_{\alpha,L}$ and $H_{\alpha,N}$ are its linear and non-linear parts, respectively. The operator \mathcal{M} also satisfies this equation for the global Hamiltonian function H , but it is far more complex than individual Hamiltonian functions and thus is not practical to use. Hence, we first need to factorize the element's operators; for the autonomous case, single-exponent representation is straightforward:

$$\mathcal{M}_\alpha = \exp([-s_\alpha(H_{\alpha,L} + H_{\alpha,N})]) = \exp([F_{\alpha,L}]) \exp([F_{\alpha,N}]), \quad (6)$$

where s_α is the element length. It is not the required form, but the linear part is simple to identify:

$$F_{\alpha,L} = -s_\alpha H_{\alpha,L}. \quad (7)$$

Decomposition of Eq. (7) can be motivated by symplectic integrators [8]. In this case, the element is first split into slices and then factorized with BCH formulae [9] and operator identities. Another possibility is to use BCH directly for $\exp([F_{\alpha,N}]) := \exp([-F_{\alpha,L}]) \exp([F_{\alpha,L} + [F_{\alpha,N}])$. This can be done for each slice or an exact expression can be obtained in both cases for pure multipole magnets, i.e., when $F_{\alpha,L} = F_{\alpha,L}(p)$.

These decomposition methods can be used to obtain approximate factorization or exact factorization in the special case. In the generic case, Magnus expansion [10, 11] can be used, which was originally introduced to obtain an exponential solution $Y(t) = \exp(\Omega(t))Y(0)$ of the matrix-differential equation:

$$Y' = A(t)Y. \quad (8)$$

The exponent $\Omega(t)$ satisfies the following differential equation with $\Omega(0) = 0$:

$$\Omega' = \sum_{k=0}^{\infty} \frac{1}{k!} B_k \{\Omega\}^k A,$$

where $\{X\}Y := \{X, Y\} = XY - YX$ denotes the commutator operator and B_k are Bernoulli numbers. This equation can be solved by iteration, $\Omega(t) = \Omega_1 + \Omega_2 + \dots$, and one then has the following recursion:

$$\begin{aligned} \Omega'_1 &= A, & \Omega'_n &= \sum_{k=1}^{n-1} \frac{1}{k!} B_k S_n^{(k)}, & n &\geq 2, \\ S_n^{(1)} &= \{\Omega_{n-1}\}A, & S_n^{(n-1)} &= \{\Omega_1\}^{n-1}A, & S_n^{(k)} &= \sum_{m=1}^{n-k} \{\Omega_m\} S_{n-m}^{(k-1)}, & 2 \leq k \leq n-1. \end{aligned}$$

Explicit solutions can be obtained as multidimensional integrals:

$$\Omega_1(t) = \int_0^t A(t_1) dt_1, \quad \Omega_2(t) = \frac{1}{2} \int_0^t dt_1 \int_0^{t_1} dt_2 \{A(t_1), A(t_2)\}.$$

For the Hamiltonian case, $\mathcal{M}' = \mathcal{M}[-H]$ with $\mathcal{M} = \exp([F])$ and $F = F_1 + F_2 + \dots$ one only needs to replace A with $-H$ and the commutator brackets with Poisson brackets, and change signs $F_n = (-1)^{n+1} \Omega_n$. Since the Hamiltonian has an unperturbed part, an additional step is required before applying the Magnus expansion:

$$\begin{aligned} \mathcal{M}' &= \mathcal{M}[-H] = \mathcal{M}[-H_L - H_N], & \mathcal{M}'_L &= \mathcal{M}_L[-H_L], & \mathcal{M}_L &= \exp([F_L]), \\ \mathcal{M}_M &:= \mathcal{M}_L \mathcal{M}_N \mathcal{M}_L^{-1}, & \mathcal{M}'_M &= \mathcal{M}_M[-\mathcal{M}_L H_N] = \mathcal{M}_M[-H_M], \\ \mathcal{M}_M &= \exp([F_M]) = \exp([F_{M,1} + F_{M,2} + \dots]), & F_N &= \mathcal{M}_L^{-1} F_M = \exp([-F_L]) F_M. \end{aligned}$$

Here, the operator \mathcal{M}_M is defined, for which the Hamiltonian H_M is first-order in perturbation. Thus, an approximation of F_M can be obtained with the Magnus expansion and F_N can then be computed from it. This formally solves the factorization problem for the element operator.

As an example, we give the factorization of a thick sextupole and a thick sextupole with a quadrupole component. In the first case, the Hamiltonian is given by

$$H = \frac{1}{2} p^2 + \frac{1}{3} k_S q^3,$$

where k_S is the sextupole amplitude. The linear part is $F_L = -\frac{L}{2} p^2$ and the non-linear part F_N can be computed up to some order with a Magnus expansion, e.g. first and second orders are given by

$$F_N^{(1)} = \frac{1}{12} k_S L^4 p^3 - \frac{1}{3} k_S L^3 p^2 q + \frac{1}{2} k_S L^2 p q^2 - \frac{1}{3} k_S L q^3,$$

$$F_N^{(2)} = \frac{1}{168}k_S^2L^7p^4 - \frac{1}{24}k_S^2L^6p^3q + \frac{1}{8}k_S^2L^5p^2q^2 - \frac{1}{6}k_S^2L^4pq^3 + \frac{1}{12}k_S^2L^3q^4,$$

where L is the element length, $F_N^{(1)}$ is the first-order perturbation given by a degree-three homogeneous polynomial with coefficients that depend on sextupole parameters, and $F_N^{(2)}$ is a degree-four polynomial.

For a thick sextupole with a quadrupole component, the Hamiltonian is $H = \frac{1}{2}(p^2 + k_Qq^2) + \frac{1}{3}k_Sq^3$, where k_S and k_Q are the sextupole and quadrupole amplitudes, respectively. $F_L = -\frac{L}{2}(p^2 + k_Qq^2)$ is the linear part and the first-order non-linear part $F_N^{(1)} = F_N^{(3,0)}q^3 + F_N^{(2,1)}q^2p + F_N^{(1,2)}qp^2 + F_N^{(0,3)}p^3$ is a degree-three polynomial with coefficients that now depend on the quadrupole amplitude:

$$\begin{aligned} F_N^{(3,0)} &= k_S \left(-\frac{\sin(L\sqrt{k_Q})}{4\sqrt{k_Q}} - \frac{\sin(3L\sqrt{k_Q})}{36\sqrt{k_Q}} \right), \\ F_N^{(2,1)} &= k_S \left(-\frac{\cos(L\sqrt{k_Q})}{4k_Q} - \frac{\cos(3L\sqrt{k_Q})}{12k_Q} + \frac{1}{3k_Q} \right), \\ F_N^{(1,2)} &= k_S \left(\frac{\sin(3L\sqrt{k_Q})}{12k_Q^{3/2}} - \frac{\sin(L\sqrt{k_Q})}{4k_Q^{3/2}} \right), \\ F_N^{(0,3)} &= k_S \left(-\frac{\cos(L\sqrt{k_Q})}{4k_Q^2} + \frac{\cos(3L\sqrt{k_Q})}{36k_Q^2} + \frac{2}{9k_Q^2} \right). \end{aligned}$$

Having obtained factorization of individual elements, we can go back to Eq. (4) and, with a slight change of notation $\mathcal{M}_\alpha = \mathcal{M}_{\alpha,L}\mathcal{M}_{\alpha,N} = \exp([F_{\alpha,L}])\exp([F_{\alpha,N}]) = \mathcal{M}[\alpha-1, \alpha]\mathcal{M}[\alpha]$, the full lattice operator can be written as

$$\mathcal{M} = \mathcal{M}[0, n]\hat{\mathcal{M}}[1] \dots \hat{\mathcal{M}}[n], \quad (9)$$

where $\mathcal{M}[0, n] = \mathcal{M}[0, 1] \dots \mathcal{M}[n-1, n]$ is the linear part, the non-linear part is given by $\hat{\mathcal{M}}[1] \dots \hat{\mathcal{M}}[n]$, with transformed perturbation, $\hat{\mathcal{M}}[\alpha] = \exp([\mathcal{M}^{-1}[\alpha, n]F_{\alpha,N}])$, and the operator identity $\exp([f])\exp([g])\exp([-f]) = \exp([\exp(g)f])$ was used. The product of linear operators is known and the product of non-linear operators can be computed using BCH formulae [9]. Finally, the factorized lattice operator is given by

$$\mathcal{M} = \mathcal{M}_L\mathcal{M}_N = \mathcal{M}[0, n]\exp([F_N^{(1)}\varepsilon + F_N^{(2)}\varepsilon^2 + \dots]). \quad (10)$$

The factorized operator can be used for the normal form and Hamiltonian control computations with generic polynomial perturbation or can be used for geometric indirect optimization (see Section 5). A comparison of element-by-element tracking and analytical model implicit tracking for a FODO example is shown in Fig. 2. We also note that non-linear perturbation computed analytically matches that obtained with COSY INFINITY [12].

3 Normal form computation

In Section 2, it was shown that a circular accelerator can be viewed as a discrete dynamic system specified by a lattice operator Eq. (10). This operator (or the one-turn map associated with it) contains all the relevant information about single-particle non-linear dynamics and thus can be used to study non-linear effects that influence the DA. In this section, for a system defined by $x_2 = f(x_1)$, we want to obtain a simpler representation $y_2 = g(y_1)$, where f is a one-turn map of original system with x_1 and x_2 the initial and final co-ordinates, and g is a normal form of f with y_1 and y_2 the initial and final normal form

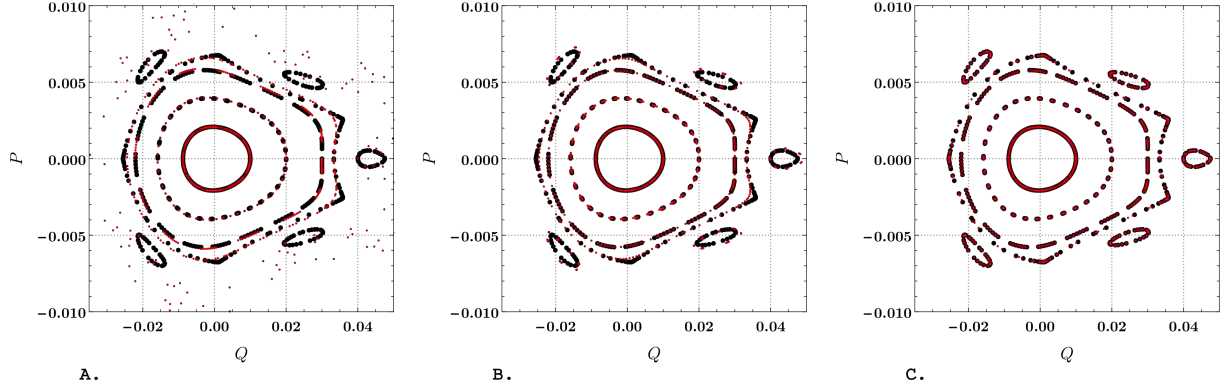


Fig. 2: Comparison of element-by-element tracking (black dots) and analytical model implicit tracking (red dots): (A) $\mathcal{M}_L \exp([F_N^{(1)} \varepsilon])$; (B) $\mathcal{M}_L \exp([F_N^{(1)} \varepsilon + F_N^{(2)} \varepsilon^2])$; (C) $\mathcal{M}_L \exp([F_N^{(1)} \varepsilon + \dots + F_N^{(6)} \varepsilon^6])$.

co-ordinates related to the original co-ordinates x by symplectic transformation $x = h(y)$. From these definitions we have

$$\begin{aligned} x_2 &= f(x_1) = f(h(y_1)) = (f \circ h)(y_1), \\ x_2 &= h(y_2) = h(g(y_1)) = (h \circ g)(y_1), \end{aligned}$$

and since y_1 is arbitrary, we obtain the functional relation $h \circ g = f \circ h$ or $g = h^{-1} \circ f \circ h$. The goal of normal form computation is to find a normal form g and a transformation h for a given one-turn map f . This functional relation can be written in operator form:

$$\mathcal{M}_g = \mathcal{M}_h \mathcal{M}_f \mathcal{M}_h^{-1}, \quad (11)$$

where the definition of the compositional operator $\mathcal{M}_f g := g \circ f$ was used and all operators can be represented by exponential operators or by the product of such operators, since the symplectic case is assumed.

For a given lattice operator $\mathcal{M}_f \equiv \mathcal{M} = \mathcal{M}_L \mathcal{M}_N$, we first want to normalize the linear part \mathcal{M}_L ; to do so, we assume that linear motion is stable (a generic case can be found in Refs. [2, 3]). In this case, \mathcal{M}_L is conjugate to rotation $\mathcal{R} = \mathcal{A} \mathcal{M}_L \mathcal{A}^{-1}$ with transformation \mathcal{A} . The normal form is given by

$$\mathcal{R} = \exp([-2\pi\nu I]), \quad (12)$$

where ν denotes the frequency, $I = 1/2 (q^2 + p^2)$ is the action, and q and p are normal form co-ordinates. For the linear case, the normal form relation Eq. (11) can be written in terms of matrices $R = A^{-1} M_L A$. If we use Courant–Snyder parametrization, then

$$\begin{aligned} M_L &= \begin{bmatrix} \cos(2\pi\nu) + \alpha \sin(2\pi\nu) & \beta \sin(2\pi\nu) \\ -\gamma \sin(2\pi\nu) & \cos(2\pi\nu) - \alpha \sin(2\pi\nu) \end{bmatrix}, & A &= \begin{bmatrix} \sqrt{\beta} & 0 \\ -\frac{\alpha}{\sqrt{\beta}} & \frac{1}{\sqrt{\beta}} \end{bmatrix}, \\ R &= A^{-1} M_L A = \begin{bmatrix} \cos(2\pi\nu) & \sin(2\pi\nu) \\ -\sin(2\pi\nu) & \cos(2\pi\nu) \end{bmatrix}, \end{aligned}$$

where α , β , and $\gamma = 1/\beta (1 + \alpha^2)$ are lattice functions and matrix R is a rotation. Operator \mathcal{R} also corresponds to rotation, for example:

$$\begin{aligned} \mathcal{R}q &= \exp([-2\pi\nu I])q = (1 - [2\pi\nu I] + \frac{1}{2}[2\pi\nu I]^2 - \frac{1}{6}[2\pi\nu I]^3 + \dots)q \\ &= q \left(1 - \frac{1}{2}(2\pi\nu)^2 + \frac{1}{24}(2\pi\nu)^4 + \dots \right) + p \left(2\pi\nu - \frac{1}{6}(2\pi\nu)^3 + \frac{1}{120}(2\pi\nu)^5 + \dots \right) \end{aligned}$$

$$= q \cos(2\pi\nu) + p \sin(2\pi\nu).$$

Having normalized the linear part, we can proceed with the non-linear part $\mathcal{M}_N = \exp([F_N])$ normalization. The effect of linear normalization on operator \mathcal{M} is to normalize its linear part and to transform the non-linear part:

$$\begin{aligned} \mathcal{M}_F &:= \mathcal{A}\mathcal{M}_L\mathcal{M}_N\mathcal{A}^{-1} = (\mathcal{A}\mathcal{M}_L\mathcal{A}^{-1}) (\mathcal{A}\mathcal{M}_N\mathcal{A}^{-1}) = \mathcal{R}\mathcal{A} \exp([F_N])\mathcal{A}^{-1} \\ &= \mathcal{R} \exp(\mathcal{A}[F_N]\mathcal{A}^{-1}) = \mathcal{R} \exp([\mathcal{A}F_N]) =: \mathcal{R} \exp([F_{F,N}]). \end{aligned}$$

Thus, a new system to normalize is

$$\mathcal{M}_F = \mathcal{R} \exp([F_{F,N}]) = \mathcal{R} \exp([\varepsilon F_{F,N}^{(1)} + \varepsilon^2 F_{F,N}^{(2)} + \dots]), \quad (13)$$

where the unperturbed part is given by operator \mathcal{R} defined by Eq. (12), the perturbation $F_{F,N}$ is given in linear normal form co-ordinates, and each order is associated with homogeneous polynomials, for example:

$$F_{F,N}^{(1)} = F_{F,N}^{(3,0)} q^3 + F_{F,N}^{(2,1)} q^2 p + F_{F,N}^{(1,2)} q p^2 + F_{F,N}^{(0,3)} p^3.$$

In general, coefficients of these polynomials depend on lattice parameters, but we can keep this dependence implicit and substitute actual coefficients in the final answer.

According to Eq. (11), the non-linear normal form can be written as

$$\mathcal{N} = \mathcal{T}\mathcal{M}_F\mathcal{T}^{-1}, \quad (14)$$

where $\mathcal{N} = \mathcal{R}\mathcal{K}$ is a normal form of \mathcal{M}_F , $\mathcal{K} = \exp([K]) = \exp([\varepsilon K^{(1)} + \varepsilon^2 K^{(2)} + \dots])$ is a non-linear part of \mathcal{N} , and the normal form transformation is $\mathcal{T} = \exp([T]) = \exp([\varepsilon T^{(1)} + \varepsilon^2 T^{(2)} + \dots])$. Then, the non-linear part is

$$e^{[K]} = \mathcal{R}^{-1} e^{[T]} \mathcal{R} e^{[F_{F,N}]} e^{[-T]} = e^{[\mathcal{R}^{-1}T]} e^{[F_{F,N}]} e^{[-T]} =: e^{[X]} e^{[Y]} e^{[Z]}.$$

The non-linear part can be computed order-by-order, using BCH formulae [9] and the relation between commutator and Poisson brackets $\{[f], [g]\} = [[f], g]$. The order k equation is then

$$K^{(k)} = X^{(k)} + Y^{(k)} + Z^{(k)} + R^{(k)},$$

where $R^{(k)}$ is known and depends on previous orders. To solve this equation, we expand all functions in resonance basis with basis functions $Q^{(n,m)}$:

$$F^{(k)} = \sum_{n,m} F^{(n,m)} Q^{(n,m)}, \quad Q^{(n,m)} = \prod_q I^{\frac{1}{2}n_q} e^{im_q \varphi_q}.$$

And since auxiliary functions $X^{(k)}$ and $Z^{(k)}$ are related to transformation $T^{(k)}$:

$$X^{(k)} = \sum_{n,m} T^{(n,m)} e^{-i2\pi m\nu} Q^{(n,m)}, \quad Z^{(k)} = - \sum_{n,m} T^{(n,m)} Q^{(n,m)},$$

the transformation coefficients are found to be

$$T^{(n,m)} = \frac{1}{2} (1 - i \cot(\pi m\nu)) (R^{(n,m)} - K^{(n,m)}). \quad (15)$$

This expression is singular when the resonance condition is satisfied, i.e., $m\nu = p \in \mathbb{Z}$, or when $m = 0$. These terms must be absorbed into normal form by setting $K^{(n,m)} = R^{(n,m)}$ to resolve singularity. For the case when $m\nu \neq p \in \mathbb{Z}$, only terms with $m = 0$ contribute to the normal form. Then K depends

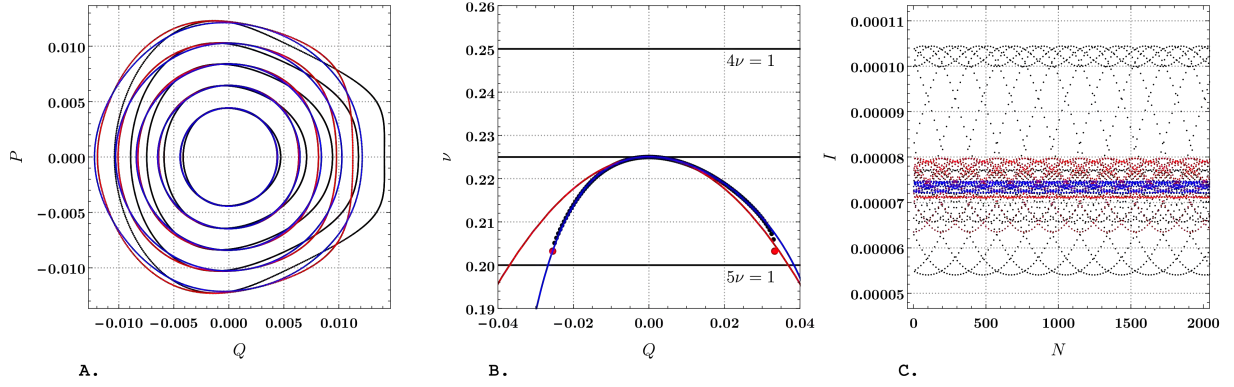


Fig. 3: Full normal form computation for FODO example: (A) effect of normal form transformation on trajectories; (B) frequency dependence on the amplitude; (C) invariant conservation for first order (black), second order (red) and sixth order (blue).

only on actions and thus commutes with the linear part \mathcal{R} . Such a full normal form allows one to obtain dependence of frequencies on the amplitude as well as invariants (Fig. 3).

As an example, we perform full normalization up to second order for the generic case and then substitute parameters for thin and thick single sextupole perturbation. The normal form procedure is also applied to the FODO example (Fig. 3). Generic perturbation in resonance basis up to the second order is given by

$$\begin{aligned} Y &= \varepsilon Y^{(1)} + \varepsilon^2 Y^{(2)}, \\ Y^{(1)} &= Y^{(-3,3)} Q^{(-3,3)} + Y^{(-1,3)} Q^{(-1,3)} + Y^{(1,3)} Q^{(1,3)} + Y^{(3,3)} Q^{(3,3)}, \\ Y^{(2)} &= Y^{(-4,4)} Q^{(-4,4)} + Y^{(-2,4)} Q^{(-2,4)} + Y^{(0,4)} Q^{(0,4)} + Y^{(2,4)} Q^{(2,4)} + Y^{(4,4)} Q^{(4,4)}. \end{aligned}$$

The first-order normal form $K^{(1)} = 0$ and the second-order expression is

$$K^{(2)} = \left(Y^{(0,4)} + \frac{3}{2} Y^{(-1,3)} Y^{(1,3)} \cot(\pi\nu) + \frac{9}{2} Y^{(-3,3)} Y^{(-3,3)} \cot(3\pi\nu) \right) Q^{(0,4)}. \quad (16)$$

This expression is not valid when resonance conditions $\nu = p$ or $3\nu = p \in \mathbb{Z}$ are satisfied. For a thin sextupole, the perturbation in original co-ordinates is

$$F_N^{(1)} = -\frac{1}{3} k_S L q^3, \quad F_N^{(2)} = 0,$$

where L is the sextupole effective length and k_S is the amplitude. The transformed perturbation is given by

$$F_{F,N}^{(1)} \equiv Y^{(1)} = -\frac{1}{3} \beta^{3/2} L q^3 k_S = -\frac{1}{6\sqrt{2}} \beta^{3/2} L k_S \left(Q^{(-3,3)} + 3Q^{(-1,3)} + 3Q^{(1,3)} + Q^{(3,3)} \right),$$

and the second-order normal form is obtained by substituting corresponding coefficients into Eq. (16):

$$K^{(2)} = \frac{1}{16} \beta^3 k_S^2 L^2 (3 \cot(\pi\nu) + \cot(3\pi\nu)) Q^{(0,4)}.$$

The thick sextupole perturbation can be computed with a Magnus expansion (see Section 2 for details). The normal form in this case is

$$K^{(2)} = \frac{1}{16} \beta^3 k_S^2 L^2 (C_1 + 3(1 + C_2) \cot(\pi\nu) + (1 + C_3) \cot(3\pi\nu)) Q^{(0,4)},$$

$$\begin{aligned}
 C_1 &= \frac{\gamma^2 L^5}{7\beta^3} + \frac{\alpha\gamma L^4}{\beta^3} + \frac{(3\alpha^2 + 1)L^3}{\beta^3} + \frac{4\alpha L^2}{\beta^2} + \frac{2L}{\beta}, \\
 C_2 &= \frac{\gamma^3 L^6}{16\beta^3} + \frac{\alpha\gamma^2 L^5}{2\beta^3} + \frac{(63\alpha^2 + 13)\gamma L^4}{36\beta^3} + \frac{\alpha(21\alpha^2 + 13)L^3}{6\beta^3} + \frac{(51\alpha^2 + 11)L^2}{12\beta^2} + \frac{3\alpha L}{\beta}, \\
 C_3 &= \frac{\gamma^3 L^6}{16\beta^3} + \frac{\alpha\gamma^2 L^5}{2\beta^3} + \frac{(7\alpha^2 + 1)\gamma L^4}{4\beta^3} + \frac{\alpha(7\alpha^2 + 3)L^3}{2\beta^3} + \frac{(17\alpha^2 + 1)L^2}{4\beta^2} + \frac{3\alpha L}{\beta}.
 \end{aligned}$$

One can see that in the limit $L \rightarrow 0$ with fixed $k_S L$ this expression is reduced to the thin sextupole case.

For DA optimization, we can perform full normalization and then fit lattice parameters to reduce the frequency dependence on the amplitude and thus reduce the tune footprint size. However, this procedure can lead to increase in resonance strengths and such resonances (that can be selected based on FMA [13]) should be reduced as well. Another option is to control the shapes of the frequency curves to avoid crossing of strong resonances. The shape of invariants can be modified to obtain curves that resemble circles. All these options do not provide direct control of DA, but can be used in indirect optimization or as a complement to a numerical one. Several examples of indirect optimization are given in Section 5.

4 Hamiltonian control theory

The goal of Hamiltonian control theory is to modify the perturbed system \mathcal{M}_F by adding a control operator $\mathcal{C} = \exp([C])$, which is second order in the perturbation parameter, i.e., $C = C^{(2)}\varepsilon^2 + C^{(3)}\varepsilon^3 + \dots$, such that the controlled system \mathcal{M}_C ,

$$\mathcal{M}_C = \mathcal{M}_F \mathcal{C} = \mathcal{R} \exp([F_{F,N}]) \exp([C]), \quad (17)$$

is conjugate to a system that is close to the unperturbed one:

$$e^{[T]} \mathcal{M}_C e^{[-T]} = \mathcal{R} e^{[G_{RF,N}]}.$$

This is the case when the control operator is defined as

$$e^{[C]} := e^{[-F_{F,N}]} e^{[(G_N - \mathcal{G})F_{F,N}]} e^{[G_{RF,N}]} e^{[G_{F,N}]}, \quad (18)$$

where \mathcal{R} is an unperturbed part of uncontrolled operator \mathcal{M}_F is given by Eq. (13), $\mathcal{G} := \mathcal{G}(1 - \mathcal{R}^{-1})\mathcal{G}$ is a pseudo-inverse operator of $(1 - \mathcal{R}^{-1})$, $\mathcal{G}_N := (1 - \mathcal{R}^{-1})\mathcal{G}$ is the non-resonant operator, $\mathcal{G}_R := 1 - \mathcal{G}_N$ is the resonant operator, and $T := \mathcal{G}F_{F,N}$ is the transformation. The controlled operator is then given by

$$\mathcal{M}_C = \mathcal{R} e^{[-\mathcal{R}^{-1}\mathcal{G}F_{F,N}]} e^{[G_{RF,N}]} e^{[G_{F,N}]} =: \mathcal{R} e^{[F_C]}. \quad (19)$$

The perturbation $F_{F,N}$ is transformed into resonance basis and the action of the above operators on the basis function is given by the following expressions:

$$\begin{aligned}
 \mathcal{G}Q^{(n,m)} &= \frac{1}{2}(1 - i \cot(\pi m\nu))\Delta(m\nu \notin \mathbb{Z})Q^{(n,m)}, \\
 \mathcal{R}^{-1}\mathcal{G}Q^{(n,m)} &= -\frac{1}{2}(1 + i \cot(\pi m\nu))\Delta(m\nu \notin \mathbb{Z})Q^{(n,m)}, \\
 \mathcal{G}_N Q^{(n,m)} &= \Delta(m\nu \notin \mathbb{Z})Q^{(n,m)}, \\
 \mathcal{G}_R Q^{(n,m)} &= \Delta(m\nu \in \mathbb{Z})Q^{(n,m)},
 \end{aligned}$$

where the function Δ is defined as $\Delta(\top) := 1$ and $\Delta(\perp) := 0$.

In general, the closed form of the controlled operator (or the control term) cannot be obtained, but it can be approximated up to some order in the perturbation parameter $F_C = F_C^{(1)}\varepsilon + F_C^{(2)}\varepsilon^2 + \dots$

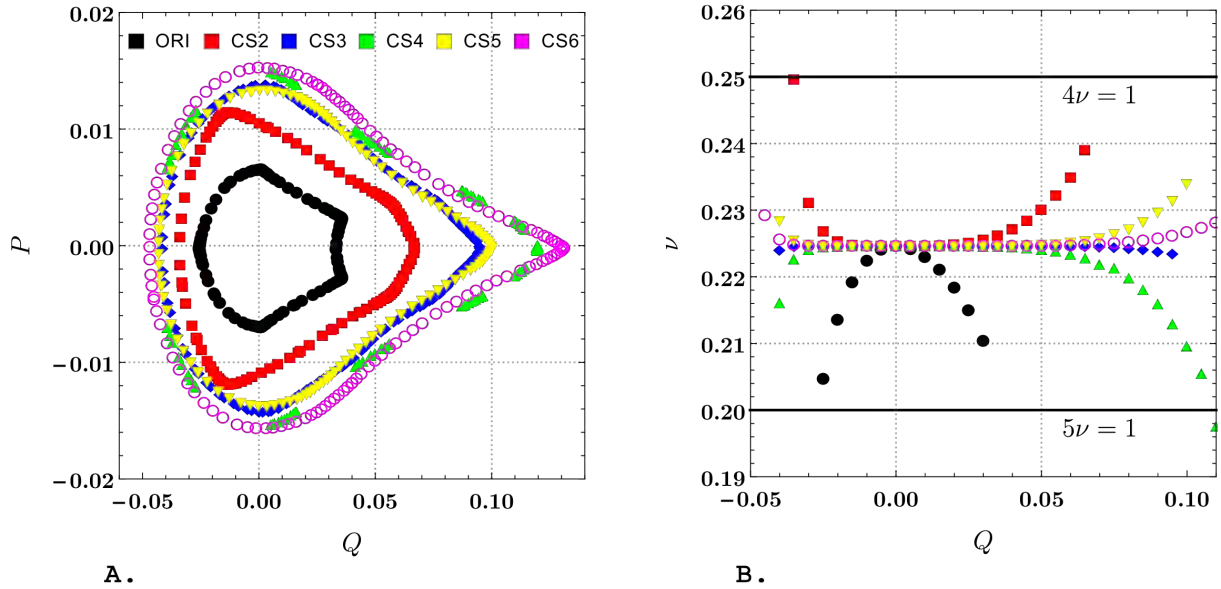


Fig. 4: Formal controlled system for FODO example: (A) DA curves for original system and controlled systems up to order six; (B) corresponding frequency dependence on the amplitude.

with BCH formulae [9]. Control does not change the first-order properties of a system, i.e., $F_C^{(1)} \equiv F_{F,N}^{(1)}$; thus, to construct the controlled operator one can choose only first-order perturbation $F_{F,N} = F_{F,N}^{(1)}\varepsilon$ and, since $F_{F,N}^{(1)}$ is associated with a homogeneous polynomial of degree three, $\mathcal{G}_R F_{F,N}^{(1)} = 0$. Hamiltonian control theory is very flexible, since one can define both the target system and the perturbation.

As an example, we compute the first term of the control operator for thin sextupole perturbation. Like normal form computation (see Section 3 for details), the perturbation is first transformed by linear normalization and then expanded into resonance basis. The first term of the control operator can then be computed:

$$C^{(2)} = -\frac{1}{16}\beta^3 L^2 k_S^2 (\cot(\pi\nu) + \cot(3\pi\nu))q^4 - \frac{1}{16}\beta^3 L^2 k_S^2 (3\cot(\pi\nu) - \cot(3\pi\nu))p^2 q^2.$$

The effect of formal control for a FODO example is shown in Fig. 4. In this case, the target system is \mathcal{R} and $F_{F,N}^{(1)}$ is a perturbation. It can be seen that formal control provides significant improvement of the DA. The frequency curves become flatter as the order of computation is increased. This is the case because the target system is a rotation. If full normal form computation is performed for a controlled system then the normal form has no tune shifts and the transformation is zero for orders greater than one.

Here, DA optimization is not direct but motivated by the fact that the controlled system is conjugate to a good one. Control can be realized as a special element or a controlled system can be obtained with suitable distribution of multipoles. In the following section, examples of fitting octupole and decapole distributions to realize a controlled system are shown (Fig. 5).

5 Examples of indirect optimization

As stated in Section 1, direct DA optimization requires particle tracking. An accelerator model for direct optimization can include a number of effects that are difficult and impractical to include in the analytical model of Eq. (10). The analytical model itself can be used for particle tracking (see Fig. 2) and can potentially speed up direct optimization.

Indirect optimization, on the contrary, does not use particle tracking and thus can be much faster. In this case, lattice parameters should be fitted to satisfy constraints derived from theory. Realization

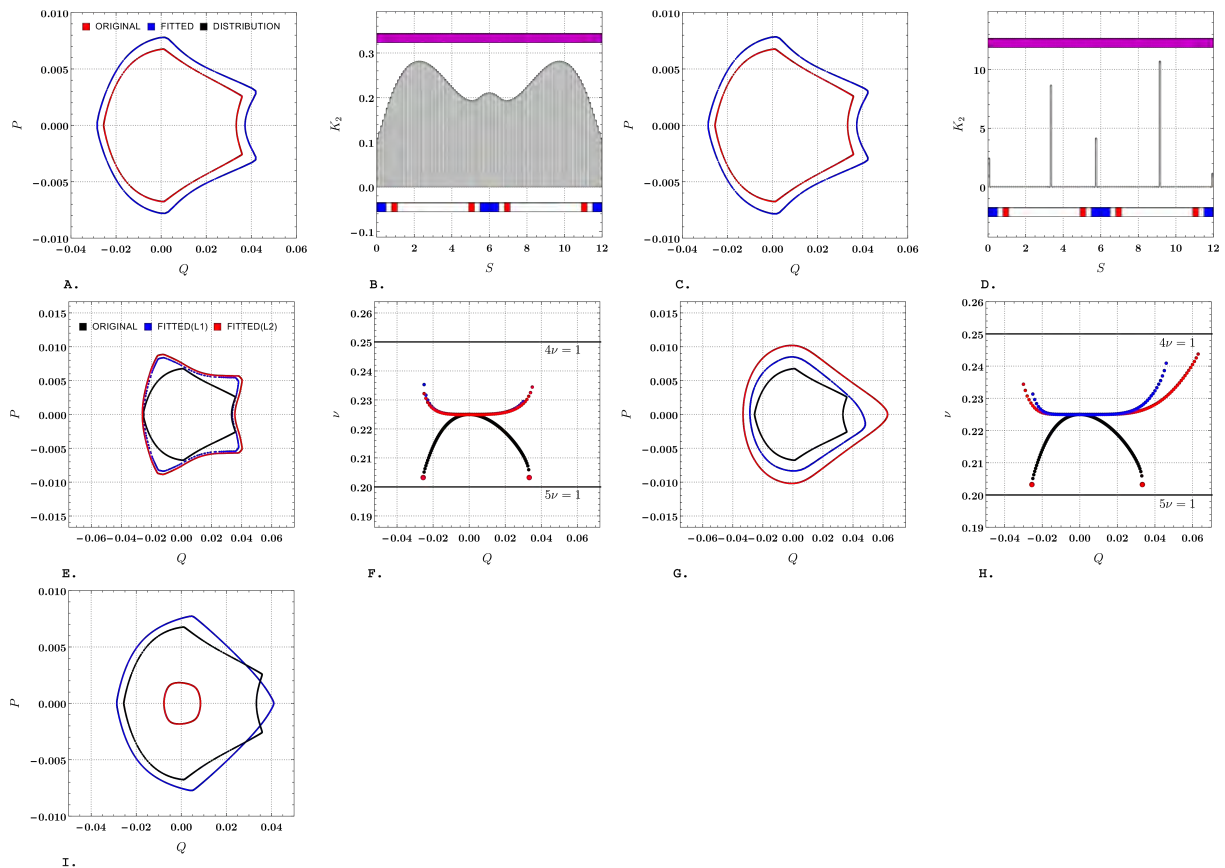


Fig. 5: Examples of linear L1 and L2 indirect optimization. Original lattice is replaced by 120 multipole magnets. (A) L2 geometric optimization, second-order perturbation removed; original DA (red) and L2 DA (blue). (B) Octupole strength distribution for (A). (C) L1 geometric optimization original, second-order perturbation removed; DA (red) and L1 DA (blue). (D) Octupole strength distribution for (C). (E) Normal form L2 and L1 optimizations, second-order tune shift removed; original DA (black), L1 DA (blue), L2 DA (red). (F) Frequency dependence on the amplitude for (E). (G) Normal form L2 and L1 optimizations, second- and fourth-order tune shifts removed and $4\nu = 1$ and $5\nu = 1$ resonances reduced; original DA (black), L1 DA (blue), L2 DA (red). (H) Frequency dependence on amplitude for (G). (I) L2 controlled system realization; original DA (black), second order (blue), third order (red).

of normal form and Hamiltonian control objectives can be reduced to a minimization problem, since in both cases one needs to fit system parameters so that the coefficients of some polynomials have desired values. In principle, one can obtain full symbolic representation of the accelerator model, including linear and non-linear parameters. Usually, one needs to find some lattice parameters (dipole and quadrupole positions and amplitudes, as well as chromatic sextupoles) and suitable distributions of multipoles. If the positions of multipoles are allowed to vary, the minimization problem is intrinsically non-linear. However, for fixed multipole positions, the problem can be partially reduced to linear minimization (here, we use L1 [14] and L2 linear minimization). This is possible, since leading-order dependence of the k th coefficients on k th-order multipole amplitudes is linear. Moreover, polynomial coefficients are linear with respect to k th-order multipole amplitudes up to order $2k - 1$, e.g., second- and third-order coefficients are linear with respect to octupole amplitudes; third, fourth, and fifth orders are linear with respect to decapole amplitudes. Thus, one can reduce indirect optimization to several linear minimization problems.

Geometric optimization can be performed directly on the model, i.e., terms in the non-linear part of the model can be removed. This procedure is motivated by the fact that stable linear systems have infinite

DA. One can then expect an increase in DA if higher-order terms can be neglected. Another option is to use normal forms. In this case, one can reduce the shape frequency dependence on the amplitude and avoid crossing of dangerous resonances. Resonance driving terms can be reduced and invariant shapes can be modified. For Hamiltonian control, DA optimization is motivated by the fact that controlled system is conjugate to a good one. The controlled system can be realized by a suitable distribution of multipole magnets. It should be noted that since fitting is performed up to some order, the effect of higher orders is assumed to be negligible; this might not be a good assumption. Examples of indirect optimization for a FODO example are shown in Fig. 5.

6 Summary

An analytical non-linear accelerator model is important for DA aperture optimization. We have implemented the procedure described in Section 2 in a symbolic manipulator. Thus, semi-realistic symbolic models of accelerator lattices can be computed. Models can include multipole magnets (possibly inside quadrupole magnets), non-linear kinematic effects, and simple fringe field effects. We also plan to include chromatic effects as our next step.

Several methods for non-linear systems analysis were implemented. The full normal form, control term, and controlled system were precomputed for generic polynomial perturbations; one simply needs to substitute corresponding polynomial coefficients to obtain results for a given model.

Various analytical constraints can be generated for a given accelerator model based on non-linear analysis methods. These constraints can be used as a complement to direct DA optimization, or indirect optimization can be performed. We also provided several examples of indirect optimization for a simple FODO cell (Fig. 5). It can be seen that indirect optimization can be used to increase DA, but uncontrolled higher-order terms can lead to DA reduction.

References

- [1] M. Borland *et al.*, Multi-objective direct optimization of dynamic acceptance and lifetime for potential upgrades of the Advanced Photon Source, Technical report APS LS-319, Advanced Photon Source, 2010. <https://doi.org/10.2172/986303>
- [2] E. Forest, *Beam Dynamics: A New Attitude and Framework* (CRC Press, Boca Raton, 1998).
- [3] E. Forest, *From Tracking Code to Analysis: Generalised Courant–Snyder Theory for Any Accelerator Model* (Springer, Tokyo, 2016). <http://doi.org/10.1007/978-4-431-55803-3>
- [4] L. Michelotti, *Intermediate Classical Dynamics with Applications to Beam Physics* (Wiley, New York, 1995).
- [5] M. Vittot, *J. Phys. A* **37** (2004) 6337. <https://doi.org/10.1088/0305-4470/37/24/011>
- [6] J. Boreux *et al.*, *Commun. Nonlinear Sci. Numer. Simul.* **17** (2011) 1725. <https://doi.org/10.1016/j.cnsns.2011.09.037>
- [7] Y. Cai *et al.*, *Rev. Mod. Phys.* **15** (2012) 054002.
- [8] H. Yoshida, *Phys. Lett. A* **150** (1990) 262. [https://doi.org/10.1016/0375-9601\(90\)90092-3](https://doi.org/10.1016/0375-9601(90)90092-3)
- [9] M. Weyrauch and D. Scholz, *Comput. Phys. Commun.* **180** (2009) 1558. <https://doi.org/10.1016/j.cpc.2009.04.007>
- [10] S. Blanes *et al.*, *Phys. Rep.* **470** (2009) 151. <http://dx.doi.org/10.1016/j.physrep.2008.11.001>
- [11] J.A. Oteo and J. Ros, *J. Phys. A* **24** (1991) 5751. <https://doi.org/10.1088/0305-4470/24/24/011>
- [12] M. Berz and K. Makino, COSY INFINITY 9.0 Beam Physics Manual, Technical report MSUHEP-060804, 2006

- [13] H.S. Dumas and J. Laskar, *Phys. Rev. Lett.* **70** (1993) 2975. <https://doi.org/10.1103/PhysRevLett.70.2975>
- [14] Y. Eldar and G. Kutyniok, *Compressed Sensing: Theory and Applications* (Cambridge University Press, Cambridge, 2015).

Fast Kicker for High Current Beam Manipulation in Large Aperture

V. Gambaryan¹ and A. Starostenko^{1,2}

¹Budker Institute of Nuclear Physics SB RAS, Novosibirsk, Russia

²Novosibirsk State University, Novosibirsk, Russia

Abstract

The pulsed deflecting magnet (kicker) project was worked out in Budker Institute of Nuclear Physics. The kicker design parameters are: impulsive force, 1 mT*m; pulse edge, 5 ns; impulse duration, 200 ns. The unconventional approach is that the plates must be replaced by a set of cylinders. The obtained magnet construction enables the field homogeneity to be controlled by changing current magnitudes in cylinders. Furthermore, we demonstrated the method of field optimization. In addition, measurement technique for the harmonic components was considered and the possibility of control harmonic components value was demonstrated.

Keywords

Kicker; impulse magnet; high current beam; field harmonic components.

1 Kicker actual design

Taking into account results obtained previously [1] at the Budker Institute of Nuclear Physics (BINP) a kicker prototype was developed. The magnet cross-section is shown in Fig. 1. The physical magnet length is ≈ 650 mm. The magnet aperture is 100 mm. The vacuum chamber diameter and the conductor cylinder diameter are 164 mm and 28 mm, respectively. The cylinders are made of steel, as is the body of the magnet. The ceramic feedthroughs were also developed at BINP.

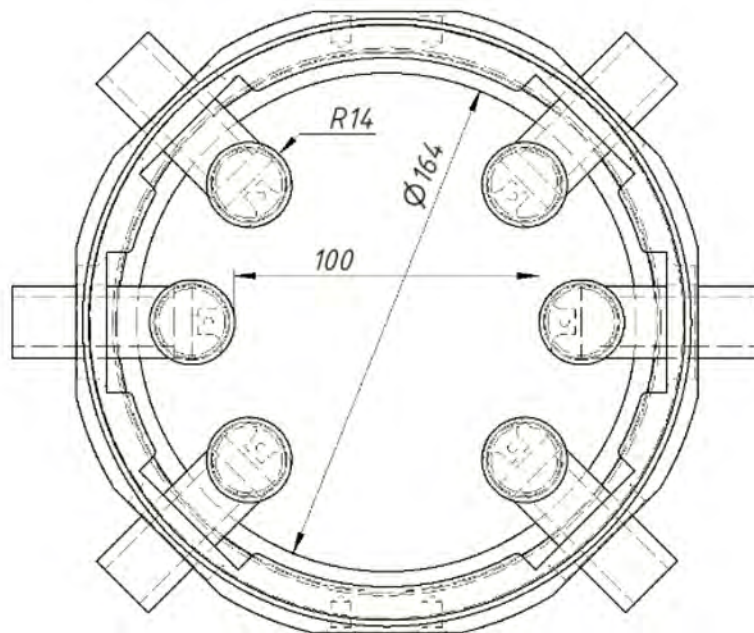


Fig. 1: Kicker actual design (all dimensions are in mm)

2 Magnetic field measurements

2.1 Experimental stand description

The experimental stand, shown in Fig. 2, consists of the following parts:

1. kicker;
2. pulse generator;
3. induction coil magnetometer;
4. VSDC2—precision digital signal integrators with accurate synchronization [2];
5. hand caliper;
6. step motors with controllers;
7. PC with specialized software.

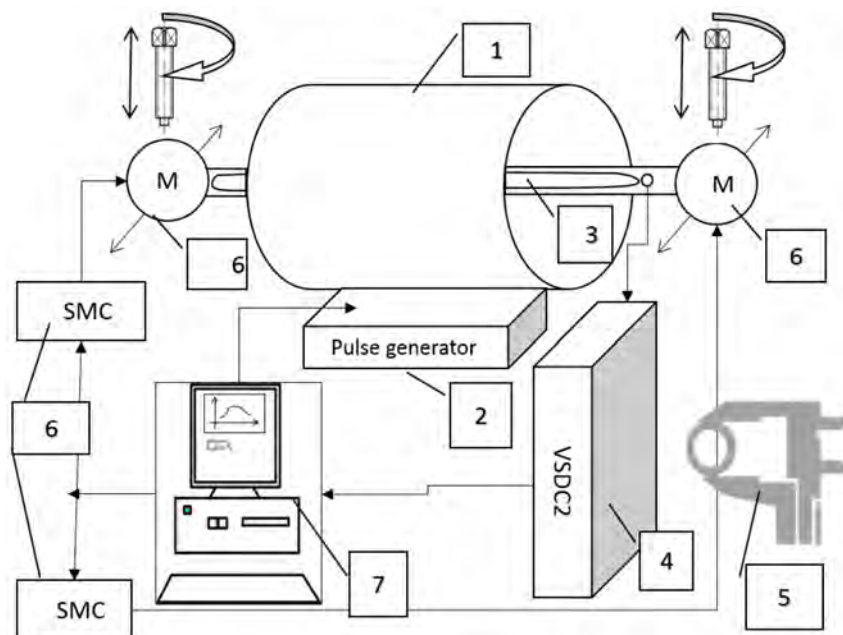


Fig. 2: Principal scheme of magnetic field measurement stand: 1, kicker; 2, pulse generator; 3, induction coil magnetometer; 4, VSDC2; 5, hand caliper; 6, step motors with controllers; 7, PC with specialized software; M, motor; SMC, step motor controller.

The kicker is fixed on a metal frame. Step motors provide movement in the horizontal plane. The vertical displacement of step motors is realized only by hand-turned screws. For both step motors, the vertical position must be controlled using a hand caliper. All of the stand components were precisely aligned with the help of the BINP Geodesy group.

2.2 Power pulse generator

The generator provides the following current characteristics: maximum frequency, 12.5 kHz; maximum current, 200 A.

At this stage in our research, we have a switching power supply that does not fully comply with our requirements. The final prototype bandwidth should be about 200 MHz. Therefore, we need to determine how precisely we can measure the magnetic field using a low frequency power supply.

A magnetic field distribution with frequency values ranging from 12.5 kHz to 1 MHz was simulated using finite element method magnetics (FEMM) [3] (see Fig. 3(a)). We need to compare the form of field dependence curves obtained. We calculate the percentage difference between the minimum and maximum values of each curve, normalized to the 1 MHz curve. Figure 3(b) demonstrates a decrease in discrepancy with increasing frequency. The discrepancy level in our case (12.5 kHz) is $\approx 4\%$. This result allows us to assume that our measurements are acceptable.

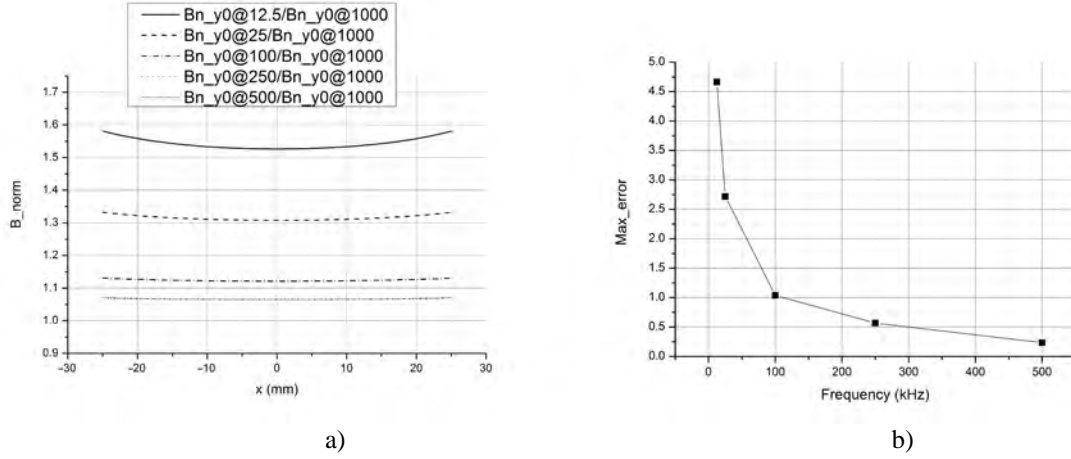


Fig. 3: (a) Magnetic field distribution versus position in central plane for different frequencies; (b) error level for different frequencies.

2.3 Induction coil magnetometer

The induction coil consists of five wire turns ($N = 5$). It has width $w = 5$ mm and length $l = 1000$ mm. The wire diameter is 0.2 mm. The coil base is made of fiberglass plastic strip. The induction coil principle is derived directly from Faraday's law:

$$E(t) = -\frac{d\Phi_B(t)}{dt}, \quad (1)$$

where E is the electromotive force (EMF) and Φ_B is the magnetic flux. Time integration of the EMF gives the magnetic flux. From the magnetic flux definition, we can determine the maximal magnetic field value:

$$B_{max} = \frac{-\int_0^{T_0} E(t) dt}{N \cdot w \cdot l}, \quad (2)$$

where T_0 is the integration time chosen such to provide a maximum integral value, N is the number of coil turns, and w and l are the coil width and length, respectively.

For example, Fig. 4 shows typical signals. The first channel (grey dashed curve) is a signal from the coil and the second channel (black curve) is a current monitor signal.

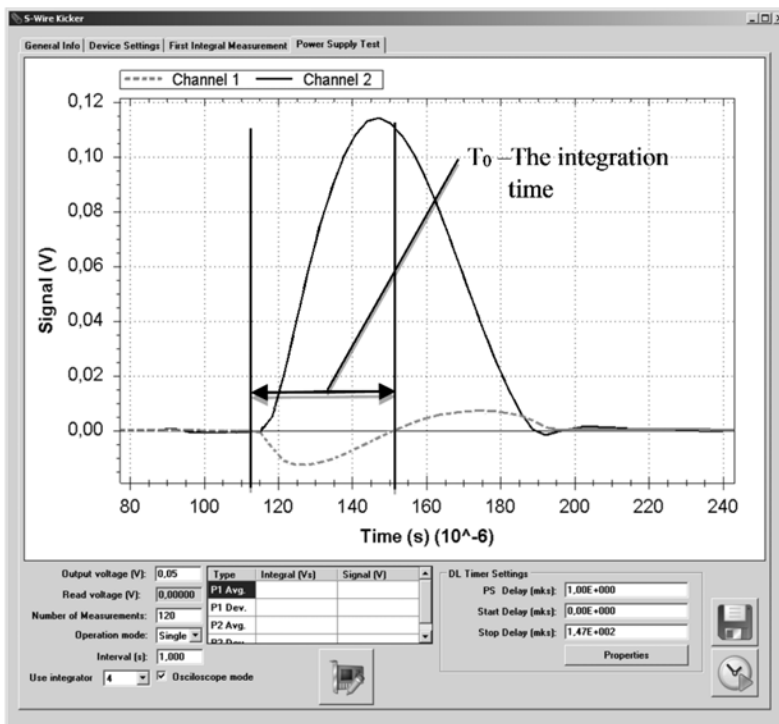


Fig. 4: Typical signals: Channel 1, signal from magnetometer; Channel 2, signal from current wave form

We supply the coil signal to VSDC2. Software ‘S-Wire Kicker’ created at BINP is integrated in the experimental stand. The program can control the step motors and pulse generator and store the measurements on a hard disk drive.

The magnetic field distribution was measured in the central part of the kicker. The area investigated is almost 2×2 cm square. Measurements were carried out at five vertical positions: -2 cm, -1 cm, 0 cm, 1 cm, and 2 cm. The horizontal shift was automatically realized using the ‘S-Wire Kicker’ program within the range -1.8 cm to 1.8 cm, in increments of 0.1 cm. Five measurements were made at each point, and the average taken. The obtained values were used to form a magnetic field distribution map. To compare experimental results with calculations, we simulated the FEMM task with the same current value obtained from the current monitor.

3 Magnetic field measurements

To measure the magnetic field distribution in the experiment, we used a single generator. The cable commutation scheme is shown in Fig 5.

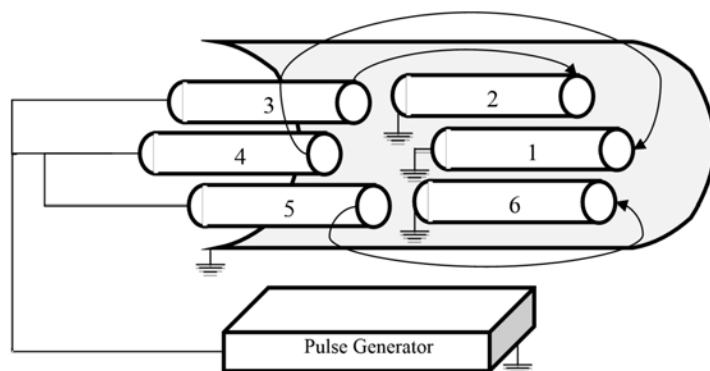


Fig. 5: Kicker commutation

A variable resistance unit was made with the aim of controlling a current in the separate cylinders. The commutation scheme with variable resistance unit is shown in Fig. 6. Using this scheme, an improved magnetic field distribution can be obtained.

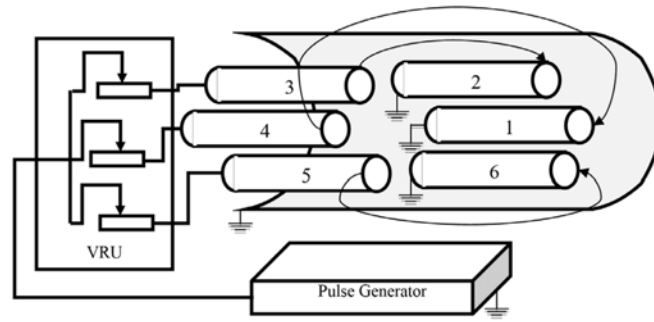


Fig. 6: Kicker commutation diagram with variable resistance unit (VRU)

3.1 Experimental results

In this part, we present the results of the magnetic field measurements. The experimental data in comparison with results calculated using FEMM are shown in Figs. 7 and 8 ((a) experimental; (b) calculation using FEMM).

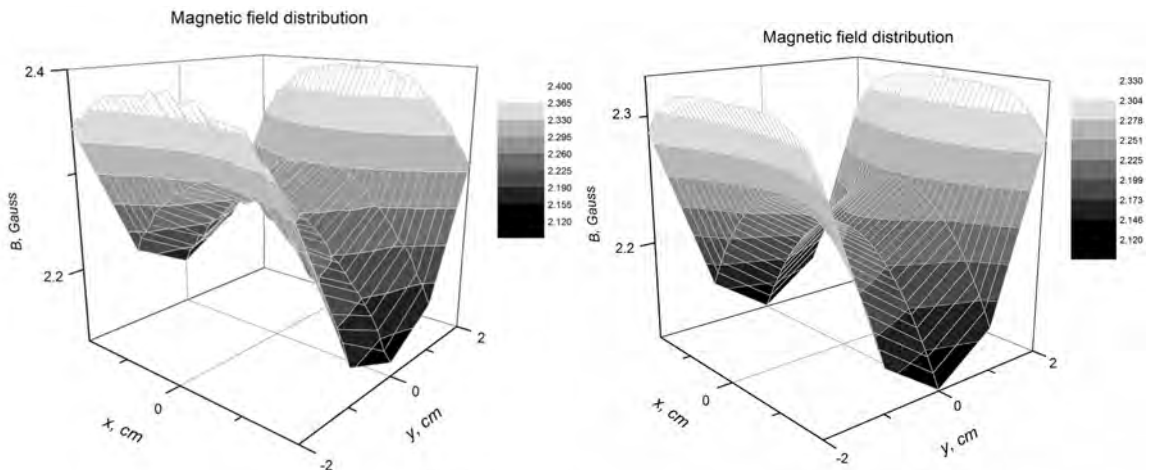


Fig. 7: Magnetic field distribution: (a) measured; (b) calculated

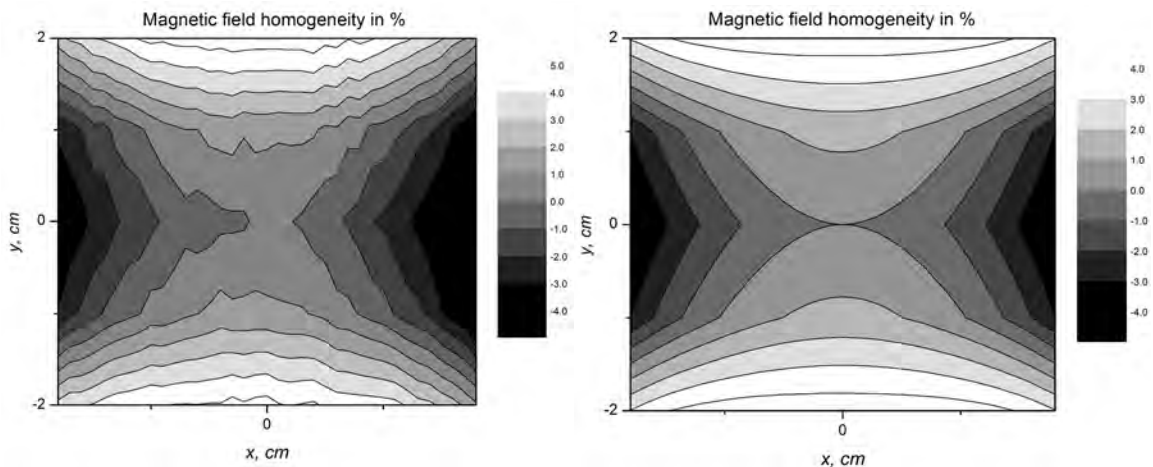


Fig. 8: Magnetic field homogeneity: (a) measured; (b) calculated

We can see that the measurements agree with the simulation to sufficient accuracy.

We have an opportunity of controlling the magnetic field distribution and homogeneity. To implement this, we need to set the specific current values in each conductor. The parametric optimization simulation was achieved in FEMM. We consider the upper and lower conductor currents to be I_0 A. The current in the central conductor is $k \cdot I_0$ A, where k is the optimizing parameter:

$$I_2 = I_6 = -I_3 = -I_5 = I_0, \quad I_1 = -I_4 = k \cdot I_0.$$

The optimization goal is to minimize ΔB , the field quality indicator:

$$\Delta B = \frac{B_{\max} - B_{\min}}{B_{\min}} \cdot 100\% . \tag{3}$$

The dependence of the magnetic field quality on the parameter k is shown in Fig. 9. As a result of the optimization, we obtain the following ratio: the first and fourth currents must be 1.5 times larger than the others, i.e. $k = 1.5$.

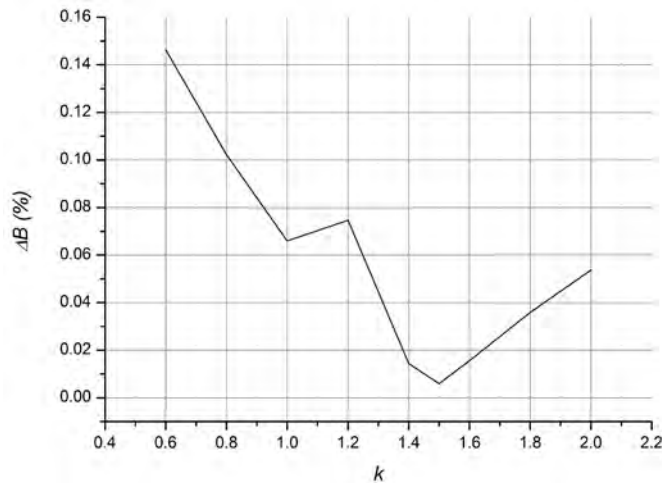


Fig. 9: Magnetic field quality as a function of current ratio

Using the variable resistance unit, the current in each conductor was tuned in accordance with the optimization results and the measurement was repeated. The results obtained are shown in Figs. 10 and 11.

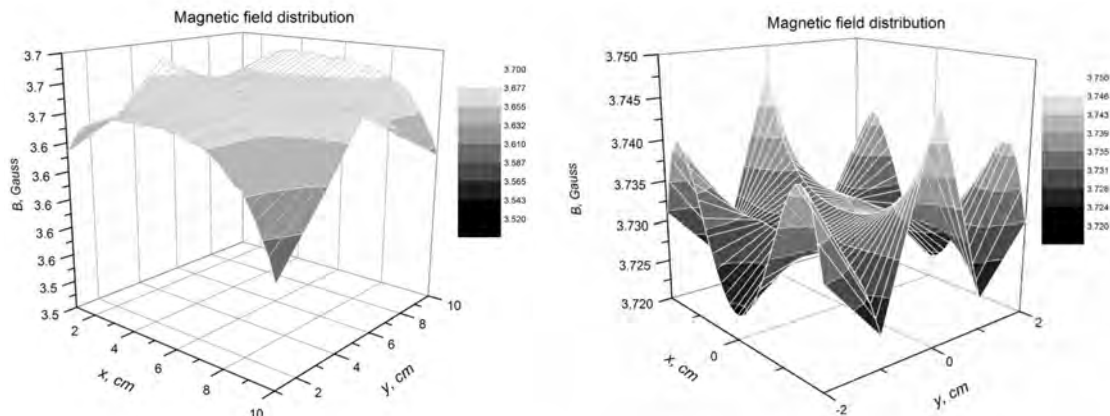


Fig. 10: Magnetic field distribution after current correction using variable resistance unit: (a) measured; (b) calculated.

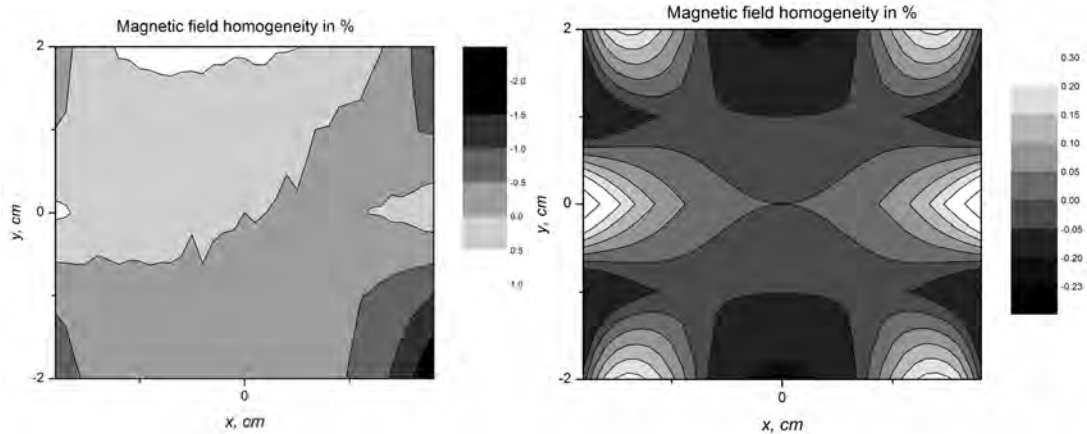


Fig. 11: Magnetic field homogeneity after current correction using variable resistance unit: (a) measured; (b) calculated.

The magnetic field measured experimentally turned out to be asymmetric. However, we see that the homogeneity value is close to the calculated one. The reason for this asymmetry is not completely explored. We have considered a number of assumptions, but they need to be checked. One of these is the limited induction coil magnetometer accuracy and another is that there may be some imperfections in the electrical contacts. We plan to repeat the measurements to provide more accurate results.

4 Field harmonics components

The chosen geometry allows us to use an interesting method of controlling the distribution of the magnetic field harmonics. Using FEMM, one can obtain the angular dependence of the normal and tangential components of the magnetic field along the circumference (see Fig. 12(a)). This dependence for an ideal dipole field is sinusoidal (see Fig. 12(b)). The field harmonics expansion allows us to judge how close to an ideal field such a field is.

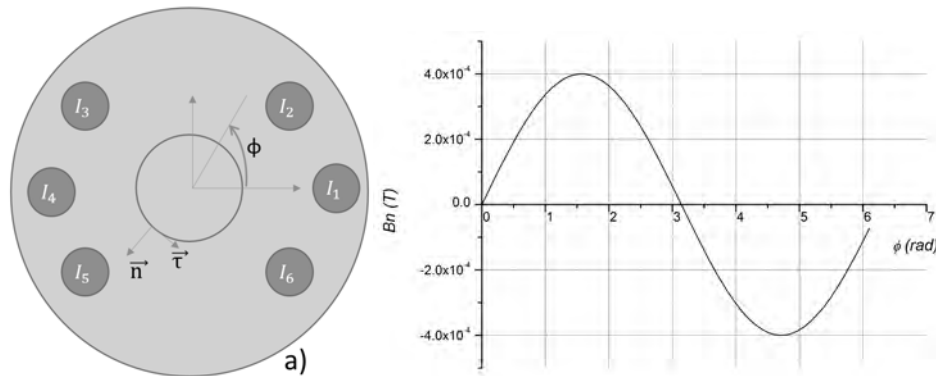


Fig. 12: Magnetic field along circumference: (a) magnet layout; (b) sinusoidal magnetic field signal

The normal and tangential magnetic field component functions can be expanded in a sine series (Eqs. 4 and 5). The coefficients of such series are harmonic components. The first coefficient is a dipole component, the second is a quadruple component, and so on.

$$B_n (\varphi) = B_{1n} \sin(\varphi) + B_{2n} \sin(2\varphi) + B_{3n} \sin(3\varphi) + B_{4n} \sin(4\varphi) + \dots \quad (4)$$

$$B_\tau (\varphi) = B_{1\tau} \sin(\varphi) + B_{2\tau} \sin(2\varphi) + B_{3\tau} \sin(3\varphi) + B_{4\tau} \sin(4\varphi) + \dots \quad (5)$$

For example, the harmonic components for an optimal current distribution case are shown in Fig. 13. As expected, all harmonics are extremely small except the first one. It is worth noting that the third and fifth components have different signs.

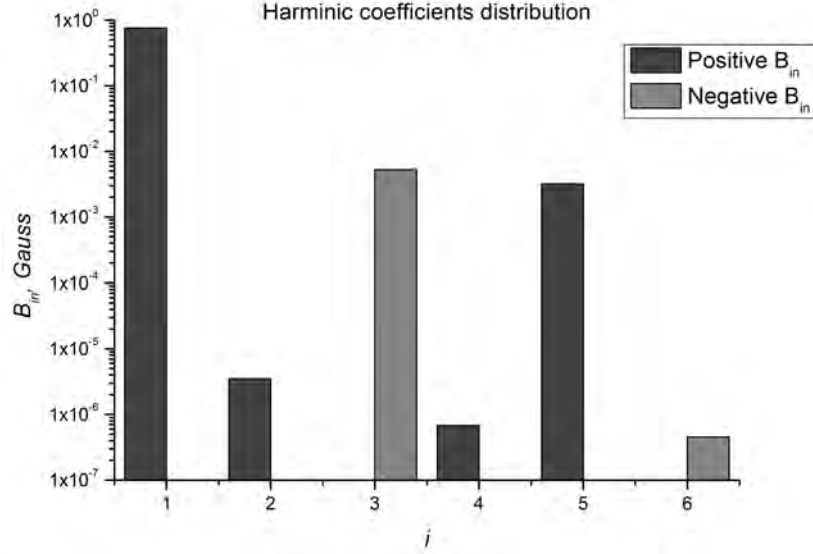


Fig. 13: Harmonic field component distribution in logarithmic scale

Owing to the presence of separated conductors, we can obtain the matrix of coefficients describing the dependence of harmonics changes on current changes in each conductor—a harmonics response matrix. This matrix was calculated:

$$K_n = \begin{pmatrix} K_{1,1} & \dots & K_{1,6} \\ \dots & \dots & \dots \\ K_{6,1} & \dots & K_{6,6} \end{pmatrix} = \begin{pmatrix} -1.28 \times 10^{-3} & -9.30 \times 10^{-4} & 9.30 \times 10^{-4} & 1.28 \times 10^{-3} & 9.30 \times 10^{-4} & -9.30 \times 10^{-4} \\ -6.73 \times 10^{-4} & 1.12 \times 10^{-4} & 1.12 \times 10^{-4} & -6.73 \times 10^{-4} & 1.12 \times 10^{-4} & 1.12 \times 10^{-4} \\ -3.05 \times 10^{-4} & 2.42 \times 10^{-4} & -2.42 \times 10^{-4} & 3.05 \times 10^{-4} & -2.42 \times 10^{-4} & 2.42 \times 10^{-4} \\ -1.31 \times 10^{-4} & 9.96 \times 10^{-5} & 9.96 \times 10^{-5} & -1.31 \times 10^{-4} & 9.96 \times 10^{-5} & 9.96 \times 10^{-5} \\ -4.52 \times 10^{-5} & 2.59 \times 10^{-5} & -2.59 \times 10^{-5} & 4.52 \times 10^{-5} & -2.59 \times 10^{-5} & 2.59 \times 10^{-5} \\ -1.30 \times 10^{-5} & 2.72 \times 10^{-6} & 2.71 \times 10^{-6} & -1.30 \times 10^{-5} & 2.73 \times 10^{-6} & 2.71 \times 10^{-6} \end{pmatrix}. \quad (6)$$

From the simulation results, we have a set of harmonics (see Fig. 13). This can be presented as a vector:

$$\vec{B}_{n0} = \begin{pmatrix} B_{1n0} \\ \dots \\ B_{6n0} \end{pmatrix} = \begin{pmatrix} 7.56 \times 10^{-1} \\ 3.52 \times 10^{-6} \\ -5.26 \times 10^{-3} \\ 6.81 \times 10^{-7} \\ 3.21 \times 10^{-3} \\ -4.55 \times 10^{-7} \end{pmatrix}. \quad (7)$$

We consider \vec{B}_{n0} as optimal. The experimentally measured set of harmonics is likely to be different from the optimal. To correct it, we need to add corrections to the currents. The current deviation vector can be obtained by multiplying the inverse matrix K by a harmonic deviation vector:

$$\vec{\Delta I} = K_n^{-1} \vec{B}_n. \quad (8)$$

To verify this approach, we present the following calculations. For an optimal current distribution, we have a certain set of harmonics $\overrightarrow{B_{n0}}$. Calculations in FEMM with random changes in the current vector give us a new set of harmonics:

$$I' = I_0 + \begin{pmatrix} -0.1 \\ 0.2 \\ 0.1 \\ -0.15 \\ 0.11 \\ 0.2 \end{pmatrix}; \quad \overrightarrow{B_{n_error}} = \begin{pmatrix} 7.56 \times 10^{-1} \\ 2.40 \times 10^{-4} \\ -5.22 \times 10^{-3} \\ 9.42 \times 10^{-5} \\ 3.21 \times 10^{-3} \\ 4.46 \times 10^{-6} \end{pmatrix}. \quad (9)$$

Then we calculate the harmonic deviation vector and multiply it by an inverse matrix. We get a vector, which is the optimum current deviation vector:

$$\overrightarrow{\Delta B_n} = \overrightarrow{B_{n_error}} - \overrightarrow{B_{n0}} = \begin{pmatrix} -2.41 \times 10^{-4} \\ 2.37 \times 10^{-4} \\ 3.07 \times 10^{-5} \\ 9.35 \times 10^{-5} \\ 2.65 \times 10^{-6} \\ 4.91 \times 10^{-6} \end{pmatrix} \quad (10)$$

$$\overrightarrow{\Delta I} = K_n^{-1} \overrightarrow{B_n} = \begin{pmatrix} -0.1 \\ 0.076315 \\ 0.055879 \\ -0.15 \\ 0.154121 \\ 0.323674 \end{pmatrix}. \quad (11)$$

Then we subtract it from the current values of the current (Eq. 12), repeat the calculation using FEMM and check the harmonics (Eq. 13):

$$\overrightarrow{I''} = \overrightarrow{I'} - \overrightarrow{\Delta I} \quad (12)$$

$$\overrightarrow{B_{n1}} = \begin{pmatrix} 7.56 \times 10^{-1} \\ 3.51 \times 10^{-6} \\ -5.26 \times 10^{-3} \\ 6.82 \times 10^{-7} \\ 3.21 \times 10^{-3} \\ -4.23 \times 10^{-7} \end{pmatrix}. \quad (13)$$

The small difference between the new values of harmonics and the optimum shows the efficiency of the method. The harmonic vector has been corrected with a very good accuracy:

$$\vec{B}_{n1} - \vec{B}_{n0} = \begin{pmatrix} -3.29 \times 10^{-10} \\ -4.64 \times 10^{-9} \\ 2.12 \times 10^{-9} \\ 8.23 \times 10^{-10} \\ -1.09 \times 10^{-8} \\ 3.19 \times 10^{-8} \end{pmatrix}. \quad (14)$$

5 Summary

We carried out magnetic field measurements. For this purpose, a magnetic measurement stand was created and tested. The correction technique for harmonic components was theoretically verified. Our future aims are to carry out more precise measurements and to implement the magnetic field quality improvement procedure.

References

- [1] V.V. Gambaryan and A.A. Starostenko, Fast kicker, Proc. 6th International Particle Accelerator Conf., Richmond, VA, 2015, paper MOPTY033, p. 1001.
<https://jacowfs.jlab.org/conf/proceedings/IPAC2015/papers/mopty033.pdf>
- [2] A.M. Batrakov *et al.*, *Optoelectron. Instrum. Data Process.* **51** (2015) 51.
<http://dx.doi.org/10.3103/S8756699015010082>
- [3] <http://www.femm.info>, last accessed September 10th 2016.

Realistic Approach to Beam Dynamics Simulation with Synchrotron Radiation in High Energy Circular Lepton Colliders

S.A. Glukhov, E.B. Levichev
BINP SB RAS, Novosibirsk, Russia

Abstract

In extremely high energy circular lepton colliders, correct consideration of synchrotron radiation is important for beam dynamics simulation. We developed a fast precise effective method to track particles in a realistic lattice when the radiation effects are distributed along the orbit [1]. In the present paper we study an effect of decreasing dynamic aperture due to radiation from quadrupole lenses in the FCC-ee lepton collider.

Keywords

Synchrotron radiation; simulation; CUDA.

1 SR simulation techniques

1.1 Concentrated SR losses

A simple way to simulate SR in a circular lattice is to apply the following transformation to the coordinates of all particles once per turn at arbitrary azimuth s_0 [2] (the formulae are simplified for the case of flat lattice without betatron coupling)

$$\begin{aligned} x &\mapsto a_x(x - \eta_x \delta) + \eta_x \delta + b_x \hat{r}_1 \\ p_x &\mapsto a_x(p_x - \eta'_x \delta) + \eta'_x \delta + b_x(\hat{r}_2 - \alpha_x \hat{r}_1)/\beta_x \\ y &\mapsto a_y y + b_y \hat{r}_3 \\ p_y &\mapsto a_y p_y + b_y(\hat{r}_4 - \alpha_y \hat{r}_3)/\beta_y \\ \delta = \Delta E/E_0 &\mapsto e^{-\frac{T_0}{2\tau_\delta}} \delta + \sigma_\delta \sqrt{1 - e^{-\frac{T_0}{\tau_\delta}}} \hat{r}_5 \end{aligned} \quad , \quad (1)$$

where

$$a_u = e^{-\frac{T_0}{2\tau_u}}, \quad b_u = \sqrt{\varepsilon_u \beta_u \left(1 - e^{-\frac{T_0}{\tau_u}}\right)},$$

E_0 — reference energy, T_0 — revolution period, σ_δ — energy spread, τ_u — damping times ($u = x, y$), ε_u — emittances, β_u , α_u , η_x and η'_x — optical functions at s_0 , and $\hat{r}_1 \dots \hat{r}_5$ — random values with standard distribution.

1.2 Distributed SR losses

There is a more natural way of SR simulation consisting in distribution of the corresponding coordinate transformations over the whole lattice. One of such techniques is described in [3]. The method used in the present paper was developed on the basis of it and described in [1].

Let us consider a dipole magnet of a length L , bending angle θ , quadrupole gradient k_1 and rotation angles φ_1, φ_2 for the entrance and exit pole faces respectively. When an electron with a relativistic factor γ enters the dipole with an initial horizontal coordinate x_0 and energy deviation δ_0 , it follows an arc with a radius $\rho = L/\theta$ and radiates N energy quanta. N has a Poisson distribution with a mean value of \bar{N} :

$$\bar{N} = \frac{5\sqrt{3}}{6} \alpha \theta \gamma_0 (1 + k_1 \rho x_0) (1 + h^* x_0),$$

where

$$h^* = \frac{1}{\rho} - \frac{\tan \varphi_1 + \tan \varphi_2}{L},$$

α is the fine structure constant. The energy radiated in each quantum is

$$\Delta_i \delta = -\frac{3\lambda_e}{2\rho} \gamma_0^2 (1 + \delta_0)^2 (1 + k_1 \rho x_0) y_i, \quad i = 1 \dots N,$$

where λ_e is the reduced electron Compton wavelength; $y_i \in SR$, which means that y_i has the so-called SR-distribution whose distribution density function is closely related to the well-known SR spectral power density function [1]. With a sufficient accuracy this distribution can be generated in the following way: let ξ have a uniform distribution over $[0; 1]$ segment, then

$$f(\xi) = C (-\ln(1 - \xi^a))^{3/a} \in SR,$$

where $C = 0.5770254$, $a = 2.535609$.

1.3 Distributed SR losses in dipoles

Energy deviation due to SR photon emission affects particle motion in the bending plane. In a flat lattice all bends are horizontal, and hence x and p_x are expected to change along with δ . The radiation damping in the magnet in both transversal planes is proportional to the magnet's contribution to the I_2 integral; the squared quantum excitation amplitude is proportional to the contribution to I_{5x} . The equilibrium distribution of the horizontal coordinates is Gaussian, and thus we can apply transformations (1) to x and p_x in each bending magnet separately, assuming that the addition due to quantum excitation in each magnet is also Gaussian. So, all radiation acts in the magnet can be simulated at once at its exit pole face. Finally, the following transformation should be applied to the coordinates of each particle after tracking through each bending magnet

$$\begin{aligned} x &\mapsto e^{c_{1x}\Delta\delta}(x - \eta_x\delta) + \eta_x(\delta + \Delta\delta) + c_{2x}\hat{r}_1\sqrt{\Delta^2\delta}, \\ p_x &\mapsto e^{c_{1x}\Delta\delta}(p_x - \eta'_x\delta) + \eta'_x(\delta + \Delta\delta) + c_{2x}\frac{\hat{r}_2 - \alpha_x\hat{r}_1}{\beta_x}\sqrt{\Delta^2\delta}, \\ y &\mapsto e^{c_{1y}\Delta\delta}y, \quad p_y \mapsto e^{a_y\Delta\delta}p_y, \quad \delta \mapsto \delta + \Delta\delta, \end{aligned} \quad (2)$$

where

$$\begin{aligned} \Delta\delta &= \sum_{i=1}^N \Delta_i\delta, \quad \Delta^2\delta = \sum_{i=1}^N (\Delta_i\delta)^2, \quad \Delta_i\delta \in SR \\ c_{1x,1y} &= \frac{3T_0}{2\tau_{x,y}r_e\gamma_0^3 I_2}, \\ c_{2x} &= \sqrt{\frac{24\sqrt{3}}{55} \frac{\varepsilon_x\beta_x \langle H_x \rangle}{\alpha\gamma_0^5\lambda_e^2 I_{5x}}} \left(1 - e^{-\frac{T_0}{\tau_x}}\right), \end{aligned}$$

I_2 and I_{5x} — radiation integrals, $\langle H_x \rangle$ — horizontal dispersion invariant averaged over the magnet, β_x , α_x , η_x and η'_x — horizontal optical functions at the exit pole of the magnet, \hat{r}_1 and \hat{r}_2 — random values with standard distribution. Quantum excitation in the vertical plane can be simulated once per turn, as in (1).

Distributed energy losses lead to variation of the equilibrium beam energy $\langle\delta\rangle$ along the lattice: it drops in bending magnets and rises in RF cavities. This is the so-called sawtooth effect, which leads to the closed orbit distortions. It can be cured by a variation of magnetic field in beamline elements in proportion to changing equilibrium energy (magnet tapering). Besides, in the simulations the following transformation should be applied to the horizontal coordinates of each particle after each dipole:

$$\begin{aligned} x &\mapsto x + \rho(1 - \cos\theta) \Delta\langle\delta\rangle, \\ p_x &\mapsto p_x + \sin\theta \Delta\langle\delta\rangle, \end{aligned}$$

where $\Delta\langle\delta\rangle$ is the variation of equilibrium energy deviation in the dipole.

1.4 Distributed SR losses in quadrupoles

A particle follows a curved trajectory and therefore emits SR photons not only in dipoles but also in other beamline elements. SR in strong final focus quadrupoles may affect particle dynamics significantly, especially at high energy. The simplest way to study this effect is to consider each strong quadrupole as a “variable strength dipole” with parallel pole faces and no quadrupole gradient. This fictitious dipole acts in both transversal planes and has different bending angles and radii of curvature on each turn for each particle. These values will be different for horizontal and vertical planes:

$$\theta_x = |p_{x1} - p_{x0}|, \quad \theta_y = |p_{y1} - p_{y0}|, \quad \rho_{x,y} = L/\theta_{x,y},$$

where p_{x0} and p_{y0} are the transversal momenta at the entrance pole face, and p_{x1} and p_{y1} are the transversal momenta at the exit pole face of the quadrupole. So, radiation in both transversal planes should be simulated independently:

$$\begin{aligned} \bar{N}_{x,y} &= \frac{5\sqrt{3}}{6} \alpha \theta_{x,y} \gamma_0, \quad N_{x,y} \in \text{Poisson}(\bar{N}_{x,y}), \\ (\Delta_i \delta)_{x,y} &= -\frac{3\lambda_e}{2\rho_{x,y}} \gamma_0^2 (1 + \delta_0)^2 y_i, \quad i = 1 \dots N_{x,y}, \\ y_i &\in SR, \end{aligned}$$

$$\begin{aligned} \Delta\delta &= \sum_{i=1}^{N_x} (\Delta_i \delta)_x + \sum_{i=1}^{N_y} (\Delta_i \delta)_y, \\ \Delta^2\delta &= \sum_{i=1}^{N_x} ((\Delta_i \delta)_x)^2 + \sum_{i=1}^{N_y} ((\Delta_i \delta)_y)^2. \end{aligned}$$

Then transformation (2) should be applied.

2 Simulation results for FCC-ee

The simulation technique described above was implemented as part of TrackKing simulation program [4]. FCC-ee is a 100-km e+e- collider with a beam energy of 45–175 GeV. Simulations were performed for a preliminary version of 175 GeV FCC-ee lattice with 4 different algorithms: without SR, with concentrated SR, with distributed SR and tapering, and with distributed SR, tapering and SR in all quadrupoles. The dynamic apertures (DAs) in units of beam sizes are shown in Fig. 1.

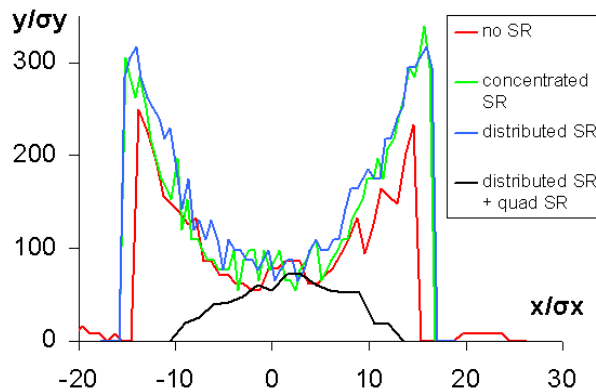


Fig. 1: DAs with different SR simulation modes

3 Discussion

Several effects can be noted in the results presented above. Firstly, the DA slightly decreases when SR is switched off. The cause is that in such a case initially unstable particles do not damp towards a stable

phase space region and are thus lost eventually. This case is not a concern because it is only hypothetical. Secondly, results for concentrated and distributed simulations of SR in dipoles are in good agreement. And finally one can see that SR in quadrupoles reduces the DA significantly.

J.M. Jowett was the first to describe the latter effect [5]. The explanation is that synchrotron motion of particles with large betatron amplitudes becomes unstable due to SR losses in quadrupoles. It is not a single turn effect because energy radiated by a particle from quadrupoles during one turn (15 MeV) is only 5% of the equilibrium beam energy spread. Fig. 2 shows phase trajectories of synchrotron and horizontal betatron motion for an ensemble of on-energy particles with an initial horizontal deviation of $12.5 \sigma_x$; the vertical motion is not excited and SR in quadrupoles is switched on. As one can see, strong synchrotron oscillations with an amplitude of up to $7 \sigma_\delta$ are induced. During the first few synchrotron periods, particles that reached the energy acceptance boundary are lost, and then the others are damped towards a stable region. Fig. 3 shows phase trajectories of synchrotron and horizontal betatron motion for

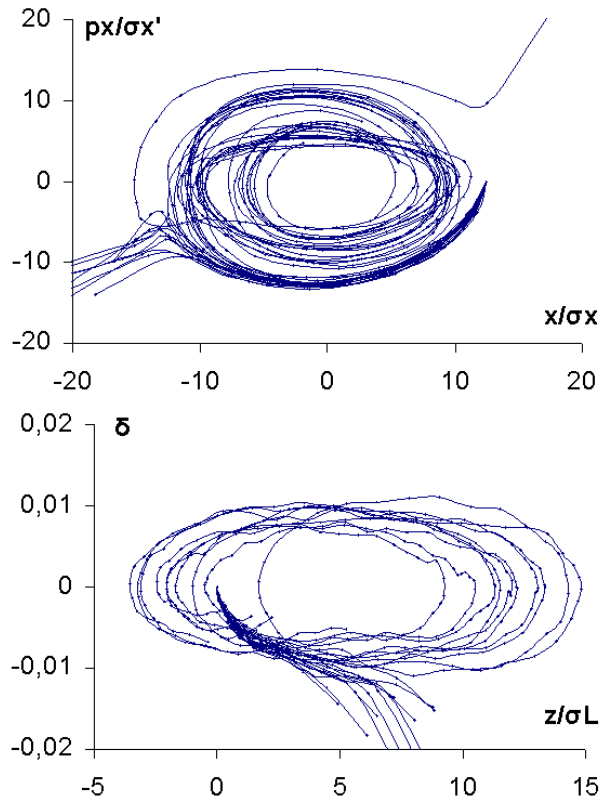


Fig. 2: Phase trajectories for particles with $x_0 = 12.5 \sigma_x$; SR in quadrupoles is switched on

particles with the same initial conditions but with SR in quadrupoles switched off. In that case there is no sign of particle losses because strong synchrotron oscillations are not induced. Therefore, the effect of the DA shrinking due to SR in quadrupoles is highly non-equilibrium. So, it cannot be fully described in terms of radiation integrals because they are applied to an equilibrium beam state only.

The maximum induced energy deviation is reached after one quarter of synchrotron period and can be estimated in the following way:

$$\langle \Delta \delta \rangle = \frac{1}{4\nu_s} \oint \frac{\langle U_q(s) \rangle ds}{E_0},$$

where U_q is the energy radiated from quadrupoles and $\langle \dots \rangle$ means averaging over beam particles. The

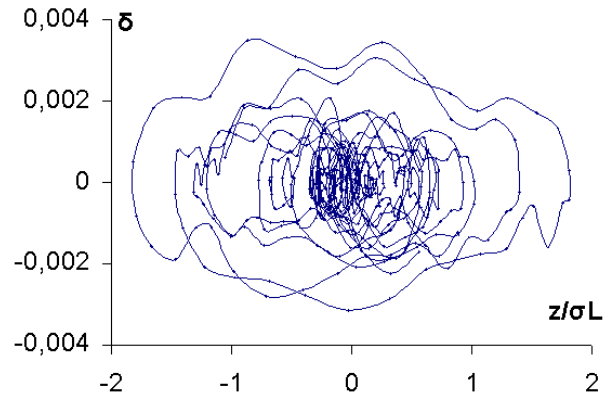


Fig. 3: Phase trajectories for particles with $x_0 = 12.5 \sigma_x$; SR in quadrupoles is switched off

energy radiated by a single particle from one quadrupole of a length L_q and strength K_1 is

$$U_q = \frac{C_\gamma E_0^4 (K_1 L_q x)^2}{2\pi L_q}.$$

Numerical estimations for the given lattice can be obtained using the following substitution:

$$x = n \sqrt{\varepsilon_x \beta_x},$$

where n is the initial horizontal coordinate expressed in horizontal beam sizes. Finally, the radiation-induced energy deviation for the lattice under consideration is the following:

$$\langle \Delta \delta \rangle = 0.58\% \left(\frac{n}{10} \right)^2 \quad (\approx 0.91\% \text{ for } x_0 = 12.5 \sigma_x).$$

It is in accordance with Fig. 2.

4 Conclusion

Conventional SR simulation techniques with SR concentrated at one azimuth is applicable even to lattices with extremely high radiation energy loss rate and tapering. SR in quadrupoles is also important for such lattices, but it can be taken into account only using distributed SR simulation techniques. Results of FCC-ee lattice simulations show that SR in quadrupoles reduces the DA significantly because of induced synchrotron oscillations of particles with large initial transversal amplitude. A large energy deviation can be reached during the first synchrotron period. If the particle is not lost after that, then it forgets its initial conditions and remains stable.

Acknowledgements

We wish to thank A.V. Bogomyagkov, P.A. Piminov, and D.N. Shatilov for the fruitful discussions on the present topic. This work has been supported by Russian Science Foundation (project N14-50-00080).

References

- [1] S. Glukhov and E. Levichev, Realistic Approach for Beam Dynamics Simulation with Synchrotron Radiation in High Energy Circular Lepton Colliders. <https://doi.org/10.18429/JACoW-ICAP2015-THCBC2>, <http://accelconf.web.cern.ch/AccelConf/ICAP2015/papers/thcbc2.pdf>

- [2] K. Ohmi, K. Hirata and K. Oide, *Phys. Rev. E* **49** (1994) 751.
- [3] G. J. Roy, *Nucl. Instrum. Meth. A* **298** (1990) 128. [https://doi.org/10.1016/0168-9002\(90\)90608-9](https://doi.org/10.1016/0168-9002(90)90608-9)
- [4] S. Glukhov, E. Levichev, S. Nikitin, P. Piminov, D. Shatilov and S. Sinyatkin, 6D Tracking with Compute Unified Device Architecture (CUDA) Technology. <https://doi.org/10.18429/JACoW-ICAP2015-WEP34>
- [5] F. Barbarin, F. C. Iselin and J. M. Jowett, Particle dynamics in LEP at very high-energy, *Conf. Proc. C* **940627** (1994) 193.

The VEPP-2000 Collider Control System: Operational Experience

A.I. Senchenko, D.E. Berkaev, A.P. Lysenko, Yu.A. Rogovsky, P.Yu. Shatunov
BINP, Novosibirsk, Russia

Abstract

The VEPP-2000 collider was commissioned and operated successfully in 2010-2013. During the operation the facility underwent continuous updates and experience in maintenance was acquired. Strong cooperation between the staff of the accelerator complex and the developers of the control system proved effective for implementing the necessary changes in a short time.

Keywords

Control system; accelerator; collider.

1 Introduction

VEPP-2000 is a collider with a luminosity up to $1 \times 10^{32} \text{cm}^{-2} \text{s}^{-1}$ and a beam energy up to 1 GeV per beam [1-2]. This project is an extension of the previous VEPP-2M facility. Construction of VEPP-2000 started in 2001. In 2007 first luminosity was produced. Since the end of 2009, the collider has delivered beams to the experiments. In 2013 a long shutdown started, which was dedicated to the upgrade of a wide range of subsystems. During operation VEPP-2000 used the injection chain of its predecessor VEPP-2M (see grey area in Fig. 1). This was later replaced with a link-up to the new injection complex VEPP-5 [2]. It consists of the old beam production system and Booster of Electrons and Positrons (BEP) with an energy limit of 800 MeV. The collider is equipped with two particle detectors [3], the Spherical Neutral Detector (SND) and the Cryogenic Magnetic Detector (CMD-3), which are located at dispersion-free low-beta straight sections. The final focusing is realized using superconducting 13 T solenoids.

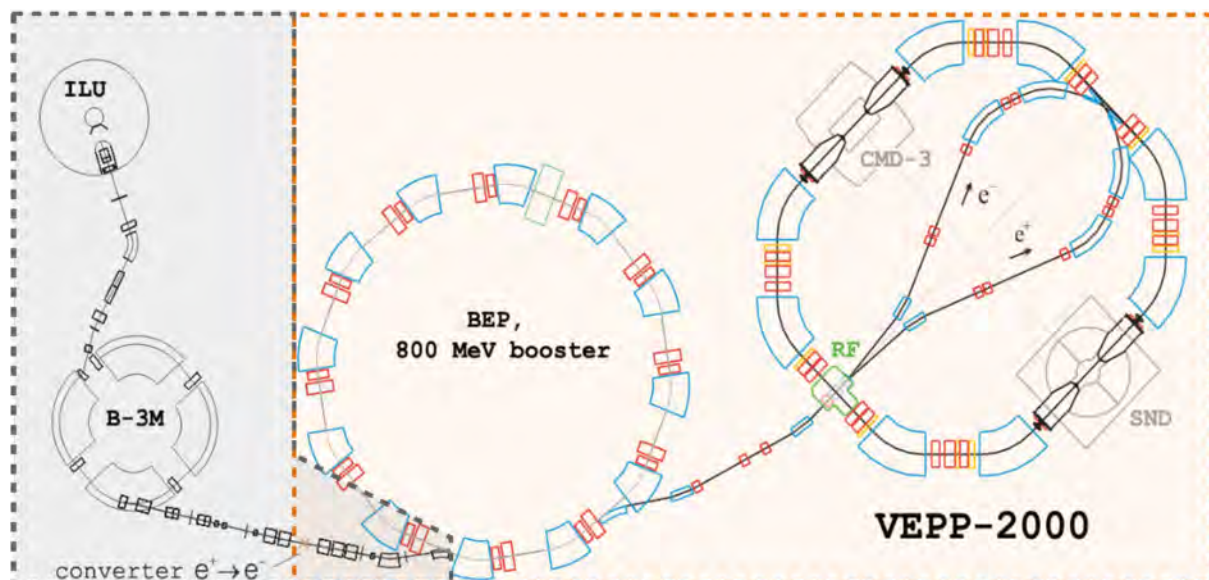


Fig. 1: The layout of the VEPP-2000 facility

2 Control system

The control system of the VEPP-2000 accelerator facility consists of the following tightly coupled parts (see Fig. 2):

- Hardware – analog-to-digital converters, digital-to-time converters, etc.,
- Software – system software (operating system, databases), application software (hardware servers, user level),
- Infrastructure – computers, networks.

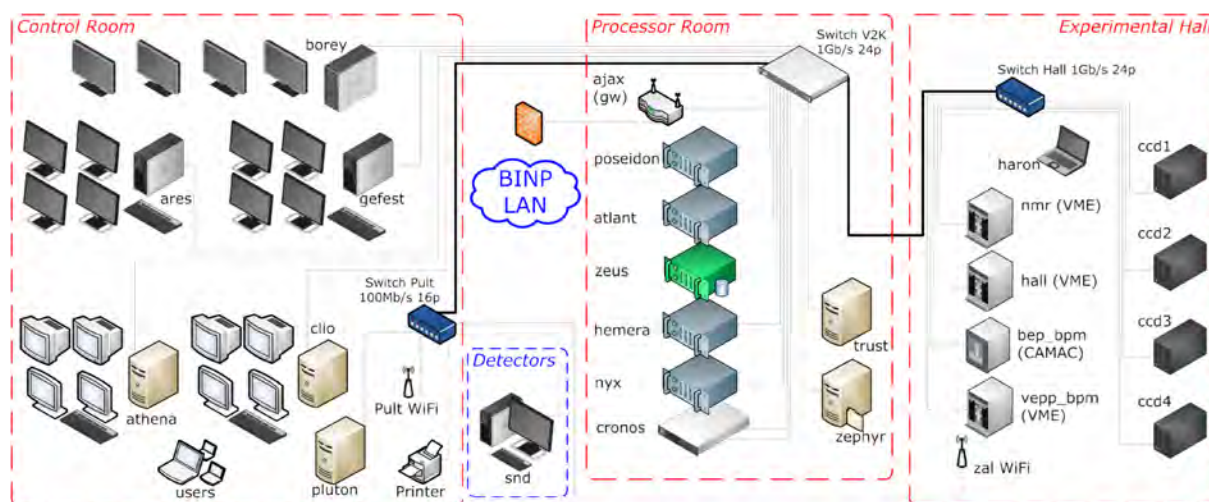


Fig. 2: The network layout of the VEPP-2000 acceleration complex

From the automation point of view, the accelerator complex VEPP-2000 is a complicated system. Over 2000 control channels and 3000 monitoring channels and their joint usage impose rigid restrictions to the control system. These channels are divided into two groups: scalars (like beam current or beam energy with a typical update rate of 1-2 Hz) and vectors (like CCD, BPM, pulsed element measurements).

2.1 Hardware

The VEPP-2M control system was based on the CAMAC standard and in-house BINP devices. Most of the CAMAC devices were designed and manufactured 20 years ago. It was decided to replace obsolete devices with modern ones. CAN-bus was chosen as the base technology [4]. CAMAC devices were left for systems with high data rates (like fast-ADCs) and legacy system which were due to be removed soon. A few VME devices were used for beam parameter measurements. All devices are BINP manufactured. Migration to CAN-bus based devices allows to install devices near the control units and to reduce the number of cabling connections.

Significant efforts were made to design hardware parts as a set of loosely coupled subsystems. Such an approach facilitates changes or upgrades of individual subsystems without affecting other subsystems. For example, CAMAC devices for the measurement of pulsed magnets were replaced by CAN-bus devices without affecting the whole control system.

2.2 Software

1.1.1 System software

Linux-based systems proved to be reliable. Therefore Gentoo Linux was chosen for the operating system. A source-based distribution was chosen, allowing for accurate configuration and tuning. During

experimental runs in 2010-2013 it appeared that system-wide updates or even software installation could only be done during shutdown periods. This resulted in high maintenance costs. Therefore it was decided to migrate to a binary distribution with long-term support, and a stable Debian release was chosen.

1.1.2 Application software

The application software development started at the same time as the assembly of the facility. A first version used for magnetic measurements had a two-layer client-server architecture. Through continuous updating the architecture was changed to a traditional tree-layer structure (see Fig. 3).

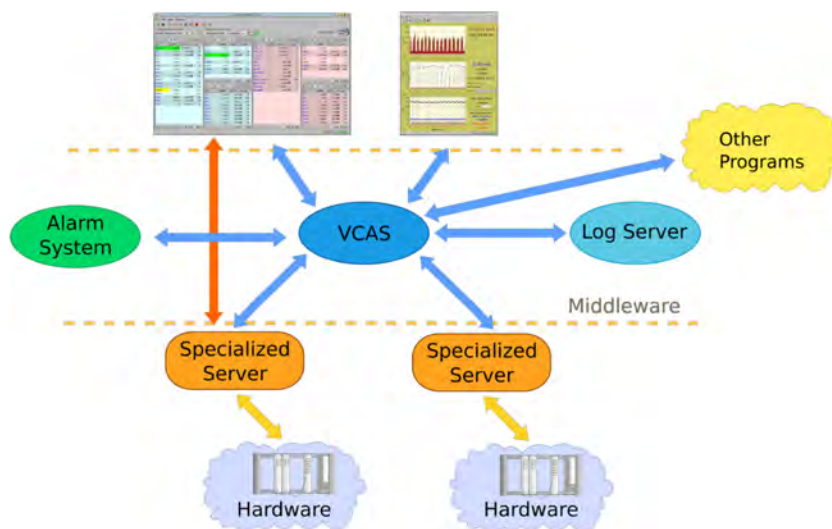


Fig. 3: The VEPP-2000 Software scheme

Special servers control CAN or CAMAC buses and provide access to hardware for client applications.

The middleware layer consists of applications that control particular subsystems and provide derived data for other applications. The main application of this layer is VCAS (VEPP-2000 Channel Access Server). It is similar to modern Message Queue Software (like AMPQ, RabbitMQ, ZeroMQ). It was developed to configure subsystems and applications via system-wide events or commands (injection, regime changing).

The third layer comprises GUI applications, which provide the operators of the accelerator complex with the controls for beam tuning and diagnostics. The developers interact frequently with the operators in order to achieve a convenient implementation.

Strict time constraints and the lack of appropriate open-source solutions resulted in the development of a text-based communication protocol. It satisfies most of the requirements (transferring small control commands and measurements with rates up to 1 Hz). However it was not designed for high data rates (CCD, BPM). This led to the creation of several incompatible protocols during operation.

Software that controls critical subsystem or should provide high responsiveness is implemented in C/C++. Python and Java are used for utilities and non-critical applications. The GUI is implemented with Qt library.

2.3 Infrastructure

The security and reliability of the network of experimental facility is an important issue. At the early stages of development of the control system it was decided to create a private network to reduce security

risks thereby preventing exposure of the control software to the Intranet. To provide access to external resources a gateway is used. This approach allows to protect the control system against Intranet failures.

Another important decision was to provide wireless connection across the facility (control room, experimental hall, control equipment room). It allows to reduce the number of cabling connections and local control panels.

3 Future applications

During the operation the VEPP-2000 team acquired significant experience in control system development and maintenance. Common use-cases were collected. This experience can be applied to other facilities. For example, new software developed for the VEPP-5 injection complex (which will be used as injector of positrons for the Super Charm-Tau factory) is based on concepts of the VEPP-2000 control software.

The experience can be also applied to the design of the control system of the Super Charm-Tau factory. Building a control system fully from scratch for such a facility would be very expensive. On the other hand, the use of out-dated or unsupported software or hardware would result in high maintenance costs. Furthermore there is the issue of technology changes and trends. More than ten years have passed since the start of the VEPP-2000 construction. During this time many new technologies and control system software applications have appeared or were significantly improved (TANGO, EPICS, BINP in-house). These are worth to be evaluated, for example in isolated subsystems or test stands. In this context work has started on developing a TANGO-based control system for a test stand at the BEP ring.

4 Conclusion

Construction of the VEPP-2000 control system started more than 10 years ago. During this period, it underwent significant changes. Experience acquired during the operation and continuous updates could be applied to other facilities, such as the Super Charm-Tau factory, a future mega-science project at BINP.

References

- [1] P.Yu. Shatunov et al., Status and perspectives of the VEPP-2000, *Phys. Part. Nuclei Lett.* **13** (2016) 995. <https://doi.org/10.1134/S154747711607044X>
- [2] A. Romanov et al., Status of the Electron-Positron Collider VEPP-2000, in Proc. of the PAC2013, Pasadena, USA, p.14. <http://accelconf.web.cern.ch/accelconf/pac2013/papers/mooaa2.pdf>
- [3] D. E. Berkaev et al., Commissioning of upgraded VEPP-2000 injection chain, in Proc. of the IPAC2016, Busan, Korea p. 3811. <http://accelconf.web.cern.ch/AccelConf/ipac2016/papers/thpor018.pdf>
- [4] T.V. Dimova et al., Recent Results on $e^+e^- \rightarrow \text{hadrons}$ Cross Sections from SND and CMD-3 Detectors at VEPP-2000 collider, *Nucl. Part. Phys. Proc.*, vol. 273-275, pp. 1991-1996, 2016.
- [5] A. Senchenko et al., VEPP2000 Collider Control System, PCaPAC'12, Kolkata, India, p. 267. <https://accelconf.web.cern.ch/accelconf/pcapac2012/papers/frcb04.pdf>